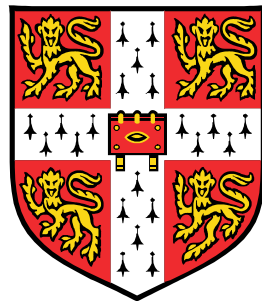


Light-Emitting Diodes from Polyfluorenes: Characterisation and Stability of Performance



Alexander J. A. B. Seeley

Trinity College, Cambridge

March 2003

**A dissertation submitted to the University of Cambridge
for the degree of Doctor of Philosophy**

Abstract

This thesis deals with polymer light-emitting diodes (LEDs) containing materials from the polyfluorene family, and investigates their behaviour when employed in device structures.

A study of poly(9,9'-dioctylfluorene-*co*-bis-N,N'-(4-butylphenyl)-bis-N,N'-phenyl-1,4-phenylenediamine) (PFB) by photothermal deflection spectroscopy (PDS) shows that the polymer undergoes a doping reaction with poly(styrene sulphonic acid). This is important because the two materials are found in intimate contact in LED structures. The conditions for reaction are investigated, and it is proposed that the reacted states are directly responsible for the drive-induced degradation of LEDs containing these two materials.

LEDs are studied which contain various combinations of poly(9,9'-dioctylfluorene-*co*-N-(4-butylphenyl)diphenylamine) (TFB) and poly(9,9'-dioctylfluorene-*co*-benzothiadiazole) (F8BT), using pulsed electroluminescence. A strongly morphology-dependent spike-transient is observed in the electroluminescence at turn-on, and this is investigated by numerical modelling. Although not all features of the system can be well represented in the model, the spike transient is explicitly predicted without the need to impose any special conditions. The origin of this feature is elucidated by repeatedly running the model to a range of end-points and studying the time-evolution of space-charge distributions which result.

Finally, F8BT devices are considered on their own, in order to study the evolution of device performance under low-intensity electrical excitation. A phenomenon is investigated in which the quantum efficiency is dramatically increased during the early stages of driving. Ionic motions are ruled out, and the observations are attributed to the trapping of charge in the vicinity of the anode, leading to enhanced hole injection. The reverse-bias behaviour of the effect, in which a further enhancement is seen, is also examined. The analogy is made with polymer LEDs in general which increase in performance following a period of reverse bias, and it is suggested that the causes may be related.

Acknowledgements

The work described in this thesis was carried out in the Optoelectronics Group at the Cavendish Laboratory, University of Cambridge, between October 1999 and November 2002. It was funded by the EPSRC in conjunction with Cambridge Display Technology. Additional support came from Trinity College, Cambridge.

My thanks go to my supervisor, Prof. Richard Friend, who has been an inspiration and a wise counsel. I also thank my industrial supervisor, Dr. Jeremy Burroughes, for the invaluable access granted to the people and facilities at CDT, and for the continued interest he and his colleagues have shown in my work.

In the lab, I am indebted to Ji Seon and Peter for their generous advice, and Neil, Jim, Dickon and Steve for their frequent insights. Catherine, Kieran, Lukas and Mike have shared the ups and downs of the Ph.D. road from day one with great good humour. JJ, Anna, Anick, Jo, Rich, Dave and a great many others have helped to make the OE Group a great place to work, while Sue, Ulrike, Richard and Roger have ensured that it continues to run smoothly. At CDT, Craig, Nicky and Nalin deserve a special mention.

No Ph.D. student can thrive without email and beer, and I am indebted to my friends for their dedicated support in those two activities – in no particular order: Andy, Carl, Martin, Sarah, Sharon, Simon, Stu, Spod, Svetty, Pooz and Punam.

I could not have got this far without Dan by my side. His understanding and encouragement from the day I decided to leave my job and embark on this journey cannot be underestimated. For him and for my family, for their love and support, I reserve my greatest thanks.

The material contained in this thesis is the result of my own work and includes nothing which is the outcome of work done in collaboration. This dissertation has not been submitted in whole or in part for the award of a degree at this or any other University, and does not exceed 60,000 words in length. The Appendices are included for completeness and do not form part of the dissertation presented for examination.

Alexander J. A. B. Seeley
March 2003

Table of Contents

1. Introduction.....	1
References	3
2. General Review.....	4
2.1 Conjugated polymers.....	4
2.2 Charged species	7
2.3 Neutral excited states – excitons.....	10
2.4 Polymer LEDs	12
2.5 Materials	20
2.6 Conclusions	23
2.7 References	23
3. Experimental Methods	29
3.1 Polymer Light Emitting Diodes.....	29
3.2 Absorption spectroscopy samples.....	36
3.3 Sample analysis	37
3.4 Device analysis	42
3.5 Numerical modelling	55
3.6 Conclusions	56
3.7 References	56
4. Interactions between PSSH and PFB	59
4.1 Background.....	59
4.2 Samples for study	60
4.3 Procedure	62
4.4 Results	62
4.5 Correlation with electrical degradation products.....	75
4.6 Likely mechanism for the oxidation	76
4.7 Discussion and Conclusions	77
4.7 References	79

5. Pulsed-Mode Measurements of Turn-on Transient Characteristics	81
5.1 Background.....	81
5.2 Devices for study	82
5.3 Pulsed measurements.....	83
5.4 Estimation of mobility	88
5.5 Modelling	91
5.6 Discussion and conclusions	99
5.7 References	100
6. Quantum Efficiency Increase in F8BT LEDs – Drive-Induced Enhancement	102
6.1 Background.....	102
6.2 Drive-Induced Enhancement – Initial Observations.....	103
6.3 Permanent degradation and recoverable enhancement.....	111
6.4 Photoluminescence efficiency and light-assisted recovery	119
6.5 Spectral changes	124
6.6 Charge backflow and thermal activation	129
6.7 Reverse bias and mobile ions	137
6.8 Impedance spectroscopy	146
6.9 Charge Modulated PDS	148
6.10 Transient measurements	152
6.11 Experimental summary	154
6.12 Candidate theory	156
6.13 Detailed consequences of hypothesis	157
6.14 Implications for device physics	161
6.15 Conclusions	162
6.16 References	163
7. Conclusions and Further Work	165
7.1 Interactions of PFB and PEDOT:PSS.....	165
7.2 Morphology and electroluminescence transients.....	166
7.3 Drive-induced enhancement effect in F8BT LEDs	166
7.4 Further investigations	167
7.5 New experiments	168
7.6 Conclusions	169
7.7 References	169

A. The PDS Rig - Notes.....	170
A.1 Part-by-part Tour	170
A.2 Replacement parts.....	172
A.3 Maintenance.....	174
A.4 Experimental procedure.....	175
A.5 Calibration and data processing.....	178
A.6 Errors during operation.....	180
A.7 Charge Modulated PDS experiment	182
A.8 Brief description	184
A.9 Program and data files	185
A.10 Late information	185
A.11 References.....	185
B. The Pulse Rig - Notes.....	186
B.1 Part-by-part tour.....	186
B.2 Replacement parts.....	190
B.3 Maintenance.....	191
B.4 Experimental procedures	191
B.5 Data processing.....	196
B.6 Problems during operation.....	196
B.7 Program files.....	197
C. The Test Box - Notes	198
C.1 Part-by-part tour.....	198
C.2 Replacement parts and maintenance	201
C.3 Experimental procedure.....	201
C.4 Data analysis	204
C.5 Charge backflow experiment	204
C.6 Program files.....	205

Abbreviations

The following abbreviations are frequently used in this thesis, and are summarised here for ease of reference.

DC	Direct Current
DMM	Digital Multimeter
EL	Electroluminescence
F8	Poly(9,9'-dioctylfluorene)
F8BT	Poly(9,9'-dioctylfluorene- <i>co</i> -benzothiadiazole)
GPIB	General Purpose Interface Bus
HOMO	Highest Occupied Molecular Orbital
IPA	Isopropanol
LED	Light-Emitting Diode
LUMO	Lowest Unoccupied Molecular Orbital
PANI	Polyaniline
PDS	Photothermal Deflection Spectroscopy
PEDOT:PSS	PEDT doped with PSSH
PEDT	Poly(3,4-ethylenedioxithiophene)
PFB	Poly(9,9'-dioctylfluorene- <i>co</i> -bis-N,N'-(4-butylphenyl)-bis-N,N'-phenyl-1,4-phenylenediamine)
PL	Photoluminescence
PMT	Photomultiplier tube
PPV	Poly(<i>p</i> -phenylene vinylene)
PSSH	Poly(styrene sulphonic acid)
PSU	Power Supply Unit
SCLC	Space-Charge Limited Current (or Conduction)
TFB	Poly(9,9'-dioctylfluorene- <i>co</i> -N-(4-butylphenyl)diphenylamine)
THF	Tetrahydrofuran
TOF	Time-of-Flight
TTL	Transistor-Transistor Logic
UV-Vis	UV-Visible Spectrometer/Spectroscopy
ZIF	Zero Insertion Force

1. Introduction

Since the first reports of electroluminescence from a conjugated polymer in 1990¹, research in the field of polymer light-emitting diodes (LEDs) and semiconducting polymers in general has attracted much attention²⁻⁹. In the intervening years advances in materials, processing and the underlying basic physics have led to devices which span the visible spectrum, endure many thousands of hours of continuous operation, and which are beginning to meet the requirements for commercial application. Indeed, the first consumer product to incorporate a polymer LED display has come to market in the past year¹⁰.

The same class of materials has been exploited for other aspects of their semiconducting properties. Both field-effect transistors^{11,12} and photovoltaic cells¹³ have been successfully demonstrated, and are undergoing development. FETs show promise for extremely high-volume and low-cost applications such as radio-frequency smart tags. Such devices may one day replace traditional laser-read barcodes on supermarket goods, allowing a whole trolley-load to be scanned in an instant. Likewise, though polymer photovoltaic cells may never approach the 33 % power conversion efficiency of the crystalline silicon solar-cells currently used on the International Space Station, their very low cost of production may allow cheap and non-polluting power to be brought to some of the poorest parts of the world.

Conjugated polymer LEDs show great promise for future use in large-area full-colour flat panel displays, due in large part to their ease of processing for instance by inkjet printing¹⁴. However a number of significant challenges remain before such goals can be achieved. Whilst single colour displays are now in production, the differential aging of the red, green and blue components in a full-colour display has not yet been resolved, and the achievement of a fuller understanding of the degradation processes of polymer LEDs is fundamental to any such solution.

This thesis discusses the behaviour of a certain state-of-the-art class of conjugated polymers – the polyfluorenes – in their role as the emissive components of polymer LEDs.

Chapter 2 provides a general review of the field. The properties of conjugated polymers and the origin of their semiconducting behaviour is described. The theory of polymer LEDs is then explored. Finally, the materials used in experimental devices in this work are reviewed.

Chapter 3 covers the experimental methods employed, beginning with the fabrication of devices and samples, and continuing with a summary of the various characterisation techniques used.

Chapter 4 is the first experimental chapter. It reports the use of Photothermal Deflection Spectroscopy (PDS) to investigate the interaction between one particular blue light-emitting polymer and a non-conjugated polymer which forms the majority component of the anode in polymer LEDs. Although these two materials are placed in intimate contact in the device structure, it is only now being realised that a reaction takes place between them which is detrimental to the device performance.

Chapter 5 reports the use of transient pulsed electroluminescence to investigate the behaviour at turn-on of polyfluorene LEDs with various internal structures. A sharp electroluminescence “spike” is seen, which is found to be strongly dependent on the morphology of the polymer layer. Although previous authors have proposed possible causes for this behaviour, numerical simulations reveal that it can be accounted for by existing principles of device behaviour.

Chapter 6 is the final and longest experimental chapter. It describes the investigation of a previously unreported phenomenon, in which the performance of a polymer LED is dramatically improved during the early stages of electrical driving. A battery of experiments are described in order to identify the nature of the behaviour and the range of situations in which it can be identified, and ultimately to propose a plausible theory for the observed phenomena.

Chapter 7 concludes the thesis, summarising the important findings, and suggesting possible avenues for further investigation.

Appendix A describes in detail the PDS Rig, providing details of its design, maintenance and operation for the benefit of future users.

Appendix B provides a similar summary for the Pulse Rig, ensuring that useful results can continue to be gained from the rig with minimal disruption and delay due to its complex behaviour.

Appendix C explains the principles and operation of the Test Box. This apparatus was designed and constructed during the course of experiments for this thesis, in order to study the long-term time-dependent

behaviour of polymer LEDs. This summary should ensure that it can continue to provide useful data on the drive-dependent behaviour of polymer LEDs.

References

- ¹ J. H. Burroughes, D. D. C. Bradley, A. R. Brown, R. N. Marks, K. Mackay, R. H. Friend, P. L. Burns, and A. B. Holmes, *Nature* **347**, 539-541 (1990).
- ² R. H. Friend, R. W. Gymer, A. B. Holmes, J. H. Burroughes, R. N. Marks, C. Taliani, D. D. C. Bradley, D. A. Dos santos, J. L. Bredas, M. Logdlund, and W. R. Salaneck, *Nature* **397**, 121-128 (1999).
- ³ N. K. Patel, S. Cina, and J. H. Burroughes, *IEEE J. Sel. Top. Quantum Electron.* **8**, 346-361 (2002).
- ⁴ D. Braun, in *Materials Today* (2002), p. 32-39.
- ⁵ M. Leadbeater, in *OEMagazine* (2002), p. 14-17.
- ⁶ I. D. Rees, K. L. Robinson, A. B. Holmes, C. R. Towns, and R. O'dell, *MRS Bull.* **27**, 451-455 (2002).
- ⁷ J. R. Sheats, H. Antoniadis, M. Hueschen, W. Leonard, J. Miller, R. Moon, D. Roitman, and A. Stocking, *Science* **273**, 884-888 (1996).
- ⁸ A. J. Heeger, *Solid State Commun.* **107**, 673-679 (1998).
- ⁹ R. H. Friend, G. J. Denton, J. J. M. Halls, N. T. Harrison, A. B. Holmes, A. Kohler, A. Lux, S. C. Moratti, K. Pichler, N. Tessler, and K. Towns, *Synth. Met.* **84**, 463-470 (1997).
- ¹⁰ Norelco 8894XL Electric Razor, Royal Philips Electronics, New York, NY.
- ¹¹ J. H. Burroughes, C. A. Jones, and R. H. Friend, *Nature* **335**, 137-141 (1988).
- ¹² H. Sirringhaus, P. J. Brown, R. H. Friend, M. M. Nielsen, K. Bechgaard, B. M. W. Langeveld-voss, A. J. H. Spiering, R. A. J. Janssen, E. W. Meijer, P. Herwig, and D. M. De leeuw, *Nature* **401**, 685-688 (1999).
- ¹³ J. J. M. Halls and R. H. Friend, in *Photoconversion of Solar Energy*, Vol. 1, edited by M. D. Archer and R. Hill (2001).
- ¹⁴ H. Kobayashi, S. Kanbe, S. Seki, H. Kigchi, M. Kimura, I. Yudasaka, S. Miyashita, T. Shimoda, C. R. Towns, J. H. Burroughes, and R. H. Friend, *Synth. Met.* **111**, 125-128 (2000).

2. General Review

This Chapter reviews the area of conjugated polymer physics, the semiconducting nature of these materials, and their uses as active components of devices. While the focus will be on aspects of direct relevance to this thesis, the books and review articles mentioned in Chapter 1 provide more in-depth analyses.

The Chapter will begin with an overview of the origin of semiconducting properties in conjugated polymers, and the types of neutral and charged species sustainable in these materials. The main section will then describe the theoretical basis for polymer light-emitting diodes (LEDs) and the factors affecting their operation. Finally, the materials employed in this thesis will be discussed.

2.1 Conjugated polymers

The class of conjugated polymers includes at its core all those materials based on a carbon backbone through which a continuous path of alternating single and double bonds can be traced.

2.1.1 Electronic structure of carbon compounds

Carbon is the sixth element in the periodic table, having a ground state electronic structure of $1s^2 2s^2 2p^2$, meaning that it can accommodate a further four electrons in its 2p shell. This shell completion is achieved through the formation of covalent bonds, and leads to the characteristic tendency of carbon to form four such bonds.

In forming covalent bonds, the 2s and 2p electrons hybridise, as seen in Figure 2.1.

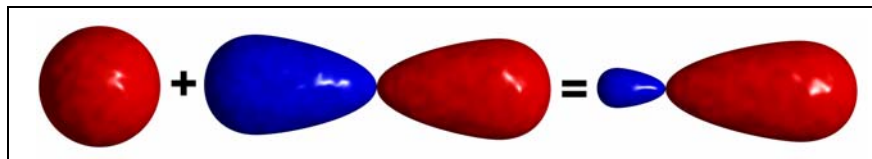


Figure 2.1: Hybridisation of a 2s and 2p_x orbital into an sp hybrid.

Depending on the number of coordinating sites, hybridisation proceeds to form sp³, sp² or sp orbitals. The familiar diamond structure, with four coordinated atoms around each carbon, employs sp³ hybridisation to yield four identical single bonds, tetrahedrally separated with a bond angle of 109°28'', as shown in Figure 2.2 (left). When there are only three coordinating atoms, the best separation can be achieved by adopting a trigonal planar geometry, with sp² hybridisation. In this case, shown in Figure 2.2 (right), the p_z orbital does not hybridise, and protrudes normal to the plane of the hybrid orbitals.

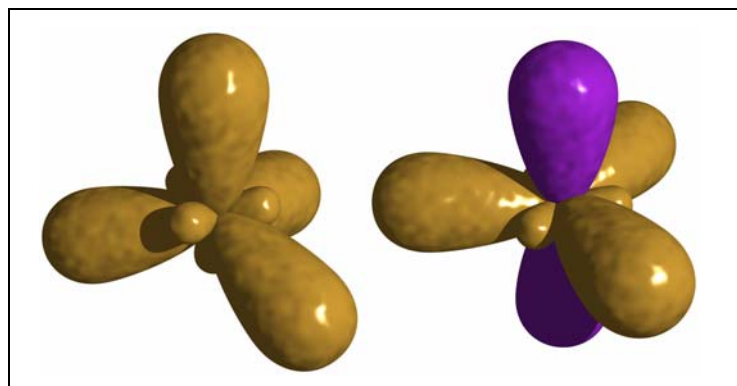


Figure 2.2: sp³ and sp² hybridised orbitals. The unhybridised p_z orbital is shown in purple.

When two sp³-hybridised atoms come together, the constructive overlap of orbitals depicted in Figure 2.3 forms a σ molecular orbital. The interaction between the positively charged nuclei and the negatively charged electron density in between leads to a net attraction between the two atoms, and this forms the basis of a single covalent bond.

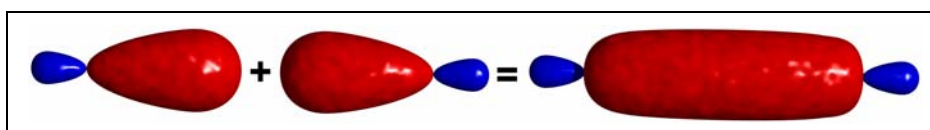


Figure 2.3: Constructive interference of two sp-hybrid orbitals to form a σ bond.

A similar process takes place when two sp²-hybridised atoms join together, with the out-of-plane p_z orbitals also producing a constructive overlap. This yields a π-orbital, shown in Figure 2.4.

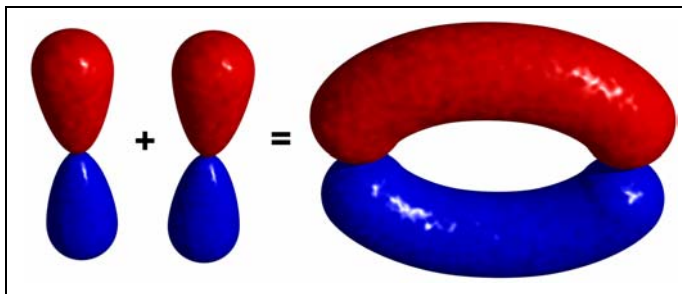


Figure 2.4: Constructive interference of two p_z orbitals to form a π bond.

When a σ and a π orbital are both present between a pair of atoms, the atoms are said to be double-bonded, with the overall molecular orbital structure depicted in Figure 2.5.

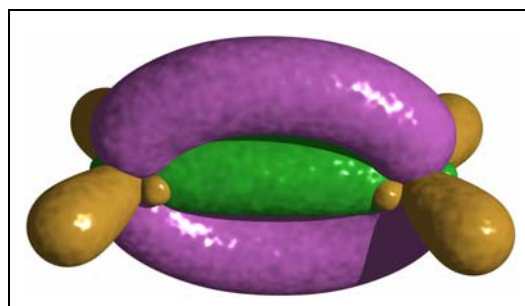


Figure 2.5: Double-bonded pair of atoms, with σ -bond in green and π -bond in purple.

2.1.2 Semiconducting nature of conjugated polymers

Whilst a single pair of adjacent sp^2 -hybridised carbon atoms are considered to be double-bonded to each other, the analysis of a chain of such identical atoms is more complex. The structure of *trans*-poly(acetylene) is the simplest such example, consisting of a linear chain of sp^2 -hybridised carbons, with each one satisfied by an additional hydrogen atom.

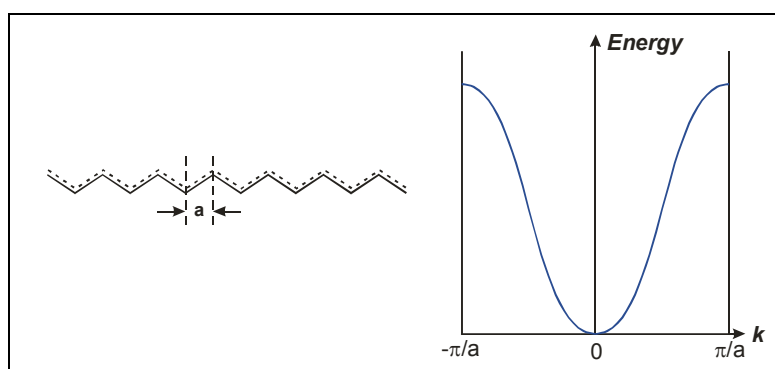


Figure 2.6: Poly(acetylene) chain and band structure, assuming uniform electron delocalisation.

Since every site along the backbone is identical, one might expect every bond to be identical in length. This would yield the molecular form shown in Figure 2.6, and the adjacent band structure which would give rise to metallic characteristics.

However, Peierls¹ determined that the lowest-energy formation is reached when the chain dimerises by forming alternating single and double bonds. This has the effect of doubling the chain's repeat length and halving the size of the Brillouin zone, leading to the formation of a gap at the zone boundary, as seen in Figure 2.7.

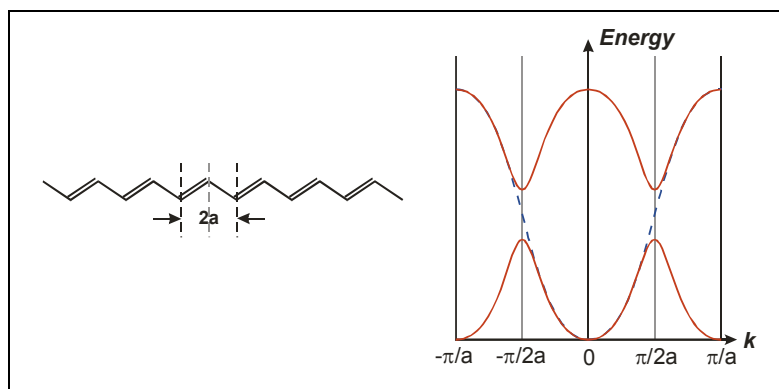


Figure 2.7: Dimerised chain, with Peierls distortion, and the new band structure.

The analysis of Longuet-Higgins and Salem² used a linear combination of atomic orbitals approach to show that the lower energy band can be considered as a filled molecular orbital with bonding character, while the upper band is an empty antibonding orbital. The material is therefore no longer metallic, but rather semiconducting, requiring the promotion of an electron from the highest occupied molecular orbital (HOMO) to the lowest unoccupied molecular orbital (LUMO) for conduction to take place.

The poly(acetylene) formalism can be extended to molecular materials with more complicated structures. When a chain of such molecules is formed, with conjugation extending between monomer units, the discrete HOMO and LUMO levels split to form quasi-continuous bands. Thus, conjugated polymer chains can be considered as semiconductors, with band-gaps defined by the energy difference between these bands.

2.2 Charged species

The bond alternation in a conjugated polymer forms the physical basis for charge storage. The chain geometry is strongly coupled to the occupancy of electronic states (electron-phonon coupling). Two cases can be identified, depending on whether the polymer has a degenerate or non-degenerate ground state.

2.2.1 Degenerate ground state – solitons

In *trans*-poly(acetylene), the two possible senses of bond alternation are wholly degenerate. A neutral defect is formed where a changeover occurs between the two possible configurations, shown in Figure 2.8. In practice, such defects are stabilised by spreading over 10 to 15 repeat units of the polymer. They are highly mobile along the chain backbone, since there is no energy difference between the two senses of bond alternation. Due to the resemblance to a solitary wave, the defect is termed a soliton.

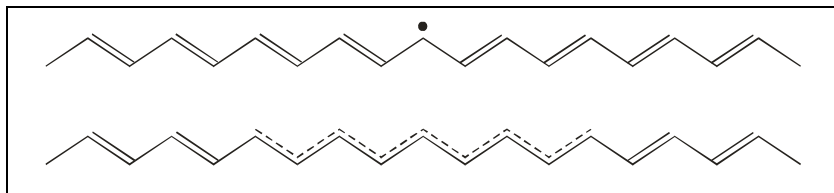


Figure 2.8: The lattice mismatch soliton, with a black dot representing the unpaired non-bonding electron, and alternatively represented as delocalised over several carbon sites.

The defect is characterised by a singly-occupied p_z orbital (which does not take part in π -bonding), and so the soliton has an associated spin of $\frac{1}{2}$. The energy level of this orbital is precisely mid-gap with respect to the HOMO and LUMO level of the polymer. Thus it is energetically favourable for a charge (either electron or hole) in the polymer to be located at such a defect. This produces a spin 0 charged soliton either by removal of the existing electron or by addition of a second electron of antiparallel spin according to the Pauli exclusion principle.

2.2.2 Non-degenerate ground state – polarons

Trans-poly(acetylene) is unusual in having a degenerate ground state. Other electroluminescent conjugated polymers, such as the archetypal poly(*para*-phenylene vinylene) (PPV), have two distinct patterns of bond alternation, termed benzoid and quinoid, seen in Figure 2.9. The benzoid form is the lowest-energy configuration, whilst the quinoid form is an excited state³, typified by a more rigid chain formation.

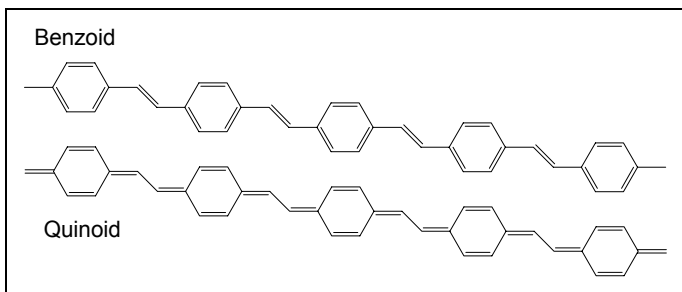
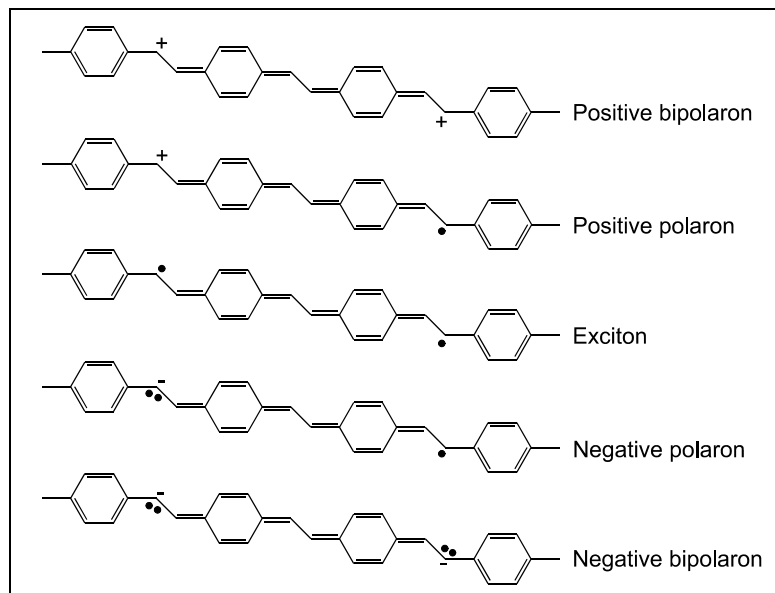


Figure 2.9: PPV in benzoid (ground state) and quinoid (excited state) forms.

Although the non-degenerate bond alternation precludes the formation of highly mobile solitons in the polymer chain, bond alternation defects do nevertheless occur in these materials. There is, however, a significant energy penalty for the lattice distortion entailed. Moreover any such defect in a chain should be accompanied by a nearby defect of opposite sense, so that the length and associated energy of the quinoid region is finite.



**Figure 2.10: Structural representation of polaronic states in PPV.
The black dots represent non-bonding electrons.**

Just as in the case of solitons, these defects are energetically favourable sites for the accommodation of electrons and holes, shown in Figure 2.10. The energy bonus produced by occupation of the site more than compensates for the energy penalty for distortion of the lattice. Thus the charge stabilises the defect, and the defect localises the charge. Such a charged state is termed a polaron. It is effectively a bound state of charge and distortion (electron and phonon), and occupies an energy position just inside the band-gap, as depicted in Figure 2.11.

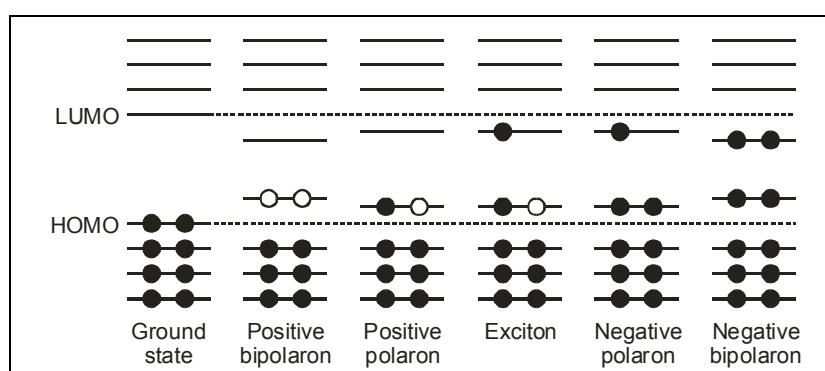


Figure 2.11: Schematic energy levels and occupancies of the polaron states.

The correlation of pairs of defects in a polymer chain led to much debate over the prominence of bipolarons⁴⁻⁷, in which both defects would be populated with charge. While a polaron has spin, a bipolaron would be spinless. The dominant species will be determined by the relative stability of a bipolaron compared with a pair of polarons. Investigations have shown that while such bipolarons can exist, singly charged polarons are the typical variant in these materials except at very high charge densities^{8,9}.

2.3 Neutral excited states – excitons

When an electron polaron and a hole polaron meet on a single chain, their Coulomb attraction can cause them to become bound in a neutral excited state known as an exciton. This process is known as recombination (even when the respective polarons are a non-geminate pair).

2.3.1 Singlets and triplets

Since the exciton arises from the combination of two spin- $\frac{1}{2}$ species, the two possible outcomes are a spin 1 triplet exciton or a spin 0 singlet exciton, visualised in Figure 2.12. As the names suggest, spin statistics dictate a 3:1 generation ratio when spin-uncorrelated electrons and holes recombine. Only the singlet emission has an allowed radiative transition to the ground state, so triplet excitons are responsible for one of the most fundamental loss mechanisms in organic LEDs.

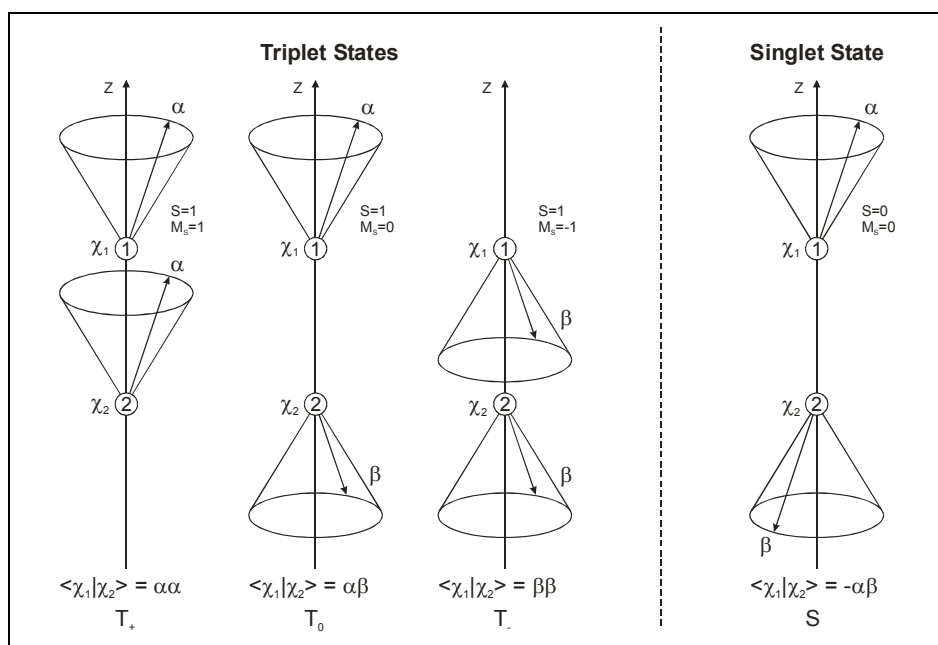


Figure 2.12: The precessing spin vectors for singlet and triplet states. χ_1 and χ_2 represent the spin states of the two electrons, whilst S and M_S are the total and magnetic spin quantum numbers. After ref. 10.

There has been much interest in attempts to harvest the triplet, particularly by the introduction of guest molecules with components such as platinum. The heavy atom allows spin-orbit coupling, leading to a partially allowed radiative transition from triplet excited state to the ground state^{11,12}. However recent experiments¹³ have shown that spin-dependent recombination can occur in real devices, leading to significant excesses of singlet excitons above the 25 % limit and reducing the triplet problem¹⁴⁻¹⁶.

2.3.2 Photoexcitation

Excitons are also produced through photoexcitation, when an incident photon of sufficient energy is absorbed by the polymer. Electronic transitions associated with the absorption of radiation occur on a timescale of approximately 10^{-15} s, whilst the nuclear rearrangements required for the relaxation into a new polaronic state occur much more slowly, around 10^{-13} s. According to the Franck-Condon principle, the absorption of energy from a photon must therefore be a vertical transition, as seen in Figure 2.13.

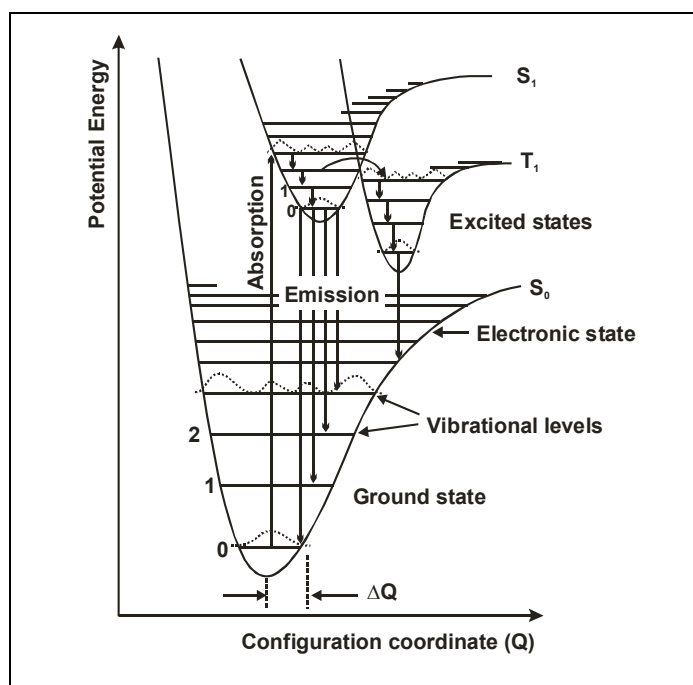


Figure 2.13: Electronic and vibrational potential energy levels of a molecule as a function of configuration coordinate. (Adapted from ref. 17)

Following the spin selection rules, the spin-change on absorption of a photon must be zero, so photogenerated excitons are always singlets. Due to the imperfect matching of configuration coordinates between S_0 (the electronic ground state) and S_1 (the first singlet excited state), absorption from the lowest vibrational state of S_0 will likely lead to a vibrationally-excited state of S_1 . This rapidly decays by depositing thermal energy into the polymer, until it reaches the lowest vibrational state of S_1 .

Since a range of conjugation lengths are sampled in the absorption process, and longer conjugation lengths are associated with lower exciton energies, the vibronic structure of absorption in a polymer is usually smeared out.

2.3.3 Radiative relaxation

Just as a singlet exciton can be produced by absorption of a photon, so a singlet exciton can radiatively decay to S_0 by emission of a photon, known as fluorescence. Once again, the imperfect matching of the potential energy curves means that relaxation taking place from the lowest vibronic state of S_1 often couples to an excited vibronic state of S_0 , which subsequently thermalises. However, whilst absorption samples a range of conjugation lengths, the lifetime and diffusion properties of the exciton allow it to travel to a nearby minimum energy state before emission takes place. Thus the vibronic structure is typically visible in emission. Emission from the triplet manifold, when it is possible as described in Section 2.3.1, is known as phosphorescence.

2.3.4 Non-radiative relaxation

The photoluminescence efficiency describes the fraction of optically generated singlet excitons which decay radiatively. The remainder relax by non-radiative methods. This entails the transfer of the excitation energy into vibrational states of the polymer matrix. Near metal surfaces, energy transfer into the metal becomes possible, quenching the exciton^{18,19}. Polarons²⁰, applied fields²¹ and defect sites such as those produced by degradation²² can all cause non-radiative relaxation of excitons.

2.4 Polymer LEDs

This thesis concerns the factors affecting conjugated-polymer-based light-emitting diodes, and in particular their behaviour during operation. The principles of operation of a polymer LED are therefore described here. The details of fabrication will be described in the next Chapter.

2.4.1 Structure

Polymer LEDs are constructed in a sandwich structure, in which the active polymer material is a thin film. These devices are built as surface emitters, and since the electrodes cover both surfaces of the polymer film,

one must be transparent. The prototypical choice for this material is indium tin oxide (ITO), used extensively in the liquid crystal display market.

The transparent conducting oxide is supported on a glass substrate, through which the emission is viewed. The work-function of ITO, at approximately 4.8 eV makes it suitable for the injection of holes into the typical polymers used. The ITO is typically cleaned by oxygen plasma treatment²³⁻²⁶ (although other treatments have been assessed²⁵⁻²⁷) in order to further enhance the work function. Recent developments have shown promise for replacing the ITO entirely by layered transition-metal dichalcogenides, with superior work function and the possibility of wet-phase deposition^{28,29}.

ITO as produced commercially by sputtering is rough^{24,30} on the scale of several nanometres, with occasional spikes tens of nanometres high. Surface spikes lead to significant field enhancement in an operating device, and pose a real risk of piercing the electroluminescent layer, which is typically less than 100 nm thick. Such a short can render the whole pixel useless.

To overcome this problem, a layer of conducting polymer is deposited on top of the ITO. The standard choice is poly(ethylene dioxythiophene) doped with poly(styrene sulphonic acid) (see Section 2.5.3), known together as PEDOT:PSS³¹, and spin-cast from aqueous solution. This material was developed as an anti-static coating, and besides producing a flat surface³² it is well-suited on two further grounds. First, the work function is similar to or even higher than the ITO whose injecting role it replaces³³. Secondly, once spun from aqueous solution and thermally cured, it is insoluble in the solvents used to deposit electroluminescent polymers on top. It has been shown unexpectedly that oxygen-plasma cleaning of the ITO surface beneath can even enhance the final work function when PEDOT:PSS is subsequently spun over the top²⁶.

The electroluminescent polymer layer is deposited next, and has perhaps the widest range of possible compositions and treatments of any section of the LED. Besides single-layer devices³⁴, there has been much interest in bi-layer structures³⁵⁻³⁷, in which each polymer is placed adjacent to its preferred electrode. Since many of the polymers used are mutually soluble in the solvents used for spinning, the two layers must be separately produced and brought together to complete the heterojunction³⁸⁻⁴⁰. Graded “fuzzy junction” devices have been produced which moderate the abrupt barriers inherent in a bi-layer system^{41,42}. In blend structures^{43,44} a demixing of the components by spinodal decomposition^{45,46} yields a fine-scale microstructure with numerous internal interfaces, and in certain cases preferential segregation of the two components towards their preferred electrodes³⁸. The operational benefits of these structures will be described later.

The second electrode is deposited directly onto the top surface of the electroluminescent polymer. In contrast to the high work-function anode, the second electrode must have a low work function to favour

electron injection, and need not be transparent. A metal such as calcium is therefore used. On account of the chemical reactivity of calcium, this is usually capped with a protective layer of aluminium. The establishment of electrical contacts to the electrodes completes the necessary components of a basic device.

2.4.2 Injection

Active operation of polymer LEDs begins with charge injection from the two electrodes, and this critical step is of great interest⁴⁷⁻⁴⁹. Modification of the injection barrier, both at the cathode⁵⁰⁻⁵⁸ and the anode⁵⁹⁻⁶⁸, has a large effect on device performance. Two distinct theoretical approaches have been used.

2.4.2.1 Field-assisted tunnelling – Fowler-Nordheim

In Fowler-Nordheim tunnelling, the charge is considered to tunnel through a triangular barrier into a continuous band of states. There is no consideration of the image charge effects which subsequently act to draw the injected charge back to the electrode surface, and no temperature dependence. At high fields, the image charge becomes proportionately less significant, and the functional form of the tunnelling model shows a good fit to experiment here^{47,69}.

2.4.2.2 Thermionic emission – Richardson-Schottky

Thermally-assisted injection in the Richardson-Schottky model treats the field-lowering effect of the image potential, and the thermal activation required to overcome the reduced barrier. Tunnelling is ignored, as is back-scattering of injected charge into the metal. At low fields, tunnelling is less important, and the functional form of the injection current here is well matched by experiment. However the magnitude of predicted current is orders of magnitude too high, due to the neglect of back-scattering. This process is particularly significant in disordered organic semiconductors, where the mean free path is so short.

Figure 2.14 shows two explicit potentials which together provide the field-lowered image charge potential: U_{image} , the image potential of the injected charge, and U_{field} , the potential of the applied field.

$$U_{image} = \frac{-e^2}{4\pi\epsilon_0\epsilon_r x} \quad (2.1)$$

$$U_{field} = -eEx \quad (2.2)$$

where E is the applied field, x the distance into the polymer, ϵ_0 and ϵ_r the permittivity of free space and the relative permittivity of the polymer, and e the charge on an electron. In the figure, Δ_{max} represents the highest point in the combined potential, and x_o the distance into the polymer at which this point occurs.

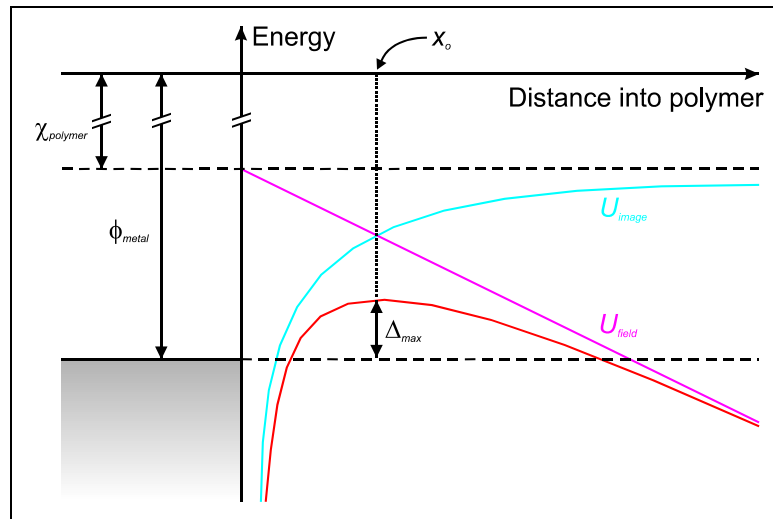


Figure 2.14: Schematic energy diagram for thermally-assisted carrier injection over an image-lowered potential barrier. After ref's 70 & 71. (See text)

2.4.2.3 Backscattering

Whilst both tunnelling and thermionic emission models have their strengths, the neglect of backscattering in the low-field thermionic case is a serious shortcoming. Recently this process has been considered in detail with inclusion of backscattering by Scott⁷⁰, achieving effective Richardson constants which better agree with experiment. A significant conclusion is that the short scattering length of conjugated polymers leads to the backscattering of the vast majority of injected charges, particularly at low fields.

Meanwhile, extension of the tunnelling formalism to include a deliberately-inserted inorganic barrier layer⁷² has shown that the large attenuation length of the inorganic allows significant tunnelling injection to the surface layers of the polymer. Additionally, the spacing effect of the barrier means that the successfully injected charge finds itself further away from the metal surface than it would have been, and possibly even beyond the maximum of the image force potential. This mechanism explains the experimentally observed effect of inserting thin interfacial layers at the cathode (e.g. Al_2O_3 ^{56,57}, LiF ^{51,54,55} and CaF_2 ^{52,53}) on the electron injection efficiency, although some of this work suggests that tunnelling may be less significant than enhancement by interfacial dipoles⁵³.

2.4.3 Charge transport

Charge transport along a conjugated polymer chain requires the transfer of the polaronic distortion along the chain backbone. This is not a particularly difficult process, necessitating only a gradual conformational change propagating along the chain. However since polymer LEDs are usually fabricated by spin-coating methods, the vast majority of chains lie in-plane⁷³, and interchain transport is necessary for bulk conduction. This process depends on the degree of overlap of π -orbitals between the two systems, their separation, and the relative energy levels. The transport from one chain to another is thus significantly more difficult than intrachain propagation, and this provides the rate-limiting factor for LED transport.

The motion of charges through a disordered organic system has been described by means of a hopping formalism, in which charges make discrete hops from site to site. The stochastic distribution of site separations, even in a material with no traps, produces results equivalent to a system containing traps distributed in energy. This leads to a convergence of the functional forms predicted by the hopping model and the trap-containing Poole-Frenkel model, due to the similarity in activation energies between a long hop and the escape from a trap⁷⁴. However, fitting experimental data to the Poole-Frenkel model requires trap densities which may be unrealistically high.

2.4.4 Bulk conduction

The cumulative effect of hopping transport through the polymer layer can be treated as a bulk current flow governed by a mobility, characteristic of the specific polymer chosen and the type of carrier under consideration. Typically, though not exclusively, holes are found to be the more-mobile carrier

2.4.4.1 Determination of mobility

Various methods have been employed to calculate the mobility values inherent in these polymers. Transient methods have employed time-of-flight (TOF)^{75,76} and pulsed electroluminescence⁷⁷⁻⁸⁰. Steady-state current-voltage characteristics have also been employed to determine carrier mobilities^{81,82}. Oscillatory methods have included pulse radiolysis time resolved microwave conductivity⁸³ and impedance spectroscopy⁸⁴⁻⁸⁶. These various techniques produce a wide divergence of experimental values. A prime reason for this is the morphology-dependence of mobility, noted by Redecker *et al* in the chain-alignment of poly(9,9-diptylfluorene)^{75,76}, and Sirringhaus *et al* in microcrystalline polymer transistors made from poly(3-hexylthiophene)⁸⁷ and aligned films of the same material⁸⁸.

Variations in morphology with film thickness, caused by the different conditions and timescales required to produce them, have been demonstrated in polymers⁸⁹. Consequently the thick films used for TOF are intrinsically different from the thin ones in devices. Small-molecule systems on the other hand, where thin and thick layers use identical vacuum deposition, show excellent agreement between pulsed electroluminescence transients and TOF⁹⁰. The oscillatory methods often reveal much higher mobilities than those seen during device operation^{86,91}, since these methods can sample microscopically aligned domains without probing the considerable obstacle of charge transport between domains⁹².

The two formalisms described earlier, of hopping between a distribution of localised states⁹³⁻⁹⁵, and repeated trapping and de-trapping^{96,97} can each explain the observed field-dependence of mobility, yielding a description of the form $\exp(\sqrt{E})$, where E is the electric field strength. Whilst in a rigorous analysis the field-dependence of mobility is an important consideration, representative results can be obtained by taking a locally applicable value of the mobility^{98,99}, particularly when the range of field strengths under consideration is limited¹⁰⁰.

2.4.4.2 Whole-device conduction

By considering the whole device, including contacts, the resulting behaviour can be described either as a space-charge limited current (SCLC) or as an injection limited current. In the former case, unhindered injection from metal into polymer means that the electrode can be considered an ohmic contact. Charge is supplied by an “inexhaustible” electrode until the injection field is reduced to zero, and as much charge is injected as the polymer can sustain. In such a situation, for a unipolar (single-carrier) device without traps, the Mott-Gurney law applies (Equation 2.3)¹⁰¹.

$$J_{SCLC} = \frac{9}{8} \epsilon_0 \epsilon_r \mu \frac{V^2}{L^3} \quad (2.3)$$

where j_{SCLC} is the space-charge limited current density, ϵ_0 and ϵ_r the permittivity of free space and the relative permittivity of the polymer, μ the charge-carrier mobility, V the applied bias minus the built-in voltage and L the thickness of the polymer layer. The current sustained is thus directly proportional to the charge-carrier mobility in the polymer.

In the alternative injection-limited scenario, the barrier to injection at the electrode constricts the flow of charge into the polymer such that charge is swept away faster than it is injected. As previously described, the modelling of this injection, which is very sensitive to small parameter variations, is an important step to better understanding the behaviour of polymer LEDs.

The distinction between the two injection cases is dependent on the height of the barrier for charge injection, as well as the charge carrier mobility (which determines how fast charge is swept away). For typical mobilities found in conjugated polymers, it has been shown that for barriers smaller than 0.3-0.4 eV, a contact may be considered ohmic, and thus the device space-charge limited for that carrier⁴⁸.

All useful LEDs must be to some extent bipolar devices, and the introduction of a second species complicates the simple picture through (a) cancellation of space-charge, which lifts the space-charge limit inherent in the Mott-Gurney equation, (b) alteration of the electric field distribution, leading to changes in local mobility, and (c) recombination of electrons and holes, providing an alternative sink to charge extraction at the counter-electrode.

2.4.5 Electron-hole recombination

The recombination of an electron and a hole to form an exciton is a diffusion-driven bimolecular process^{17,100,102}, as originally described by Langevin¹⁰³. This is applicable because the mean free path of charge carriers in a conjugated polymer is smaller than the mutual capture radius. Recombination therefore is deemed to take place when the two charged polarons approach to within a capture radius, defined as the point where the Coulombic attraction between the two exceeds the thermal energy, kT .

The net result of the Langevin analysis is that the recombination rate is proportional to the electron density, the hole density and the sum of the electron and hole mobilities. As described in Section 2.3.1, in the absence of any spin correlation effects, spin statistics predict exciton formation in a 3:1 ratio in favour of triplets over singlets.

2.4.6 Light emission

The ultimate source of light emission in a polymer LED is the radiative relaxation of singlet excitons¹⁰⁴. Before emission takes place, the lifetime and diffusion properties allow the exciton to diffuse some distance, known as the exciton diffusion length. During this process, depending on the local conditions encountered, it may undergo energy transfer to an adjacent polymer or guest molecule, dissociation into unbound charges, or quenching as described in Section 2.3.4.

Emission itself is partially governed by the cavity nature of the LED structure, which is typically a fraction of a wavelength from front to back. Thus emission suppression in the vicinity of the metallic electrode is an important phenomenon, and the resulting optical interference effects¹⁰⁵⁻¹¹¹ can provide rich information for

instance on the location of the emission zone inside the device¹¹². Specially designed cavity devices can allow control over the colour of emission¹¹³, often with undesirable colour variation at off-normal angles¹¹⁴, though with suitable engineering this too can be reduced^{108,115}.

Outcoupling of emitted light is a significant and related concern¹¹⁶. Total internal reflection at internal interfaces, at relatively modest angles, leads to confinement of the light within the device or the glass substrate until it escapes at the sides, sometimes referred to as waveguiding. Introduction of a silica-based “aerogel”, with intermediate refractive index, significantly improves the fraction of light outcoupled in the forward direction^{117,118}, whilst texturing of the substrate can force confined modes to scatter out of the device¹¹⁹.

2.4.7 Degradation and time-dependent variations

One of the greatest challenges facing polymer LED technology is the instability of light emission with respect to time, and most importantly the issue of permanent, irreversible degradation^{120,121}. This occurs either uniformly across the face of the LED, due to intrinsic factors such as the chemical interactions at interfaces between the device components¹²² or the instability of the polymer against the injected polarons¹²³, or extrinsically through the growth of localised “dark spots” at which contaminants such as oxygen and moisture enter the device through breaks in the cathode¹²⁴⁻¹²⁷.

The ingress of contaminants can itself be responsible for degradation in a number of ways, for instance by chemical oxidation of the reactive metal cathode¹²⁸, production of trap sites in the polymer layer¹²⁹, or mediation of an irreversible chemical reaction in the electroluminescent polymer during driving¹²⁷. The oxidation of the polymer is of particular current interest in polyfluorene work, where it has been seen that the production of keto- defect sites is accompanied by the evolution of a new green emission^{120,130}. The keto- sites themselves have been seen to be formed *ex situ* by heating of the polyfluorene in air¹³¹ and in the older PPV-based polymers by photo-oxidation¹³². They have been formed *in situ* during electrical driving^{133,134} and shown to be responsible for quenching of singlet excitons²².

Intrinsic degradation can also originate in a number of ways. Both indium¹³⁵ and oxygen¹³⁶ from the ITO are suspected of having detrimental effects on the adjacent polymer layer, prompting the insertion of barrier layers including self-assembled monolayers to shield the adjacent PEDOT:PSS¹³⁷. Ion-implantation during the stressful cathode evaporation stage can produce quenching sites even before the device has been completed¹³⁸, emphasising the importance of controlling every stage of the fabrication process.

A few authors have reported reversible reductions in device performance during driving¹³⁹⁻¹⁴¹, and whilst these cannot be considered true degradation they are still an issue for the development of commercial devices. Some such behaviour has been attributed to permanent dipole realignment¹⁴¹, or the presence of traps in the polymer layer¹⁴²⁻¹⁴⁴. Charge traps may be intrinsic to the polymer, reversibly¹⁴⁵ or irreversibly¹⁴⁶ introduced by the presence of oxygen, or permanently induced by the stress of electrical driving¹²³. Experiments have shown that they are typically exponentially distributed as a function of trap depth^{96,147}.

Whilst all these processes are reported to yield a drop in the device performance, conversely the presence of mobile ions deliberately implanted in the polymer matrix yields a light-emitting electrochemical cell (LEC)¹⁴⁸ which improves in performance during the early stages of driving. The ionic drift under the applied field leads to an accumulation of charged ions at the interfaces and a corresponding enhancement of injection and charge balance with time^{149,150}. Indeed this approach is so effective that low work-function metals are not required for the cathode. Due to the presence of mobile ions, LECs show a characteristic reversibility under reverse bias, which will be an important point in the analysis of Chapter 6.

2.5 Materials

Materials for use in conjugated polymer LEDs are under constant development. The particular materials used in this thesis are briefly described here, along with the various parameters which are later employed.

2.5.1 Cathode materials

Calcium is the standard cathode metal in conjugated polymer LEDs on account of its low work function, which allows ohmic injection of electrons into most polymers. A selection of other cathode materials are used in this work, and summarised in Table 2.1. Nichrome is an 80:20 alloy of nickel and chrome.

Metal	Work function, ϕ (eV)
Calcium	2.9
Magnesium	3.7
Aluminium	4.3
Nichrome	5.1

Table 2.1: Cathode materials and their work functions.

2.5.2 Light emitting polymers

Although conjugated polymers, being organic systems, are capable of immense variety particularly in the substitution of side-groups, only a small selection are used in this work.

The simplest of the polyfluorenes is poly(9,9'-dioctylfluorene), usually abbreviated to F8 or PFO^{151,152}. As shown in Figure 2.15, it contains the fluorene unit alone, seen as a bridged pair of benzene rings. The octyl side-chains act to solubilise the polymer, and tend to point out of the plane of the main chain. All the electroluminescent polymers treated in this work are based on polyfluorene. A liquid crystalline polymer, F8 has been the subject of a great deal of interest, particularly as a model material for the wealth of structural and electronic changes produced by chain alignment^{120,153-158}. F8 is a blue emitter in electroluminescence, and is only briefly treated in this work.

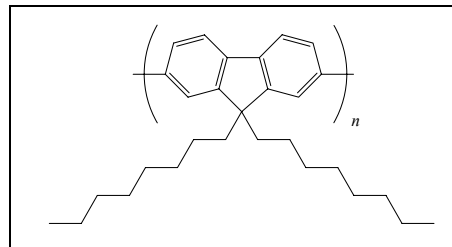


Figure 2.15: Structure of F8.

The most extensively examined polymer in this thesis is poly(9,9'-dioctylfluorene-*co*-benzothiadiazole), usually abbreviated to F8BT¹⁵². As shown in Figure 2.16, F8BT contains a fluorene unit copolymerised with the benzothiadiazole unit. The polymer displays a green emission, and its HOMO and LUMO levels have been determined to be 5.90 eV and 3.55 eV respectively⁴⁶. F8BT is unusual amongst conjugated polymers for being a high-mobility electron transporter, whilst most such materials are hole transporters.

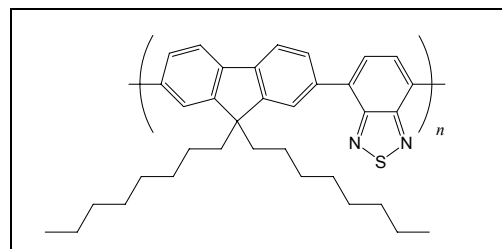


Figure 2.16: Structure of F8BT.

Poly(9,9'-dioctylfluorene-*co*-N-(4-butylphenyl)diphenylamine), known as TFB⁷⁶, is shown in Figure 2.17. The fluorene unit is seen again, this time with a triarylamine unit. TFB is blue in electroluminescence. The HOMO and LUMO levels are 5.35 eV and 2.30 eV respectively⁴⁶.

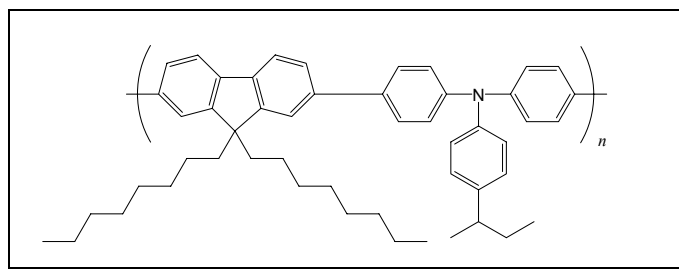


Figure 2.17: Structure of TFB.

The last standard polymer studied is poly(9,9'-dioctylfluorene-*co*-bis-N,N'-(4-butylphenyl)-bis-N,N'-phenyl-1,4-phenylenediamine), conveniently abbreviated to PFB⁷⁶, and shown in Figure 2.18. Once again the fluorene unit is present, this time with a bistriarylamine component, which is an extended version of the triarylamine unit seen in TFB. It is also blue in electroluminescence, with HOMO and LUMO levels of 5.10 eV and 2.30 eV respectively⁴⁶.

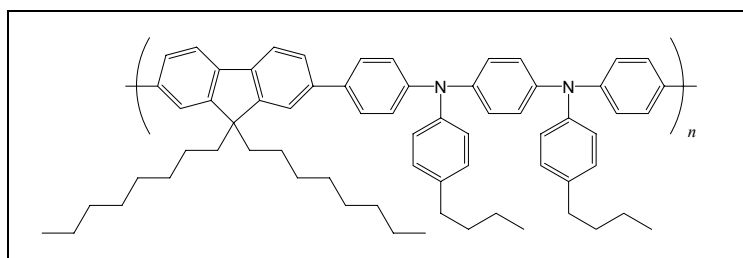


Figure 2.18: Structure of PFB.

Two copolymers are also studied in this work, both of which contain the F8BT and TFB units described above. The random copolymer includes these units assembled into the chain in a random order, whilst the block copolymer contains blocks of multiple F8BT units separated by similar blocks of TFB, together comprising the main chain.

2.5.3 Anode materials

The polymer-doped polymer system which forms the state-of-the-art anode contains poly(3,4-ethylenedioxythiophene), known as PEDT, doped with poly(styrene sulphonic acid), known as PSSH. The structures are shown in Figure 2.19. The matrix of the two materials combined, which forms the anode itself, is known as PEDOT:PSS³¹. The PEDOT:PSS system displays a work function of 5.1 eV, suitable for the injection of holes into many conjugated polymer materials.

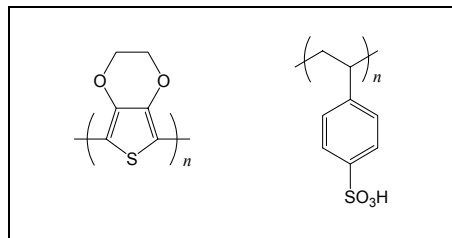


Figure 2.19: Structure of PEDT and PSSH.

2.6 Conclusions

In this Chapter, the theoretical background for semiconduction in conjugated polymers has been detailed, the structure and operation of polymer-based LEDs explained, and the materials to be used in this thesis described.

2.7 References

- ¹ R. E. Peierls, *Quantum Theory of Solids* (Clarendon Press, Oxford, 1955).
- ² H. C. Longuet-Higgins and L. Salem, *Proc. Roy. Soc. London A* **251**, 172-185 (1959).
- ³ J. L. Bredas, R. R. Chance, and R. Silbey, *Phys. Rev. B* **26**, 5843-5854 (1982).
- ⁴ A. R. Brown, K. Pichler, N. C. Greenham, D. D. C. Bradley, R. H. Friend, P. L. Burn, and A. B. Holmes, *Synth. Met.* **57**, 4117-4122 (1993).
- ⁵ M. G. Harrison, K. E. Ziemelis, R. H. Friend, P. L. Burn, and A. B. Holmes, *Synth. Met.* **55**, 218-223 (1993).
- ⁶ A. R. Brown, K. Pichler, N. C. Greenham, D. D. C. Bradley, R. H. Friend, and A. B. Holmes, *Chem. Phys. Lett.* **210**, 61-66 (1993).
- ⁷ H. S. Woo, S. C. Graham, D. A. Halliday, D. D. C. Bradley, R. H. Friend, P. L. Burn, and A. B. Holmes, *Phys. Rev. B* **46**, 7379-7389 (1992).
- ⁸ Y. Furukawa, *J. Phys. Chem.* **100**, 15644-15653 (1996).
- ⁹ K. Pichler, D. A. Halliday, D. D. C. Bradley, R. H. Friend, P. L. Burn, and A. B. Holmes, *Synth. Met.* **55**, 230-234 (1993).
- ¹⁰ N. J. Turro, *Modern Molecular Photochemistry* (University Science Books, Sausalito, CA, 1991).
- ¹¹ V. Cleave, G. Yahioglu, P. Le barny, R. H. Friend, and N. Tessler, *Adv. Mater.* **11**, 285-288 (1999).
- ¹² M. A. Baldo, D. F. O'brien, Y. You, A. Shoustikov, S. Sibley, M. E. Thompson, and S. R. Forrest, *Nature* **395**, 151-154 (1998).
- ¹³ J. S. Wilson, A. S. Dhoot, A. J. A. B. Seeley, M. S. Khan, A. Kohler, and R. H. Friend, *Nature* **413**, 828-831 (2001).
- ¹⁴ A. S. Dhoot, D. S. Ginger, D. Beljonne, Z. Shuai, and N. C. Greenham, *Chem. Phys. Lett.* **360**, 195-201 (2002).

- 15 A. S. Dhoot and N. C. Greenham, *Adv. Mater.* **14**, 1834-1837 (2002).
- 16 A. S. Dhoot and N. C. Greenham, *Materials Research Society Symposium Proceedings* **725**, 8.2.1-8.2.6 (2002).
- 17 M. Pope and C. E. Swenberg, *Electronic Processes in Organic Crystals and Polymers*, 2nd ed. ed. (Oxford Science Publications, Oxford, 1999).
- 18 H. Becker, A. Lux, A. B. Holmes, and R. H. Friend, *Synth. Met.* **85**, 1289-1290 (1997).
- 19 H. Becker, S. E. Burns, and R. H. Friend, *Phys. Rev. B* **56**, 1893-1905 (1997).
- 20 E. J. W. List, C. H. Kim, A. K. Naik, U. Scherf, G. Leising, W. Graupner, and J. Shinar, *Phys. Rev. B* **64***15*, art. no.-155204 (2001).
- 21 M. Deussen, M. Scheidler, and H. Bassler, *Synth. Met.* **73**, 123-129 (1995).
- 22 H. Antoniadis, L. J. Rothberg, F. Papadimitrakopoulos, M. Yan, M. E. Galvin, and M. A. Abkowitz, *Phys. Rev. B* **50**, 14911-14915 (1994).
- 23 J. S. Kim, R. H. Friend, and F. Cacialli, *Appl. Phys. Lett.* **74**, 3084-3086 (1999).
- 24 C. C. Wu, C. I. Wu, J. C. Sturm, and A. Kahn, *Appl. Phys. Lett.* **70**, 1348-1350 (1997).
- 25 J. S. Kim, F. Cacialli, M. Granstrom, R. H. Friend, N. Johansson, W. R. Salaneck, R. Daik, and W. J. Feast, *Synth. Met.* **101**, 111-112 (1999).
- 26 J. S. Kim, M. Granstrom, R. H. Friend, N. Johansson, W. R. Salaneck, R. Daik, W. J. Feast, and F. Cacialli, *J. Appl. Phys.* **84**, 6859-6870 (1998).
- 27 T. Kugler, A. Johansson, I. Dalsegg, U. Gelius, and W. R. Salaneck, *Synth. Met.* **91**, 143-146 (1997).
- 28 K. J. Reynolds, J. A. Barker, N. C. Greenham, R. H. Friend, and G. L. Frey, *J. Appl. Phys.* **92**, 7556-7563 (2002).
- 29 G. L. Frey, K. J. Reynolds, and R. H. Friend, *Adv. Mater.* **14**, 265-+ (2002).
- 30 Y. H. Tak, K. B. Kim, H. G. Park, K. H. Lee, and J. R. Lee, *Thin Solid Films* **411**, 12-16 (2002).
- 31 Y. Cao, G. Yu, C. Zhang, R. Menon, and A. J. Heeger, *Synth. Met.* **87**, 171-174 (1997).
- 32 S. A. Carter, M. Angelopoulos, S. Karg, P. J. Brock, and J. C. Scott, *Appl. Phys. Lett.* **70**, 2067-2069 (1997).
- 33 T. M. Brown, J. S. Kim, R. H. Friend, F. Cacialli, R. Daik, and W. J. Feast, *Appl. Phys. Lett.* **75**, 1679-1681 (1999).
- 34 J. H. Burroughes, D. D. C. Bradley, A. R. Brown, R. N. Marks, K. Mackay, R. H. Friend, P. L. Burns, and A. B. Holmes, *Nature* **347**, 539-541 (1990).
- 35 B. K. Crone, P. S. Davids, I. H. Campbell, and D. L. Smith, *J. Appl. Phys.* **87**, 1974-1982 (2000).
- 36 D. V. Khramtchenkov, V. I. Arkhipov, and H. Bassler, *J. Appl. Phys.* **81**, 6954-6962 (1997).
- 37 A. W. Grice, D. D. C. Bradley, M. T. Bernius, M. Inbasekaran, W. W. Wu, and E. P. Woo, *Appl. Phys. Lett.* **73**, 629-631 (1998).
- 38 C. M. Ramsdale, *Ph.D. Thesis, University of Cambridge*, 2002.
- 39 T. F. Guo, S. Pyo, S. C. Chang, and Y. Yang, *Adv. Funct. Mater.* **11**, 339-343 (2001).
- 40 T. F. Guo, G. He, S. Pyo, and Y. Yang, *Appl. Phys. Lett.* **80**, 4042-4044 (2002).
- 41 H. Riel, W. Brutting, T. Beierlein, E. Haskal, P. Muller, and W. Riess, *Synth. Met.* **111**, 303-306 (2000).
- 42 C. W. Chen, T. Y. Cho, C. C. Wu, H. L. Yu, and T. Y. Luh, *Appl. Phys. Lett.* **81**, 1570-1572 (2002).
- 43 H. Vestweber, R. Sander, A. Greiner, W. Heitz, R. F. Mahrt, and H. Bassler, *Synth. Met.* **64**, 141-145 (1994).
- 44 I. N. Kang, D. H. Hwang, H. K. Shim, T. Zyung, and J. J. Kim, *Macromolecules* **29**, 165-169 (1996).

- ⁴⁵ A. C. Arias, J. D. Mackenzie, R. Stevenson, J. J. M. Halls, M. Inbasekaran, E. P. Woo, D. Richards, and R. H. Friend, *Macromolecules* **34**, 6005-6013 (2001).
- ⁴⁶ A. C. Arias, *Ph.D. Thesis, University of Cambridge*, 2001.
- ⁴⁷ I. D. Parker, *J. Appl. Phys.* **75**, 1656-1666 (1994).
- ⁴⁸ G. G. Malliaras and J. C. Scott, *J. Appl. Phys.* **85**, 7426-7432 (1999).
- ⁴⁹ U. Wolf, S. Barth, and H. Bassler, *Appl. Phys. Lett.* **75**, 2035-2037 (1999).
- ⁵⁰ G. Parthasarathy, C. Shen, A. Kahn, and S. R. Forrest, *J. Appl. Phys.* **89**, 4986-4992 (2001).
- ⁵¹ L. S. Hung, C. W. Tang, and M. G. Mason, *Appl. Phys. Lett.* **70**, 152-154 (1997).
- ⁵² J. Lee, Y. Park, S. K. Lee, E. J. Cho, D. Y. Kim, H. Y. Chu, H. Lee, L. M. Do, and T. Zyung, *Appl. Phys. Lett.* **80**, 3123-3125 (2002).
- ⁵³ X. H. Yang, Y. Q. Mo, W. Yang, G. Yu, and Y. Cao, *Appl. Phys. Lett.* **79**, 563-565 (2001).
- ⁵⁴ T. M. Brown, R. H. Friend, I. S. Millard, D. J. Lacey, J. H. Burroughes, and F. Cacialli, *Appl. Phys. Lett.* **79**, 174-176 (2001).
- ⁵⁵ T. M. Brown, R. H. Friend, I. S. Millard, D. J. Lacey, J. H. Burroughes, and F. Cacialli, *Appl. Phys. Lett.* **77**, 3096-3098 (2000).
- ⁵⁶ S. Kho, S. J. Bae, and D. G. Jung, *J. Mater. Res.* **17**, 1248-1250 (2002).
- ⁵⁷ F. Li, H. Tang, J. Anderegg, and J. Shinar, *Appl. Phys. Lett.* **70**, 1233-1235 (1997).
- ⁵⁸ S. J. Kang, D. S. Park, S. Y. Kim, C. N. Whang, K. Jeong, and S. Im, *Appl. Phys. Lett.* **81**, 2581-2583 (2002).
- ⁵⁹ I. H. Campbell, J. D. Kress, R. L. Martin, D. L. Smith, N. N. Barashkov, and J. P. Ferraris, *Appl. Phys. Lett.* **71**, 3528-3530 (1997).
- ⁶⁰ Y. L. Shen, D. B. Jacobs, G. G. Malliaras, G. Koley, M. G. Spencer, and A. Ioannidis, *Adv. Mater.* **13**, 1234-1238 (2001).
- ⁶¹ I. M. Chan, T. Y. Hsu, and F. C. Hong, *Appl. Phys. Lett.* **81**, 1899-1901 (2002).
- ⁶² B. Choi, J. Rhee, and H. H. Lee, *Appl. Phys. Lett.* **79**, 2109-2111 (2001).
- ⁶³ P. K. H. Ho, M. Granstrom, R. H. Friend, and N. C. Greenham, *Adv. Mater.* **10**, 769-774 (1998).
- ⁶⁴ X. M. Ding, L. M. Hung, L. F. Cheng, Z. B. Deng, X. Y. Hou, C. S. Lee, and S. T. Lee, *Appl. Phys. Lett.* **76**, 2704-2706 (2000).
- ⁶⁵ Z. B. Deng, X. M. Ding, S. T. Lee, and W. A. Gambling, *Appl. Phys. Lett.* **74**, 2227-2229 (1999).
- ⁶⁶ S. J. Cho, D. K. Park, T. W. Kwon, D. S. Yoo, and I. G. Kim, *Thin Solid Films* **417**, 175-179 (2002).
- ⁶⁷ H. J. Jiang, Y. Zhou, B. S. Ooi, Y. W. Chen, T. Wee, Y. L. Lam, J. S. Huang, and S. Y. Liu, *Thin Solid Films* **363**, 25-28 (2000).
- ⁶⁸ H. Frohne, D. C. Muller, and K. Meerholz, *ChemPhysChem* **3**, 707-+ (2002).
- ⁶⁹ G. G. Malliaras and J. C. Scott, *J. Appl. Phys.* **83**, 5399-5403 (1998).
- ⁷⁰ J. C. Scott and G. G. Malliaras, *Chem. Phys. Lett.* **299**, 115-119 (1999).
- ⁷¹ D. J. Pinner, *Ph.D. Thesis, University of Cambridge*, 2000.
- ⁷² U. Wolf and H. Bassler, *Appl. Phys. Lett.* **74**, 3848-3850 (1999).
- ⁷³ T. Kawase, D. J. Pinner, R. H. Friend, and T. Shimoda, *Synth. Met.* **111**, 583-586 (2000).
- ⁷⁴ S. V. Novikov, D. H. Dunlap, V. M. Kenkre, P. E. Parris, and A. V. Vannikov, *Phys. Rev. Lett.* **81**, 4472-4475 (1998).
- ⁷⁵ M. Redecker, D. D. C. Bradley, M. Inbasekaran, and E. P. Woo, *Appl. Phys. Lett.* **73**, 1565-1567 (1998).

- 76 M. Redecker, D. D. C. Bradley, M. Inbasekaran, W. W. Wu, and E. P. Woo, *Adv. Mater.* **11**, 241-+ (1999).
- 77 D. J. Pinner, R. H. Friend, and N. Tessler, *J. Appl. Phys.* **86**, 5116-5130 (1999).
- 78 N. Tessler, P. K. H. Ho, V. Cleave, D. J. Pinner, R. H. Friend, G. Yahioglu, P. Le barny, J. Gray, M. De souza, and G. Rumbles, *Thin Solid Films* **363**, 64-67 (2000).
- 79 T. C. Wong, J. Kovac, C. S. Lee, L. S. Hung, and S. T. Lee, *Chem. Phys. Lett.* **334**, 61-64 (2001).
- 80 J. Wang, R. G. Sun, G. Yu, and A. J. Heeger, *Journal of Applied Physics* **91**, 2417-2422 (2002).
- 81 D. Natali and M. Sampietro, *J. Appl. Phys.* **92**, 5310-5318 (2002).
- 82 P. W. M. Blom, M. J. M. Dejong, and M. G. Vanmunster, *Phys. Rev. B-Condens Matter* **55**, R656-R659 (1997).
- 83 A. M. van de Craats, *Ph.D. Thesis, T.U. Delft*, 2000.
- 84 P. W. M. Blom, H. C. F. Martens, and J. N. Huiberts, *Synth. Met.* **121**, 1621-1624 (2001).
- 85 H. C. F. Martens, J. N. Huiberts, and P. W. M. Blom, *Appl. Phys. Lett.* **77**, 1852-1854 (2000).
- 86 H. C. F. Martens, H. B. Brom, and P. W. M. Blom, *Phys. Rev. B-Condens Matter* **60**, R8489-R8492 (1999).
- 87 H. Sirringhaus, R. J. Wilson, R. H. Friend, M. Inbasekaran, W. Wu, E. P. Woo, M. Grell, and D. D. C. Bradley, *Appl. Phys. Lett.* **77**, 406-408 (2000).
- 88 H. Sirringhaus, P. J. Brown, R. H. Friend, M. M. Nielsen, K. Bechgaard, B. M. W. Langeveld-voss, A. J. H. Spiering, R. A. J. Janssen, E. W. Meijer, P. Herwig, and D. M. De leeuw, *Nature* **401**, 685-688 (1999).
- 89 C. Y. Yang, F. Hide, M. A. Diaz-garcia, A. J. Heeger, and Y. Cao, *Polymer* **39**, 2299-2304 (1998).
- 90 A. G. Muckl, S. Berleb, W. Brutting, and M. Schwoerer, *Synth. Met.* **111**, 91-94 (2000).
- 91 H. C. F. Martens, H. B. Brom, P. W. M. Blom, J. N. Huiberts, and H. F. M. Schoo, *Synth. Met.* **121**, 1643-1644 (2001).
- 92 H. C. F. Martens, O. Hilt, H. B. Brom, P. W. M. Blom, and J. N. Huiberts, *Physical Review Letters* **8708**, art. no.-086601 (2001).
- 93 H. Bassler, *Phys. Status Solidi B-Basic Res.* **175**, 15-56 (1993).
- 94 Y. N. Gartstein and E. M. Conwell, *Chem. Phys. Lett.* **245**, 351-358 (1995).
- 95 D. H. Dunlap, P. E. Parris, and V. M. Kenkre, *Phys. Rev. Lett.* **77**, 542-545 (1996).
- 96 P. E. Burrows, Z. Shen, V. Bulovic, D. M. Mccarty, S. R. Forrest, J. A. Cronin, and M. E. Thompson, *J. Appl. Phys.* **79**, 7991-8006 (1996).
- 97 P. W. M. Blom, M. J. M. Dejong, and J. J. M. Vleggaar, *Appl. Phys. Lett.* **68**, 3308-3310 (1996).
- 98 M. Koehler, M. G. E. Da luz, and I. A. Hummelgen, *J. Phys. D-App. Phys.* **33**, 2096-2107 (2000).
- 99 J. C. Scott, S. Karg, and S. A. Carter, *J. Appl. Phys.* **82**, 1454-1460 (1997).
- 100 P. W. M. Blom and M. J. M. De jong, *IEEE J. Sel. Top. Quantum Electron.* **4**, 105-112 (1998).
- 101 N. F. Mott and D. Gurney, *Electronic Processes in Ionic Crystals* (Oxford University Press, London, 1940).
- 102 P. W. M. Blom, M. J. M. Dejong, and S. Breedijk, *Appl. Phys. Lett.* **71**, 930-932 (1997).
- 103 P. Langevin, *Ann. Chim. Phy.*, 289 (1903).
- 104 D. D. C. Bradley and R. H. Friend, *J. Phys.-Condes. Matter* **1**, 3671-3678 (1989).
- 105 A. Dodabalapur, L. J. Rothberg, R. H. Jordan, T. M. Miller, R. E. Slusher, and J. M. Phillips, *J. Appl. Phys.* **80**, 6954-6964 (1996).
- 106 S. E. Burns, N. C. Greenham, and R. H. Friend, *Synth. Met.* **76**, 205-208 (1996).
- 107 H. Becker, S. E. Burns, N. Tessler, and R. H. Friend, *J. Appl. Phys.* **81**, 2825-2829 (1997).

- ¹⁰⁸ N. Tessler, S. Burns, H. Becker, and R. H. Friend, *Appl. Phys. Lett.* **70**, 556-558 (1997).
- ¹⁰⁹ B. Y. Jung, N. Y. Kim, C. H. Lee, C. K. Hwangbo, and C. Seoul, *Materials Research Society Symposium Proceedings* **621**, Q3.5.1-Q3.5.6 (2000).
- ¹¹⁰ J. Gruner, F. Cacialli, and R. H. Friend, *J. Appl. Phys.* **80**, 207-215 (1996).
- ¹¹¹ T. A. Fisher, D. G. Lidzey, M. A. Pate, M. S. Weaver, D. M. Whittaker, M. S. Skolnick, and D. D. C. Bradley, *Appl. Phys. Lett.* **67**, 1355-1357 (1995).
- ¹¹² J. S. Kim, P. K. H. Ho, N. C. Greenham, and R. H. Friend, *J. Appl. Phys.* **88**, 1073-1081 (2000).
- ¹¹³ A. Dodabalapur, L. J. Rothberg, and T. M. Miller, *Appl. Phys. Lett.* **65**, 2308-2310 (1994).
- ¹¹⁴ F. S. Juang, L. H. Laih, C. J. Lin, and Y. J. Hsu, *Jpn. J. Appl. Phys. Part 1 - Regul. Pap. Short Notes Rev. Pap.* **41**, 2787-2789 (2002).
- ¹¹⁵ D. G. Lidzey, D. D. C. Bradley, S. J. Martin, and M. A. Pate, *IEEE J. Sel. Top. Quantum Electron.* **4**, 113-118 (1998).
- ¹¹⁶ M. Tammer, R. W. T. Higgins, and A. P. Monkman, *J. Appl. Phys.* **91**, 4010-4013 (2002).
- ¹¹⁷ M. H. Lu, M. S. Weaver, T. X. Zhou, M. Rothman, R. C. Kwong, M. Hack, and J. J. Brown, *Appl. Phys. Lett.* **81**, 3921-3923 (2002).
- ¹¹⁸ T. Tsutsui, M. Yahiro, H. Yokogawa, and K. Kawano, *Adv. Mater.* **13**, 1149-+ (2001).
- ¹¹⁹ R. Windisch, P. Heremans, A. Knobloch, P. Kiesel, G. H. Dohler, B. Dutta, and G. Borghs, *Appl. Phys. Lett.* **74**, 2256-2258 (1999).
- ¹²⁰ U. Scherf and E. J. W. List, *Adv. Mater.* **14**, 477-+ (2002).
- ¹²¹ Y. Sato, S. Ichinosawa, and H. Kanai, *IEEE J. Sel. Top. Quantum Electron.* **4**, 40-48 (1998).
- ¹²² J. S. Kim, P. K. H. Ho, C. E. Murphy, A. J. A. B. Seeley, I. Grizzi, J. H. Burroughes, and R. H. Friend, *Adv. Mater., Submitted* (2003).
- ¹²³ G. C. M. Silvestre, M. T. Johnson, A. Giraldo, and J. M. Shannon, *Appl. Phys. Lett.* **78**, 1619-1621 (2001).
- ¹²⁴ W. Wang, S. F. Lim, and S. J. Chua, *J. Appl. Phys.* **91**, 5712-5715 (2002).
- ¹²⁵ S. F. Lim, W. Wang, and S. J. Chua, *Adv. Funct. Mater.* **12**, 513-518 (2002).
- ¹²⁶ Y. F. Liew, H. Aziz, N. X. Hu, H. S. O. Chan, G. Xu, and Z. Popovic, *Appl. Phys. Lett.* **77**, 2650-2652 (2000).
- ¹²⁷ J. S. Kim, P. K. H. Ho, C. E. Murphy, N. Baynes, and R. H. Friend, *Adv. Mater.* **14**, 206-+ (2002).
- ¹²⁸ G. G. Andersson, M. P. De jong, G. J. J. Winands, A. W. D. Van der gon, L. J. Van ijzendoorn, H. H. Brongersma, and M. J. A. De voigt, *J. Phys. D-Appl. Phys.* **35**, 1103-1108 (2002).
- ¹²⁹ C. Giebelser, S. A. Whitelegg, D. G. Lidzey, P. A. Lane, and D. D. C. Bradley, *Appl. Phys. Lett.* **75**, 2144-2146 (1999).
- ¹³⁰ E. Zoyer, A. Pogantsch, E. Hennebicq, D. Beljonne, J. L. Bredas, P. S. De freitas, U. Scherf, and E. J. W. List, *J. Chem. Phys.* **117**, 6794-6802 (2002).
- ¹³¹ J. I. Lee, G. Klaerner, and R. D. Miller, *Chem. Mat.* **11**, 1083-1088 (1999).
- ¹³² G. D. Hale, S. J. Oldenburg, and N. J. Halas, *Appl. Phys. Lett.* **71**, 1483-1485 (1997).
- ¹³³ B. H. Cumpston, I. D. Parker, and K. F. Jensen, *J. Appl. Phys.* **81**, 3716-3720 (1997).
- ¹³⁴ J. C. Scott, J. H. Kaufman, P. J. Brock, R. Dipietro, J. Salem, and J. A. Goitia, *J. Appl. Phys.* **79**, 2745-2751 (1996).
- ¹³⁵ A. R. Schlatmann, D. W. Floet, A. Hilberer, F. Garten, P. J. M. Smulders, T. M. Klapwijk, and G. Hadzioannou, *Appl. Phys. Lett.* **69**, 1764-1766 (1996).

- ¹³⁶ N. Johansson, F. Cacialli, K. Z. Xing, G. Beamson, D. T. Clark, R. H. Friend, and W. R. Salaneck, *Synth. Met.* **92**, 207-211 (1998).
- ¹³⁷ K. W. Wong, H. L. Yip, Y. Luo, K. Y. Wong, W. M. Lau, K. H. Low, H. F. Chow, Z. Q. Gao, W. L. Yeung, and C. C. Chang, *Appl. Phys. Lett.* **80**, 2788-2790 (2002).
- ¹³⁸ M. Stoessel, G. Wittmann, J. Staudigel, F. Steuber, J. Blassing, W. Roth, H. Klausmann, W. Rogler, J. Simmerer, A. Winnacker, M. Inbasekaran, and E. P. Woo, *J. Appl. Phys.* **87**, 4467-4475 (2000).
- ¹³⁹ D. C. Zou, M. Yahiro, and T. Tsutsui, *Appl. Phys. Lett.* **72**, 2484-2486 (1998).
- ¹⁴⁰ M. Yahiro, D. C. Zou, and T. Tsutsui, *Synth. Met.* **111**, 245-247 (2000).
- ¹⁴¹ D. C. Zou, M. Yahiro, and T. Tsutsui, *Synth. Met.* **91**, 191-193 (1997).
- ¹⁴² P. H. Nguyen, S. Scheinert, S. Berleb, W. Bruetting, and G. Paasch, *Organic Electronics* **2**, 105-120 (2001).
- ¹⁴³ H. S. Majumdar, A. Bandyopadhyay, A. Bolognesi, and A. J. Pal, *J. Appl. Phys.* **91**, 2433-2437 (2002).
- ¹⁴⁴ A. J. Campbell, D. D. C. Bradley, and D. G. Lidzey, *J. Appl. Phys.* **82**, 6326-6342 (1997).
- ¹⁴⁵ C. Giebel, S. A. Whitelegg, A. J. Campbell, M. Liess, S. J. Martin, P. A. Lane, D. D. C. Bradley, G. Webster, and P. L. Burn, *Appl. Phys. Lett.* **74**, 3714-3716 (1999).
- ¹⁴⁶ J. Steiger, S. Karg, R. Schmeichel, and H. Von seggern, *Synth. Met.* **122**, 49-52 (2001).
- ¹⁴⁷ J. W. Jang, D. K. Oh, C. H. Lee, C. E. Lee, D. W. Lee, and J. I. Jin, *Synth. Met.* **119**, 475-476 (2001).
- ¹⁴⁸ Q. B. Pei, G. Yu, C. Zhang, Y. Yang, and A. J. Heeger, *Science* **269**, 1086-1088 (1995).
- ¹⁴⁹ J. C. deMello, N. Tessler, S. C. Graham, X. Li, A. B. Holmes, and R. H. Friend, *Synth. Met.* **85**, 1277-1278 (1997).
- ¹⁵⁰ J. C. deMello, N. Tessler, S. C. Graham, and R. H. Friend, *Phys. Rev. B-Condens Matter* **57**, 12951-12963 (1998).
- ¹⁵¹ M. Ranger, D. Rondeau, and M. Leclerc, *Macromolecules* **30**, 7686-7691 (1997).
- ¹⁵² M. T. Bernius, M. Inbasekaran, J. O'brien, and W. S. Wu, *Adv. Mater.* **12**, 1737-1750 (2000).
- ¹⁵³ D. D. C. Bradley, M. Grell, X. Long, H. Mellor, and A. Grice, *Proceedings of the SPIE - The International Society for Optical Engineering* **3145**, 254-259 (1997).
- ¹⁵⁴ M. Grell, D. D. C. Bradley, X. Long, T. Chamberlain, M. Inbasekaran, E. P. Woo, and M. Soliman, *Acta Polym.* **49**, 439-444 (1998).
- ¹⁵⁵ M. Grell, D. D. C. Bradley, G. Ungar, J. Hill, and K. S. Whitehead, *Macromolecules* **32**, 5810-5817 (1999).
- ¹⁵⁶ M. Ariu, D. G. Lidzey, M. Sims, A. J. Cadby, P. A. Lane, and D. D. C. Bradley, *J. Phys.-Condes. Matter* **14**, 9975-9986 (2002).
- ¹⁵⁷ A. J. Cadby, P. A. Lane, H. Mellor, S. J. Martin, M. Grell, C. Giebel, D. D. C. Bradley, M. Wohlgemann, C. An, and Z. V. Vardeny, *Phys. Rev. B* **62**, 15604-15609 (2000).
- ¹⁵⁸ A. J. Cadby, P. A. Lane, M. Wohlgemann, C. An, Z. V. Vardeny, and D. D. C. Bradley, *Synth. Met.* **111**, 515-518 (2000).

3. Experimental Methods

This Chapter explains the design and fabrication of the various devices and samples described in the experimental Chapters. It then outlines the range of characterisation techniques used to study them.

3.1 Polymer Light Emitting Diodes

The bulk of the experimental work in this thesis was based on the measurement of polymer light-emitting diodes. These test devices were constructed according to a basic design, to which modifications were made in order to best study the characteristic of interest.

3.1.1 Standard Polymer LEDs

The standard structure for a polymer LED is as shown in Figure 3.1. The indium tin oxide (ITO, see Section 2.4.1) provides a transparent conducting path without significant voltage drop across the face of the LED. The PEDOT:PSS layer (Sections 2.4.1 and 2.5.3) acts to planarise the anode surface, and to aid injection of holes into the conjugated polymer by means of its high work function. The electroluminescent polymer layer is the active region where charge transport, recombination and emission takes place, as detailed in Section 2.4. Calcium is used as a cathode due to its low work-function, suitable for efficient electron injection into the polymer LUMO level. Finally, the aluminium cap protects the calcium layer from oxidation and provides added conductivity across the face of the cathode.

Standard polymer LEDs were produced on ITO-coated glass with sheet resistance approximately $13 \Omega/\square$ ¹. The 1.1 mm thick glass is covered with a 20 nm silicon dioxide barrier layer, to block diffusion of sodium ions from the glass into the ITO, on top of which the ITO is deposited. The surface roughness of this ITO has previously been measured as approximately 2 nm, although it is the presence of infrequent spikes on the scale of many tens of nanometres which can destroy the device properties². The glass was cut into 12 mm

squares, with the ITO etched into a central stripe defining the maximum extent of the active area. Substrates were received in this pre-prepared form, with a protective layer of photoresist.

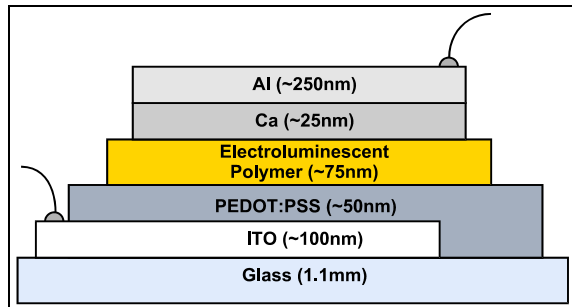


Figure 3.1: Cross section of a typical polymer LED, with anode and cathode connections.

Device fabrication began by cleaning of the substrates. This consisted of rinsing in acetone to remove the majority of the photoresist, immersion in acetone in an ultrasonic bath for 10 minutes, drying under flow of nitrogen from a filtered gun, ultrasonic cleaning in isopropanol (IPA) for 10 minutes, and drying again with the nitrogen gun. Next the substrates were treated in an oxygen plasma barrel etcher, with 250 W incident power and negligible reflected power, for 10 minutes³. This not only removed any residual organic traces, but left the ITO and glass surface strongly hydrophilic.

An aqueous solution of PEDOT:PSS (containing PEDT and PSS in a 1:16 ratio) was spin-cast onto the substrates to a thickness of approximately 50-70 nm, using a commercially available photoresist spin-coater in air. Immediately after spin-coating, the substrates were baked under flow of nitrogen at 200 °C for two hours to drive off excess water.

The emissive polymer layer was similarly spin-cast from solution onto the surface of the PEDOT:PSS layer. Typical solvents for this step included mixed xylenes, *p*-xylene and toluene, with a polymer concentration (w/v) of typically 10 mg/ml. The cured PEDOT:PSS layer was not susceptible to dissolution in these solvents.

After polymer spin-coating, the cathodes were applied. The samples were inverted onto shadow masks defining 8 pixel areas, with contacts extending to the sides of the device area, and loaded into a vacuum chamber. The chamber was pumped down to a pressure of $\sim 10^{-6}$ mbar, and calcium thermally evaporated from an alumina crucible, heated by a tungsten filament, through the shadow mask onto the surface of the polymer at typical rates of 5 Å/s. The total thickness of approximately 25 nm was determined from the oscillations of a quartz crystal monitor. Finally the capping layer of aluminium was thermally evaporated at rates rising to 2 nm/s, up to a thickness of between 250 and 400 nm. Figure 3.2 shows the layout of the various components.

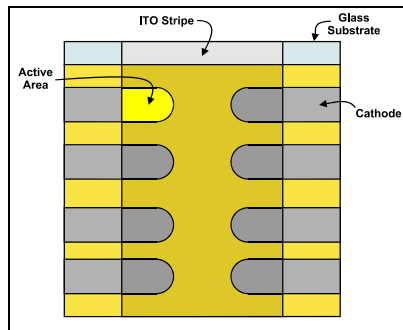


Figure 3.2: Diagram of a finished device, seen from the viewing side through the glass.

At this point the devices were complete in their simplest form, and could be electrically driven by making electrical contacts to the selected pixel cathode and the ITO anode.

3.1.2 Variations on the standard design

The standard design provides a template to which alterations can be made to suit the desired measurement.

3.1.2.1 Bilayer devices

When a well-defined polymer heterojunction was desired in the semiconducting portion of the device, fabrication proceeded as usual until the first (anode-side) polymer layer had been deposited. The second (cathode-side) polymer layer was then spin-cast to the desired thickness on a cleaned blank glass slide. The polymer layer was mechanically removed around the edges of the slide by a suitably soft point such as a wooden cocktail stick. This prevented unwanted adhesion of the polymer layer to the glass slide by clinging over the rough cut edges.

The glass slide was then gently lowered into de-ionised water, whereupon the water lifted the polymer film, leaving it floating on the surface. The substrate (including the anode-side of the device) was then quickly lowered into the water, manoeuvred beneath the floating film, and raised through the surface to “catch” the polymer film on the top surface of the device. This often resulted in a few wrinkles in the film, which would simply become inactive areas of the device due to their excess thickness. The heterostructure was placed under vacuum overnight, at a temperature of approximately 100 °C, to drive off any excess moisture and ensure good contact between layers, following which cathode deposition proceeded as usual.

3.1.3 Encapsulation

Polymer light-emitting diodes are highly susceptible to attack by oxygen and water, causing degradation as described in Section 2.4.7. One approach advocates testing all devices under a dry nitrogen atmosphere, but this can be impractical for extended periods of testing, and severely limits the range of equipment which can be used. Instead, for most devices studied in this work, the active layers were permanently encapsulated to preclude oxygen and moisture, allowing storage and testing to take place under ambient conditions. Two different methods were used for encapsulation.

3.1.3.1 Epoxy/glass sandwich

Since the encapsulation process necessarily renders the device surface inaccessible, permanent contacts were first made to the active area. This took place in the dry nitrogen glovebox, into which the samples were brought directly from the evaporation chamber without passing through air. Standard semiconductor testing legs, as seen in the completed device in Figure 3.3, were applied transversely to the substrate edges, clamping themselves onto the glass and forming a continuous electrical pathway to the anode or cathode, according to the positioning of the legs. With the legs in place, using them to support the device with its bare surface uppermost, a drop of epoxy resin⁴ was placed directly onto the surface. The resin and hardener had previously been degassed by heating under a partial vacuum to remove oxygen and low molecular weight components. Finally, a glass slide was placed on top of the resin, sandwiching it into a thin layer and forming a barrier against vertical ingress of oxygen and moisture. The resin expelled at the edges served to bond the contact legs into place.

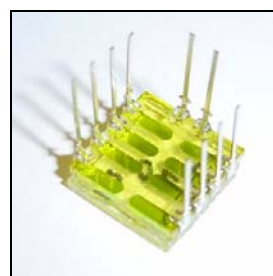
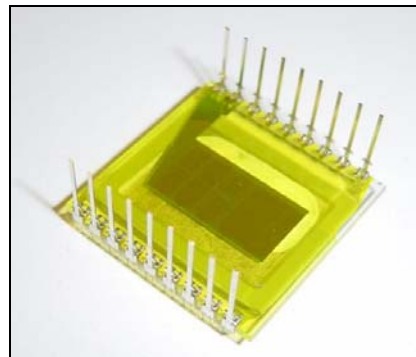


Figure 3.3: Glass/Epoxy encapsulated device with legs. Seen from active side. Glass is 12 mm square.

3.1.3.2 “Tin can”

This procedure was performed by an automated system in the facilities of Cambridge Display Technology. The “tin cans” consisted of a rectangular aluminium plate big enough to cover the active area, but not so large as to interfere with the legs at each side. A rim around the edge of the plate completed the shallow tray

of aluminium. Into each can was inserted a commercially available getter, to sequester any residual or future ingress of oxygen and water.



**Figure 3.4: Tin-can encapsulated device, containing getter seen in white behind cathode.
Patterned ITO anodes can barely be seen. Glass is 25 mm square.**

An automated nozzle dispensed UV-cure epoxy around the edge of each tin can, and the substrates were inverted and pressed into place. A template mask was placed over the substrates to cover the active areas, and the remainder exposed to UV light to cure the adhesive. Legs were finally applied in the normal way, and a stripe of standard epoxy used along each row of legs to secure them to the device and cover the exposed cathode connection. Figure 3.4 shows a device completed in this way.

3.1.4 Substrate and mask design

A selection of substrate designs were used in order to tailor the test devices to the intended experiment. In each case, matching shadow masks provided the desired layout for evaporation of the cathode.

3.1.4.1 Wide-stripe ITO substrates

The simplest substrates used consisted of a 12 mm square glass substrate with a wide ITO stripe extending from top to bottom and occupying the central 7 mm of the substrate area, as described in Section 3.1.1.

These substrates were usually used in conjunction with the previously described patterned cathode mask, with eight “fingers”, which resulted in a common anode and eight individually addressable cathodes. The active area of each pixel in this scheme was approximately 3.1 mm^2 . This is the scheme shown in Figures 3.2 and 3.3. On occasion, when a single large pixel was required, a wide-stripe cathode mask was used, with the cathode oriented perpendicular to the ITO stripe. The active area here was approximately 50 mm^2 .

When required, encapsulation of these devices was always by the epoxy/glass sandwich method. All processing steps for these devices took place in the cleanroom facilities of the Cavendish Laboratory.

3.1.4.2 Type II substrates

Type II substrates provided a selection of pixel sizes on a single large 25 mm square device. Unlike the wide-stripe ITO substrates, here the ITO was patterned to define the shape of each pixel, with six pixels at 10 mm^2 , one pixel at 50 mm^2 and one pixel at 0.5 mm^2 . In each case the ITO extended to the side of the device, to provide individually addressable anodes. A cathode mask provided a single cathode, common to all eight pixels, covering the central area of the substrate and extending out to one corner to provide a connection point. This is the scheme used for the device shown in Figure 3.4.

These devices were always encapsulated, initially with the epoxy/glass sandwich method, and as the technique became available, with tin cans. Device preparation on these substrates was carried out in the cleanroom facilities of Cambridge Display Technology Ltd.

3.1.4.3 Large pulse substrates

For fast-modulated electroluminescence experiments, the characteristic RC time of a system becomes an important factor. Therefore, special substrates were used which minimised the series resistance of the devices by use of aluminium tracking around the ITO regions.

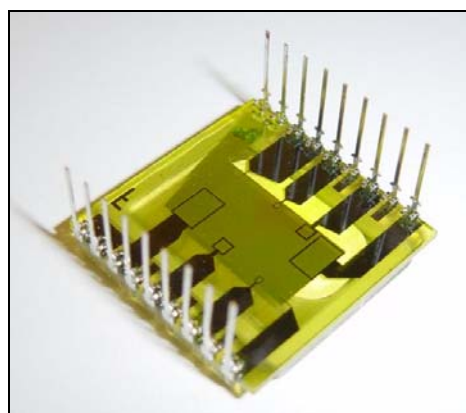


Figure 3.5: F8BT device fabricated on a large pulse substrate, with tin-can encapsulation.

On 25 mm square substrates, eight ITO pads were defined – two each at (nominally) 10 mm^2 , 1 mm^2 , 0.1 mm^2 and 0.01 mm^2 . The pads themselves were slightly larger than these dimensions to allow for overlap with the aluminium tracking, which was deposited next. The tracking surrounded each pixel and extended

to the side of the substrate to provide individually addressable anodes. Finally, a 1 μm thick polyamide layer covered all the aluminium and glass areas, leaving only a well-defined area of each ITO pad to become the active area of the pixel. Such a device is shown in Figure 3.5.

Just as for Type II substrates, a single-cathode mask was used with these substrates. Encapsulation was initially by the epoxy/glass method, and later with tin cans. Device preparation on these substrates was carried out in the cleanroom facilities of Cambridge Display Technology Ltd.

3.1.4.4 Small pulse substrates

Analogous to the large pulse substrates, but suited for processing in the facilities of the Cavendish Laboratory, a small version was specially designed by modification of a previous design⁵.

ITO pads at 1 mm^2 (three pads), 0.5 mm^2 (two pads), 0.25 mm^2 (two pads) and 0.1 mm^2 (one pad) were connected by aluminium tracking to each other and to a common anode connection at the substrate edge. Care was taken to minimise the amount of aluminium tracking in the immediate vicinity of the pixel area, to avoid eventual overlap with the cathode areas and any resulting excess capacitance. Once again, a polyamide layer defined the exact pixel areas on the ITO to produce well-defined active areas in the finished devices.

Encapsulation, when required, was always by the epoxy/glass sandwich method.

3.1.5 Procedures for consistency and device reproducibility

When characterising polymer semiconducting devices, reproducibility between devices is an important concern. Therefore certain procedures were adopted to minimise contamination and enhance the uniformity of the finished devices.

3.1.5.1 Solution preparation

Solutions were generally specified in weight-for-volume (w/v) concentrations. Typical concentrations were in the region of 10 mg/ml, and typical batch sizes were up to approximately 5 ml. Amber vials were used to minimise the amount of short wavelength light reaching the solutions. This light can cause photoexcitations which, in the presence of oxygen, can lead to unwanted photo-oxidation.

The vial, supplied sealed with a PTFE-lined cap, was blown clean internally with a filtered nitrogen gun. Powder-free gloves were used to avoid any unwanted material sticking to the vial. Polymer solid was measured directly into the vial, using a nickel spatula and weighing with a Sartorius 1601 pan balance accurate to 0.1 mg. The vial was removed from the balance at each addition of polymer solid, to prevent any excess solid falling onto the pan. Solvent was measured out using a clean, dry and dust-free glass syringe, to the volume required. Depending on the solution being prepared, the vial was either sealed and placed on a roller, or heated and magnetically stirred to ensure that the polymer was fully dissolved.

3.1.5.2 Device preparation under nitrogen atmosphere

Certain polymers, in particular the large band-gap blue-emitting polymers, are known to be particularly sensitive to oxygen and moisture in operation. Therefore it is important to exclude these contaminants as far as possible during the device fabrication stage. To this end, the substrates were transferred into a nitrogen-filled glovebox (<5 ppm O₂) before spinning took place. Transfer to the evaporation chamber was then accomplished without removing the devices into air.

3.1.5.3 Contamination

To minimise the inclusion of dust particles in the finished devices, the polymer solutions were passed through a PTFE-based 0.45 µm filter as they were dispensed onto their substrates.

3.2 Absorption spectroscopy samples

Samples for absorption spectroscopy did not normally require cathode or anode contacts, but usually required the elimination of glass which shows absorption and fluorescence features of its own in the spectral regions of interest.

3.2.1 Substrates

For UV-Visible absorption spectroscopy, Spectrosil-B⁶ quartz substrates were used. For photothermal deflection spectroscopy (PDS), which is highly sensitive deep into the infrared, water free Spectrosil-WF⁶ quartz substrates were used. Substrates were cleaned in ultrasonic baths of acetone and IPA, just as in the case of device preparation.

3.2.2 Film preparation

Polymer films were usually spin-coated from solution to the required thickness. Solutions were prepared exactly as for device production. Samples were usually prepared and stored under nitrogen to exclude oxygen and moisture. In the case of PDS, which is a front-surface technique, films were often prepared by drop-casting, which yielded a thicker film and thus a stronger signal.

3.3 Sample analysis

A selection of techniques are available for the measurement and analysis of polymer samples which have not been incorporated into device structures.

3.3.1 Surface profilometry

In order to measure the thickness of films used, a Sloan Dektak IIA surface profilometer was used. The film was scratched through with a sharp point, and the profilometer needle scanned across the scratch to reveal its depth and yield the film thickness.

3.3.2 UV-Visible absorption spectroscopy

Simple measurements of optical absorbance were made with a Hewlett Packard HP8453 UV-Vis absorption spectrometer. This equipment illuminates the sample with tungsten and deuterium lamps, recording the transmitted light to calculate the sample's absorption spectrum. Comparison with a "blank" control substrate yields the absorbance due to the film alone.

The range of wavelengths accessible is 190 to 1100 nm. UV-Vis data acquisition is extremely quick, taking a matter of seconds per sample. This technique is useful for strong absorptions, which produce low-noise signals in the resulting data. Since the system only actually measures transmitted light, any surface scattering can cause spurious absorption signals to appear. Thus the technique does not work well for very low level absorptions, nor for highly scattering samples. Since a wide spectral region is simultaneously illuminated, fluorescence pumped at one wavelength can lead to an artificially low absorption readout at the emission wavelength, possibly complicating data analysis.

3.3.3 Photothermal Deflection Spectroscopy

Photothermal Deflection Spectroscopy (PDS)⁷ is a highly sensitive absorption technique, particularly suited to the analysis of polymer films^{8,9}. The apparatus used here was originally constructed by Dr D. S. Thomas, and a full description of its design and construction appears in his Ph.D. thesis¹⁰. See also Appendix A.

Most absorption spectrometers measure transmitted light, but this causes any scattering or reflection to be recorded as an erroneous absorption signal. In PDS, absorption is directly probed by measuring the heating effect of an illumination beam on the sample, as it scans through the wavelengths of interest. The PDS Rig covers the wavelength range from 380 to 2050 nm, and a typical scan takes several hours to acquire.

3.3.3.1 PDS fundamentals

PDS proceeds by front-surface illumination of the sample with a chopped beam of monochromated light. According to the absorbance of the polymer film, a portion of the incident light is absorbed. All other light, scattered, reflected or transmitted, plays no further part. The absorbed light produces a minuscule heating effect in the film, which is then conducted out into a surrounding fluid medium¹¹. The resulting temperature gradient, momentarily present in the fluid, produces a corresponding refractive index gradient which can be probed by a transverse probe laser beam¹². The laser beam deflection, which is proportional to the absorption¹⁰, is monitored by a pair of photodiodes and accurately measured by a lock-in amplifier locked to the chop frequency of the light. The detailed theory has been previously described in a 1-D formalism¹³, in 3-D⁷, and in the context of measuring thin polymer films¹⁰.

Whereas UV-Vis has a lower limit in the region of perhaps 1 % absorption, due to reflection and scattering, PDS directly measures absorption and this apparatus can reveal features as much as 5 or 6 orders of magnitude weaker than the main $\pi-\pi^*$ absorption. Such sensitivity is achieved by running the Rig as a lock-in modulation experiment.

3.3.3.2 Rig components

Figure 3.6 shows a schematic diagram of the Rig components. The illumination beam is provided by a custom-built 100 W xenon arc-lamp designed by Light Support Ltd. The chopper wheel and driver is a model 3501 from New Focus Inc, driven at 13 Hz to avoid mains interference. The monochromator is a CVI Digikröm DK240, which feeds the heating beam via optical fibre to the vibration-isolated main table. The probe laser is a 4 mW 670 nm Peltier-stabilised fibre-coupled diode laser from Point Source Ltd. Like the heating beam, to avoid vibrations only the delivery fibre enters the main experiment area.

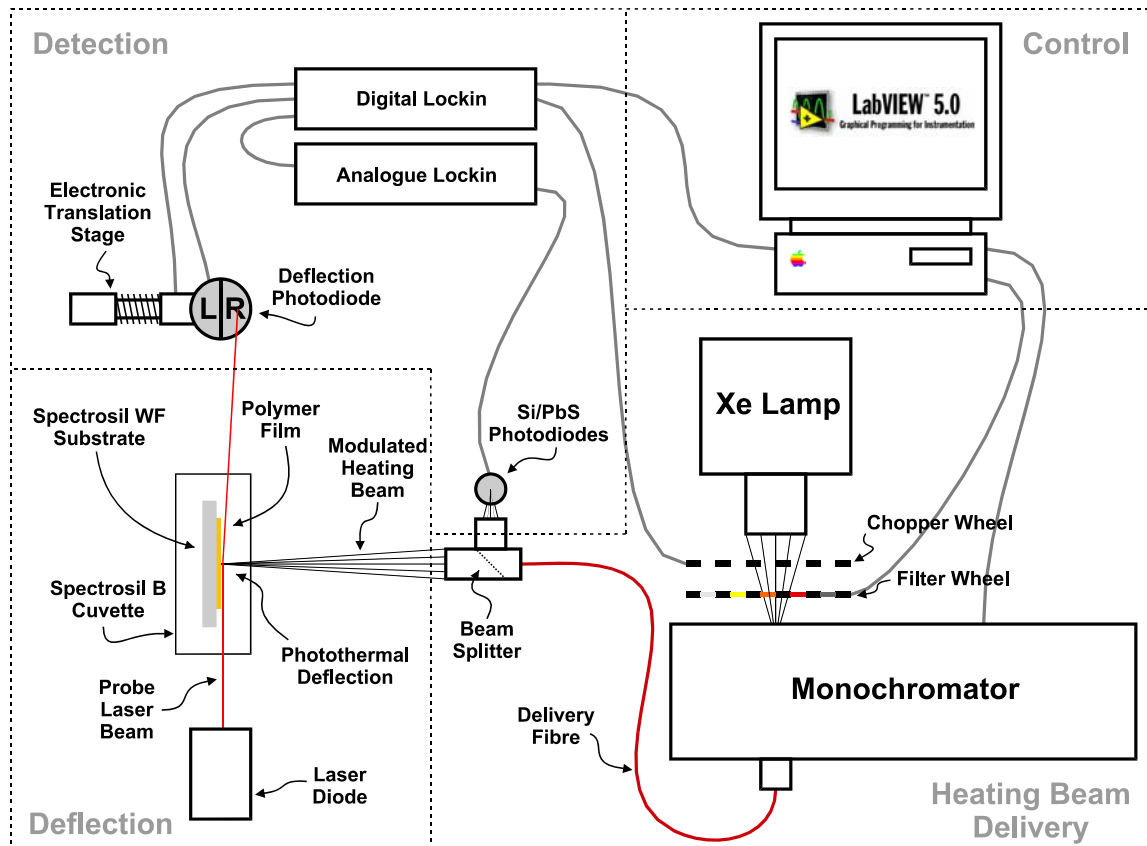


Figure 3.6: Schematic diagram of the PDS Rig. Four main divisions are identified.

Due to the spectral features of the xenon lamp, a dual photodiode consisting of PbS and Si components measures the intensity of a portion of the probe beam as it enters the experiment, for normalisation purposes. The probe laser deflection is detected by a silicon quadrant photodiode, wired into a Left pair and a Right pair, and the signal obtained as Right minus Left. PDS theory states that this value is directly proportional to the absorbance of the material¹⁰. The photodiode stem is mounted on an electronic translation stage to allow for automatic re-alignment of the photodiode as the DC component of beam deflection drifts.

The deflection medium consists of fully-fluorinated short carbon chain molecules, formerly marketed by 3M Corp (St Paul, MN, US) as Fluorinert FC-104. This colourless liquid is ideal for the PDS experiment as it has no measurable absorption in the wavelength range of interest and does not swell or react with the polymer films. The sample cell, containing the Fluorinert, is a polished Spectrosil-B cuvette with a polyethylene insert to hold the sample in place and a silicone rubber seal.

Measurements are made with a Stanford Instruments SR830 DSP lock-in amplifier, and the whole experiment controlled and recorded on a Power Macintosh desktop computer equipped with a GPIB interface bus and running specially written controller software in the LabView environment.

3.3.3.3 Apparatus modifications

During the course of work for this thesis, one significant modification was made to optimise the performance of the rig.

The internal filter wheel had provided space for only six low-pass filters for higher-order removal. More closely-spaced filters were required to eliminate artefacts which appeared at the band-edge. To accommodate these, a new filter wheel was constructed with space for 10 filters. This wheel was attached in place of the existing circular graded-index neutral density filter wheel, external to the monochromator.

The old graded neutral density filter had been used to attenuate the heating beam, but only its higher transmittance end was ever used, and this had been burnt by the lamp. Instead, a series of five reflective metal film neutral density filters at discrete optical densities were inserted into the monochromator filter wheel, leaving the sixth slot non-attenuating.

The LabView controller application was modified to cater for the exchange of the two filter wheels, the extra order-sorting filters, and the discretely-spaced attenuating filters.

3.3.3.4 Experimental procedure

To prevent photo-oxidation, samples for PDS are normally stored under nitrogen prior to measurement, thus minimising the oxygen content of the film. The sealed sample chamber containing Fluorinert and any previously-measured sample is introduced to the dry nitrogen-filled glovebox. A simple screw-release allows the sample insert to be removed from the cuvette, whereafter another screw unfastens the used sample. The new sample is screwed into place, the Fluorinert topped up if necessary and the sample chamber re-sealed before removal from the glovebox.

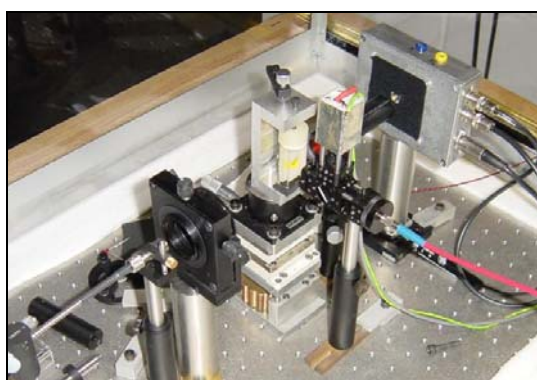


Figure 3.7: Sample area of PDS Rig showing sample (centre, yellow), heating beam delivery fibre (red), probe beam delivery (left, metal-clad), and deflection photodiode surrounded by a square of black felt (rear right).

The sample chamber is placed back inside the Rig, shown in Figure 3.7, and the process of aligning it begins. In order to maximise the PDS signal, the sample must be very accurately aligned such that the probe beam passes close to the sample surface. To this end, a strongly absorbing region of the spectrum is selected to maximise the measured signal. For many of the polymers studied, this is found around $\lambda = 440$ nm. After selection of the desired wavelength, the filter wheels and monochromator slits are set so as to maximise the throughput of light in the heating beam. A manual iterative process is then required to adjust the sample position along the x -axis (the direction of the heating beam) and rotation about the y -axis, so that the fixed probe beam (shining down the z -axis) can be made to pass directly across the surface of the film.

Once the signal intensity has been maximised, the wooden vibration-proof box can be lowered over the top of the apparatus and control taken over with the computer. Parameters for the experiment are set in the LabView environment, normally including a scan range from 3.2 eV down to 0.6 eV in 0.01 eV steps. Finally, a data output filename is specified after which data is collected automatically. The time taken for a scan to complete can vary greatly. At low absorptions, the controller application automatically increases the time constant and the number of averages taken. Thus, depending on the sample absorption, a scan can last between a couple of hours and approximately one day.

3.3.3.5 Data analysis

The controller application produces a file containing wavelength and energy, raw measured deflection, the value of the normalising signal from the two-component photodiode, and the normalised signal. Further columns are available for use with a calibration file, generated by measuring the response of a black sample which fully saturates the deflection signal, and for the finalised data, corrected with this calibration file. Data is then usually plotted showing corrected absorbance on a logarithmic scale against the photon energy in eV on a linear scale.

The calibration data obtained in experiment almost exactly fit a linear response function. Therefore an idealised calibration file was generated by linear regression. This was done purely to avoid the introduction of experimental noise from the calibration experiment into every data set, and does not compromise the integrity of the data thus calibrated. The calibration used, and a typical experimental calibration data set, are presented in Section A.5.1.

Since the deflection values measured by the experiment are subject to the precise alignment of the sample, no absolute absorption values can be determined by PDS alone. For true calibration, it is usually possible to compare a point on the band-edge with the equivalent point on a UV-Vis scan. However this is only accurate for homogeneous samples, since PDS is progressively less sensitive to buried layers.

It is important to note that under high absorption the measured PDS deflection saturates. Therefore the shape of the $\pi-\pi^*$ peak as observed in PDS may be distorted and its uppermost values not meaningful. For a faithful comparison of the high-absorption regime to the sub-gap region where PDS comes into its own, it is more useful to correlate the PDS spectrum with a UV-Vis spectrum as previously described. The normalisation must be done at a point where the PDS spectrum has not saturated, but where the UV-Vis signal is strong enough to be relatively noise-free – usually on the band-edge itself.

The wavelength resolution of the PDS rig depends on a number of factors, but most importantly the monochromator slit widths. Whilst wider slits admit more light and lead to a stronger signal, they also admit a greater bandwidth of light. With the slits set to their 2000 μm maximum width, as they were for the duration of this work, the FWHM observed for known sharp features was no greater than 30 nm, corresponding approximately 0.1 eV in the region of 2 eV below the bandgap. Polymer sub-gap features are typically *several* tenths of an eV wide, whilst spikes due to noise can be isolated since they appear on the 0.01 eV scale of spacing between individual data points.

3.3.4 Photoluminescence microscopy and spectrophotometry

An Olympus BX60 optical microscope, equipped with a mercury lamp, was used for photoluminescence (PL) microscopy. The microscope allowed for blue (450 to 480 nm) or UV (330 to 385 nm) excitation of the sample, with long-pass filters present in the return beam to prevent detection of the illumination wavelengths. White light illumination was also available, without any filtering of the returned light. Two integral neutral density filters were available to attenuate the excitation beam, along with an iris to vary the spot size without altering the flux. Finally, beam splitters between the objective and the eyepiece allowed for attachment of a camera and a spectrophotometer. PL spectra were measured using an Ocean Optics CCD spectrophotometer, directly coupled to the microscope via a fused silica fibre bundle.

3.4 Device analysis

The following electrical probes were used to characterise devices containing polymer films.

3.4.1 Current – Voltage – Luminance (IVL)

The simplest study of a polymer LED is the IVL scan. All devices fabricated on the large (25 mm square) substrates were measured in the automatic test facility at Cambridge Display Technology. This apparatus

performs a voltage scan through the range specified, and measures the current passed and the light emitted at each step. This is automatically repeated for all eight pixels on up to eight devices in a batch. A spreadsheet macro developed by CDT collates the data to show plots of efficiency, luminance and current against voltage, and other useful data.

3.4.2 Electroluminescence microscopy

For optical microscopy of working devices *in situ*, the same Olympus BX60 microscope was used as for PL microscopy. The LED under study was driven in constant current mode by a Keithley 220 current source.

3.4.3 Electroluminescence spectrophotometry

EL spectrophotometry was performed with the Olympus BX60 microscope and Ocean Optics CCD spectrophotometer. This allowed for controlled, repeatable measurements of the same area of an LED, from a position normal to the LED surface. The mercury lamp beam was shut off, and the filters set to prevent any filtering of the emitted light.

3.4.4 Time-resolved pulsed electroluminescence intensity

Time-resolved pulsed electroluminescence¹⁴⁻¹⁶ allows the early stages of light emission from a polymer LED to be analysed. This yields data including the time taken for onset of light emission¹⁷, the rise-time of the intensity¹⁷, and various other features¹⁸⁻²⁰. From this data, information can be extracted about the operation of the LED, including the charge carrier mobility^{17,21,22}. The apparatus used in this thesis has been developed at the Cavendish Laboratory over a number of years^{17,19,21,23-29}, with frequent refinements to improve its characteristics and ease of use. The rig is described in detail by Dr D.J. Pinner in his Ph.D. thesis⁵, along with a wide range of experiments performed using the rig. See also Appendix B.

3.4.4.1 Pulse rig fundamentals

The Pulse Rig consists of two independent portions: the drive circuitry and the detection apparatus. The drive circuitry provides square voltage pulses of the desired duration and frequency. The shortest useful pulses produced by the rig are a few tens of nanoseconds long, below which the pulse shape is not sufficiently square to be useful. Drive voltages can be specified in increments of 0.1 V up to a maximum of 150 V. The range most usually of interest falls between approximately 2 V and 20 V.

The link between drive and detection sections is the polymer LED itself. The detection system then uses a photomultiplier tube (PMT) to measure light intensity, an inductively coupled current probe to measure instantaneous current and a voltage probe to measure the voltage dropped across the device. Any two of these three channels (usually light intensity and current) are fed to a digitising oscilloscope which records the data as a function of time during the pulse and either displays the results on screen or sends them for storage and analysis on a desktop computer.

3.4.4.2 Rig components

Figure 3.8 shows a schematic diagram of the components of the Pulse Rig. Pulse duration and frequency are specified with a Hewlett Packard 8116A 50 MHz Pulse/Function Generator. This is set to output square pulses of amplitude 2.5 V during the desired “on” periods, which are fed via low-resistance silver coax cables to the pulse generation board at the centre of the rig. It also produces a TTL output used for triggering the oscilloscope.

In addition to the duration and frequency signal from the function generator, the pulse generation board also requires a voltage source with which to specify and supply a voltage for driving the LED in the “on” phase. This is provided by a Farnell PSD1011A current-limited voltage source, equipped with a small capacitor bank to prevent voltage droop when delivering short bursts of high current.

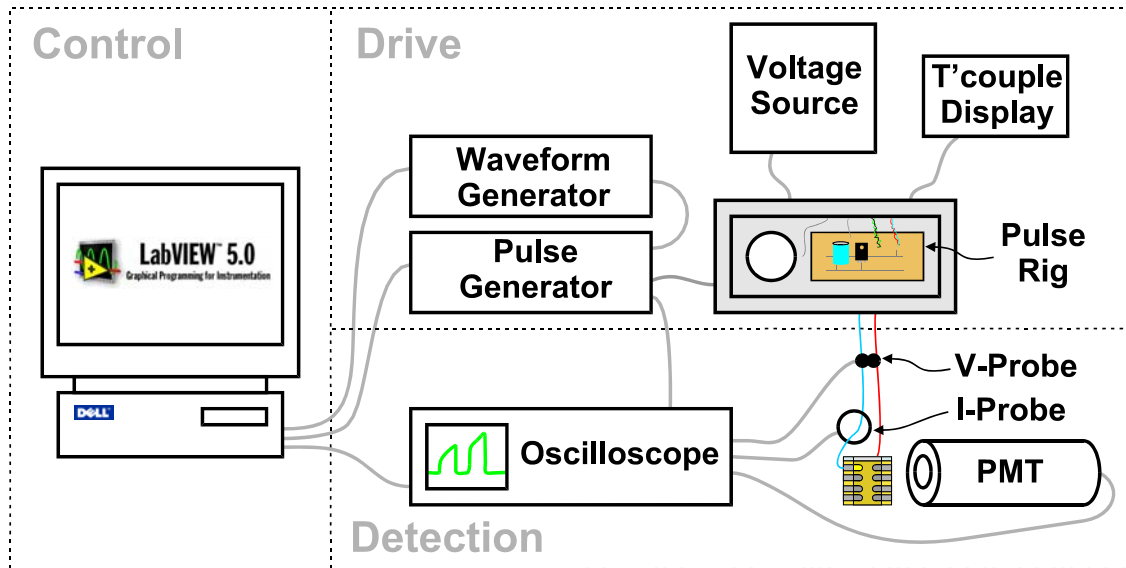


Figure 3.8: Schematic diagram of the Pulse Rig.

The Pulse Rig board itself was custom built by Mr C.J. Moss of the Electronics Workshop at the Cavendish Laboratory, and incorporates most importantly a high-specification fast MOSFET. This device feeds the voltage presented by the voltage source through to the test LED, being switched by the output from the

function generator. By this arrangement, a sharp switch-on of the LED is achieved without being limited to the voltage range, current supply or pulse shape fidelity of the function generator. It is important to note that in the off-phase, the MOSFET simply disconnects the LED into open-circuit and does not short it to 0 V. To improve turn-off characteristics, therefore, a $7\ \Omega$ resistor is placed in parallel with the test LED. This resistor draws a proportion of the current in the on-state, but in the off-state it allows the LED to drain any excess capacitor charge with an RC time constant comparable to that seen during the initial charging phase. Charges re-extracted from the polymer bulk are also sunk by this resistor. The circuitry is powered by a dedicated 12 V power source, incorporating a high-voltage power supply (no longer used) available for driving test LEDs at higher voltages than those available with the separate voltage source

The photomultiplier tube is a Hamamatsu R1387 device operated on its lowest sensitivity setting with an acceleration potential of approximately 900 V. The voltage probe, integrated into the pulse generation board, provides an output signal of 0.1 V for each Volt dropped across it. The inductively-coupled current probe is a CT-GP/A device from Bergoz Instrumentation. It produces 0.2 V output per Amp flowing through it. All three of these devices were selected on their ability to respond with at least 10 ns time resolution, exceeding the specifications of the pulse delivery system itself. Any two of these three devices can be monitored on the Hewlett Packard HP54502A 400 MHz digitising oscilloscope. Input impedances are set at $50\ \Omega$ for the current probe and $1\ M\Omega$ for the PMT or voltage probe. A custom-built amplifier allows pre-amplification of the current-probe or PMT signals if required. The second function generator, a Hewlett Packard HP33120A 15 MHz Function/Arbitrary Waveform Generator, is available as a trigger source for the main function generator. This allows for production of trains of identical pulses, repeated at specified intervals.

The rig incorporates a thick aluminium vacuum chamber with Perspex windows, suitable for measuring non-encapsulated LEDs. It is also equipped with a cold finger and liquid nitrogen reservoir, and a calibrated thermocouple, to allow for low-temperature measurements.

The experiment is controlled by a PC running the LabView environment and equipped with a GPIB interface. Controller applications were written during the course of work on this thesis, to automate various functions. These applications incorporate a component previously written by Dr N.C. Greenham to acquire data from the digital oscilloscope, and a component written by Dr D.J. Pinner, to address the function generators. The voltage source and thermocouple readout cannot be remotely addressed via GPIB.

3.4.4.3 Apparatus modifications

During the course of work for this thesis, modifications were made to the original⁵ configuration.

A major inconvenience in the past had been the reliance on using a vacuum chamber to protect the test LED from oxygen. Not only did this require the chamber to be returned to atmospheric pressure to change LEDs, but this was necessary even to change pixels on a single LED. An external selection knob was not present, in order to minimise the length of wire between the pulse generator and the LED.

In converting from delicate “open” devices to durable encapsulated devices, the rig has been equipped with zero insertion force (ZIF) connectors. These allow easy replacement of the test LEDs, with their standardised leg connectors, without the need to seal and evacuate the chamber. An array of pins on the rear of the ZIF sockets allow easy alteration of the currently addressed pixel.

It was found that the LED side of the circuit suffered from resonant oscillations at turn-on, which created artefacts in the observed characteristics. After careful experimentation, an $80\ \Omega$ damping resistor was added in series with the LED which critically damped the system when testing a typical LED without unacceptable detriment to the RC rise time of the circuit.

Although not presented in this thesis, an experiment was designed including a monochromator to make wavelength-dependent measurements of the transient response of LEDs, as seen in Section B.4.1.2. Thus the transient electroluminescence could be plotted as a function of both time and wavelength, which may prove particularly enlightening when applied to the study of bi-layer devices.

A selection of LabView applications were written to control the apparatus. This included a “snapshot” facility to record the oscilloscope traces on demand, a timed-repeat function to gather a series of traces at specified points in time, and a monochromator control program to record the light output of the LED at selected wavelengths, by first passing it through the computer-controlled monochromator.

3.4.4.4 Experimental procedure

Standard experimental procedure began by securing pair of loose ZIF sockets onto the test device. The back of the device was attached to an xyz translation stage with Blu-Tac, leaving the active area visible from the front. Pixel selection followed by connecting the Rig outputs to the chosen pins on the back of the ZIF sockets. In order to record a current trace, just one of the supply wires was threaded through the hole in the current probe. With the device secured in place, the photomultiplier tube was manoeuvred into position so as to maximise the through-coupling of light. The PMT was secured with a magnetic stand onto the optical table and it was found that electrically insulating the PMT from the bench, by simply inserting a sheet of paper, greatly stabilised the recorded traces. Finally the experimental area was shielded from light with a thick black cloth cover to prevent interference with the PMT. At this point, all parts of the rig could be

powered up, including the rig power supply, the high voltage PMT supply, the digital oscilloscope, the function generator(s) and the device-drive power supply. This was initially set to 0 V, to prevent inadvertent damage to the test LED.

Next, the drive regime was specified. Although a LabView application was available to create trains of pulses with both function generators working in tandem, it was most usual to specify a single-pulse scheme manually on the main function generator. Information required here was the pulse frequency and the pulse duration, balancing the two carefully so as to produce a low duty cycle and prevent premature burn-out of the test device. The square-wave output was always specified with a 2.5 V amplitude and +2.5 V offset, so the resulting signal was +5 V in the on-state and 0 V in the off-state, as required to switch the Pulse Rig.

Finally the function generator output was enabled, and the voltage on the drive PSU manually increased until a trace was seen on the oscilloscope. At any time, the PC could be used to query the oscilloscope. This resulted in the scope registers being cleared and a fresh set of data collected, with the time-base and sensitivity remaining exactly as specified, and this data dumped to the computer.

3.4.4.5 Experimental variations

It was experimentally determined that the PMT began to behave non-linearly when its output rose above approximately 50 mV. Therefore, for signals above this level, neutral density filters were applied to reduce the incident light at the PMT. For analysis of the electroluminescence at specified wavelengths, interference filters were available. Likewise, bandpass filters allowed sections of the spectrum to be selectively removed.

Although not presented in this thesis, low-temperature measurements were performed on non-encapsulated devices, mounted in the custom-built sample holder on the cold finger inside the vacuum chamber. An accurate measurement of the temperature could be made by use of the thermocouple, with its tip inserted into the copper heat-sink. Subsequent temperature control was achieved by allowing the apparatus to absorb heat from the surroundings, which proceeded slowly enough to allow individual measurements at an effectively constant temperature.

3.4.5 Long-term electroluminescence intensity evolution

The Test Box was designed and constructed to monitor the long-term evolution of LED performance, by driving the test LED under known conditions and measuring the light intensity at specified time intervals.

3.4.5.1 Test Box design

Minimum requirements for the Test Box were as follows:

- Mounting suitable for measuring large-substrate devices
- Built-in variable voltage source for direct LED drive
- External connector for LED drive by an alternative source
- Knob for selection of desired pixel
- Internal large-area silicon photodiode
- Built-in amplifier for photodiode signal
- Time-averaging circuitry to produce a mean signal under pulsed drive

The output would be measured by a digital multimeter (DMM), interrogated by the computer via GPIB. A circuit layout was designed to accommodate a pair of ZIF sockets (for the 18-leg encapsulated LED) and a variable voltage regulator with its attendant components. The time-averaging amplifier was designed with the assistance of Dr P. Routley of Cambridge Display Technology Ltd.

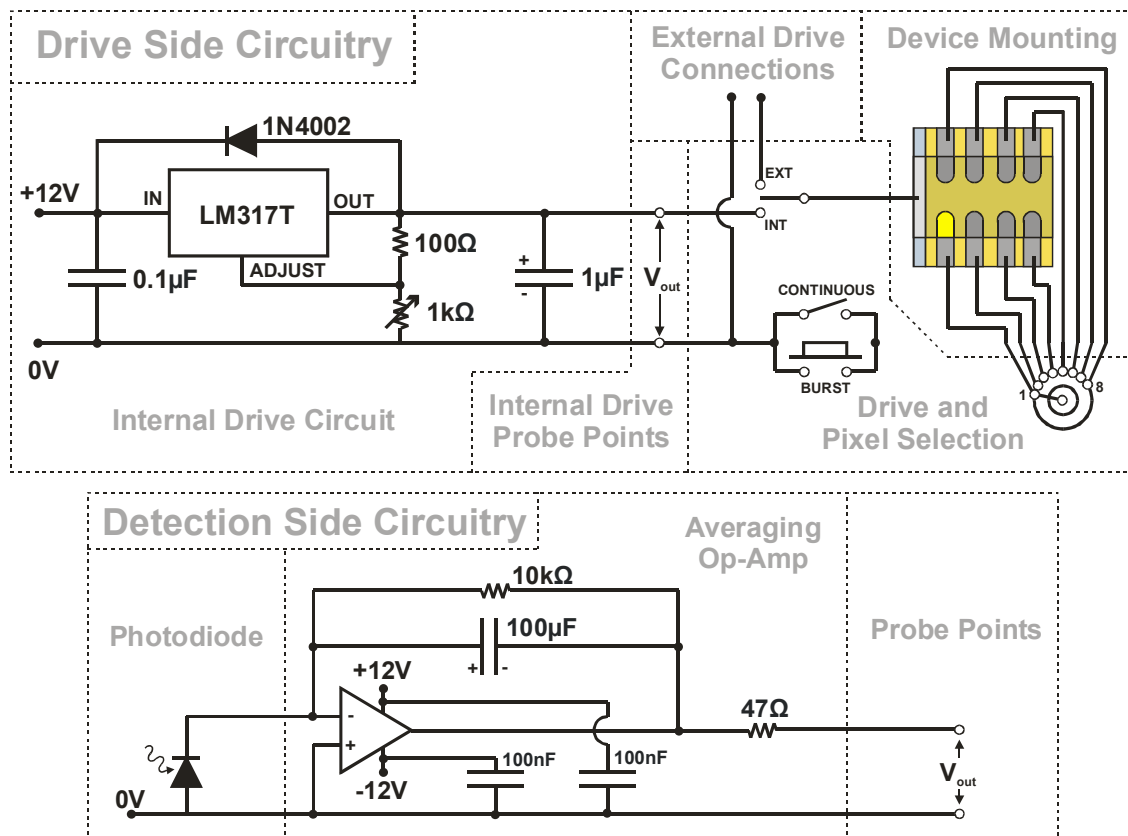


Figure 3.9a: Drive side circuitry for the Test Box. LM317T is the variable voltage regulator.

Figure 3.9b: Detection circuitry for the Test Box.

The circuits, as shown in Figures 3.9a and 3.9b, were constructed on a section of Vero board, with the large-area silicon photodiode mounted between the two rows of ZIF connectors which hold the LED. This unit was then mounted inside a die-cast aluminium box, to act as a light-proof enclosure. Figure 3.10 shows the completed Test Box, with the lid removed. External connectors and controls allowed for:

- Connection to a ± 12 V PSU to power up the Test Box
- Connection to an alternative drive source for the test LED
- Switch to select internal or external LED drive
- Push-button for short manual-controlled drive and override switch for continuous drive
- Knob to control amplitude of internal voltage source (1.25 V to 12.0 V)
- Knob to select pixel of interest
- Contacts for sampling the internally generated voltage
- Contacts for measuring the photodiode amplifier output



Figure 3.10: Test Box, with a glass-encapsulated device in place.

3.4.5.2 Test Box operation

The Test Box remains closed, except when exchanging test devices. The Box can be operated in a variety of modes, depending on the external set-up. A multi-function LabView application was written to control the experiment and collect data.

A) Constant voltage

Most straightforwardly, the LED is driven under constant voltage conditions by the internal source. Figure 3.11a shows a schematic diagram of the setup. The output is fed to a HP34401A DMM, which is interrogated at specified intervals by the computer. The device drive regime is not computer-controlled, leaving only data collection to the computer.

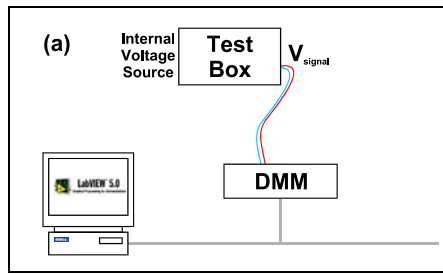


Figure 3.11a: Constant voltage configuration for the Test Box.

B) Modulated constant voltage

In this case, shown in Figure 3.11b, a Keithley 6517A electrometer (incorporating a voltage source) is connected to the external-drive inputs of the Box, and employed under computer control to drive the LED. The drive voltage can be switched on and off by the computer at specified times, and intensity measurements taken at specified times during the on-phase.

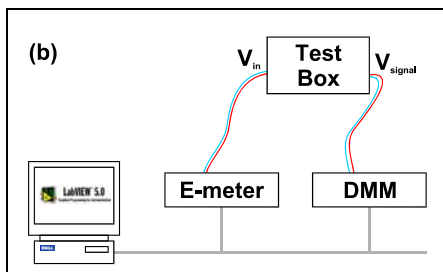


Figure 3.11b: Modulated constant current configuration for the Test Box.

A basic time-unit is user-defined, for example 10 seconds. The user then specifies the number of consecutive “on” units to drive the LED, with an intensity measurement at the end of each, followed by a number of “off” units in which the LED is rested. This cycle can itself be repeated a specified number of times. In this configuration, for example, the device could be driven for 5 minutes, with intensity measurements every 10 seconds, then rested for 2 minutes and the whole cycle repeated.

C) Modulated constant current

This most complex set-up, shown in Figure 3.11c, proved to be the most useful. A Keithley 220 constant current source was used to provide the external drive for the LED. The source was manually configured to a two-stage step-through cycle, with step “0” being off and step “1” being on. The 6517A electrometer was then used under computer control to trip the current source through its cycle. Thus measurements could be taken analogously to variation (b), but with known current density instead of known applied bias. As always, a HP34401A DMM was used to record the measured intensity from the photodiode. In addition,

and whenever required, a second identical DMM was used to measure the applied voltage supplied by the constant current source.

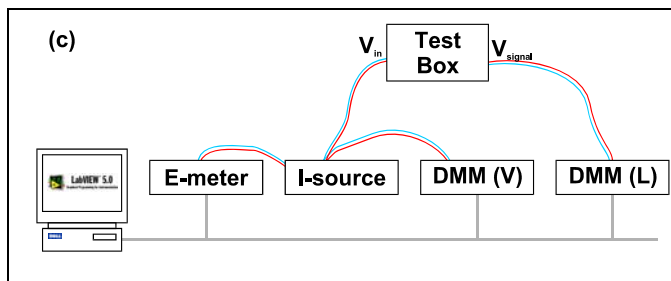


Figure 3.11c: Modulated constant current configuration for the Test Box.

3.4.5.3 Test Box experimental variations

In order to accommodate small (12 mm square) encapsulated devices, a carrier was built with legs in the same formation as the large devices, an array of connectors on top to power up the small device, and a well-defined glass window to ensure that all pixels achieved approximately equal exposure to the silicon photodiode when mounted inside the Test Box (see Figure C.1). It is important to note that the small devices had a common-anode format whilst the large devices were common-cathode. Therefore the pixel-selector knob now made electrical contact with the cathode, so the polarity of the external source had to be reversed. Thus the (fixed polarity) internal source is not suitable for use with small devices. A small adaptor was constructed to reverse the external drive polarity where it enters the Test Box (see Figure C.2).

In order to measure at known elevated temperatures, the thermocouple from the Pulse Rig was put into contact with the die-cast aluminium box, deep into one of the four corner screw-holes. The entire die-cast box was placed on a temperature-controlled hotplate, for use at temperatures up to approximately 70 °C.

In order to measure the back-flow of charge from a device after driving it, a Keithley 6517A electrometer was connected across the external drive contacts, and placed under automated computer control to take regular measurements. The test device was driven with the internal voltage source, and at the required time the “internal/external” switch was flipped, disconnecting the LED from the drive source and immediately connecting it to the electrometer. By this method, an extremely quick changeover from drive to drainage could be achieved. For the case of a constant current pre-drive followed by charge drainage through the electrometer, it was necessary to rapidly disconnect the current source and then connect the electrometer. The Pye connectors made this relatively simple, and it could usually be completed within two or three seconds. Further details are provided in Appendix C.

3.4.6 Charge Modulated PDS

During the course of the work presented here, it became apparent that detection of the absorption of species in an operational device would be desirable. By modification of the PDS Rig, an *in situ* induced absorption experiment became possible. In this way, measurements could be made of the variations in absorption caused by electrical driving of a real LED. Further details are provided in Appendix A.

Measurements of polaron absorption are not new to conjugated polymer physics, having been performed on metal-insulator-semiconductor capacitors³⁰ by charge modulation spectroscopy³¹, polymer samples by photo-induced absorption^{23,32}, and working LEDs by measuring changes in device reflectance³³⁻³⁸ and transmittance^{39,40}. Charge modulated PDS takes a different approach, by directly detecting the heating effect due to induced absorptions of the incident light. The experimental set-up is described in this section, and although a full characterisation of the system behaviour was beyond the scope of this work, one series of simple experiments was performed and the results are presented in Chapter 6.

3.4.6.1 Charge-modulated PDS fundamentals

In an operational device illuminated by a light source, there are two unwanted sources of heating which would appear like absorptions in an unmodified PDS experiment. The operation of the device itself generates heat, as well as the optical absorption of the incident illumination beam in the various layers of the LED. Neither of these was the quantity of interest. Rather, it was desired to measure the incremental heating effect created in the LED when it was being both driven electrically and illuminated optically.

The heating effect of the LED on its own is orders of magnitude larger than the photothermal effect, and must not be allowed to interfere with the measurement. In addition, the optical absorption is very significant in a device structure where glass, ITO, PEDOT:PSS and metal layers are present, in addition to the polymer itself. These two effects, though very large, must be eliminated completely in order to measure the very small nonlinear component when they appear together.

After consultation with Dr D.S. Thomas who originally designed and built the PDS Rig¹⁰, it was decided to proceed by use of a double lock-in technique. This entails driving the device electrically at one frequency, whilst chopping the probe beam at a different frequency.

Considering the total PDS signal,

$$S = S_L + S_I \quad (3.1)$$

where S is the total signal, S_L is the signal due to light absorption inside the LED, and S_I is the signal due to current-heating of the device. If the incident light is modulated at ω_L and the drive current is modulated at ω_I , then the total PDS signal can be re-written as

$$S = A_L \alpha(\lambda) \sin(\omega_L t) + A_I F_I(I) \sin(\omega_I t) \quad (3.2)$$

where A_L and A_I are constants of proportionality, partly dependent on the sample alignment in the rig, and $F(I)$ is a function of current. The absorption coefficient α , which is a function of illumination wavelength λ , has components from both the intrinsic absorption and the current-induced absorption. This can be expressed as

$$\alpha(\lambda) = \alpha_L(\lambda) + \alpha_I(\lambda)F_L(I) \sin(\omega_I t) \quad (3.3)$$

Substituting back into Equation 3.2 gives

$$\begin{aligned} S &= A_L (\alpha_L(\lambda) + \alpha_I(\lambda)F_L(I) \sin(\omega_I t)) \sin(\omega_L t) + A_I F_I(I) \sin(\omega_I t) \\ &= A_L \alpha_L(\lambda) \sin(\omega_L t) + A_L \alpha_I(\lambda) F_L(I) \sin(\omega_L t) \sin(\omega_I t) + A_I F_I(I) \sin(\omega_I t) \\ &= A_L \alpha_L(\lambda) \sin(\omega_L t) + \frac{A_L \alpha_I(\lambda) F_L(I)}{2} (\cos(\omega_I - \omega_L)t - \cos(\omega_I + \omega_L)t) + A_I F_I(I) \sin(\omega_I t) \end{aligned} \quad (3.4)$$

Therefore, the current-induced absorption, $\alpha_I(\lambda)$, can be detected by locking in at either the sum or the difference frequency of the two drive frequencies. This eliminates the two extrinsic heating processes, whilst recording only the signal which cannot be accounted for by a linear combination of the two effects.

3.4.6.2 Rig modifications

A number of modifications were required to the PDS Rig in order to implement the Charge Modulated PDS experiment. It was of paramount importance that these be easily reversible, so that the ordinary PDS absorption experiment could be reinstated.

The 2-slot chopper wheel was exchanged for a concentric 7/5 slot wheel. The chopper's internal frequency source was used to specify the chop frequency of the outer 7-slot portion, which generated a TTL output at f . The illumination beam passed through the inner 5-slot portion, and was thus chopped at $5f/7$. The chopper unit now formed the frequency-generation centre for the experiment, rather than using a sync signal from the lock-in amplifier, and 17 Hz was selected to avoid any mains hum interference. Additionally, the

chopper unit provides both sum and difference frequency outputs, which can be used to trigger the lock-in amplifier. A drive box was designed to convert the TTL output of the chopper unit into a triggered variable-voltage supply to drive the LED. This was based around the same variable voltage regulator design used in the Test Box. The circuit diagram is shown in Figure 3.12, and the finished drive box is shown in Figure A.7. Finally, one of the sample mounts from the PDS Rig was converted to include electrical connections, shown in Figure A.6. A hole was drilled through the top, and re-sealed after the wires had been passed through.

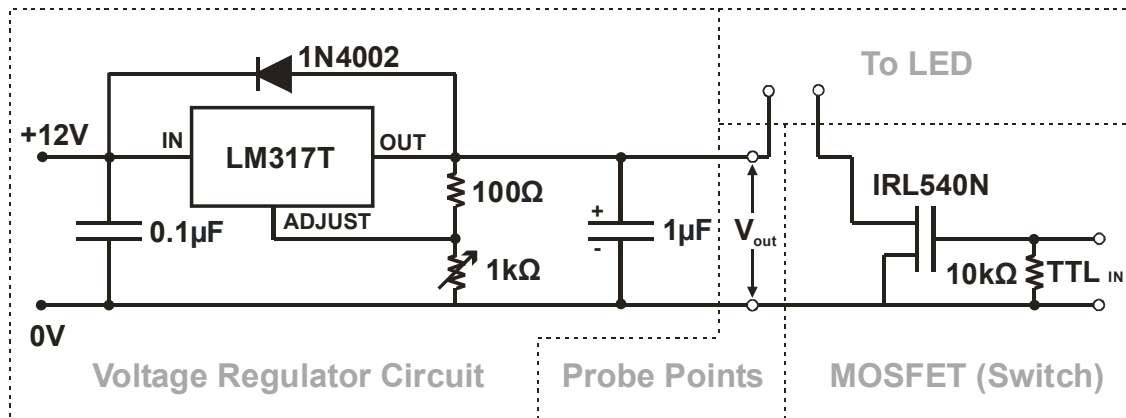


Figure 3.12: Drive Box circuitry for Charge Modulated PDS. LM317T is a variable voltage regulator.

3.4.6.3 Experiment operation

Experimental procedure began by fabrication of non-encapsulated devices in the normal way, on small wide-stripe ITO substrates with round-ended pixels. While still inside the glovebox, a device was mounted cathode-side-up in the modified holder, and the connection wires secured in place with silver dag paste. The device was oriented such that when the probe beam was later directed horizontally across the face of the device it was not obstructed by the connections, as in Figure A.6. After drying of the paste, the sample holder was inserted into the Fluorinert-filled cuvette and sealed shut with the fastening screw.

The cuvette was mounted in the PDS rig in the reverse orientation to the standard configuration, so that the illumination beam struck the selected pixel from the glass side, through the pre-existing hole in the sample holder. The probe laser beam was directed across the cathode surface of the device, ensuring that the device connections did not obscure it. Alignment proceeded purely by eye, since unlike absorption PDS, there is no strong signal to lock on to in this configuration. Finally, a drive voltage was selected on the drive box, and this was connected to the LED *in situ*. The PDS program required no modification and could be used to collect data immediately.

3.4.6.4 Data processing

Since the lock-in frequency used is no longer equal to the illumination chop frequency, the calibration photodiode records no illumination intensity data. However this data is a function of the lamp, and since the beam attenuation does not change in this experiment, a previously collected lamp intensity data set is used to normalise the data.

Finally, the phase information becomes important in this experiment. The PDS rig collects r,θ data, and since the standard PDS experiment shows only absorptions, the phase is virtually constant, indicating a positive deflection in the probe beam. The presence of noise in the phase signal is indicative of reaching a noise floor in the experiment. However in this experiment, since the device is reversed with respect to the deflection photodiodes, any absorption signal will have the opposite sign (180° out of phase) compared to standard PDS absorption data. Consequently, any deflection having the same sign as a standard PDS absorption corresponds to a bleaching of absorption in the sample. Once again, noise in the phase signal can be used to identify regions where the deflection signal is unreliable.

3.5 Numerical modelling

In order to better understand the operation of the devices under test, it was instructive to work with a computer-based model to simulate their behaviour. Extensive use has been made of such models in the past to investigate the transient⁴¹⁻⁴⁷ and DC⁴⁸⁻⁵⁴ behaviour of LEDs and compare them to experiment.

The model used was constructed in the MatLab environment by Dr J. A. Barker of the Cavendish Laboratory, and based on similar principles to the model previously constructed by Dr N. Tessler⁴² and successfully utilised by Dr D. J. Pinner⁵. The model divides the polymer layer into a series of elements, and proceeds by simultaneously solving the continuity equations and the Poisson equation within each element. Recombination is treated as a Langevin process, as described in Section 2.4.5. The rate of change of electron and hole number densities, n and p , are given by

$$\frac{dn}{dt} = -\frac{d}{dz} \left[\mu_n n E + \mu_n \frac{k_B T}{e} \frac{dn}{dz} \right] - \frac{n p e}{\epsilon_0 \epsilon_r} (\mu_n + \mu_p) \quad (3.5)$$

$$\frac{dp}{dt} = \frac{d}{dz} \left[\mu_p p E - \mu_p \frac{k_B T}{e} \frac{dp}{dz} \right] - \frac{n p e}{\epsilon_0 \epsilon_r} (\mu_n + \mu_p) \quad (3.6)$$

$$\frac{dE}{dz} = \frac{e}{\epsilon_0 \epsilon_r} (p - n) \quad (3.7)$$

The mobilities $\mu_{n(p)}$ are field-dependent, following the form $\mu_{n0(p0)}\exp(\gamma\sqrt{E})$ ⁵⁵⁻⁶⁰. E is the local value of the electric field, z is the distance from the cathode. For the particular cases studied in this work, the limited range of fields used justifies the substitution of a simple field-independent mobility obtained by experiment in the regime of interest^{50,61,62}.

In the continuity equations, 3.5 and 3.6, the bracketed term contains both the charge carrier drift and diffusion, whilst the second term describes the Langevin recombination rate which produces a reduction of the charge carrier density. Charge carrier injection is modelled either ohmically without a barrier, or by the Scott injection mechanism⁶³ described in Section 2.4.2.3, which provides for injection over a barrier with backscattering taken into account. Tunnelling models for charge injection and extraction, though available in the model, were not employed in this work. The model was recently described and successfully used to simulate the behaviour of novel devices⁶⁴. A particular strength is that it can be executed iteratively to predict the time evolution of the device properties, which can be compared with experiment.

Within the model environment, a set of real-world parameters are specified to define the device. Each electrode is defined in terms of the model for charge injection, and the energy barrier for injection if applicable. Up to two polymer layers may be specified, along with the energy barriers for charge transport across the heterojunction. Each polymer is defined in terms of its electron and hole mobility and field and temperature dependence of mobility (where required). As the simulation proceeds, the state of each cell is influenced by its neighbours and the local field during each step. Following each iteration, the total exciton generation rate is calculated and appended to a data set as a function of time, and after the final iteration exciton generation rate, charge carrier density, and various other pertinent parameters are recorded as a function of position inside the device. The resulting data set includes the time-dependence of exciton formation, which can be compared with the results of transient electroluminescence measurements, and the final distributions of electrons, holes and electric field inside the device.

3.6 Conclusions

This Chapter has described the methods employed in production, testing and modelling of devices and samples. Further information on the PDS Rig, Pulse Rig and Test Box can be found in the appendices.

3.7 References

¹ Donnelly Applied Films Corporation, Boulder, CO.

- ² C. C. Wu, C. I. Wu, J. C. Sturm, and A. Kahn, *Appl. Phys. Lett.* **70**, 1348-1350 (1997).
- ³ J. S. Kim, R. H. Friend, and F. Cacialli, *Appl. Phys. Lett.* **74**, 3084-3086 (1999).
- ⁴ Robnor Resins, Swindon, UK. Cat nos. RX9681C/NC and HX681C/NC.
- ⁵ D. J. Pinner, Ph.D. Thesis, University of Cambridge, 2000.
- ⁶ UQG Optics, Cambridge, UK.
- ⁷ W. B. Jackson, N. M. Amer, A. C. Boccara, and D. Fournier, *Appl. Optics* **20**, 1333-1344 (1981).
- ⁸ C. H. Seager, M. Sinclair, D. McBranch, A. J. Heeger, and G. L. Baker, *Synth. Met.* **49-50**, 91-97 (1992).
- ⁹ M. Tzolov, W. Brutting, V. Petrova-koch, J. Gmeiner, and M. Schwoerer, *Synth. Met.* **122**, 55-57 (2001).
- ¹⁰ D. S. Thomas, Ph.D. Thesis, University of Cambridge, 1999.
- ¹¹ A. Rosencwaig and A. Gersho, *J. Appl. Phys.* **47**, 64-69 (1976).
- ¹² A. C. Boccara, D. Fournier, and J. Badoz, *Appl. Phys. Lett.* **36**, 130-132 (1980).
- ¹³ D. Fournier and A. C. Boccara, in *Photoacoustic and Thermal Wave Phenomena in Semiconductors*, edited by A. Mandelis (North Holland, New York, 1987), p. 237-255.
- ¹⁴ D. Braun, D. Moses, C. Zhang, and A. J. Heeger, *Appl. Phys. Lett.* **61**, 3092-3094 (1992).
- ¹⁵ D. Braun, D. Moses, C. Zhang, and A. J. Heeger, *Synth. Met.* **57**, 4145-4150 (1993).
- ¹⁶ C. Hosokawa, H. Tokailin, H. Higashi, and T. Kusumoto, *Appl. Phys. Lett.* **60**, 1220-1222 (1992).
- ¹⁷ D. J. Pinner, R. H. Friend, and N. Tessler, *J. Appl. Phys.* **86**, 5116-5130 (1999).
- ¹⁸ A. V. Yakimov, V. N. Savvate'ev, and D. Davidov, *Synth. Met.* **115**, 51-56 (2000).
- ¹⁹ D. J. Pinner, R. H. Friend, and N. Tessler, *Appl. Phys. Lett.* **76**, 1137-1139 (2000).
- ²⁰ J. M. Lupton, V. R. Nikitenko, I. D. W. Samuel, and H. Bassler, *J. Appl. Phys.* **89**, 311-317 (2001).
- ²¹ N. Tessler, P. K. H. Ho, V. Cleave, D. J. Pinner, R. H. Friend, G. Yahioglu, P. Le barny, J. Gray, M. De souza, and G. Rumbles, *Thin Solid Films* **363**, 64-67 (2000).
- ²² T. C. Wong, J. Kovac, C. S. Lee, L. S. Hung, and S. T. Lee, *Chem. Phys. Lett.* **334**, 61-64 (2001).
- ²³ G. J. Denton, N. Tessler, M. A. Stevens, and R. H. Friend, *Synth. Met.* **102**, 1008-1009 (1999).
- ²⁴ N. Tessler, *Adv. Mater.* **11**, 363-370 (1999).
- ²⁵ N. Tessler and R. H. Friend, *Synth. Met.* **102**, 1122-1123 (1999).
- ²⁶ N. Tessler, G. Denton, N. T. Harrison, M. A. Stevens, S. E. Burns, and R. H. Friend, *Synth. Met.* **91**, 61-64 (1997).
- ²⁷ D. J. Pinner, N. Tessler, and R. H. Friend, *Synth. Met.* **102**, 1108-1109 (1999).
- ²⁸ D. J. Pinner, R. H. Friend, and N. Tessler, *Appl. Phys. Lett.* **77**, 1493-1495 (2000).
- ²⁹ N. Tessler, D. J. Pinner, V. Cleave, D. S. Thomas, G. Yahioglu, P. Le barny, and R. H. Friend, *Appl. Phys. Lett.* **74**, 2764-2766 (1999).
- ³⁰ K. E. Ziemelis, A. T. Hussain, D. D. C. Bradley, R. H. Friend, J. Ruhe, and G. Wegner, *Phys. Rev. Lett.* **66**, 2231-2234 (1991).
- ³¹ P. J. Brown, Ph.D. Thesis, University of Cambridge, 2000.
- ³² D. D. C. Bradley and R. H. Friend, *J. Phys.-Condes. Matter* **1**, 3671-3678 (1989).
- ³³ N. Tessler, N. T. Harrison, and R. H. Friend, *Adv. Mater.* **10**, 64-+ (1998).
- ³⁴ M. Redecker and H. Bassler, *Appl. Phys. Lett.* **69**, 70-72 (1996).
- ³⁵ A. R. Brown, K. Pichler, N. C. Greenham, D. D. C. Bradley, R. H. Friend, and A. B. Holmes, *Chem. Phys. Lett.* **210**, 61-66 (1993).

- ³⁶ I. H. Campbell, D. L. Smith, C. J. Neef, and J. P. Ferraris, *Phys. Rev. B* **6403**, 5203-+ (2001).
- ³⁷ I. H. Campbell, D. L. Smith, C. J. Neef, and J. P. Ferraris, *Appl. Phys. Lett.* **78**, 270-272 (2001).
- ³⁸ K. Book, V. R. Nikitenko, H. Bassler, and A. Elschner, *J. Appl. Phys.* **89**, 2690-2698 (2001).
- ³⁹ A. S. Dhoot and N. C. Greenham, *Adv. Mater.* **14**, 1834-1837 (2002).
- ⁴⁰ A. S. Dhoot, D. S. Ginger, D. Beljonne, Z. Shuai, and N. C. Greenham, *Chem. Phys. Lett.* **360**, 195-201 (2002).
- ⁴¹ G. G. Malliaras and J. C. Scott, *J. Appl. Phys.* **85**, 7426-7432 (1999).
- ⁴² N. Tessler, D. J. Pinner, and R. H. Friend, *Synth. Met.* **111**, 269-272 (2000).
- ⁴³ N. Tessler, *Appl. Phys. Lett.* **77**, 1897-1899 (2000).
- ⁴⁴ K. Book, H. Bassler, V. R. Nikitenko, and A. Elschner, *Synth. Met.* **111**, 263-267 (2000).
- ⁴⁵ V. R. Nikitenko and H. Bassler, *J. Appl. Phys.* **88**, 1886-1892 (2000).
- ⁴⁶ V. R. Nikitenko and H. Bassler, *J. Appl. Phys.* **85**, 6515-6519 (1999).
- ⁴⁷ V. R. Nikitenko, V. I. Arkhipov, Y. H. Tak, J. Pommerehne, H. Bassler, and H. H. Horhold, *J. Appl. Phys.* **81**, 7514-7525 (1997).
- ⁴⁸ P. W. M. Blom, M. J. M. Dejong, C. T. H. F. Liedenbaum, and J. J. M. Vleggaar, *Synth. Met.* **85**, 1287-1288 (1997).
- ⁴⁹ B. K. Crone, I. H. Campbell, P. S. Davids, D. L. Smith, C. J. Neef, and J. P. Ferraris, *J. Appl. Phys.* **86**, 5767-5774 (1999).
- ⁵⁰ P. W. M. Blom and M. J. M. De jong, *IEEE J. Sel. Top. Quantum Electron.* **4**, 105-112 (1998).
- ⁵¹ G. G. Malliaras and J. C. Scott, *J. Appl. Phys.* **83**, 5399-5403 (1998).
- ⁵² V. I. Arkhipov, U. Wolf, and H. Bassler, *Phys. Rev. B-Condens Matter* **59**, 7514-7520 (1999).
- ⁵³ V. Kumar, S. C. Jain, A. K. Kapoor, W. Geens, T. Aernouts, J. Poortmans, and R. Mertens, *J. Appl. Phys.* **92**, 7325-7329 (2002).
- ⁵⁴ V. I. Arkhipov, P. Heremans, E. V. Emelianova, G. J. Adriaenssens, and H. Bassler, *J. Phys.-Condens. Matter* **14**, 9899-9911 (2002).
- ⁵⁵ M. Redecker, D. D. C. Bradley, M. Inbasekaran, and E. P. Woo, *Appl. Phys. Lett.* **73**, 1565-1567 (1998).
- ⁵⁶ E. Lebedev, T. Dittrich, V. Petrovavkoch, S. Karg, and W. Brutting, *Appl. Phys. Lett.* **71**, 2686-2688 (1997).
- ⁵⁷ I. H. Campbell, D. L. Smith, C. J. Neef, and J. P. Ferraris, *Appl. Phys. Lett.* **74**, 2809-2811 (1999).
- ⁵⁸ H. Meyer, D. Haarer, H. Naarmann, and H. H. Horhold, *Phys. Rev. B* **52**, 2587-2598 (1995).
- ⁵⁹ P. W. M. Blom, M. J. M. Dejong, and M. G. Vanmunster, *Phys. Rev. B-Condens Matter* **55**, R656-R659 (1997).
- ⁶⁰ S. V. Novikov, D. H. Dunlap, V. M. Kenkre, P. E. Parris, and A. V. Vannikov, *Phys. Rev. Lett.* **81**, 4472-4475 (1998).
- ⁶¹ M. Koehler, M. G. E. Da luz, and I. A. Hummelgen, *J. Phys. D-App. Phys.* **33**, 2096-2107 (2000).
- ⁶² J. C. Scott, S. Karg, and S. A. Carter, *J. Appl. Phys.* **82**, 1454-1460 (1997).
- ⁶³ J. C. Scott and G. G. Malliaras, *Chem. Phys. Lett.* **299**, 115-119 (1999).
- ⁶⁴ K. J. Reynolds, J. A. Barker, N. C. Greenham, R. H. Friend, and G. L. Frey, *J. Appl. Phys.* **92**, 7556-7563 (2002).

4. Interactions between PSSH and PFB

The PEDOT:PSS system (see Section 2.5.3) has become a standard feature of conjugated polymer LEDs, chosen for its electrical conductivity, work function suitable for injection of holes into light emitting polymers and its planarity and transparency when spun from solution.

PSSH – a polymeric organic acid – dopes PEDT to make it conductive. Unlike classical semiconductor/dopant systems, PSSH is the majority component of the PEDOT:PSS layer, comprising nearly 95 % of the material by weight. Although acids, as proton donors, are well-known dopants of conjugated polymers¹, there has been no systematic study of the effect of PSSH on electroluminescent conjugated polymers in a device structure. One experiment appeared to show sub-gap changes in PPV², however the results presented in this Chapter suggest that the intrinsic absorption of PSSH was largely responsible.

This chapter describes a detailed photothermal deflection spectroscopy (PDS) study of the interface of PSSH with the conjugated polymer PFB, conducted to better understand the nature and extent of the interaction between the two molecules.

4.1 Background

PFB, introduced in Section 2.5.2, is a copolymer of the ubiquitous fluorene unit with a variant of the triarylamine unit used in small-molecule organic semiconductor work³. It produces a bright blue emission in electroluminescence, and is closely related to polymers which show promise for future incorporation into commercial products. Blue emitters are of particular importance because they yield the highest-energy photon emission of the three colours required for RGB displays. One promising future route to full colour applications would use a blue emitter only, with phosphors for down-conversion to red and green where necessary. This would eliminate the problems of differential aging, but would require extremely robust and stable blue emitters. White light emission, by phosphor down-conversion of blue light has recently been demonstrated⁴.

Degradation is a vital consideration in the optimisation of light-emitting polymer technology for commercial applications. Degradation processes can be divided into the extrinsic, governed by ingress of moisture and oxygen, ultraviolet radiation, and other ambient phenomena, and the intrinsic, limited by the chemical stability of the polymers and interfaces of the device itself. As progress has been made towards eliminating the extrinsic paths, the intrinsic phenomena have become considerably more important in the search to improve device lifetimes.

In recent work by Kim *et al*⁵ an electrochemical degradation path has been elucidated by which the reversible injection of holes onto the amine centres of the PFB becomes a quasi-irreversible oxidation, leading to a gradual reduction of the charge injection properties of the device. This Chapter investigates the role of PSSH in this process.

4.2 Samples for study

A series of samples were prepared as described in Section 3.2, with the compositions detailed in Table 4.1

Sample	PSSH 130-150 nm	PFB 75-85 nm	Treatment
4A	-	Spun	-
4B	Spun	-	-
4C	Spun	Spun	-
4D	Spun	Cast	-
4E	Spun & Baked	-	-
4F	Spun & Baked	Spun	-
4G	Spun	Spun	-
4G*	Spun	Spun	Vac-annealed
4H	Spun	Cast	-
4H*	Spun	Cast	Vac-annealed
4I	Slow Spun	-	-
4I*	Slow Spun	-	Vac-baked

Table 4.1: Composition and preparation of PDS samples for this chapter.

Spun PFB films were made from 1 % toluene solution at a thickness of 75 to 85 nm. Cast PFB films were used when a thicker layer was desired, yielding films around 500 nm thick. In the case of baked samples,

the PSSH film was baked at 200 °C under nitrogen flow for one hour and then cooled slowly to room temperature. After initial testing, samples 4G and 4H were annealed under vacuum at 100 °C –below the glass transition temperature (T_g) for PFB of 120 °C – for 2 hours before re-measurement, whilst 4I (which contained no PFB) was baked under vacuum for 2 hours at 200 °C. The slow-spun PSSH sample yielded a much thicker film, suitable for UV-visible absorption spectroscopy, and was prepared on a Spectrosil-B substrate. All other samples were prepared on Spectrosil-WF, for use in the PDS Rig.

Note that an aqueous solution of PSSH was used, as opposed to the PEDOT:PSS emulsion normally found in LED device structures. PEDT itself is strongly absorbent in the visible region, which would negatively impact the sensitivity of this experiment to low-absorption detail. Work by Greczynski *et al*⁶ suggests that the upper surface of a PEDOT:PSS film is phase-segregated to contain almost entirely PSSH, and furthermore PSSH itself is the overwhelming majority component of PEDOT:PSS. Therefore, for the purposes of this study it is both advantageous and sufficient to work with PSSH only.

A further set of samples was produced using tetrahydrofuran (THF) as a solvent. THF is a polar organic solvent, and provides an ideal method for intimate mixing of PSSH (normally used in aqueous solution) and PFB (normally dissolved in xylene or toluene). Table 4.2 describes the samples.

Sample	PSSH	PFB
4J	Yes	-
4K	-	Yes
4L	Yes	Yes

Table 4.2: Three samples produced with THF.

PSSH is supplied in aqueous solution, and this was vacuum dessicated to leave a brittle transparent amber solid. The solid was added to anhydrous THF at a concentration of approximately 3.3 mg/ml, wetting the PSSH to form a glutinous opaque gel, but not dissolving it. The vial was placed into an ultrasonic bath for five minutes at room temperature, which produced a milky suspension of PSSH particles in the THF which was stable against precipitation for at least several months. Sample 4J was drop-cast from this suspension onto Spectrosil-WF. PFB dissolves readily in THF – indeed the solvent is often used for cleaning in polymer labs. A solution of 10 mg/ml PFB in THF was made up and magnetically stirred. This was drop-cast onto Spectrosil-WF to produce sample 4K. Finally, PFB was added to the PSSH-suspension at a concentration of 10 mg/ml and the mixture stirred magnetically until it had dissolved. This mixture, containing dissolved PFB and suspended PSSH in a 3:1 ratio by weight was drop-cast on Spectrosil-WF to produce sample 4L.

4.3 Procedure

Excluding samples 4J to 4L, all other samples were stored in the dark under nitrogen, and measured in the PDS Rig as described in Section 3.3.3. They were loaded into the PDS sample holder without removal from the glovebox, and measurements were taken from 3.2 eV down to 0.6 eV, at 0.01 eV spacings. Samples for UV-visible absorption spectroscopy were transported through and measured in air, using the HP8453 UV-Vis spectrometer as described in Section 3.3.2.

4.4 Results

By comparing pairs of data-sets, individual features of the system can be isolated.

4.4.1 PFB-only absorption spectrum

The PDS spectrum of PFB, shown in Figure 4.1, demonstrates the dynamic range of the Rig. For comparison, an identical film spun on ITO-glass is also shown. Features can be discerned in the Spectrosil sample which are two orders of magnitude weaker than the ITO absorption in the visible region.

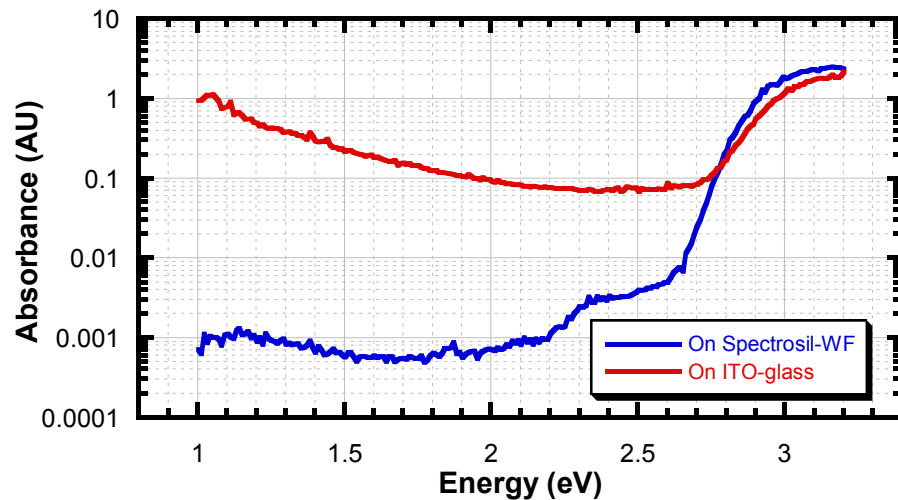


Figure 4.1: PDS spectrum of spin-coated PFB on Spectrosil-WF (sample 4A) and on ITO-glass.

The PFB sample on Spectrosil-WF shows a fairly well-defined band-edge above 2.8 eV, with small sub-gap features at about 1.15 eV and 2.35 eV. The apparent feature at 1.85 eV is an artefact of the rig at the wavelength of the probe laser and is much narrower than the typical real features seen with this technique. It should be noted that the two real sub-gap features are not always observed in PFB absorption spectra,

depending on the batch examined. These extrinsic absorptions are likely to be due to very slight unintentional doping of the polymer.

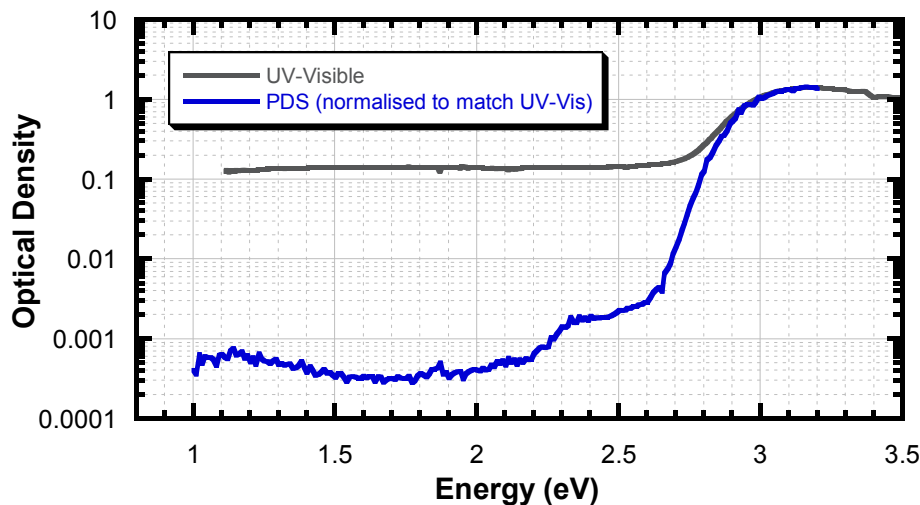


Figure 4.2: Spin-cast PFB (4A) measured by both UV-Vis and PDS (normalised at 3.0 eV).

At high signal strengths, the PDS signal is known to saturate, resulting in non-linearity at high absorptions. However this occurs in the region which is well-covered by UV-Visible spectroscopy. By using UV-Vis in combination with PDS, the presence of any saturation can be determined, and the absolute absorption of the film at a given photon energy determined. Figure 4.2 shows the same spin-coated PFB sample on Spectrosil-WF as seen in Figure 4.1, comparing the absorption spectra recorded by PDS and UV-Vis. The UV-Visible spectrometer is not sensitive below OD 0.1, whereas the PDS spectrum extends nearly 3 orders of magnitude lower. The broad absorption at 1.15 eV, which will be examined later, is approximately 2000 times weaker than the $\pi-\pi^*$ absorption.

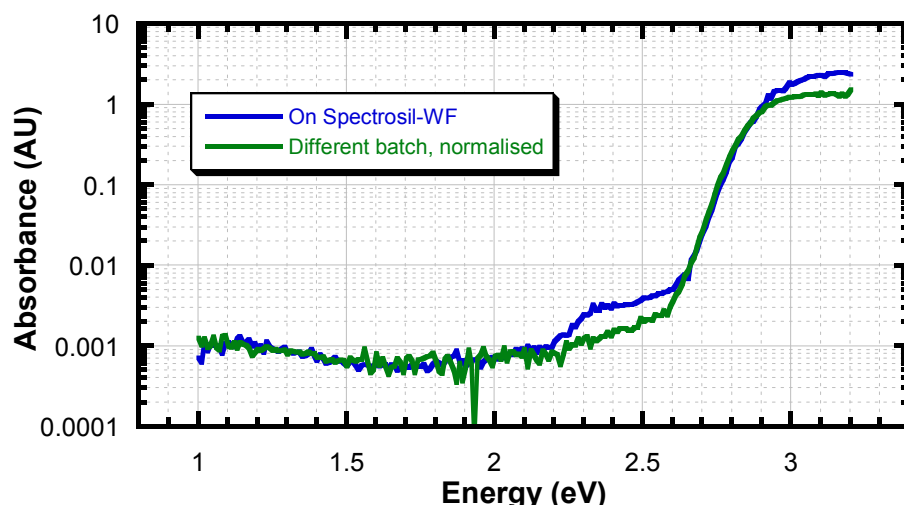


Figure 4.3: PDS spectra of spin-cast PFB (4A) and a similar sample from another polymer batch.

Another PFB film, from a different batch (seen in Figure 4.3) shows that the two sub-gap features are independent. Although the data is somewhat noisier, the 1.15 eV feature matches well, whilst the 2.35 eV feature is not seen. Thus these two features do not move in parallel.

4.4.2 Baking of PSSH alone

A standard procedure in the fabrication of polymer LEDs is the baking of the PEDOT:PSS layer to remove residual water from the aqueous spin-casting stage. Figure 4.4 shows PSSH as-spun and after baking (samples 4B and 4E respectively). These spectra are intriguing. PDS alone does not allow for absolute measurements, but with practice one can expect to achieve uniformly good sample alignment in the Rig, leading to sample spectra which can almost be compared directly. The relative PDS signal intensities for the two samples suggest that a dramatic increase in absorbance has occurred on baking of the PSSH. Above about 1.25 eV, the apparent change is uniform across the entire spectrum. This increase is quite unexpected.

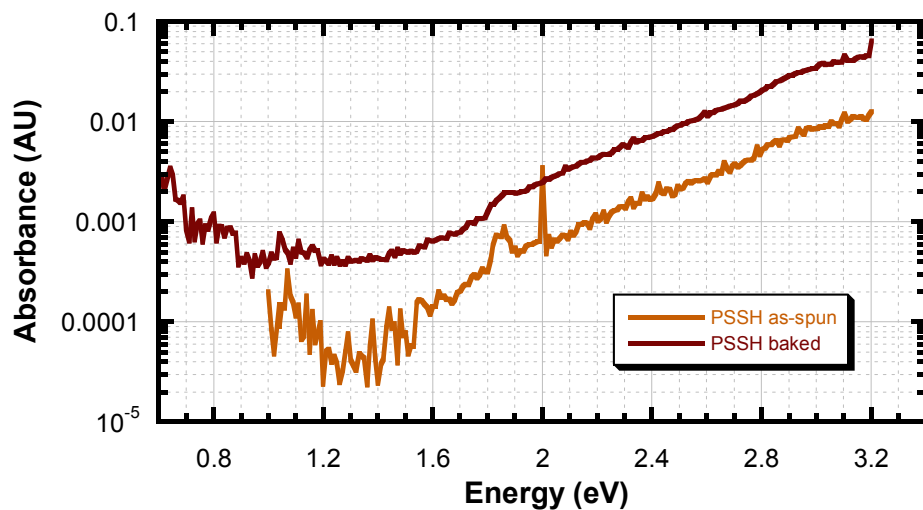


Figure 4.4: PDS spectra of PSSH as-spun (4B) and after baking (4E).

In this example, there is a factor of 4.5 increase in the measured signal from the baked sample over the as-spun one. This is significantly more than the few tens of percent one would expect from misalignment of the Rig, although no inference of absolute absorption by PDS can be completely conclusive. This apparent change will be addressed below, but the feature below 1.25 eV is first examined.

Figure 4.5 shows a PDS scan of a film identical to 4B, but measured to lower energies. Features are seen with a spacing of approximately 0.20 eV, which appear to be vibrational in origin. The inset shows absorption spectroscopy data for liquid water reported by Palmer and Williams⁷ in 1974, with the same vibrational progression which can be attributed to the ν_2 symmetric bending mode of the water molecule at

1595 cm^{-1} (0.2 eV). The similarities between the two spectra are striking, and although we note that sulphonic acids contain OH groups, they are attached to an electron-withdrawing component containing a heavy sulphur atom which is likely to produce a very different bending mode to that seen in H-O-H. Indeed, the corresponding bending mode for sulphonic acids is centred around 1200 cm^{-1} (0.15 eV). Therefore the observed absorption feature in the PSSH film must be attributed to water. Since the film was spun from aqueous solution and not baked, and since sulphonic acids are known to be hygroscopic, this conclusion is not surprising.

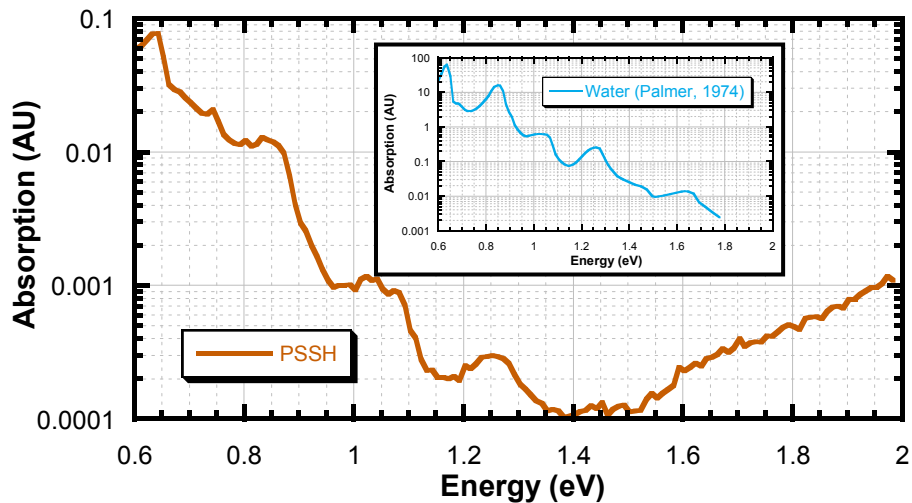


Figure 4.5: Absorption of unbaked PSSH extending to lower energies.

Inset: Absorption spectrum of water, from Palmer (1974)⁷.

The baked PSSH film (4E), which was measured down to 0.6 eV displays the same vibrational signature. Assuming that there is no serious misalignment of the PDS Rig, and that the relative absorptions of as-spun and baked PSSH are accurately represented, a rough comparison can be made of the relative intensity of the vibrational signature in the two films. By extrapolating the main PSSH spectrum (above 1.5 eV) exponentially to below the 1.05 eV peak for both data sets in Figure 4.4, and then subtracting from the peak amplitude in each case, the absolute intensity of the vibrational structures can be estimated. The data are rather noisy, however in the arbitrary units used both samples yield an excess signal of approximately 2×10^{-4} units over the underlying extrapolated data. This suggests that the incidence of the vibrational species is the same in both films.

The water in the baked film is likely to be re-adsorbed atmospheric moisture which entered the film during cooling. The nitrogen flow will not have completely prevented this, considering the hygroscopic behaviour of sulphonic acids. The two films were then stored in identical conditions in a nitrogen glovebox, and equilibration with the glovebox environment likely resulted in the very similar moisture content.

4.4.3 UV-Visible absorption of as-spun PSSH and baked PSSH

The UV-Vis absorption spectrometer allows for absolute comparison between samples. 4I and 4I* are the same sample before and after baking, and Figure 4.6 shows the UV-Vis spectra in the two instances. Both show oscillatory behaviour tailing off at higher energies, which are likely to be interference features caused by partial reflection off the front and back surfaces of the film. The absolute PSSH absorption does show an increase on baking in an inert atmosphere, confirming the suspicions raised by PDS. The measured increase is approximately a factor of seven at its greatest, but the underlying cause is not investigated here.

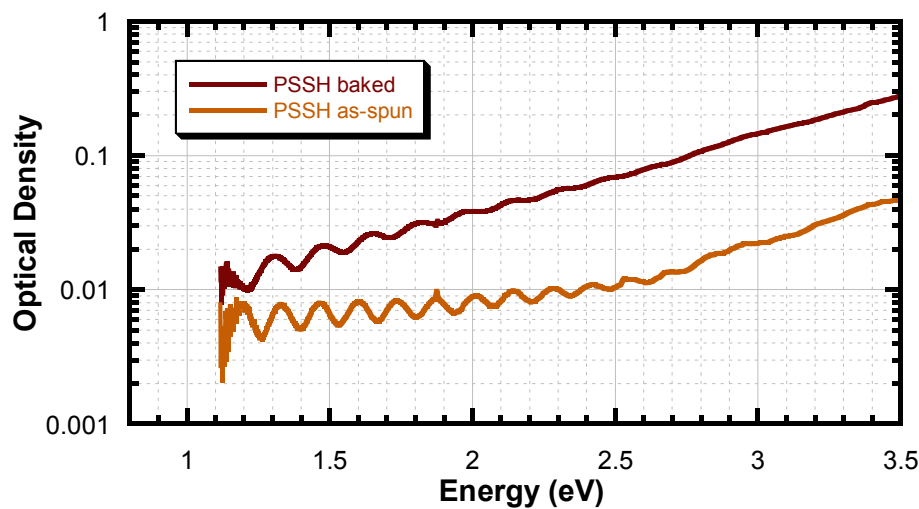


Figure 4.6: UV-visible absorption of as-spun PSSH (4I) and baked PSSH (4I*).

The film thickness after baking was measured to be $2.8\text{ }\mu\text{m}$ – unusually thick for a spin-coated sample, but attributable to the high viscosity of the PSSH solution – leading to the interference fringes seen. This implies a refractive index for PSSH of approximately 1.3. There is a 23 % increase in the fringe spacing between un-baked and baked spectra, which may be attributed to a decrease in refractive index, or more likely a decrease in film thickness on baking.

4.4.4 PFB on as-spun PSSH and on baked PSSH

By comparing PFB on as-spun PSSH with PFB on baked PSSH (Figure 4.7), the effect of baking PSSH on the subsequent interactions can be identified. Both PSSH-containing samples show a strongly enhanced absorption throughout the sub-gap region, compared to the pure-PFB sample. This appears to be comprised of two separate regimes:

Above 2.0 eV, two explanations are possible for the elevated absorption. It is most likely due to the intrinsic absorption of PSSH, as elucidated in the previous section, linearly contributing to the total absorption.

However we cannot rule out a contribution from an enhancement of the sub-gap feature seen at 2.35 eV in pure PFB, although its shape is barely reflected in the unbaked PSSH sample and completely obscured in the baked sample.

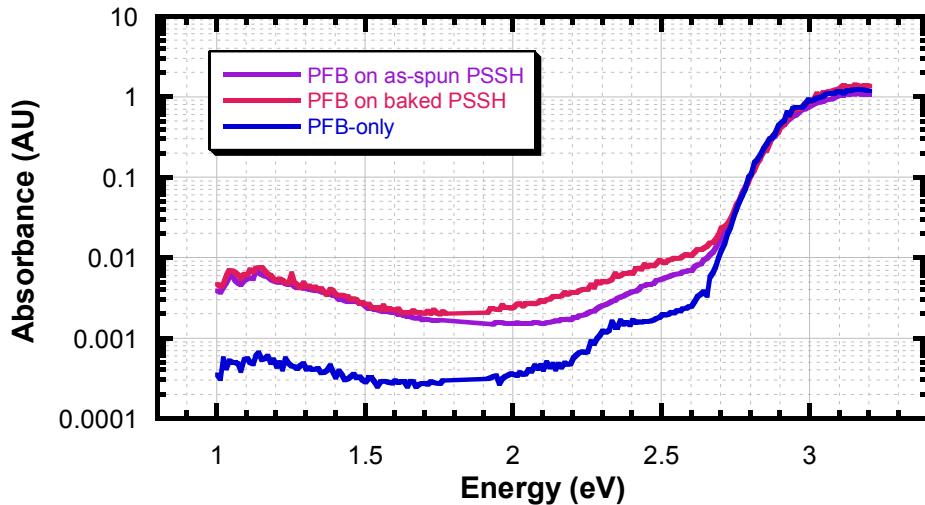
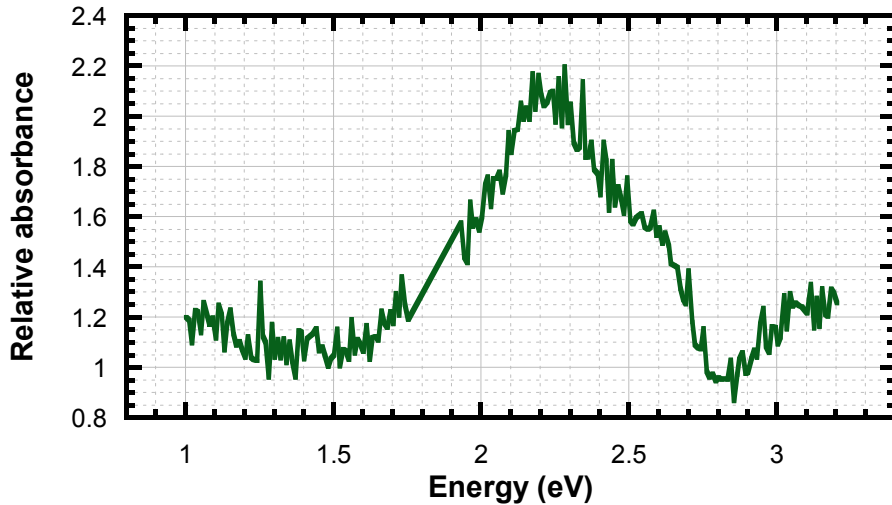


Figure 4.7: PDS spectra of spun PFB on as-spun (4C) and baked (4F) PSSH, with spun PFB-only (4A) for comparison. Note that for clarity the artefact at 1.85 eV has been spliced out of the data. The three spectra have been normalised on the band-edge for ease of comparison.

Below 2.0 eV, with the intrinsic PSSH absorption falling away rapidly, the enhanced absorption cannot be attributed to the simple sum of PFB and PSSH spectra. The PDS signal is an order of magnitude larger than that of pure PFB, but with a very similar shape. This absorption must be attributed to a new chemical species induced by the interaction between PFB and PSS. Since it is present – albeit to a very much smaller degree – in the native PFB, it can be specifically identified as a reaction product in the PFB itself. The feature has no apparent dependence on the baked/unbaked state of the PSSH.

The data can be further analysed by dividing through the “baked” spectrum by the “as-spun” spectrum. This yields the apparent change in absorption on switching to baked PSSH, shown in Figure 4.8. Above the bandgap (about 2.8 eV), slight differences in film thickness yield different apparent onsets of the $\pi-\pi^*$ absorption, and this section of the data can safely be ignored.

Between 1.5 eV and 2.75 eV, a large peak is visible. One would expect a simple absorption feature to be represented by a smooth, probably Gaussian, peak and this is clearly not the case here. There is certainly no evidence that the change is simply an increase in the feature seen at 2.35 eV in PFB. Therefore the observed increase in absorption is probably due to the increased PSSH absorption on baking. Whilst the PSSH absorption increases almost monotonically across the spectrum, when vignetted against the PFB spectrum it can only be detected in the section where PFB absorbs least.



**Fig 4.8: Relative change in absorbance caused by baking of PSSH before spinning PFB.
Note that the artefact at 1.85 eV has been spliced out for clarity.**

Superimposing the absorption of PSSH over the baked-PSSH sample (Figure 4.9) shows that the gradients of the two curves match perfectly between 2.0 and 2.6 eV.

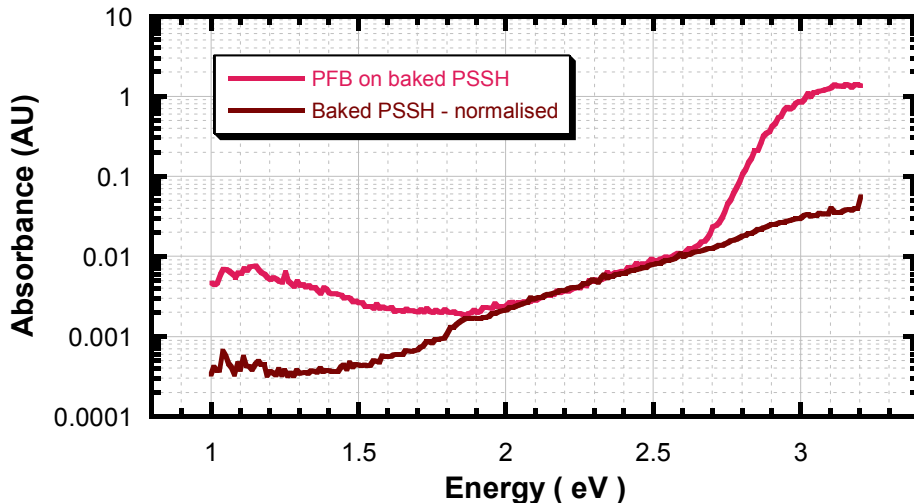


Figure 4.9: Spun PFB on baked PSSH (4F), and baked PSSH alone (4E, normalised).

The baked PSSH signal therefore accounts entirely for the absorption measured in PFB on baked PSSH in this region of the spectrum.

4.4.5 PFB on unbaked PSSH – before and after annealing

Baking the PSSH *in situ* (after spin-coating the PFB layer) provides further data on the interaction. For a diffusion-limited reaction that had not yet proceeded to completion, one would expect the extent of reaction

to increase on annealing. Figure 4.10 shows the absorption of PFB on PSSH, before and after baking the whole structure. The data are strikingly similar to Figure 4.7, in which the PSSH baking took place before the PFB was spin-coated. Indeed the inset shows that there is no qualitative difference between baking the PSSH before PFB deposition and baking the whole composite sample afterwards. The sub-gap features are offset by a small and constant margin, possibly due to sample alignment in the rig. Using the intrinsic absorption of PSSH (1.9–2.7 eV) in the inset as a reference, there seems to be no difference between baking the PSSH alone and baking *in situ*. Thus baking at 100 °C for 2 hours under vacuum has no measurable effect on the PFB absorption. Again, the broad feature peaking at 1.15 eV is present, as is a hint to the feature around 2.35 eV, which disappears (or is obliterated by a stronger feature) in the annealed sample.

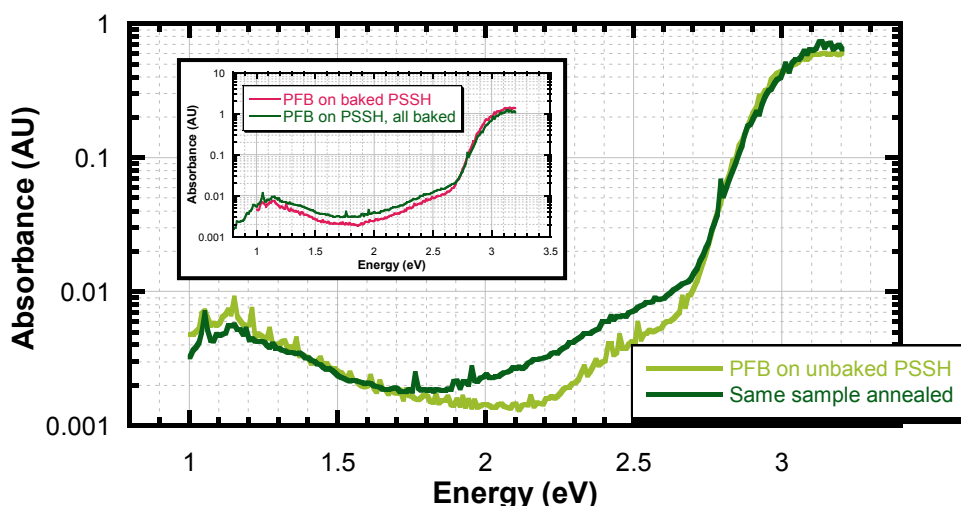


Figure 4.10: Spun PFB on unbaked PSSH (4G) and the same after annealing (4G*), normalised.
Inset: Spun PFB on pre-baked PSSH (4F) and the post-annealed sample (4G*) again.

We conclude that the reaction between the two layers proceeds no further on annealing. Either the reaction has proceeded through the entire film already, or it is confined to the interface and does not advance any further. The PSSH absorption again increases on baking.

4.4.6 Thick-cast PFB films

Comparison of a thick cast PFB film with a thin spun one reveals the extent of reaction from the interface into the bulk of the PFB film, and unexpectedly elucidates an activation mechanism for the reaction. Figure 4.11 shows the PDS spectra of spun (thin) and cast (thick) PFB on PSSH. The apparent shift in band-edge is not real; the thicker film contains more material, yielding a stronger PDS signal, and the vertical shift in the curve, coupled with the unchanged saturation level, gives the appearance of a shift towards lower energies. No normalisation has been performed on the data sets, but the strong correlation between the immediate sub-gap regions (2.2 to 2.6 eV) – corresponding to PSSH absorption – show that the two

samples were similarly aligned in the rig. The PSSH layers were identical in each case, so it is valid to use the curves for direct comparison of the total absorption.

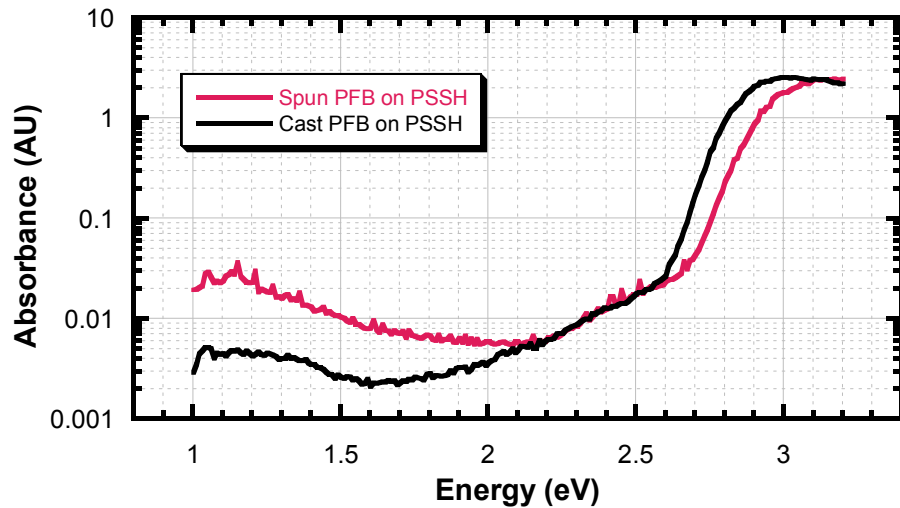


Figure 4.11: Spun PFB on spun PSSH (4G) and cast PFB on spun PSSH (4H).

The important differences become clear below 2 eV. If the reaction between PFB and PSSH proceeded throughout the entire film, then the induced feature at 1.15 eV would be several times stronger in the cast-film case, just as the band-edge absorption is several times greater. However this is not observed experimentally and therefore the induced state does not progress into the bulk. Taken in conjunction with the annealing experiment in the previous section, this implies that the affected region of the polymer is strongly confined, probably to the interfacial layer only.

Interestingly, the measured signal in the thick film is actually smaller than that in the thin film. This cannot be due to attenuation of the thermal signal as it passes out through a greater depth of PFB, since the underlying PSSH signal is not seen to be attenuated in such a way. This implies that the absolute number of states is actually larger in the thin film case. Two possible explanations are suggested: The reaction may be mediated by the presence of oxygen, or alternatively may be triggered by the presence of excited states (which in this non-device context must be photogenerated, but in a device might be formed electrically).

In the case of oxygen diffusion, the PFB layer can be considered as a barrier between the interface region and the external environment. However oxygen content equilibration in conjugated polymer thin films is known to be extremely fast^{8,9}, and the reaction products observed in this experiment are known to occur intrinsically in sealed devices, where oxygen ingress is not a consideration⁵.

More plausible is the influence of photogenerated states. Referring to Figure 4.2, the optical density of the thin PFB film at 3.0 eV is 1.0 (giving an absorption coefficient of 0.029 nm^{-1}). Therefore 10 % of all

incident light reaches the PFB/PSSH interface. The cast film, however, is approximately 6 times thicker, producing an optical density around 6.0, and a transmittance of just one part in a million. Thus, as the PDS experiment proceeds in the usual way from blue towards red excitation, the interface in the thin-film case is exposed to significant levels of above-band-gap light, whilst in the thick case there is approximately 10^5 times less exposure. The spectrum of the thick film most closely resembles that of a pure PFB film overlaid with the absorption of PSSH, without chemical interaction. The thin film shows strong evidence for an interaction, by the enhancement of the 1.15 eV peak, which under this hypothesis is photoinduced.

Comparison of the thick and thin films is thus highly instructive, revealing that the interaction is strongly confined to the interface, and suggesting that it can be induced by photogenerated excited states.

4.4.7 Photoactivation

In order to test this photoactivation hypothesis, a fresh sample, identical to 4G (spun PFB on spun PSSH), was produced and protected from light exposure. The PDS signal from this sample was measured at 1.15 eV, with intervening periods of exposure at 3.2 eV, to determine whether the high-energy illumination induced any change in the sub-gap absorption.

The sample was placed in the PDS Rig and aligned as usual by using blue illumination in the high-absorption region of the polymer. This affected a small area of the sample only. The blue illumination was discontinued, and the monochromator, filters and grating adjusted to provide maximum throughput at 1.15 eV, being the peak of the sub-gap feature of interest. The sample stage was then shifted in the y -direction, preserving the favourable rig-alignment but exposing a fresh area of polymer to the illumination beam. The lock-in sensitivity and time-constant were now increased, and a final adjustment made to the sample alignment. After the lock-in had settled, a reading was taken of the PDS signal. The illumination beam was then blocked, adjusted to provide 3.2 eV (approximately the peak on the PDS spectrum) with maximum throughput, and then unblocked for 10 s. Returning to 1.15 eV, the sample absorption was re-measured, and this cycle was repeated with lengthening exposure times until a series of data points were accumulated, showing the absorption at 1.15 eV as a function of exposure time at 3.2 eV.

Figure 4.12 shows the data, indicating a clear increase in absorption caused by exposure to light above the band-gap. Fitting the data to a constant minus exponential curve gives a reasonable fit (better at long times) with a lifetime of about 40 minutes. The power throughput of the Rig has previously been measured as approximately 0.2 mW at 1.95 eV. Response curves from any standard PDS measurement (e.g. blue curve in Figure 6.42) show that the power at 3.2 eV is approximately 8.5 % of this value, or 0.017 mW. The illumination spot diameter is approximately 2 mm, leading to a flux of approximately 0.14 mW/cm^2 , or

3×10^{14} photons/cm²s. It has already been demonstrated that only 10 % of these photons reach the interface. Using the same absorption coefficient, and assuming that any absorption within 10 nm of the interface (approximately an exciton diffusion length) can be taken into consideration, about 25 % of the arriving photons produce photogenerated excitons within a diffusion length of the interface.

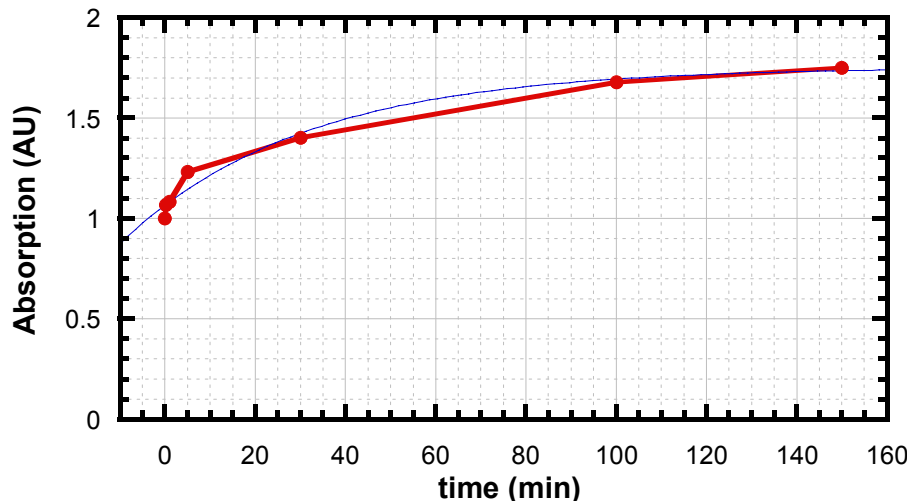


Figure 4.12: Absorption of spun PFB on spun PSSH at 1.15 eV as a function of time exposed at 3.2 eV.
Blue curve is a best fit for exponential approach to a final value (A-exp form)

This provides approximately 7×10^{12} events/cm²s. The density of triarylamine sites at the interface is on the order of 10^{13} /cm². The time-to-reaction of these sites was calculated from the fit as 2400 s, producing a quantum yield from excitons of close to 5×10^{-4} . This number is many orders of magnitude higher than the 10^{-10} cited for the quantum yield from holes⁵, although the mechanisms are clearly different and the figures not mutually exclusive. These measurements suggest that for every 2000 excitons photogenerated within a diffusion length of the interface, one of the triarylamine sites undergoes a change. Considering the first ten seconds of illumination alone, the effect is even stronger, since the rate of change at early times is very much faster than the exponential fit. During that period, the reaction proceeds approximately 9 % towards completion. This implies an extremely high quantum yield of one part in 70.

The reaction between the two polymers is thus significantly activated by the absorption of light in the vicinity of the interface.

4.4.8 Intimate mixing of PFB and PSSH

Samples 4J, 4K and 4L were produced to examine the intimate mixing of PFB and PSSH. The structures studied thus far contain a bi-layer with a well-defined interface, providing only a very limited surface area for interaction between the two materials. THF is a solvent in which PSSH can form a stable suspension and

PFB is readily soluble. The large surface area of the PSSH particles should cause a significant enhancement in the extent of reaction. To ensure that the THF itself does not adversely affect the two components, each is first tested separately in a sample produced from THF.

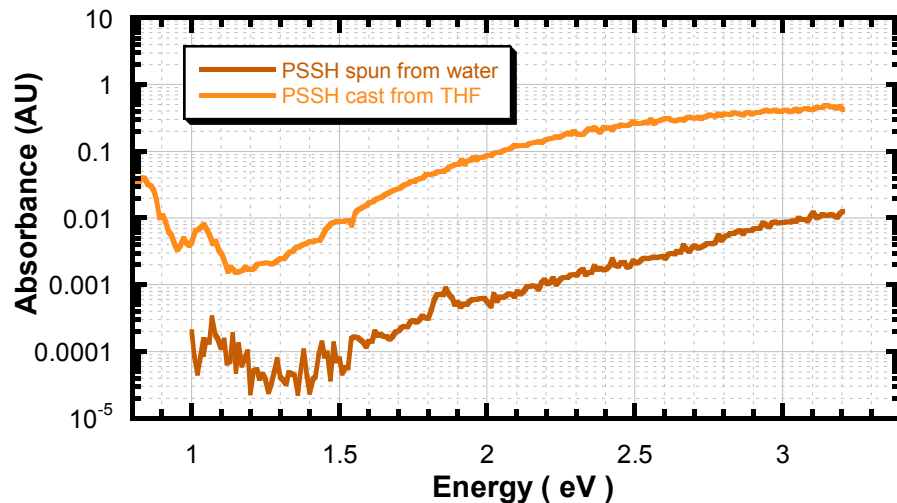


Figure 4.13: PSSH spun from water (4B) vs. cast from THF (4J).

The PSSH sample cast from THF, shown in Figure 4.13, yields a much greater PDS signal than the film spun from water. This is due to the relative thickness of the two samples, since the cast film was approximately 100 μm thick. The curvature of the absorption signal is likely due to saturation of the PDS signal by the thick sample. The characteristic water absorption is seen again at low energies. There is no evidence for any absorption feature created by interaction with THF.

It is even more important to compare PFB cast from THF with a standard film spun from toluene.

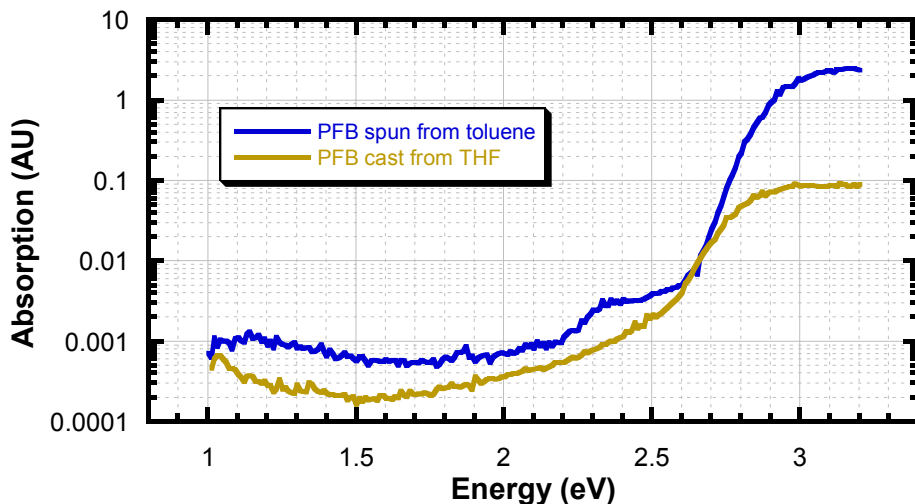


Figure 4.14: PFB spun from toluene (4A) and cast from THF (4K), normalised at the band-edge.

The resulting cast film is highly scattering and poorly adherent to the Spectrosil substrate. However unlike UV-Visible, PDS is not compromised by scattering, so a faithful spectrum, seen in Figure 4.14, can be recorded. Although the two spectra are different, most likely as a result of interchain aggregation¹⁰⁻¹³ during the slow evaporation of THF, there is no evidence for enhancement of either the 1.15 or 2.35 eV peaks due to the presence of THF.

Having characterised PSSH and PFB alone, the mixed film can be examined to highlight any changes which cannot be accounted for by linear combination of the two constituents. Again, the film is highly scattering, making UV-Vis measurements virtually impossible. However the PDS signal, shown in Figure 4.15, provides a faithful representation of the absorption. To the naked eye, the film appears reddish-brown, unlike PSSH alone (amber) and PFB (pale yellow). It is thus instantly apparent that a chemical change has occurred.

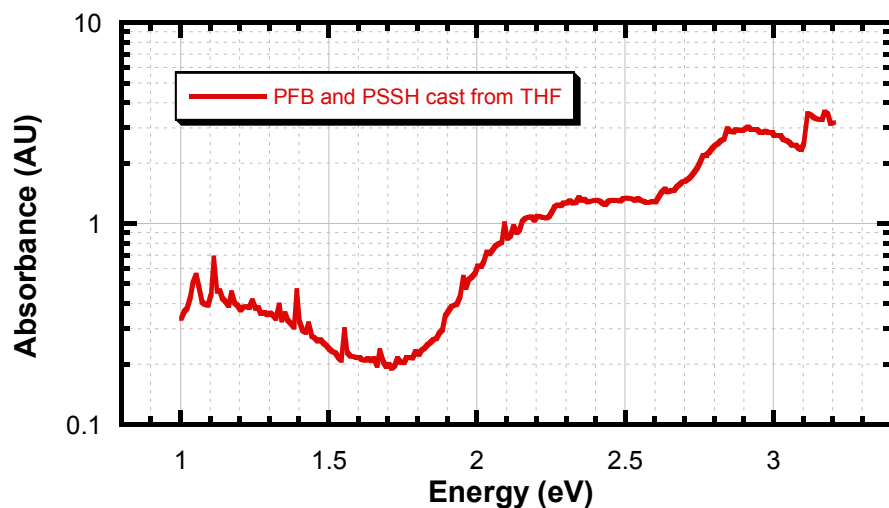


Figure 4.15: PDS spectrum of the intimately mixed PFB/PSSH film (4L).

The discontinuity at 3.1 eV is an artefact due to the auto-ranging of the experiment and the signal should in fact be continuous. Above about 2.6 eV the band-edge of the polymer is seen. As a result of the film thickness and the strong sub-gap features, it does not display the usual orders-of-magnitude rise above the sub-gap region. Peaking around about 2.35 eV a strong sub-gap absorption can be clearly seen. This appears to be the same absorption as revealed previously in native PFB, and which may have been partially visible in the PFB-PSSH bi-layers with un-baked PSSH. At 1.15 eV the other sub-gap feature previously seen is again visible.

Figure 4.16 shows the relative change on adding PSSH to PFB, by dividing the “mixture” spectrum by the PFB-only spectrum. The low-end peak, previously assigned at 1.15 eV can now be more clearly distinguished, and appears to lie rather higher in energy, towards 1.4 eV. This may indicate two separate

absorptions, with the 1.15 eV peak predominating in the weakly doped regime and the 1.4 eV peak at higher levels. Nevertheless, the intimate mixing sample confirms at least the 2.35 eV absorption detected at low levels by PDS measurements on bi-layers.

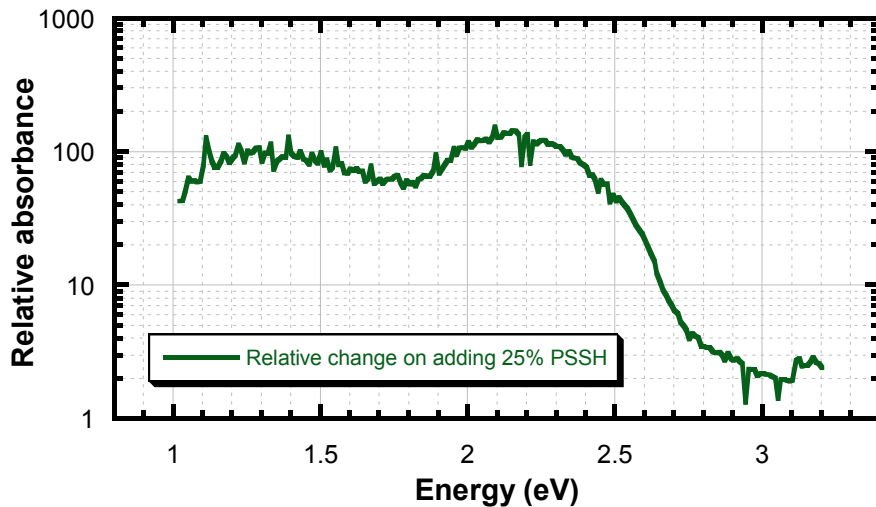


Figure 4.16: Relative change in absorption from PFB-only (4K) to PFB-PSSH mixture (4L).

4.5 Correlation with electrical degradation products

Having established that certain characteristic absorptions are induced by the interaction between PFB and PSSH, it can be shown that the same underlying changes take place during the electrical degradation of PFB-based LEDs. Raman spectroscopy allows deductions to be made about the nature of the reacted states in the polymer. The work in this section was performed by Dr J.S. Kim of the Cavendish Laboratory⁵, and is briefly described here for completeness.

4.5.1 Raman spectroscopy and electrochemical oxidation

Micro-Raman spectroscopy is a non-destructive technique which allows chemical and structural data to be collected from surface layers and even buried films. The optical probe used for micro-Raman work is relatively undiminished by the ITO/glass substrate (unlike infrared measurements) and can be selected to excite chosen structural units in a multi-component system.

The key finding of the micro-Raman work is in the subtle change in relative height of the Raman peaks at 1180 and 1164 cm⁻¹ as the device is electrically degraded. The 1180/1164 ratio begins around 0.8 in the undriven hole-only PFB device, and increases to around 1.0 as the device conductivity starts to drop.

PFB films were also electrochemically oxidised on clean ITO, and the resulting oxidised films displayed the same rebalancing of peaks in the Raman experiment as observed for the degraded device. This showed that the evolution of the electrically driven LED can be attributed to oxidation of the PFB.

Finally, the absorption spectrum of the electrochemically oxidised sample was compared to the absorption spectrum of sample 4L (seen in Figure 4.15), in which the PFB and PSSH were intimately mixed. The oxidised sample showed sub-gap peaks at 1.45, 1.9 and 2.3 eV. The first and last of these three peaks are very clearly seen in the PFB/PSSH mixture, whilst the middle one if present is obscured by the intensity and broadness of the other two.

It therefore appears that all three samples – degraded device, electrochemically oxidised PFB and mixed PFB/PSSH – show the same underlying change, namely an oxidation of the PFB itself. This is attributed, at least in the device/LED case, to an irreversible hole doping of the PFB. This is supported by the observation that the singly-charged cation of the model compound N,N,N',N'-tetraphenyl-*p*-phenylenediamine shows sub-gap absorptions at 3.0 eV and 1.5 eV, and the dication at 1.9 eV, the latter two of which closely match the absorptions seen in the electrochemically oxidised film.

4.6 Likely mechanism for the oxidation

Acid-doping of conjugated polymers is a well-known route for the introduction of charge onto the polymer backbone^{1,14,15}. The doping of polyaniline (PANI) is the classic example¹⁶. The emeraldine form of PANI contains equal proportions of aminic and iminic nitrogen sites. Figure 4.17 shows the process of acid doping of emeraldine to the conducting state. The protons donated by the acid attach preferentially to the iminic nitrogen sites, known as quaternisation, to produce the bipolaron form. As discussed in Section 2.2.2, bipolarons are spinless, and thus are the expected product when there is no loss or gain of electrons (oxidation or reduction) at the host molecule. The bipolaron can subsequently dissociate into a pair of polarons by conversion of the intermediate quinoid ring to the benzoid form, and these can delocalise along the chain.

PFB also contains nitrogen sites (see Figure 2.18), and although these are all aminic rather than iminic, they too can be quaternised under appropriate conditions, in which case a positively charged proton would sit on the nitrogen lone pair. Normal hole transport in triarylamines involves a transient oxidation of the nitrogen lone pair sites, followed by an immediate reduction as the hole hops to the next site. Protonation, however does not entail the loss of an electron, and therefore strictly will lead to the production of bipolarons. However, as seen in the case of PANI, a bipolaron so created can dissociate into a pair of polarons. It has

been noted⁵ that the strong intrachain and interchain coupling means that the polaron and bipolaron states of PFB may not be readily distinguished. Doping of PPV by FeCl₃ has similarly been shown to produce absorptions which cannot exclusively be assigned to either polarons or bipolarons¹⁷. Polaronic absorption features have been addressed by calculation¹⁵ and direct measurement¹⁸⁻²³ on several occasions, and sub-gap features seen in the PFB/PSSH experiments presented are consistent with polaron-like absorptions.

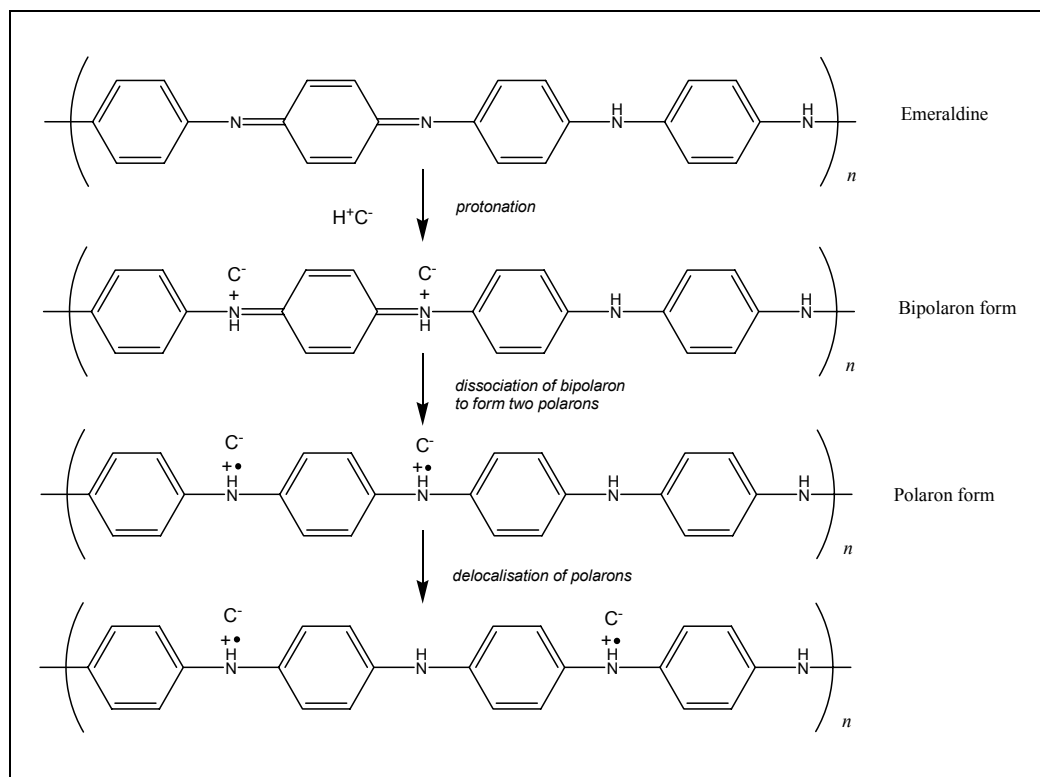


Figure 4.17: Protonation of emeraldine form of polyaniline to produce the doped conducting form

The comparison with electrochemically oxidised PFB described in Section 4.5.2 showed that the reaction between PFB and PSSH likely produces a mixture of radical cationic PFB⁺ and dicationic PFB²⁺ states. With the supporting evidence from the model compound described in Section 4.5, we can be confident that acid doping of the PFB by PSSH produces the same states, which have been observed in PDS.

4.7 Discussion and Conclusions

Comparison of pairs of samples has revealed the behaviour of the PFB-PSSH interaction as various parameters are altered.

4.6.1 Findings

As-spun PFB shows two very weak absorptions, approximately 2000 times weaker than the main $\pi\text{-}\pi^*$ absorption. Such features can usually be attributed to low level doping of the polymer. The features appear at 1.15 and 2.35 eV and are rather broad, displaying a FWHM of a few hundreds of meV. A different batch does not show the 2.35 eV feature at all.

Baking of PSSH results in a dramatic increase in absorption, by a factor of approximately 6 in the visible region. The absorption in the visible region increases approximately exponentially with the excitation energy. This yields a characteristic diagonal “cut-off” below which any other features in a bi-layer sample are usually obscured. Characteristic water absorptions are seen in both baked and unbaked PSSH, and this is attributed in part to the hygroscopic nature of sulphonic acids in general.

Regardless of whether the PSSH is baked or not, the weak absorption seen at 1.15 eV in native PFB is strongly enhanced by spinning on top of PSSH. The other absorption at 2.35 eV in native PFB may also be enhanced, but it is mostly obscured by the absorption of unbaked PSSH and completely obscured by baked PSSH. The PSSH can even be baked *in situ*, after spinning of PFB, and the same behaviour is observed. This baking process does not cause the reaction zone to extend any deeper into the polymer, suggesting that there is no ongoing diffusion-limited reaction process.

Studying a thick cast film in comparison with a thin spun film in the bi-layer structure reveals that the PFB and PSSH only interact in a confined region of the polymer. Furthermore the observation that the thinner film shows a greater induced absorption leads to the finding that the reaction is photoactivated, and that the thick film acts as an optical filter reducing the penetration of light to the reaction interface. This provides a direct link with the degradation processes observed in LED structures made from the same material, where the presence of electrically excited states leads to degradation.

Intimate mixing provides a very large interface area for interaction and ensures the maximum possible extent of reaction. In this case, both the 1.15 and 2.35 eV absorption features are extremely strong, and within an order of magnitude of the $\pi\text{-}\pi^*$ absorption, which must itself have been concomitantly bleached²⁴. The lower-energy feature appears to have either shifted to slightly higher energy or been superseded by a higher-energy peak at 1.4 eV.

Micro-Raman spectroscopy investigations have focused on the exact nature of the reacted species when PFB and PSSH interact. By comparing a device *in situ* and an electrochemically oxidised sample, the reaction has been identified as an irreversible oxidation of the PFB. The observed absorption features in the

PDS experiments are consistent with the proton-doping of the polymer, ultimately forming positive polarons and bipolarons on the chain.

4.6.2 Context and implications

PSSH is in direct contact with the electroluminescent polymer in a device structure, and it has been shown that injected holes at this interface mediate the irreversible oxidation of the PFB, with the PSS^- required to play the part of counter-ion. The p-doping of the surface, in conjunction with the counterions in the PSS, set up an electric field which opposes the injection field. Thus the performance of an LED built with this structure is gradually degraded as electrical driving proceeds.

4.6.3 Conclusions

This Chapter has shown that, regardless of processing conditions, PSSH can react locally with the PFB layer in the presence of excited states. The result is a proton-doped polymer chain which displays polaronic absorption features. This is an important consideration for the study and modelling of devices containing triarylamine-based polymers such as PFB, and should be taken into consideration when considering other electroluminescent polymers which are used in direct contact with PSSH. The intimate mixing technique described provides an easy route for initial assessment of such a system. Any absorption feature not expected from a linear combination of PSSH and conjugated polymer absorption spectra indicates the presence of a new species, and a possible detrimental effect on the polymer performance.

4.7 References

- ¹ C. C. Han and R. L. Elsenbaumer, *Synth. Met.* **30**, 123-131 (1989).
- ² A. C. Arias, M. Granstrom, D. S. Thomas, K. Petritsch, and R. H. Friend, *Phys. Rev. B-Condens Matter* **60**, 1854-1860 (1999).
- ³ M. Redecker, D. D. C. Bradley, M. Inbasekaran, W. W. Wu, and E. P. Woo, *Adv. Mater.* **11**, 241-+ (1999).
- ⁴ A. R. Duggal, J. J. Shiang, C. M. Heller, and D. F. Fouss, *Appl. Phys. Lett.* **80**, 3470-3472 (2002).
- ⁵ J. S. Kim, P. K. H. Ho, C. E. Murphy, A. J. A. B. Seeley, I. Grizzi, J. H. Burroughes, and R. H. Friend, *Adv. Mater., Submitted* (2003).
- ⁶ G. Greczynski, T. Kugler, and W. R. Salaneck, *Thin Solid Films* **354**, 129-135 (1999).
- ⁷ K. F. Palmer and D. Williams, *J. Opt. Soc. Am.* **64**, 1107-1110 (1974).
- ⁸ J. R. Sheats, H. Antoniadis, M. Hueschen, W. Leonard, J. Miller, R. Moon, D. Roitman, and A. Stocking, *Science* **273**, 884-888 (1996).

- ⁹ Y. G. Gobato, A. Marletta, R. M. Faria, F. E. G. Guimaraes, J. M. De souza, and E. C. Pereira, *Appl. Phys. Lett.* **81**, 942-944 (2002).
- ¹⁰ D. S. Thomas, *Ph.D. Thesis, University of Cambridge*, 1999.
- ¹¹ D. D. C. Bradley, M. Grell, X. Long, H. Mellor, and A. Grice, *Proceedings of the SPIE - The International Society for Optical Engineering* **3145**, 254-259 (1997).
- ¹² M. Grell, D. D. C. Bradley, X. Long, T. Chamberlain, M. Inbasekaran, E. P. Woo, and M. Soliman, *Acta Polym.* **49**, 439-444 (1998).
- ¹³ U. Scherf and E. J. W. List, *Adv. Mater.* **14**, 477-+ (2002).
- ¹⁴ D. A. Halliday, D. D. C. Bradley, P. L. Burn, R. H. Friend, and A. B. Holmes, *Synth. Met.* **41**, 931-934 (1991).
- ¹⁵ K. Fesser, A. R. Bishop, and D. K. Campbell, *Phys. Rev. B* **27**, 4804-4825 (1983).
- ¹⁶ A. Talaie, J. Y. Lee, Y. K. Lee, J. Jang, J. A. Romagnoli, T. Taguchi, and E. Maeder, *Thin Solid Films* **363**, 163-166 (2000).
- ¹⁷ M. Tzolov, V. P. Koch, W. Bruetting, and M. Schwoerer, *Synth. Met.* **109**, 85-89 (2000).
- ¹⁸ M. Redecker and H. Bassler, *Appl. Phys. Lett.* **69**, 70-72 (1996).
- ¹⁹ A. R. Brown, K. Pichler, N. C. Greenham, D. D. C. Bradley, R. H. Friend, and A. B. Holmes, *Chem. Phys. Lett.* **210**, 61-66 (1993).
- ²⁰ N. Tessler, N. T. Harrison, and R. H. Friend, *Adv. Mater.* **10**, 64-+ (1998).
- ²¹ K. Book, V. R. Nikitenko, H. Bassler, and A. Elschner, *J. Appl. Phys.* **89**, 2690-2698 (2001).
- ²² A. S. Dhoot, D. S. Ginger, D. Beljonne, Z. Shuai, and N. C. Greenham, *Chem. Phys. Lett.* **360**, 195-201 (2002).
- ²³ A. S. Dhoot and N. C. Greenham, *Adv. Mater.* **14**, 1834-1837 (2002).
- ²⁴ I. H. Campbell, D. L. Smith, C. J. Neef, and J. P. Ferraris, *Appl. Phys. Lett.* **78**, 270-272 (2001).

5. Pulsed-Mode Measurements of Turn-on Transient Characteristics

In this Chapter, the turn-on characteristics of homopolymeric, copolymeric, blended, and bi-layer LEDs are studied. Large electroluminescence spikes at turn-on have been previously reported in polymer LEDs^{1,2}, for which a selection of possible explanations have been conjectured but not convincingly confirmed. Devices with a range of morphologies are here examined, and compared to numerical models. The presence of an electroluminescence turn-on spike is shown to be a straightforward consequence of both the initial injection and subsequent transport properties, and thus to have a significant dependence on the device morphology.

5.1 Background

Pulsed-mode electrical excitation has been successfully employed as a characterisation tool to examine polymer LEDs *in situ*²⁻¹³. The ability to gather transient voltage, current and luminance data allows inferences to be made regarding the injection properties, charge transport, and recombination inside a working device. Previous work has explained the delay time to onset of electroluminescence¹², and provided insights into the causes of the subsequent fast and slow rises in the electroluminescence intensity¹³. However, unexplained spikes in the electroluminescence at turn-on have been observed in certain polymer LEDs under certain conditions, and the explanations for these have to date been based on educated speculation, without a consistent theory.

Besides single-polymer devices, bi-layer¹⁴⁻¹⁸ and blend^{19,20} devices have been the subject of great interest in polymer LED research, on account of the property mismatches at internal interfaces which lead to localisation of recombination, and the ability to match each electrode with a suitable polymer for favourable charge injection conditions. The two polymers studied here, in various combinations are F8BT and TFB, which can each be used to produce high performance LEDs²¹. In this Chapter, bi-layer LEDs are studied first, on account of their strong tendency to show turn-on spikes. The device morphology is then varied by moving to blended, block co-polymer and random co-polymer configurations, in order to observe the

changes in the turn-on spike. Finally, a numerical model is used to simulate the processes inside the LEDs and understand why the turn-on spike occurs.

5.2 Devices for study

6 structures were used in the main section of this work. The devices, listed in Table 5.1, were prepared by Mr L.P.H. Lu of the Cavendish Laboratory, on small pulse substrates according to the procedures described in Section 3.1.1. PEDOT:PSS was spun to 65 nm. Device 5A contained 90 nm of F8BT. Device 5B contained 70 nm of TFB. Device 5C contained 50 nm of F8BT laminated on top of 50 nm of TFB, following the procedure in Section 3.1.2. Devices 5D to 5F were all spun to 80 nm. The solvent in all cases was toluene. Calcium and aluminium cathodes were evaporated to thicknesses of 200 nm each. Finally legs were applied and the devices encapsulated by the epoxy sandwich, as described in Section 3.1.3.

Device	Structure
5A	F8BT only
5B	TFB only
5C	Bi-layer
5D	Blend
5E	Block co-polymer
5F	Random co-polymer

Table 5.1: Devices for study.

Four unipolar devices were produced for the determination of electron and hole mobilities in F8BT and TFB, as listed in Table 5.2. Electron-only devices were fabricated with calcium cathodes and aluminium anodes. Hole-only devices were fabricated with Nichrome cathodes and PEDOT:PSS anodes.

Device	Polymer	Purpose
5A⁺	F8BT (82 nm)	Hole-only
5A⁻	F8BT (90 nm)	Electron-only
5B⁺	TFB (70 nm)	Hole-only
5B⁻	TFB (70 nm)	Electron-only

Table 5.2: Devices for mobility determination

5.3 Pulsed measurements

The six LEDs were studied under pulsed electroluminescence on the Pulse Rig as described in Section 3.4.4, with particular attention to the luminescence transients produced at turn-on.

5.3.1 F8BT only

Measurements were made on the Pulse Rig using 4 μ s pulses at closely-spaced voltages ranging from 3.5 V up to 20 V. The pulse repeat rate was 30 Hz. Device 5A produced results typical for transient electroluminescence from F8BT devices. Figure 5.1 shows a representative selection of the drive voltages accessed, and displays a number of features typical of transient electroluminescence measurements.

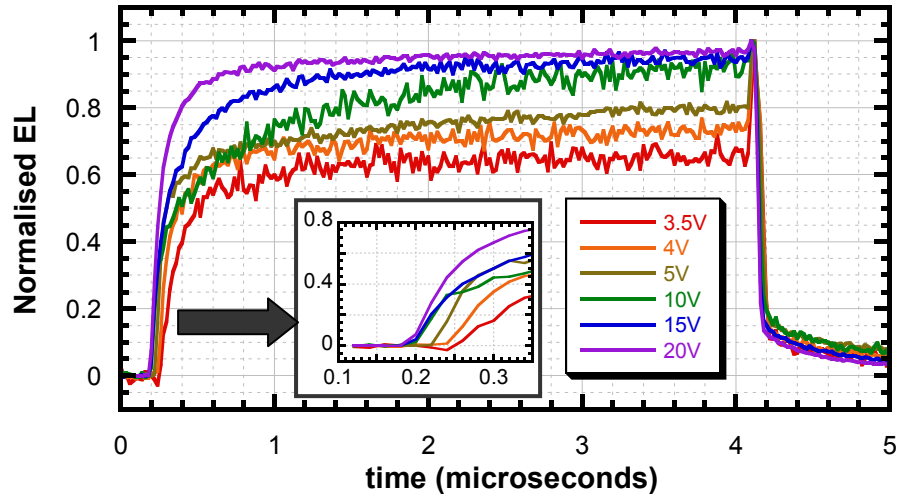


Figure 5.1: Normalised transient electroluminescence from Device 5A (F8BT only), at 30 Hz.

Inset: Enlarged view of turn-on delay.

At the earliest times, near 0.2 μ s (enlarged in the inset), a voltage-dependent delay to turn-on can be seen, spanning a range of approximately 70 ns. This delay is caused by the time taken for the fast carrier (electrons in F8BT) to transit the polymer layer¹², which is shorter under the accelerated drift caused by higher applied fields. In the limit of high voltages, the delay does not fall to zero, due to a constant zero-offset on the Rig of about 180 ns. The subsequent electroluminescence begins with a fast rise which is steeper at higher voltages and followed by a very much slower secondary rise. This secondary rise is too slow to see below 5 V on the timescale chosen, whilst it is complete within the first 2 μ s at 15 V.

The spike at the end of the pulse, seen at 4 μ s in Figure 5.1, is an artefact of the Pulse Rig, which causes a small overvoltage just before turn-off. It is unrelated to the turn-off spikes which have been reported just

after the end of the pulse^{1,2,22}. It has no physical importance in this study. Finally, after the end of the pulse, a fast modulation followed by a slow decay in the electroluminescence is seen. This slow decay has been shown to be exponential and caused by the recombination of the existing population of electrons and holes in the much-reduced field experienced after the external voltage is removed¹³.

These features are all characteristic of a general polymer LED. With sufficiently good data, the electron transit time could be used to extract a value for the electron mobility, but there is no universally agreed opinion in the literature as to any other parameters which can be reliably extracted.

5.3.2 TFB only

The device containing TFB only was measured in the same way, and the results shown in Figure 5.2. Many of the same features are seen to be present as in Device 5A, but each one is emphasised to a different extent.

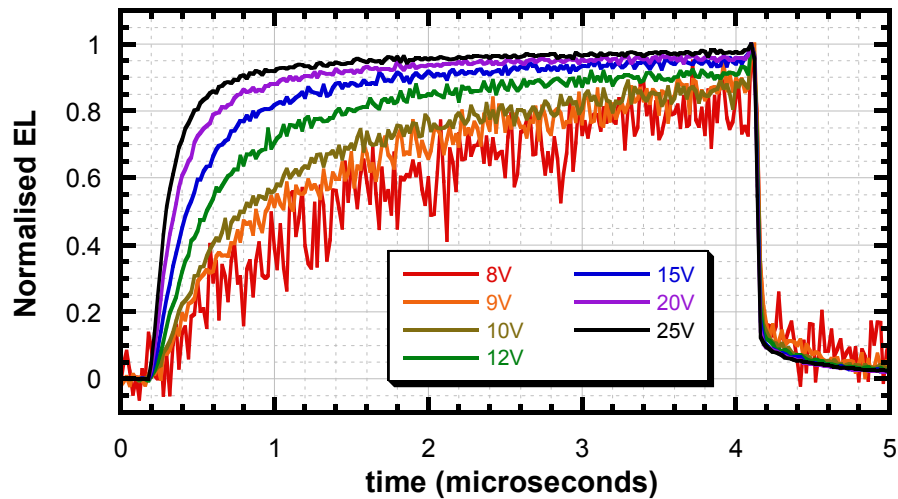


Figure 5.2: Normalised transient electroluminescence from Device 5B (TFB only), pulsed at 30 Hz.

The voltage range examined begins at a higher initial level, since detectable levels of light are only achieved above 8 V. The delay time, however, does not show any voltage dependence, even when analysed in high magnification. This may mean that at 8 V, the drift velocity of the fast carriers (holes in this case) is already too fast for adequate resolution by the Pulse Rig. Alternatively it may indicate that even the 30 Hz repeat rate used for measurement is too fast for effective carrier extraction between pulses, and that the recorded delay time does not reflect the transit of holes across the film thickness. The spike-artefact at turn-off, and the slow exponential tail are both visible once again.

In the case of TFB, then, no quantitative data can be reliably gathered from the pulsed measurements, since the fast-carrier mobility is not straightforwardly accessible. The trends in the device behaviour as a function of voltage can however be seen.

5.3.3 Bi-layer device

Device 5C contained a bi-layer structure, with TFB adjacent to the anode, and F8BT adjacent to the cathode. The bi-layer provides total separation of the two polymers in the LED structure, with the hole-transporting and electron transporting layer each in contact with its preferred electrode. The mobility mismatches for both carriers at the abrupt internal interface ensure that recombination is localised in this region of the device, and therefore occupies a very well-defined position inside the device structure^{15,16,23}. Pulsed measurements of this structure produced a radically different result to either of the homopolymer devices seen above.

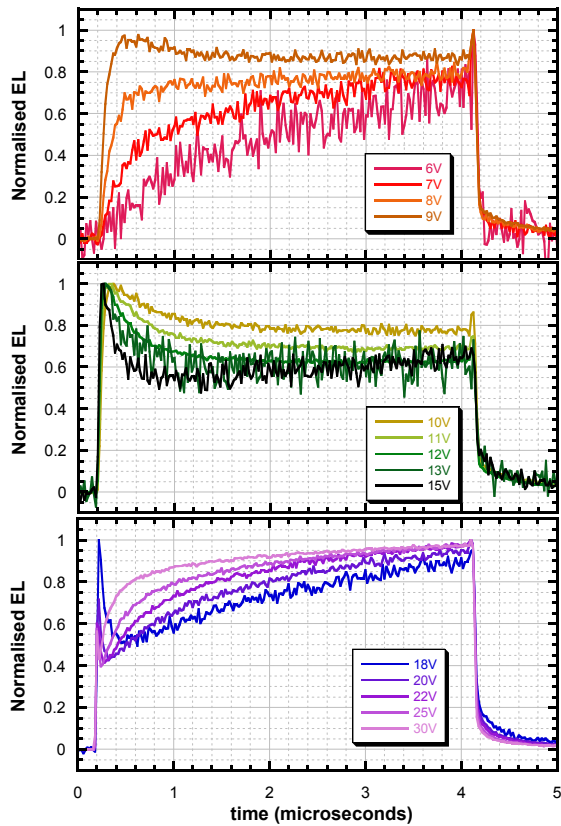


Figure 5.3: Normalised transient electroluminescence from bi-layer LED, pulsed at 30 Hz.

Three characteristic regions of behaviour are shown.

The response of the bi-layer LED, shown in Figure 5.3, is marked by the presence of a turn-on spike, which develops at drive voltages above about 8 V (Figure 5.3a), and becomes less significant compared to the long-term EL from about 18 V (Figure 5.3c). It is, however, still present right up to 30 V. The spike is

largest, relative to the long-term EL, at about 15 V (Figure 5.3b), where it is approximately two-thirds greater than the steady-state EL. Such turn-on spikes have been described previously², and it has been shown that for high repetition rates ($>>1$ kHz) the spike magnitude begins to diminish as residual charge carriers cause inter-pulse interference^{24,25}. 30 Hz was selected for this series of experiments to be a sufficiently slow pulse rate to minimise such effects without introducing oscilloscope triggering errors which occur at very low frequencies.

The delay to turn-on is not clearly visible on the time-scale shown in Figure 5.3, but magnification reveals that there is a voltage-dependent delay of up to 40 ns at the lowest voltages. This is consistent with the earlier observations that although TFB shows no delay time, F8BT shows a voltage-dependent delay. Due to the recombination zone confinement at the interface, the rate-limiting step is therefore expected to be transport through the F8BT.

5.3.4 Blend structure

The polymer blend structure provides a more complex heterostructure with F8BT-rich and PFB-rich phases. Previous work has shown that polyfluorene blends from high boiling point solvents such as isodurene show large scale phase separation²⁶ whilst low boiling point solvents such as chloroform show very fine scale features^{27,28}. The selection of toluene, an intermediate solvent produces mid-scale separation, similar to that seen in the related photovoltaic blend of F8BT and PFB²⁹. The data shown in Figure 5.4 show the turn-on spike once again, which is much less significant than in the bi-layer case. It is first seen at around 4 V, but by 10 V it is dominated by the main electroluminescence. The greatest excess over the long-term EL, seen around 6 V, is approximately 20 %, compared to nearly 70 % in the bi-layer case.

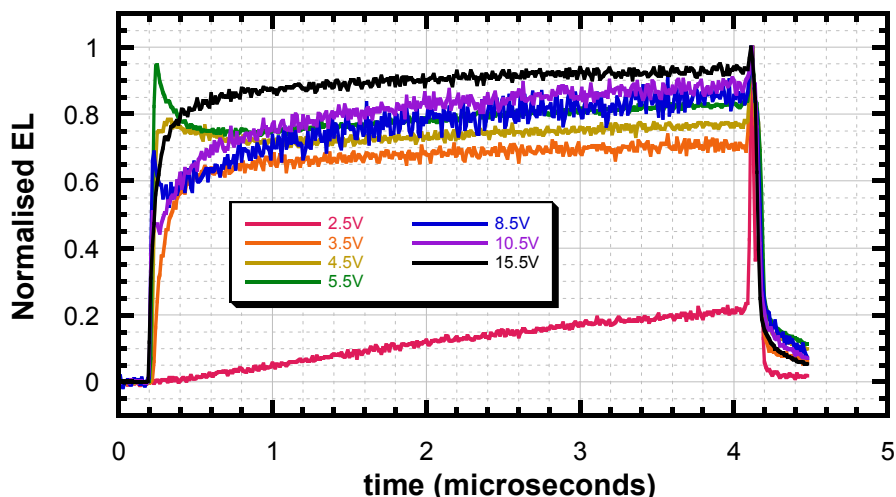


Figure 5.4: Transient electroluminescent response from blend device, pulsed at 30 Hz.

5.3.5 Block copolymer

The block copolymer is expected to provide a much finer scale of phase separation, with like sections of the polymer chain tending to form localised separations, but severely limited by the available block lengths. It must be noted that there is no data on the block length in this particular polymer. However, it is certain to be significantly shorter than the phase separation seen in the blend device. Figure 5.5 shows a barely discernible turn-on spike, identifiable as only a kink in the transient response except at the lowest voltages. A trend towards reducing spike significance with decreasing phase separation is now apparent.

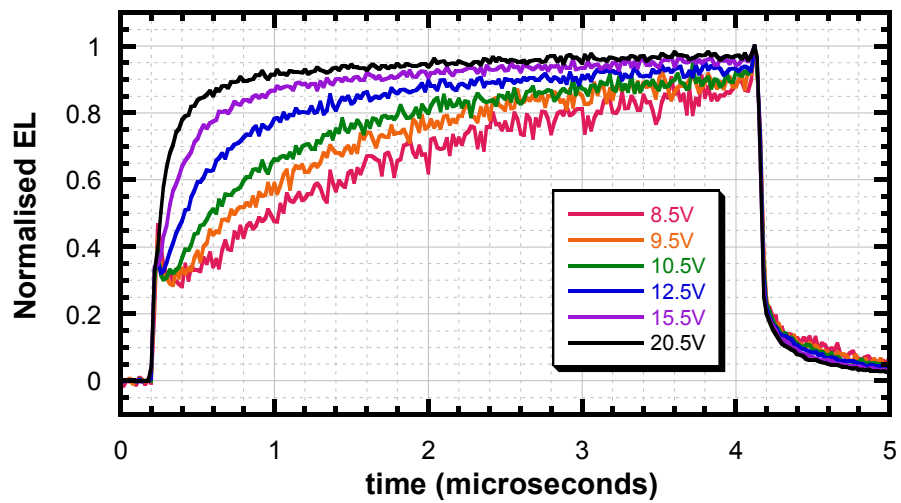


Figure 5.5: Normalised transient electroluminescence from block copolymer device, at 30 Hz.

5.3.6 Random copolymer

The final device in the series contains a random copolymer, which is expected to give the minimum degree of phase separation. There is very little freedom for the chains to form even small regions rich in either polymer. The turn-on transients are presented in Figure 5.6. The lowest voltage measurements (at 3 and 3.5 V) were measured with longer pulses to ensure that no slow-developing features were being missed. The lengthened pulses do not affect the turn on behaviour observed at early times. Similarly, at high voltage the oscilloscope resolution was increased, discarding the featureless behaviour beyond 2 μ s.

Following the trend as the morphology becomes finer, there is virtually no spike at all in this device. The slight evidence of a bump in the first microsecond, above about 14 V, does not prove to develop any further at higher voltage. Instead, by comparison with the block copolymer in Figure 5.5, the most likely remnant of the spike is visible only in the 3.5 V trace, where the main rise in EL appears to be preceded by an early

onset of luminescence. A significant delay time is expected at such low voltages, but tracing the main electroluminescence rise back to the x -axis, a small amount of pre-emission is observed.

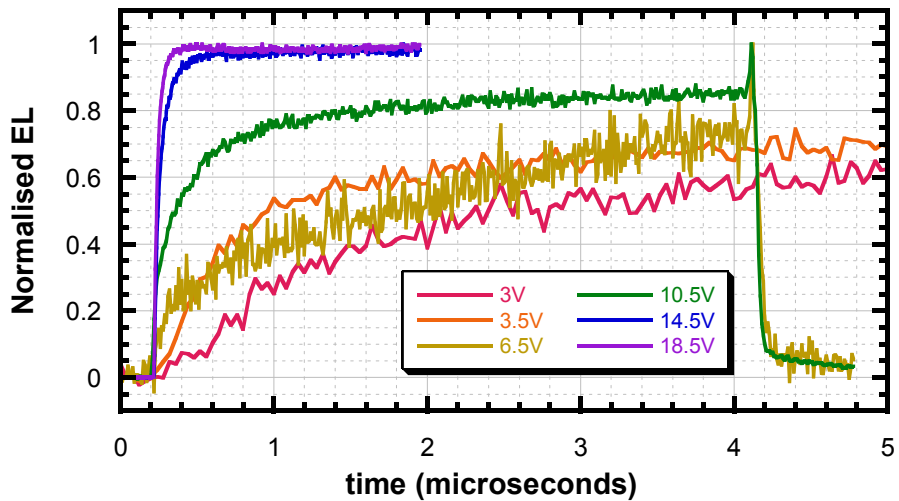


Figure 5.6: Normalised transient electroluminescence from the random copolymer, at 30 Hz.

5.3.7 Summary

The two homopolymer devices produce variations on the classic transient behaviour for a polymer LED. The combination devices produce a new feature – an initial spike in electroluminescence – which appears to be directly linked to the device morphology. The device with the most abrupt heterostructure shows the strongest spike, whilst the most homogeneous device shows almost no evidence for it at all.

5.4 Estimation of mobility

In order to compare the experimental findings with a numerical model of the devices under test, it is necessary to know the two charge carrier mobilities in each of the two base polymers. Since these values vary over a range of many orders of magnitude, an approximate determination of their values is likely to produce a realistic simulation.

For this reason, the four unipolar devices described in Section 5.2 were used to estimate the four mobilities required to model the simple devices. In this basic treatment, the field-dependence of mobility is not taken into consideration. Although this is a significant approximation, it is justifiable in the limited range of applied fields encountered in this work (see Section 2.4.4.1).

5.4.1 F8BT mobilities from unipolar devices

According to the Mott-Gurney Law, the current density in the trap-free unipolar space-charge limit is proportional to the square of the applied voltage³⁰.

$$j_{SCLC} = \frac{9}{8} \varepsilon_0 \varepsilon_r \mu \frac{V^2}{L^3} \quad (5.1)$$

where j_{SCLC} is the space-charge limited current density, ε_0 and ε_r the permittivity of free space and the relative permittivity of the polymer, μ the charge-carrier mobility, V the applied bias minus the built-in voltage and L the thickness of the polymer layer. Thus, if the relative permittivity and device thickness are known, an estimate of the mobility can be gained from the current-voltage characteristics of a unipolar space-charge limited device. The relative permittivity of F8BT has been previously measured by impedance spectroscopy to be 3.3 ± 0.1 .³¹

The hole-only (A^+) and electron-only (A^-) F8BT devices were measured in the IVL rig as described in Section 3.4.1. The current density–voltage responses were fitted to the positive side of a quadratic function, allowing free parameters for the built-in voltage and a constant of proportionality, as required by Equation 5.1. The results are shown in Figure 5.7. It has been previously demonstrated that the trap-free unipolar space-charge limited regime does not apply at the lowest applied biases¹, and thus the curves show good fits to the V^2 functional form only at higher voltages. The assumption of field-independence is justified in this region by the quality of the fits.

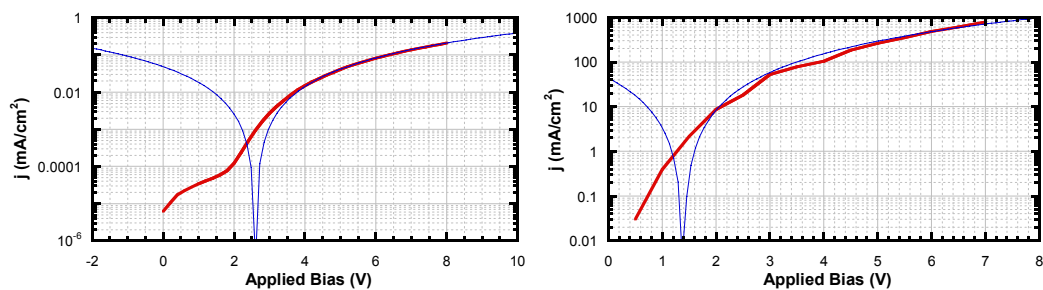


Figure 5.7: j-V curves and quadratic fits for hole-only and electron-only F8BT devices.

It should be noted that whilst the free-fitted value of the built-in voltage in the electron-only device is in excellent agreement with the 1.4 V predicted by the work-function difference of calcium and aluminium (see Section 2.5.1), the fit for the hole-only case is very different from the 0.1 V expected from the Nichrome and PEDOT:PSS work functions. This may be in part due to the known poor transport properties of holes in F8BT³² leading to a reduction of the injection bias by trapped charge inside the polymer. Table 5.1 summarises the devices and the constant-of-proportionality fit parameters obtained.

Device	x (nm)	k (mA/cm ² V ²)
A^+	82	0.0072
A^-	90	22.4

Table 5.1: Fit parameters, k , for the two unipolar F8BT devices measured in Figure 5.7.

By application of the Mott-Gurney Law, taking the fit parameters in Table 5.1 as equal to $\frac{9}{8}\epsilon_0\epsilon_r\mu$, two mobility values for F8BT are extracted:

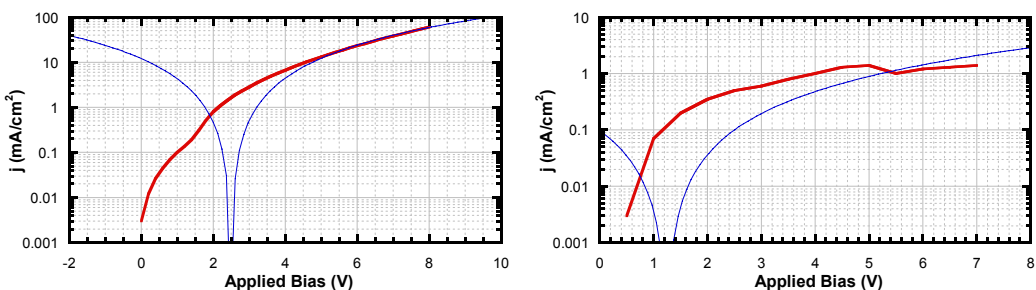
$$\mu_h(\text{F8BT}) = 1.2 \times 10^{-8} \text{ cm}^2/\text{Vs}$$

$$\mu_e(\text{F8BT}) = 4.9 \times 10^{-5} \text{ cm}^2/\text{Vs}$$

These values, though only estimates and ignoring any field-dependent behaviour, can now be used as input parameters in the numerical model. The electron mobility value is in good agreement with a rigorous analysis³³, further justifying the validity of this simple method.

5.4.2 TFB mobilities from unipolar devices

The same methodology is applied to the two unipolar TFB devices, to extract the charge carrier mobilities. Figure 5.8 shows the current density–voltage behaviour for the two devices. The fits shown are rather poor, particularly for the electron-only device. However it should be possible to extract at least order-of-magnitude estimates for the mobilities. The extracted fit parameters are presented in Table 5.2.

**Figure 5.8: j - V curves and quadratic fits for hole-only and electron-only TFB devices**

Device	x (nm)	k (mA/cm ² V ²)
B^+	70	1.95
B^-	70	0.063

Table 5.2: Fit parameter, k , for the two unipolar TFB devices measured in Figure 5.8

In the absence of a measured value for the relative permittivity of TFB, the value for F8BT is used as a best estimate. Application of the Mott-Gurney Law again, with the values in Table 5.2, yields the mobilities.

$$\mu_h(TFB) = 2.0 \times 10^{-6} \text{ cm}^2/\text{Vs}$$
$$\mu_e(TFB) = 6.5 \times 10^{-8} \text{ cm}^2/\text{Vs}$$

Energy levels indicate that for electrons in TFB and holes in F8BT, injection is unlikely to be ohmic. These values are therefore used simply as rough estimates.

5.5 Modelling

Numerical simulations were performed on the three well-defined bipolar LED configurations, namely F8BT-only, TFB-only and the bi-layer, to ascertain whether the presence of a turn-on spike is a direct consequence of known physics in the bi-layer structure. The numerical model employed is described in Section 3.5.

5.5.1 F8BT only

The F8BT-only device was modelled first. The mobilities calculated in the Section 5.4.1 were used, along with a relative permittivity of 3.3. As previously discussed, the mobility was approximated to be field-independent. Electron injection was taken to be ohmic, and hole injection subject to a barrier of 0.8 eV, due to the difference between the PEDOT work function and the F8BT HOMO level. Electron extraction at the anode was taken to be unhindered, although there is strong experimental evidence for a barrier to electron extraction at the PEDOT anode³⁴. Altering this condition produced results which conformed less well to experiment. The simulation was run using a 100 nm notional device thickness, for a duration of 5 μs , at a selection of applied voltages. A typical result is seen in Figure 5.9, which was calculated at 15 V, and is plotted with the corresponding experimental trace taken from Figure 5.1.

The correspondence between model and experiment is not perfect. The experiment shows an arbitrary delay due to the constant zero-error of the experiment. The model shows a small “hump” in the electroluminescence output around 0.2 μs , the analogue of which may be faintly discernible at about 0.4 μs in the experimental trace, which would coincide after subtraction of the zero-offset. A similar feature is also seen in the 5 V trace in Figure 5.1. Alternatively it may be that dispersive electron transport³² in the real device leads to smoothing of such delicate features. However, the overall result is a qualitative match, particularly on the overall timescale of the electroluminescence development.

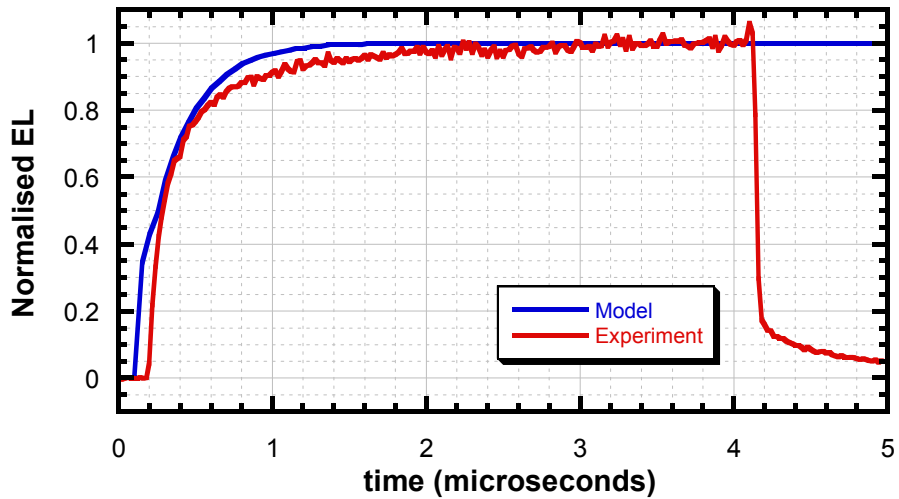


Figure 5.9: Numerical model and experimental data for an F8BT-only device driven at 15 V

Figure 5.10 shows two lower-voltage simulations. No value of applied voltage in the model can be found to force the “hump” to become more significant, although the simulation always shows it to be more pronounced than experiment. Neither can it be made to produce a full-blown front-spike, which concurs with the experimental findings. Analysis of the bi-layer device (below) will show more about this feature.

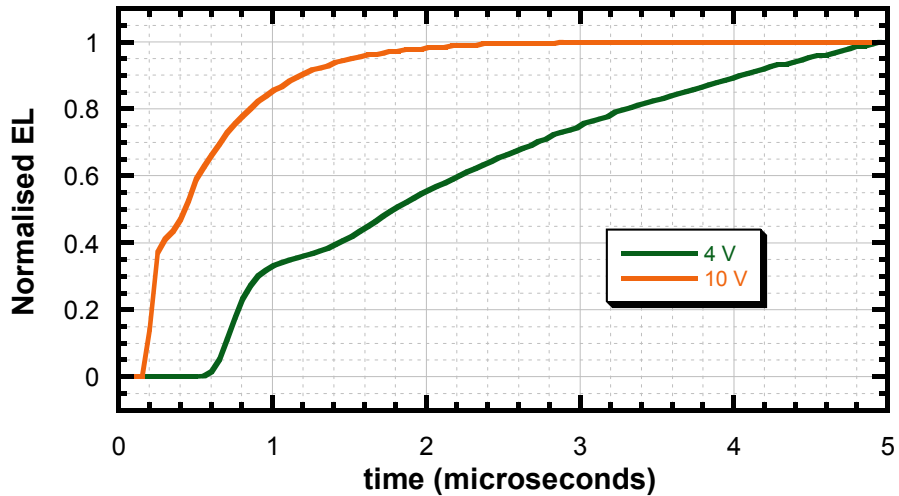


Figure 5.10: Simulated transient EL in F8BT-only LED at 4 V and 10 V

5.5.2 TFB only

The TFB-only device was now simulated in the same manner. The parameters chosen included the two mobility values calculated in Section 5.4.2, a relative permittivity of 3.3, a 70 nm device thickness, and a 0.6 eV offset for electron injection at the cathode. The barrier for hole injection is just 0.23 eV, so this was represented as either a 0.23 eV step, or as an ohmic contact, with very similar results. The second model,

used in the results presented here, follows the assertion that such a contact can be taken as ohmic at room temperature³⁵. Figure 5.11 shows that the simulated results are significantly inconsistent with experiment. The simulated traces have been normalised to their steady state values by separately running the simulation to the point of equilibrium. The most obvious difference is in the delay time. The model predicts values from 1 μ s to more than 2 μ s, whilst experiment shows no discernible delay whatsoever. The simulation also shows a very large “hump” reminiscent of that predicted in the F8BT model, which is not observed in experiment. Thus in this example, the model is not a good representation of the experimental observations.

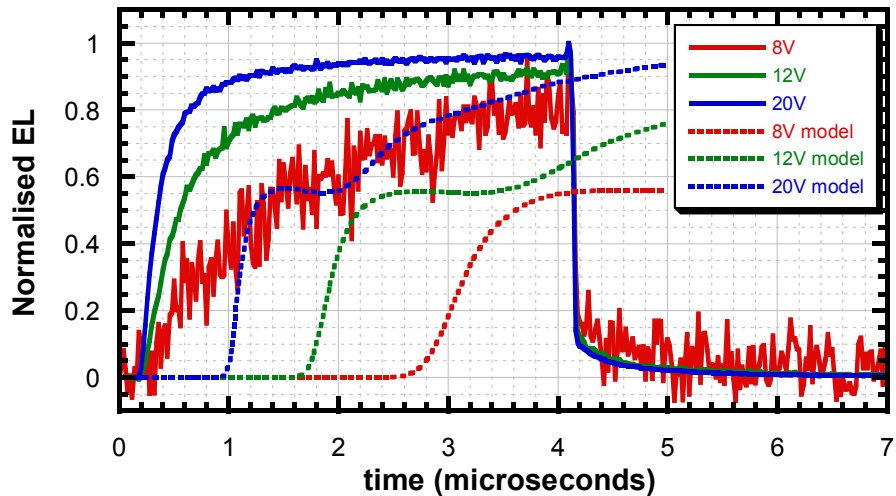


Figure 5.11: Experiment and simulation of TFB-only LEDs. The modelled traces do not stabilise within 5 μ s.

The determining factors for delay time are the hole mobility, the device thickness, and the applied field. The latter two are specified in the model precisely as in the experiment. The hole mobility, however, presents a serious problem. Redecker *et al*²¹ describe time-of-flight (TOF) measurements on TFB revealing a hole mobility three orders of magnitude higher – around 10^{-3} cm²/Vs – than the one used here, obtained from space-charge limited conduction. Time-of-flight measurements are contentious as indicators of real device behaviour due among other things to the large layer thickness usually required for good measurements, which can result in very different film morphology³⁶, as discussed in Section 2.4.4.1.

Modelling with these higher TOF mobility values does not improve the fidelity of the simulation, yielding results at the opposite extreme: the light emission stabilises at the DC value in less than 250 ns, even at just 8 V applied bias. This is more than an order of magnitude faster than is experimentally observed, and cannot be compensated by varying the simulated electron injection properties.

Crude manipulation of the hole mobility in the model produces the simulation shown in Figure 5.12. These optimum results are yielded with a mobility much nearer to the SCLC value than the TOF value, being five times greater than the former and two orders of magnitude smaller than the latter.

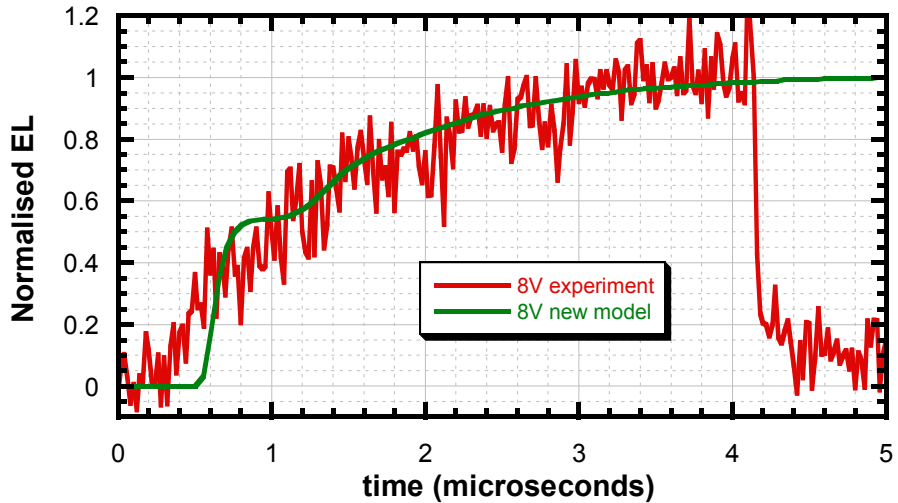


Figure 5.12: Re-modelled TFB response with five times original (SCLC) hole mobility.

Traces are normalised to best fit each other, not for comparison to steady state.

Both the rise-rate for electroluminescence, and the delay time before turn-on are better represented here. However whilst guesswork may produce a reasonable fit to experiment, without understanding the reasons for the discrepancy such a mobility value is difficult to adopt.

Given the choice between SCLC and TOF mobilities, we choose to use the former (lower) value from here onwards. The higher value cannot be reconciled with the observed experimental behaviour, due to the unrealistically fast turn-on transient. However, the lower mobility can be accommodated in a physically realistic picture of the device behaviour. The model considers a single independent pulse, whilst pulses are delivered sequentially at a rate of 30 Hz in experiment. Poor charge extraction between pulses could cause “instantaneous” arrival of some holes at the cathode during the subsequent pulse, while the time taken to reach steady state operation is still dependent on the arrival of holes from the anode. It has previously been shown¹ that pulse repetition rates as low as 0.01 Hz can leave residual charge inside certain LEDs. However 30 Hz was chosen for this experiment as the slowest rate at which data could reasonably be acquired without introducing the oscilloscope triggering problems which occur at very low repeat rates.

We must therefore concede that the model does not produce a good representation of the experimentally measured turn-on transients, but that nevertheless the SCLC mobility values employed, if a little low, are more compatible with experiment than the very much higher values implied by TOF. The absence of a turn-on delay is attributed to the poor extraction of charge between pulses. The lack of the predicted “hump” can be attributed to the same cause, since the initial state of the real device is not free from injected charge.

Nevertheless the strong presence of this modelled feature hints at the origin of the full-blown turn-on spike seen in the bi-layer, and suggests that it may be explained without the introduction of any new physics.

5.5.3 Bi-layer structure

The bi-layer structure is now simulated with the numerical model. The same cathode-side parameters were used as in the F8BT-only model, and the same anode-side parameters as in the TFB-only model. Two polymer layers were specified, each 50 nm thick, with barriers of 1.23 eV and 0.56 eV for the transit of electrons and holes respectively across the heterojunction. The results of modelling at a range of applied biases are presented in Figure 5.13. The model shows a resemblance to the experimental measurements seen in Figure 5.3, with a full-blown transient front-spike which exceeds the steady-state EL by up to 60 % just as in experiment. This contrasts with the single-polymer simulations, neither of which showed spikes exceeding the DC luminescence. The highest (relative) spikes are seen in the model around 16 V, which is also surprisingly close to the 15 V seen in experiment.

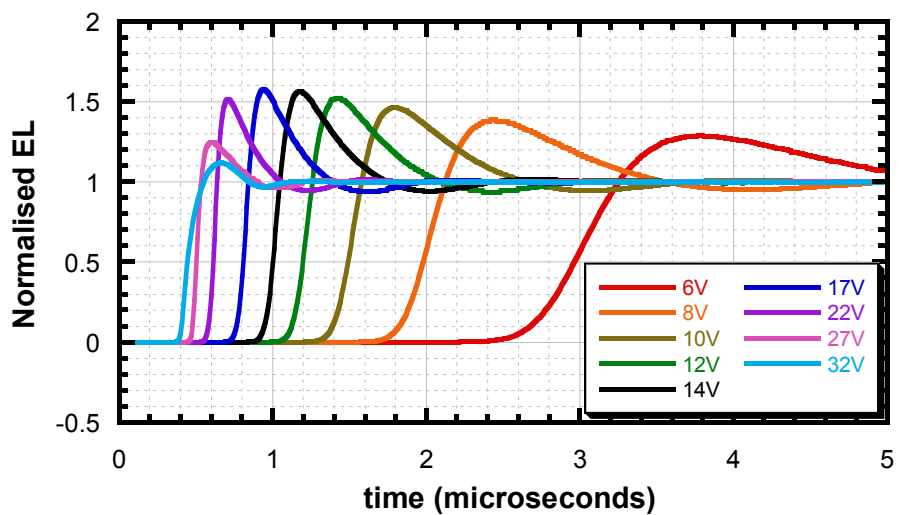


Figure 5.13: Modelled EL from the simulated bi-layer device. Normalised to the steady-state EL.

However, the delay time is again poorly represented. Experiments showed a voltage-dependent delay time of up to 40 ns, attributed to the transport through the F8BT, and consistent with the respective findings for F8BT and TFB single-polymer devices. The model, however, produces a very long delay attributable to the transport of holes through the TFB layer. It is intriguing that despite the poor agreement over the delay time, the turn-on spike is nevertheless well modelled in terms of voltage-dependence and amplitude. This can be further analysed by examining the time-dependent evolution of charge distributions inside the model.

5.5.4 Time-dependent evolution of the model

In order to explain the origin of the turn-on spike in the model, the charge density distributions are now examined as a function of time. The same bi-layer model as previously described was re-run a number of

times at 6 V applied bias, with the end-time of the simulation varied from 5 μ s down to 25 ns, to yield a series of time-varying data sets describing the state of the device. After each full run, the model records the final electron density, hole density and exciton generation rate as a function of position inside the device, and these can be collated to produce a time- and position-dependent data set. Figure 5.14 shows the exciton generation rate as a function of both time and position inside the modelled device, at 6 V, collected by extracting the exciton generation rate (as a function of position in the device) from the repeated runs of the model to different end-times. The delay to turn-on is clearly visible, followed by the turn-on spike and the beginnings of the subsequent rise in EL. Spatially, only the central 10 nm of the device is plotted, showing that the recombination zone is strongly confined at the interface. In fact, close inspection of the data files shows that essentially all recombination occurs on the F8BT side of the interface, as shown in Figure 5.15.

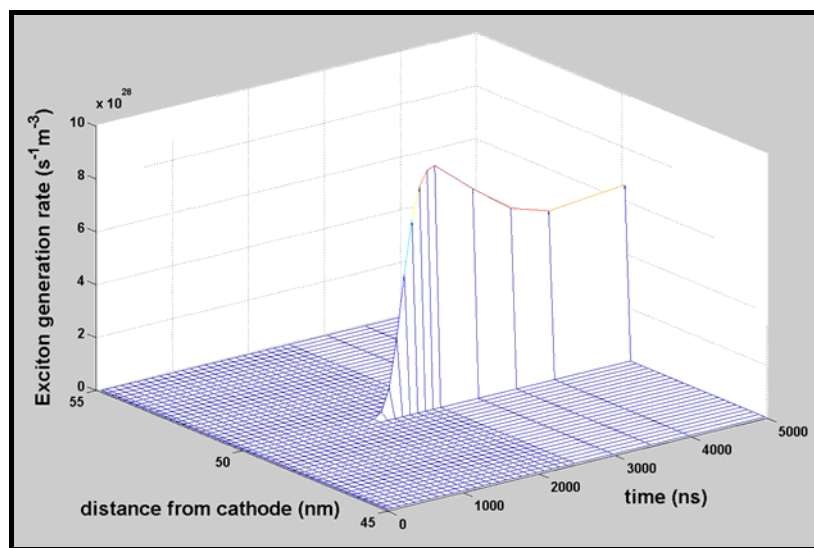


Figure 5.14: Modelled spatial and temporal evolution of recombination in the bi-layer at 6 V. The same model conditions are used as in Section 5.5.3. Emission is confined to the centre of the device, with onset around 1.5 μ s.

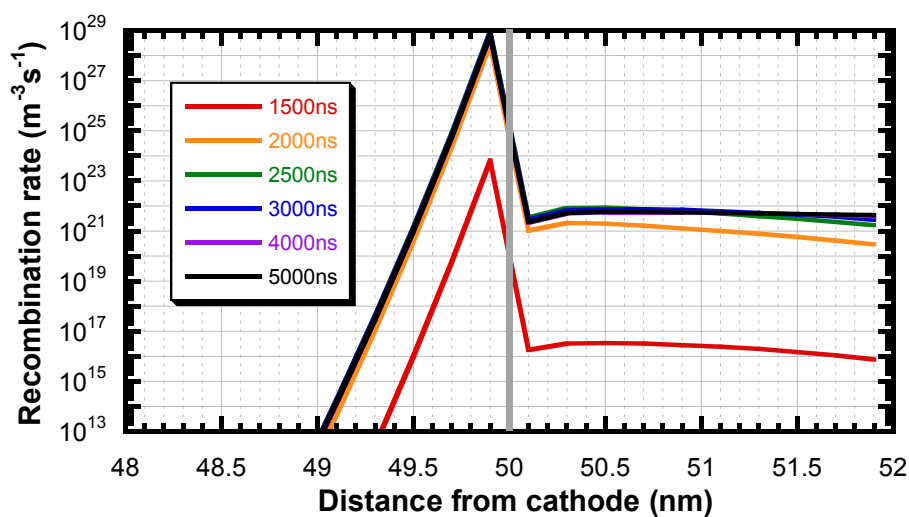


Figure 5.15: Recombination profile in the simulated bi-layer at 6 V, at selected times. Cell size 0.2 nm.

The data show that at all times the recombination is nearly 8 orders of magnitude greater on the F8BT side of the interface, although due to the limited hole mobility it also drops away very much more rapidly on that side.

These data are interesting but do not explain the origin of the turn-on spike. Much more revealing is the evolution of hole density. This is collected from the same simulations which produced Figure 5.14, taking data from only the TFB side of the device. The hole density evolution in the TFB layer is presented in Figure 5.16. The front of the hole packet can be seen arriving at the polymer heterojunction ($x = 50$ nm) after approximately 2 μ s. This is the rate-determining step for light emission, since the transit of electrons through F8BT is significantly faster (see below).

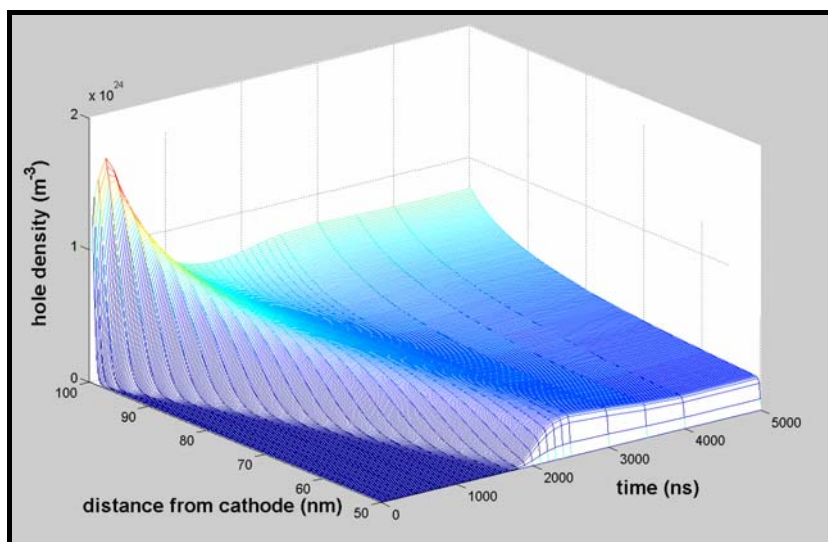


Figure 5.16: Modelled spatial and temporal evolution of hole density in the TFB layer at 6 V.
The same simulations are used as in Figure 5.14, with the parameters previously described.

The origin of the front-spike can be identified towards the left of the plot, resulting from an initial burst of injection into the polymer. At time zero, the electric field at the anode is due solely to the applied voltage across the parallel plate system. Holes are consequently injected into the surface layer of the polymer and begin to drift under the action of the field. This injected space-charge partially screens the anode, causing the local field and thus injection rate to drop. The initial burst of holes continues to propagate into the device, broadening by diffusion as it travels. This charge-screening explanation is seen to be self-consistent, since a minimum hole injection rate is observed precisely when the initial burst of holes reaches the interface. As this positive space-charge dissipates (by recombination at the heterojunction), the rate of injection at the anode finally rises once again.

The evolution of electron space-charge density in the F8BT layer can likewise be extracted from the same set of simulations, and presented as a function of time and position inside the F8BT layer, as seen in

Figure 5.17. A subtle feature shown in the data is the slight excess of electron density near the cathode at early times, at the “front” of the plot. This soon decreases as electron space-charge screens the bulk field.

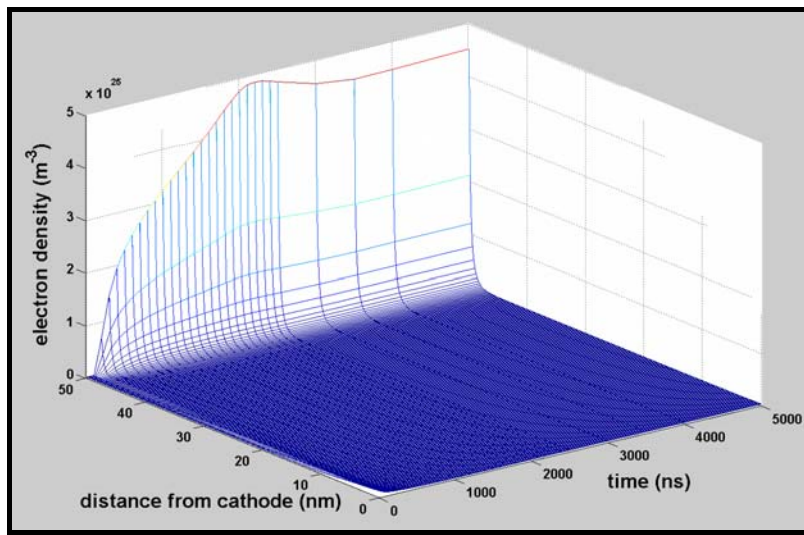


Figure 5.17: Modelled spatial and temporal evolution of electron density in the F8BT layer at 6 V.

The same simulations were used as in Figures 5.14 and 5.16.

As electrons drift (rapidly) towards the heterojunction, the applied bias across the device is dropped ever more strongly across the TFB layer alone. This “ramping-up” of the injection field in the TFB results in an additional contribution of injected holes not seen in the single-layer TFB device where there is no such field-boost at early times. Likewise as holes drift (more slowly) through the TFB layer, the field in the F8BT is correspondingly increased. This produces the slow linear rise in electron density at the heterojunction, exactly mirroring the progress of the hole packet through the TFB. The fast electrons in F8BT effectively respond instantaneously to changes caused by the slow-moving holes in TFB. When the hole spike approaches the interface, a corresponding electron spike is induced by this phenomenon. Since the recombination rate is proportional to the product of electron and hole densities, as discussed in Section 2.4.5, the spike in electroluminescence is proportionally greater than the spike in either electron or hole density alone. Thus the turn-on spike is predicted by application of known device physics.

5.5.5 Model summary

The model has revealed in detail how physically realistic charge carrier mobilities combined with known injection and transport properties can predict a turn-on spike in the electroluminescence. The model still does not represent the time delay correctly, and it has been pointed out that this may be due to poor charge extraction from the TFB between pulses. Although this would modify the subsequent transient behaviour, it is apparently insufficient to prevent the predicted occurrence of the turn-on spike.

5.6 Discussion and conclusions

Single-layer devices do not in general show turn-on spikes, although by careful manipulation of the relative charge carrier mobilities, such features can be induced in a model environment, and are occasionally seen in certain real devices. This chapter has examined two polymers which usually show no such spike when employed in single-polymer devices, but which do show a strong spike in a bi-layer formation.

5.6.1 Summary of transient formation in bi-layer devices

Modelling has provided confirmation that the overshoot can be understood with existing device models. Charge injection into the slower-transport polymer is enhanced at early times by an increase in electric field, due to the rapid transport of charge through the adjacent (fast) polymer layer. Following this injection boost, which is caused by the interface inherent in the device geometry, the electrode becomes screened by the injected charge, and injection subsequently reduces. When the slow-carrier spike arrives at the heterojunction, the fast-reacting adjacent polymer responds with an enhanced charge density, and the recombination rate experiences a boost proportional to the product of the electron and hole density. Finally, as the excess charge dissipates (through recombination), screening of the injecting electrode reduces, and the injection rate rises again towards its steady-state value.

5.6.2 Morphology dependence of turn-on spike

The model-based explanation for the turn-on spike relies on the presence of an internal interface between two polymers, and two different characteristic timescales for the arrival of charge at this interface from the two electrodes. The model as it stands cannot be used to simulate more complex morphologies such as the blend system. Nevertheless the reasoning can be extended to explain the experimental results in these cases.

The blend device is phase segregated, leading to internal interfaces similar to that in the bi-layer, but not so well localised in terms of depth. The presence of these interfaces appears sufficient to create a turn-on spike in the blend device as seen in experiment, but to a lesser degree than in the bi-layer case. There is no direct experimental evidence for phase segregation in the block copolymer device. Nevertheless, the pulse transients show evidence for a turn-on spike of limited size, and in a small voltage range. Following the reasoning of internal interfaces, this is consistent with phase separation on a small scale inside the polymer, such as might be expected from a block copolymer. The random copolymer is least likely to show phase separation, and indeed the pulse transients show virtually no evidence at all for a turn-on spike.

5.6.3 Conclusions

A series of devices have been examined in order to determine the origin of the turn-on spike in a bi-layer device. Experiments showed the strongest spike in the bi-layer, and weaker representations in the blend and block copolymer. No spike was seen in the homopolymer devices, nor in the random copolymer.

In order to proceed with numerical modelling, charge carrier mobilities were estimated by preparing and measuring unipolar space-charge limited devices for each of the four required mobilities. Numerical simulations of the bi-layer device show a convincing manifestation of the turn-on spike. However the behaviour of the TFB layer is not correctly represented in the model. This misrepresentation is attributed to the poor extraction of charge from TFB between pulses, producing a faster-than-expected turn-on in experimentally driven devices.

The turn-on spike itself is attributed to a series of connected phenomena:

- The fast equilibration of half of the device, leading to a rapid increase in the field in the other half
- The injection of carriers in the “slow” half of the device, at an increasing rate as the field increases
- The subsequent decrease in injection rate as the injected space-charge screens the electrode
- The arrival of the initial burst of “slow” charge at the interface, matched by a corresponding enhancement in the counter-charge density in the “fast” polymer
- Recombination at the interface, proportional to the product of both local charge densities

In this sense, the overshoot at turn-on can be seen as a damped positive feedback of transients between the two layers in the structure. The presence of the interface is crucial to these findings. Thus as the interface becomes less well defined through the morphological progression from bi-layer to random copolymer, the turn-on spike shrinks and finally disappears.

5.7 References

-
- ¹ D. J. Pinner, *Ph.D. Thesis, University of Cambridge, 2000.*
- ² A. V. Yakimov, V. N. Savvate'ev, and D. Davidov, *Synth. Met.* **115**, 51-56 (2000).
- ³ D. Braun, D. Moses, C. Zhang, and A. J. Heeger, *Appl. Phys. Lett.* **61**, 3092-3094 (1992).
- ⁴ D. Braun, D. Moses, C. Zhang, and A. J. Heeger, *Synth. Met.* **57**, 4145-4150 (1993).
- ⁵ N. Tessler, P. K. H. Ho, V. Cleave, D. J. Pinner, R. H. Friend, G. Yahioglu, P. Le barny, J. Gray, M. De souza, and G. Rumbles, *Thin Solid Films* **363**, 64-67 (2000).
- ⁶ G. J. Denton, N. Tessler, M. A. Stevens, and R. H. Friend, *Synth. Met.* **102**, 1008-1009 (1999).

- 7 N. Tessler, *Adv. Mater.* **11**, 363-370 (1999).
- 8 N. Tessler and R. H. Friend, *Synth. Met.* **102**, 1122-1123 (1999).
- 9 N. Tessler, G. Denton, N. T. Harrison, M. A. Stevens, S. E. Burns, and R. H. Friend, *Synth. Met.* **91**, 61-64 (1997).
- 10 V. Savvateev, A. Yakimov, and D. Davidov, *Adv. Mater.* **11**, 519-+ (1999).
- 11 J. Wang, R. G. Sun, G. Yu, and A. J. Heeger, *Journal of Applied Physics* **91**, 2417-2422 (2002).
- 12 D. J. Pinner, R. H. Friend, and N. Tessler, *J. Appl. Phys.* **86**, 5116-5130 (1999).
- 13 D. J. Pinner, R. H. Friend, and N. Tessler, *Appl. Phys. Lett.* **76**, 1137-1139 (2000).
- 14 Y. He, S. Gong, R. Hattori, and J. Kanicki, *Appl. Phys. Lett.* **74**, 2265-2267 (1999).
- 15 B. K. Crone, P. S. Davids, I. H. Campbell, and D. L. Smith, *J. Appl. Phys.* **87**, 1974-1982 (2000).
- 16 D. V. Khramtchenkov, V. I. Arkhipov, and H. Bassler, *J. Appl. Phys.* **81**, 6954-6962 (1997).
- 17 V. R. Nikitenko, V. I. Arkhipov, Y. H. Tak, J. Pommerehne, H. Bassler, and H. H. Horhold, *J. Appl. Phys.* **81**, 7514-7525 (1997).
- 18 D. J. Pinner, N. Tessler, and R. H. Friend, *Synth. Met.* **102**, 1108-1109 (1999).
- 19 H. Vestweber, R. Sander, A. Greiner, W. Heitz, R. F. Mahrt, and H. Bassler, *Synth. Met.* **64**, 141-145 (1994).
- 20 I. N. Kang, D. H. Hwang, H. K. Shim, T. Zyung, and J. J. Kim, *Macromolecules* **29**, 165-169 (1996).
- 21 M. Redecker, D. D. C. Bradley, M. Inbasekaran, W. W. Wu, and E. P. Woo, *Adv. Mater.* **11**, 241-+ (1999).
- 22 J. M. Lupton, V. R. Nikitenko, I. D. W. Samuel, and H. Bassler, *J. Appl. Phys.* **89**, 311-317 (2001).
- 23 J. Morgado, R. H. Friend, and F. Cacialli, *Appl. Phys. Lett.* **80**, 2436-2438 (2002).
- 24 D. J. Pinner, R. H. Friend, and N. Tessler, *Appl. Phys. Lett.* **77**, 1493-1495 (2000).
- 25 A. Chowdhury and A. J. Pal, *Synth. Met.* **106**, 85-88 (1999).
- 26 N. Corcoran, A. C. Arias, J. S. Kim, J. D. Mackenzie, and R. H. Friend, *Appl. Phys. Lett.* **82**, 299-301 (2003).
- 27 A. C. Arias, J. D. Mackenzie, R. Stevenson, J. J. M. Halls, M. Inbasekaran, E. P. Woo, D. Richards, and R. H. Friend, *Macromolecules* **34**, 6005-6013 (2001).
- 28 A. C. Arias, *Ph.D. Thesis, University of Cambridge*, 2001.
- 29 C. M. Ramsdale, I. C. Bache, J. D. Mackenzie, D. S. Thomas, A. C. Arias, A. M. Donald, R. H. Friend, and N. C. Greenham, *Physica E* **14**, 268-271 (2002).
- 30 N. F. Mott and D. Gurney, *Electronic Processes in Ionic Crystals* (Oxford University Press, London, 1940).
- 31 A. J. A. B. Seeley, *Unpublished*, (2002).
- 32 A. J. Campbell, D. D. C. Bradley, and H. Antoniadis, *Appl. Phys. Lett.* **79**, 2133-2135 (2001).
- 33 A. S. Dhoot, *Ph.D. Thesis, University of Cambridge*, 2002.
- 34 K. Murata, S. Cina, and N. C. Greenham, *Appl. Phys. Lett.* **79**, 1193-1195 (2001).
- 35 G. G. Malliaras and J. C. Scott, *J. Appl. Phys.* **85**, 7426-7432 (1999).
- 36 C. Y. Yang, F. Hide, M. A. Diaz-garcia, A. J. Heeger, and Y. Cao, *Polymer* **39**, 2299-2304 (1998).

6. Quantum Efficiency Increase in F8BT LEDs – Drive-Induced Enhancement

This chapter describes a study on the properties of LEDs based on poly(9,9'-dioctylfluorene-*co*-benzothiadiazole), known as F8BT (see Section 2.5.2). During exploratory measurements, this polymer was observed to display a significant increase in luminance in the early stages of electrical driving. This was experimentally confirmed as a real increase in the external electroluminescence quantum efficiency of the device, and subsequently investigated in detail.

The experiments described here suggest that the effect is caused by the trapping of significant quantities of charge, leading to an enhanced field for hole injection at the anode. This improves the injection balance in the polymer, producing the observed rise in quantum efficiency. Experiments on the effect of reverse biasing the LED for short periods help to explain the frequently-observed enhancement of LED behaviour in pulsed-mode drive schemes when the off cycle consists of a reverse bias. These insights will have a bearing on the design of drive schemes for commercial applications.

6.1 Background

F8BT is used as an efficient green emitter in polymer LEDs and as a component in blend systems. It is unusual in a number of ways, most notably because it is an efficient electron transporter¹, and also because it is known as one of the most extreme violators of the 25 % singlet-triplet ratio expected from spin statistics, reaching over 94 % in experiment².

The properties of F8BT and its blends make it the subject of much current interest. However, one puzzling aspect of its behaviour has before now been neither reported nor explained. An ordinary F8BT-based LED, in any typical LED structure, displays a dramatic increase in quantum efficiency during the early stages of driving at low intensity.

Although this phenomenon is not described in the literature, one single paper, by Ma *et al*³, describes a similar effect in an unrelated molecular semiconductor. However, that report shows the opposite behaviour in terms of current density evolution to that which will be revealed here. The evidence presented by Ma *et al* appears to indicate a decrease in the injection of the majority carrier, leading to improved quantum efficiency, although they do not explicitly address this in their discussion. Furthermore, they do not mention whether they see any subsequent recovery process, as observed in this work. Another instance of “electrical annealing”⁴ has been attributed simply to the ionic drift processes on which LECs depend (see Section 2.4.7), but will be shown not to be applicable in the effect seen here.

The following sections detail a series of experiments on the phenomenon, and the deductions that can be reached in each case. The work presented was conducted over an extended period of time, and as such it was not often possible to use the same device in more than one experiment. Indeed, a number of devices were designed for specific experiments and would have been of no further use. As a result, wherever a new device is introduced, it is identified in terms of the thickness of the F8BT layer. Pixel areas are quoted where necessary, and changes to the structure or composition are highlighted wherever relevant. In all other cases, the device structure is as follows: Glass (1.1 mm) / ITO (100 nm) / PEDOT:PSS (60 nm) / F8BT (as specified) / Ca (>25 nm) / Al (~250 nm). The method of device fabrication is described in Section 3.1. For traceability, the batch numbers of F8BT used in this study are stated to be F8BT/96 and F8BT/119.

6.2 Drive-Induced Enhancement – Initial Observations

The effect was initially observed during pulsed studies of F8BT-based LEDs, when it became clear that luminance measurements on a single LED at a single voltage were not reproducible. The obstacle was not device degradation, but rather a significant *increase* in luminance at constant voltage.

6.2.1 Electroluminescence increase at constant voltage

Devices had been prepared on large pulse substrates encapsulated with glass, and containing an 86 nm layer of F8BT in the standard device structure. The Test Box (see Section 3.4.5) was specially designed and constructed as a suitable apparatus for long-term measurements of LEDs in a reproducible manner.

The directionality of the PMT in the Pulse Rig (Section 3.4.4), the difficulty in precisely realigning it after each pixel change, the requirement to use pulsed drive in order to gather data with the PMT, and the laboriousness of extracting a single value for light and current density, made the Pulse Rig unsuitable for prolonged measurements on multiple devices. The Test Box contained a large-area silicon photodiode,

which as well as being the most suitable device for the purpose would also eliminate any artefact inherent in the PMT measurements.

With the LED of interest mounted in the Test Box, and driven at constant voltage by an external voltage source, the light output and current throughput were measured at intervals under computer control. This is a variant of system setup C described in Section 3.4.5.2.

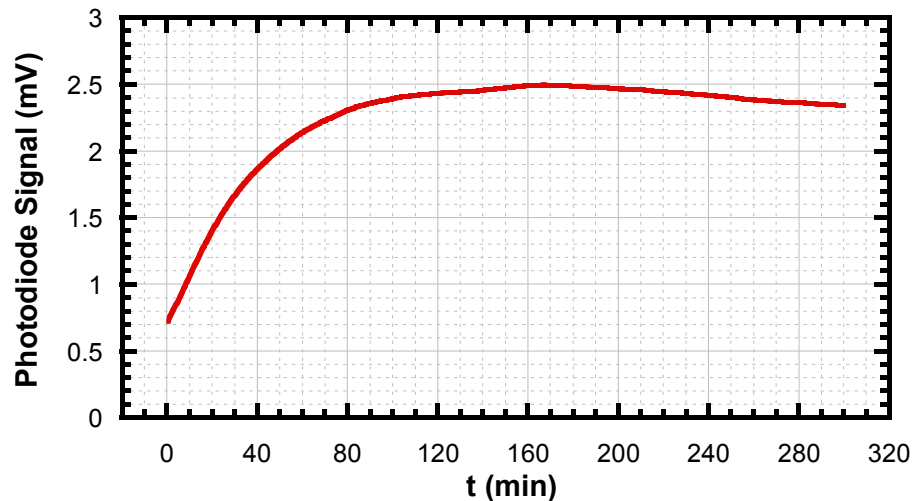


Figure 6.1: Measured electroluminescence from the 86 nm F8BT LED, area 1 mm², driven at 3.25 V for 5 hours. Data points are separated by 30 s, with the first measurement taken after 30 s.

Figure 6.1 shows the variation in electroluminescence intensity with time. The device shows an increase in EL intensity of more than 250 % in the first three hours. The absolute luminance of this pixel at 3.25 V was previously measured to be 6.7 cd/m², in a fast sweep (~0.5 V/s) from reverse bias to forward bias. Using the photodiode signal at the start of measurement, this gives an effective calibration for the Test Box of approximately 0.01 cd/V.

This particular measurement is made substantially below the 100 cd/m² considered useful for commercial applications and against which lifetime tests are normally quoted. In comparison to the data shown here, harsher drive schemes, test-times of thousands of hours, and significant degradation in fresh devices all conspire to make the initial increases almost invisible when standard lifetime tests are plotted graphically. However zooming in on the first few data points, as long as they are not too far spaced out in time, invariably reveals an initial improvement in F8BT devices.

The experiment was repeated on a number of similar devices and shown to be completely reproducible. Thus, both experimental artefacts in the apparatus and the possibility of a rogue device were eliminated.

6.2.2 Quantum Efficiency

In tandem with the electroluminescence measurement of Figure 6.1, the current was simultaneously measured. Dividing electroluminescence by current produces a measure of the external quantum efficiency of the device. The data in Figure 6.2 show a drift in the current density, with a shape resembling the electroluminescence signal in Figure 6.1, even down to the apparent bump artefact seen between 120 and 160 minutes. The quantum efficiency trace shows an increase in external quantum efficiency, peaking at +99 % after about 2 hours, relative to the first measured value recorded after 30 s. However, the artefact at 120-160 minutes, which appears in both light and current traces, disappears when they are divided through to yield quantum efficiency. Thus whatever external factor causes it, the effect is to vary the overall conductivity of the device without changing the quantum efficiency.

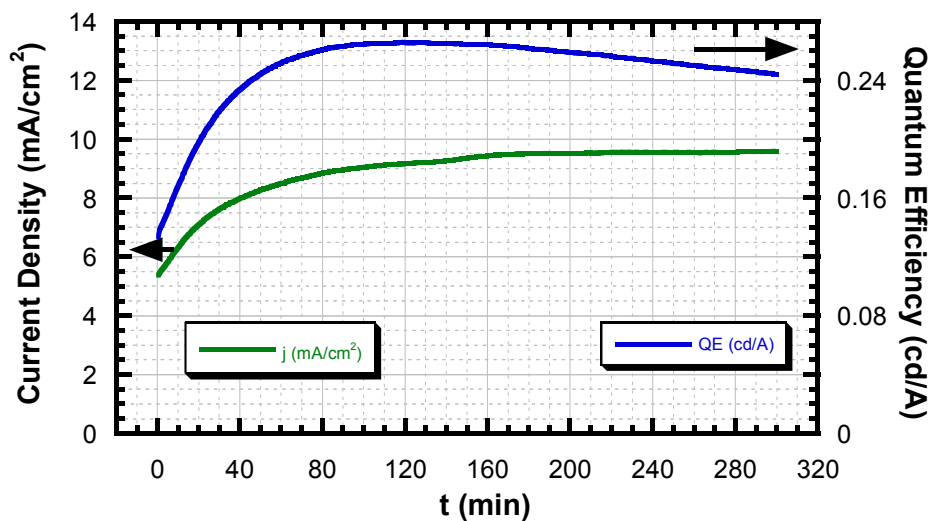


Figure 6.2: Current density and quantum efficiency from the same experiment as Figure 6.1.

The feature is further elucidated by studying a longer series of measurements on a larger pixel from the same device, at 3.0 V. Figure 6.3 shows nearly 17 hours of data from this pixel, displaying almost-regular oscillations with average period approximately 56 minutes. This was traced to small temperature fluctuations due to the air conditioning in the laboratory, and was seen in several sets of constant-voltage data, with time periods between 45 and 75 minutes. A person entering the confined space where the experiment runs was enough to produce a rise in the current and luminance within a few minutes. This increase in current with temperature has been reported before⁵⁻⁷. Critically, however, the quantum efficiency shows no sign of fluctuation as the temperature varies. To minimise these thermal variations, all subsequent measurements were made with the Test Box in good thermal contact with a solid steel optical table, to act as a giant thermal reservoir.

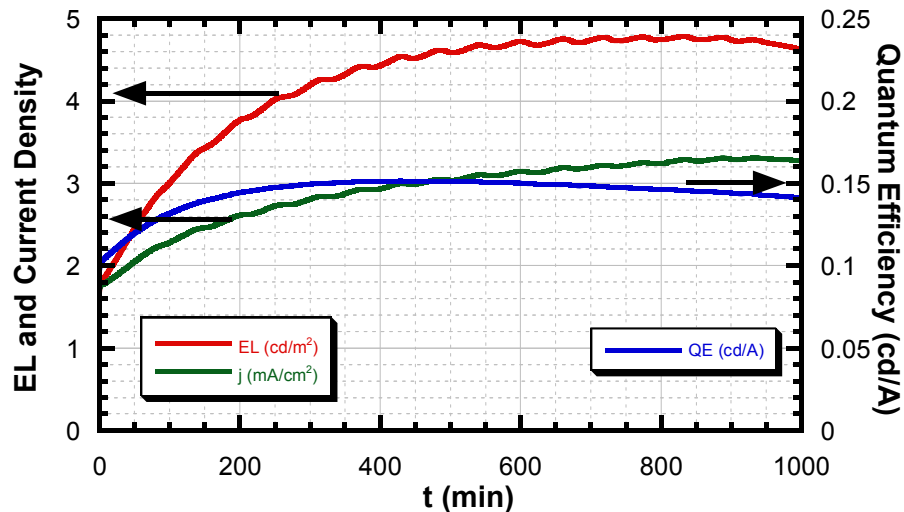


Figure 6.3: Luminance, current density and external quantum efficiency of a larger pixel at 3.0 V.

In each data-set presented, the quantum efficiency peaks before the absolute luminance. Even though the quantum efficiency begins to drop, most likely due to the onset of degradation in the device, the ongoing increase in device conductivity causes the absolute luminance to continue to rise. Especially at early times, heating is likely to be a significant factor. Joule heating is likely to raise the device temperature⁸⁻¹¹, increasing the conductivity⁵⁻⁷ (as seen during air conditioning cycles). It should be noted that the experiments by Ma *et al*³ showed a decrease in device conductivity, whereas an increase is typically reported in light-emitting electrochemical cells (LECs)^{12,13} where the motion of ions leads to improved injection (Section 2.4.7). Device degradation provides a competing channel for changes in quantum efficiency, without necessarily affecting the device conductivity. In the long-term limit degradation must inevitably take over, at which point the quantum efficiency curve peaks.

In the light of all these findings, the external quantum efficiency is seen to be the underlying characteristic of interest, whilst the luminance at constant voltage is a by-product of this and other phenomena. Therefore, throughout the rest of this Chapter, luminance measurements are made at constant current in order to directly probe the external quantum efficiency.

6.2.3 Extent of behaviour

In order to establish the range of conditions under which drive-induced enhancement takes place, a series of devices were fabricated and tested. All were made on small standard substrates, with 3.1 mm^2 pixels and encapsulated with epoxy and glass, as described in Section 3.1.

The choice of polymer was tested first. A selection of polymers, and some commonly-used blends, were examined for the presence of drive-induced enhancement. All devices were fabricated with a calcium cathode, PEDOT:PSS anode, and 90 to 100 nm of electroluminescent polymer. They were driven at a range of constant currents, both when fresh and partially degraded, in an attempt to identify any evidence for the presence of the effect. The findings are summarised in Table 6.1.

	F8	F8BT	TFB	PFB	F8BT/PFB Blend	Green Bi-Blend	Red Tri-Blend	Blue Copolymer
Effect seen	✗	✓	✗	✗	✓	✓	✓	✗

Table 6.1: Occurrence of the effect in a ITO/PEDOT:PSS/x/Ca/Al device. The polymers are described below.

As described in Section 2.5.2, the four polymers are closely related, all being based on the fluorene monomer. The “Green Bi-Blend” contained F8BT and TFB, whilst the “Red Tri-Blend” contained the same two polymers plus a proprietary red component. The “Blue Copolymer” is a copolymer of the F8 fluorene unit with the TFB and PFB units.

The Table shows that, amongst the simple polymer devices examined, only F8BT shows the drive-induced enhancement effect. There was some evidence that F8 displayed the effect during the first 2-3 seconds of operation, and only at extremely low current densities of $50 \mu\text{A}/\text{cm}^2$. However, the peak value observed on the digital multimeter was achieved even before the first automated measurement was recorded. F8 devices have been seen to show signs of the effect under pulsed electroluminescence, where time-averaged currents can be made many orders of magnitude lower simply by decreasing the duty cycle. TFB and PFB showed no rising component whatsoever. The blends, which all contained F8BT, all showed drive-induced enhancement. It therefore appears that, at least on the timescales accessible in a DC experiment, the effect is only seen in the presence of F8BT.

A second series of devices was made to test the cathode dependence of drive-induced enhancement. Four cathodes were measured: calcium, magnesium, aluminium and Nichrome (see Section 2.5.1). All devices contained a 100 nm F8BT layer, and a PEDOT:PSS anode. Initial tests showed the effect in calcium and magnesium devices only. Calcium is an ideal cathode for an F8BT device, having a work function of just 2.9 eV, compared with the F8BT LUMO level of 3.55 eV, thus providing an ohmic contact. Magnesium has a work-function of 3.7 eV, which is close enough to the polymer LUMO that ohmic behaviour is also expected¹⁴.

As seen in Figure 6.4, the magnesium-cathode device starts to degrade sooner than the calcium device, and in this particular case fails suddenly within four minutes, probably due to a break in the cathode. The required drive voltages were comparable, and both show very similar peak quantum efficiencies.

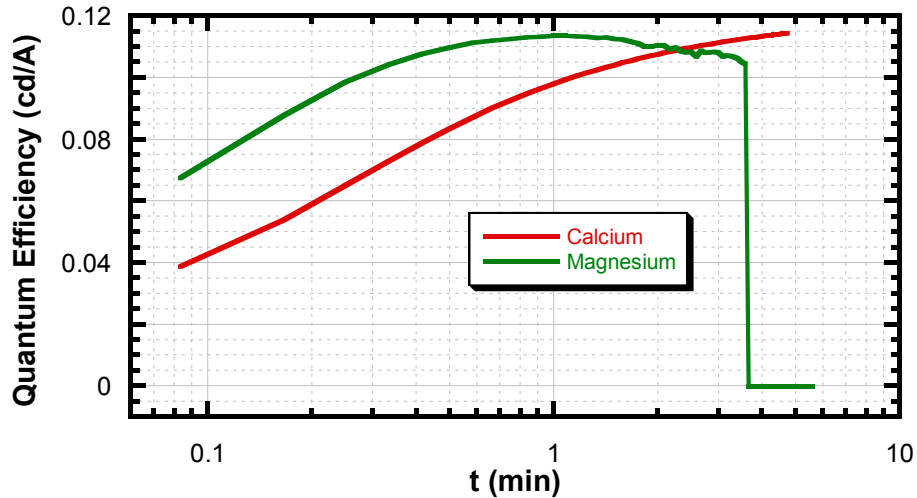


Figure 6.4: Quantum efficiency of F8BT LEDs driven at 1 mA/cm^2 with calcium and magnesium cathodes.
The magnesium-cathode device is seen to fail after about 3 and a half minutes.

When measuring the aluminium-cathode devices under the same conditions, the drive-induced enhancement effect was seen on the digital multimeter display during the first few seconds. However, degradation had already set in before the first computer measurement was recorded. The peak quantum efficiency observed in the aluminium device was approximately double that of the calcium and magnesium cases. Such a difference is to be expected, since aluminium is not an ohmic cathode for F8BT, and the electron flow is correspondingly constricted, improving charge balance. This restricted charge injection is accompanied by a significantly increased drive voltage required to drive the device.

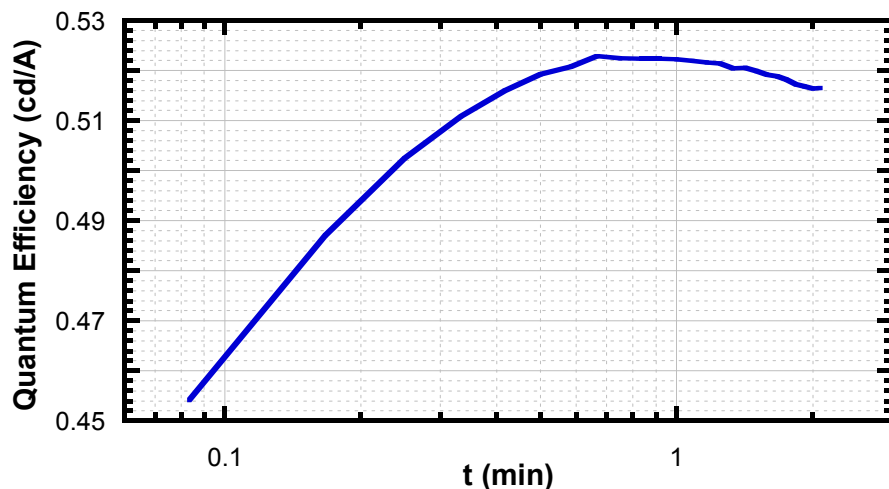


Figure 6.5: Quantum efficiency of aluminium-cathode device at 0.1 mA/cm^2 .

Since the quantum efficiency was seen to peak so quickly, the experiment was repeated on a fresh pixel at one-tenth of the current density, shown in Figure 6.5. The aluminium-cathode device now clearly shows the

drive-induced enhancement effect. Under these conditions, the peak quantum efficiency is more than twice again that mentioned in the previous paragraph.

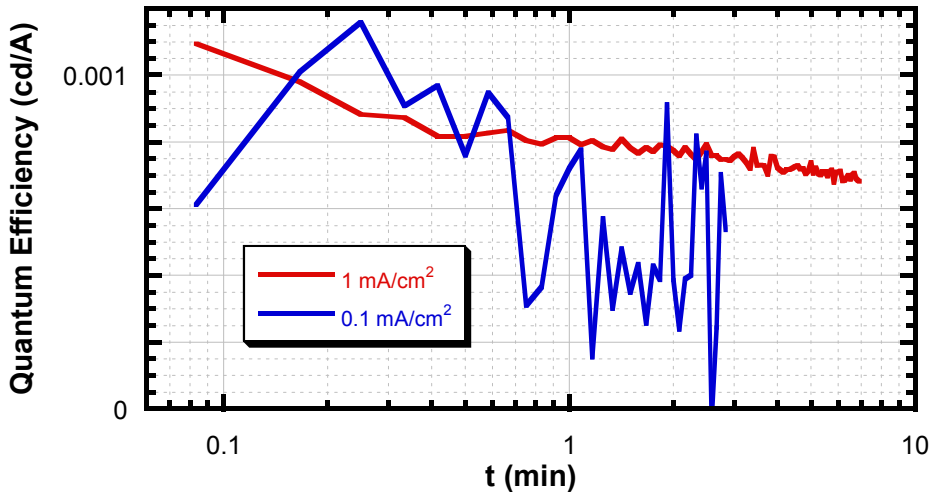


Figure 6.6: Electroluminescence from Nichrome device at two current densities.

Finally, the Nichrome cathode was tested both at 1 and at 0.1 mA/cm^2 . Electron injection from Nichrome is virtually impossible, since its work function is approximately 5.1 eV – the same as ITO and PEDOT which are used as hole injectors. The barrier for injection is therefore 1.55 eV and as such, significant light emission is not expected. As seen in Figure 6.6, 1 mA/cm^2 produces a small amount of light emission at a peak quantum efficiency 100 times less than in the calcium and magnesium devices. This suggests that the devices were effectively unipolar hole-only devices. There was no evidence for the effect. At 0.1 mA/cm^2 , quantum efficiency is similar, but the absolute levels of light are at the detection limits of the apparatus, producing noisy data. There is some evidence that the light intensity does increase before it decreases, although this may simply be due to noise. Table 6.2 summarises the cathode dependence results.

	Ca	Mg	Al	NiCr
Effect seen	✓	✓	✓	?

Table 6.2: Occurrence of drive-induced enhancement as a function of varying cathode.

Finally, anode dependence was tested. Anode materials are discussed in Section 2.5.3. So far in this Chapter only the standard PEDOT:PSS anode has been tested. ITO is a ceramic, with a rough surface, and it is thought that the indium atoms present can diffuse into the adjacent polymer layer¹⁵. PEDOT:PSS on the other hand is an ionic polyelectrolyte complex, with a highly planar surface, in which any contaminants are thought to be benign, and which may incorporate a thin insulating layer at its surface^{16,17}. Measurements on an ITO-based device with a 62 nm F8BT layer show a clear signature of the effect, seen in Figure 6.7.

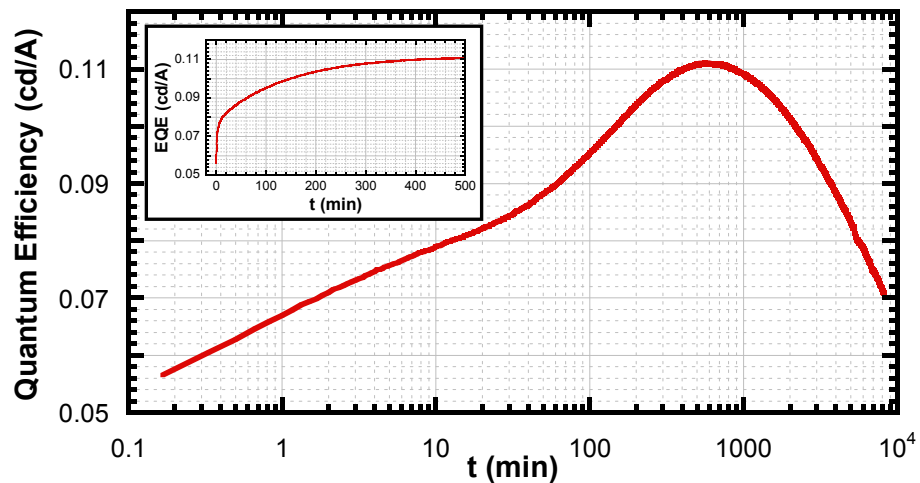


Figure 6.7: Quantum efficiency of an ITO-based device driven at 1 mA/cm^2 .

Inset shows the first 500 minutes on a linear time axis.

The data show two separate phases, which may indicate two separate effects. However the rise in quantum efficiency on driving is clearly present. Table 6.3 summarises the anode-variation results.

	ITO / PEDOT:PSS	ITO only
Effect seen	✓	✓

Table 6.3: Occurrence of drive-induced enhancement as a function of varying anode.

Finally, the degree to which the effect produces a real enhancement in the quantum efficiency was to be determined. As already seen, the fractional increase observed is dependent on the current density applied, as well as the amount of enhancement which is “lost” before the first data point is collected. A significant number of measurements appeared to show a ceiling of 300 % for the total increase achievable. This would have been very interesting from the point of view of singlet/triplet ratio, which is known to be above 94 % in an operational F8BT device, as this may have been indicated a drive-dependent drift from the spin-independent expected value of 25 % up to this higher level – an increase of nearly 280 %.

However, measurements at lower current densities, where the effect proceeded more slowly and could be tracked from earlier stages, revealed significant advances on this figure. Figure 6.8 shows the results of a 1 mA/cm^2 drive on a standard PEDOT:PSS / F8BT (100 nm) / Ca device, yielding a quantum efficiency increase of over 13 times. Indeed, before the first automated measurement was recorded, the DMM output was seen to climb gradually through the 0.003 cd/A mark, indicating an eventual rise of more than 60 times in quantum efficiency. There appears to be no decisive fundamental limit to the extent to which the effect can progress, but rather it seems to depend on the arbitrarily low quantum efficiency when first observed, any intrinsically limiting maximum efficiency, and the onset of degradation in the limit of long times.

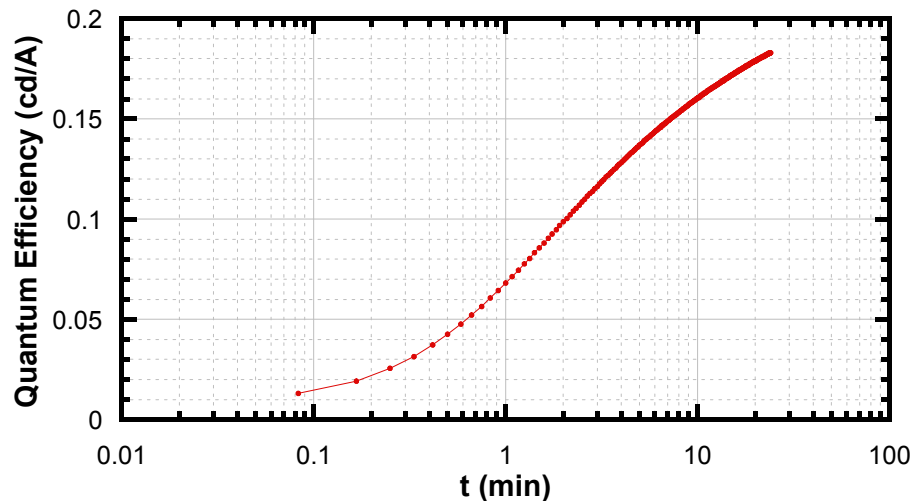


Figure 6.8: Constant current light output of an F8BT LED at 1 mA/cm^2 , showing $15\times$ increase.

6.2.4 Summary of findings

In summary, the drive-induced enhancement effect has so far displayed the following characteristics:

- Increased external quantum efficiency without significant temperature-dependence
- Observed at low voltages and current densities, near the threshold of bipolar injection
- Accompanied by an increase in the conductivity of the device, which
 - has a temperature dependent component
 - continues to rise for a time after the onset of degradation
 - leads, in combination with the external quantum efficiency increase, to a significant boost in absolute electroluminescence at constant voltage
- Measurable in F8BT and F8BT-blends only (in DC experiments)
- Independent of anode
- Independent of cathode, where measurable
- Enhancement begins from arbitrarily low values of quantum efficiency

6.3 Permanent degradation and recoverable enhancement

It has been seen that the external quantum efficiency reaches a peak, which may be caused by the onset of degradation. Thus it is important to understand the role of degradation in limiting the enhancement effect. In distinguishing degradation, it will be seen that enhancement is, in contrast, a recoverable phenomenon.

6.3.1 Time to peak

Measurements of the drive-induced enhancement were carried out on three identical pixels on a new single device, containing a 115 nm F8BT layer. Each pixel was driven at a different current density, namely 1, 10 or 100 mA/cm². Figure 6.9 shows the results. The curves were normalised to their peak values on the quantum efficiency axis, and converted into terms of total charge passed on the time axis, to allow direct comparison. Data were collected at 5-second intervals in each case, with the first data point *after* five seconds. This delay avoids any transients in the measurement apparatus, and is needed because the averaging circuitry in the Test Box introduces a small time lag in registering instantaneous changes, such as the initial turn-on. However this also means that the first 5 seconds of the LED's response is not recorded.

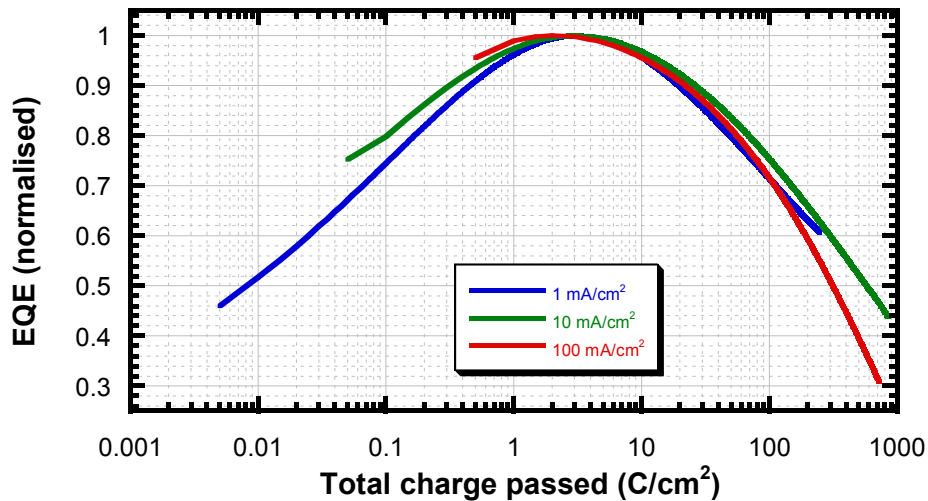


Figure 6.9: Normalised quantum efficiency as a function of total charge passed, at three current densities.

The three characteristic curves show remarkable consistency, even though the drive regimes employed span two orders of magnitude in current density. There is clearly a universal behaviour, however, the most universal part – the peak position – is simply due to the onset of degradation. By definition the curves all peak at unity on the normalised quantum efficiency axis, and since degradation is closely linked to the total charge passed¹⁸, the onset of degradation occurs at the same point on the x-axis in all cases. Thus it is degradation which causes the three peaks to line up so well, rather than the enhancement effect. The enhancement-dominated portions of the curves, which are typical of those seen in such experiments, can be matched reasonably well with logarithmic fits, although there is no particular theoretical support for this.

It has been shown that degradation is responsible for the point at which the enhancement process peaks, since these two phenomena compete for influence over the quantum efficiency. Drive-induced enhancement dominates at short times, and degradation at long times. Therefore, any attempt to measure the extent of the enhancement process must take account of the onset of degradation.

6.3.2 Rate of degradation

Measurements of any long-term phenomenon in polymer LEDs are complicated by the occurrence of drive-induced degradation. Degradation effects are most significant in new devices. This is demonstrated in Figure 6.10, which shows the quantum efficiency of a new 70 nm F8BT LED as a function of time when driven at 50 mA/cm^2 . This equates to a high initial luminance of around 500 cd/m^2 . Fits to the first and last 10 minutes of data show an exponential lifetime of approximately 65 minutes in the LED when first driven, compared with 2000 minutes after 43 hours of constant current drive. The total degradation in quantum efficiency is nearly 99 %. The first 40 seconds of data, when magnified (not shown), show a small but real enhancement of 6.0 %. The actual degree of enhancement is always under-represented in these measurements, and more so at high current density, because of the delay before the first measurement. In this case the first measurement was taken after 8 seconds, and a large proportion of the effect may have taken place by this time.

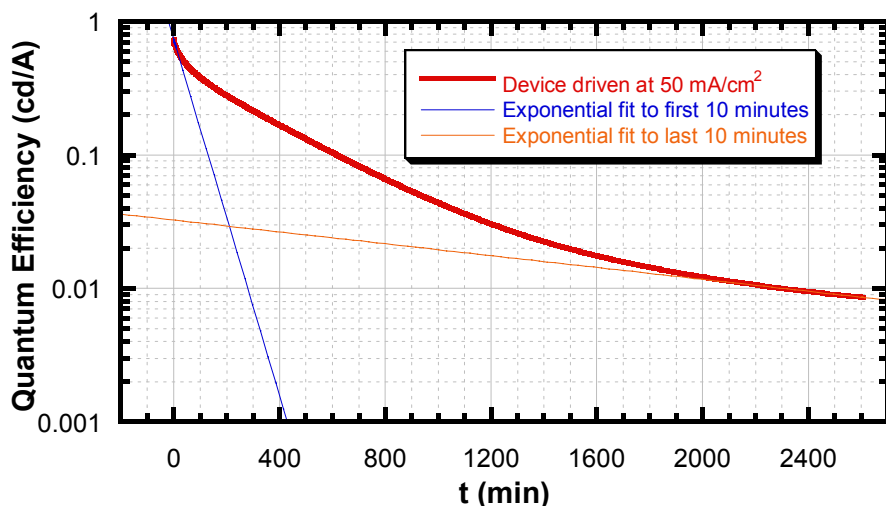


Figure 6.10: External Quantum Efficiency of a 70 nm F8BT LED driven at 50 mA/cm^2 for 43 hours.

The device degradation is accompanied by a long-term decrease in the device conductivity. During the course of the measurements shown in Figure 6.10, the drive voltage required to maintain constant current increased from 3.36 V to 3.90 V. If the degradation is permanent, subsequent drive cycles on the same LED should not suffer from the catastrophic 65-minute initial lifetime seen initially.

6.3.3 Presence of recovery and re-measurement of time to peak

Whilst degradation is expected to be a permanent, irreversible effect, re-measurement of the 10 mA/cm^2 pixel (from Figure 6.9) shows that the enhancement effect is recoverable. Figure 6.11 shows the light output

from the pixel, both in the original experiment and in a repeat measurement, made after resting the device for 3 days. The data show decisively that the degradation process carries on exactly where it left off, whilst the enhancement has been “reset” by resting the device, and begins again from scratch.

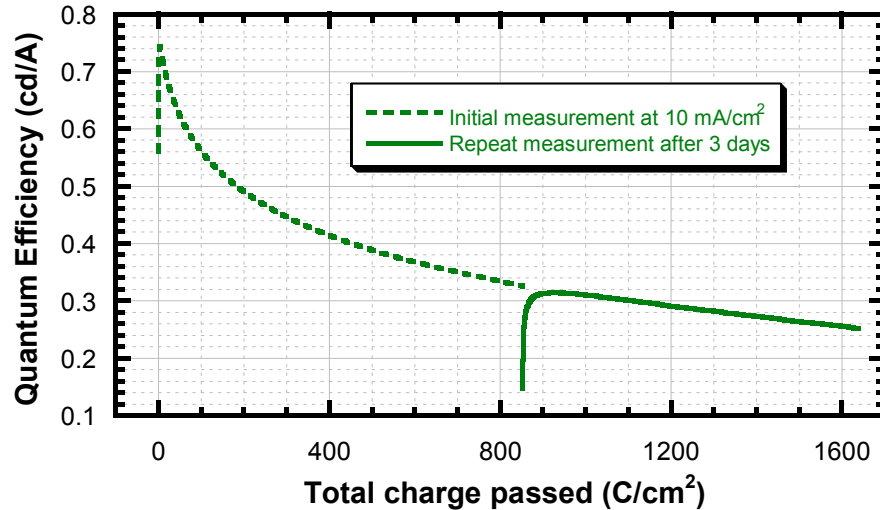


Figure 6.11: 10 mA/cm² pixel (from Figure 6.9), original data and re-measured after 3 days, showing permanent degradation and recoverable enhancement. Time (integrated charge) is plotted on a linear axis.

Intriguingly, although the *relative* increase in quantum efficiency due to drive-induced enhancement is much greater the second time around, the *absolute* increase is almost identical in both cases. This suggests that there may be two completely separate channels at work. The main route to electroluminescence does not experience enhancement, but does experience significant degradation, whilst a secondary channel exists which is at first relatively insignificant, but since it does not suffer from such serious degradation comes to dominate the electroluminescence at later stages of the device’s lifetime. This may indeed help to explain why the degradation curve of F8BT LEDs, as seen in Figure 6.10, is not a single exponential function. Clearly, though, as seen in Figure 6.10, degradation must eventually overcome even the portion attributable to enhanced luminescence, since that curve does not hit a floor at 6.0 % of the original luminance, which was the extent of enhancement seen initially in that experiment.

Re-measurements of the other two pixels used in Figure 6.9 confirm the reversibility of the drive-induced enhancement effect. All three pixels were eventually re-measured, at least 3 days after the first measurement. For direct comparison between the three pixels, all were tested this time at 10 mA/cm². Figure 6.12 shows the results, with the same colours used to identify the pixels as before.

These curves illustrate several points. First, the total charge required before onset of degradation has significantly increased, from approximately 3 C/cm² in the initial measurements to around 70 C/cm². This is

consistent with the observation that, in a degraded device, the degradation lifetime is much increased. At short times, the enhancement effect dominates.

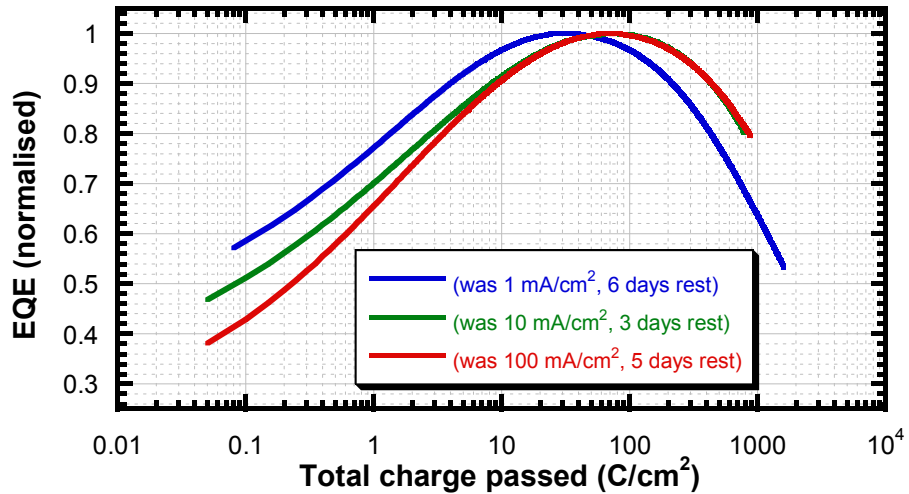


Figure 6.12: Second drive cycle showing re-occurrence of the enhancement effect on pixels from Figure 6.9. All three pixels driven this time at 10 mA/cm^2 .

Secondly, it is seen that the pixel previously driven at 1 mA/cm^2 peaks after about 30 C/cm^2 – significantly earlier than the other two. Figure 6.9 showed that during the initial drive, this pixel experienced approximately one third of the total charge flow seen by the other two pixels, and thus degraded less. Once again, this shows how the onset of degradation is the determining factor for the peak position in an enhancement measurement. Correspondingly, the rise achieved on re-driving this pixel is smaller than the other two, since degradation truncates the enhancement effect sooner.

Thirdly, of the two heavily-driven pixels, one appears to have recovered more than the other. This more-recovered pixel was rested for 5 days, compared to only 3 days for the less affected one. This suggests that the time-scale for recovery of the effect is very long indeed, and this issue is addressed next.

6.3.4 Timescale of recovery

For the following measurements, it was vital that degradation play as small a part as possible in the measurements on the device. Therefore, a heavily degraded device was used, where the subsequent degradation would be minimally significant. A series of measurements were made on the same 70 nm thick F8BT LED previously used for the 99 % degradation trace in Figure 6.10. The data were collected by repeatedly driving the device at 50 mA/cm^2 , each time until the device reached its peak quantum efficiency, incorporating various rest periods between cycles.

Before the first measurement (and immediately after the experiment shown in Figure 6.10) the device was rested for precisely 1 minute by momentarily switching off the constant current source. Data collection was re-started as soon as the drive current recommenced. Subsequent measurements were taken in a similar manner, with rest periods of 5 seconds, 1 second, 10 minutes, 20 hours and 100 hours, seen in Figure 6.13. Crucially, any further degradation of the device was minimised by halting the experiment as soon as the peak value had been reached. Once again, constant current drive served to isolate the quantum efficiency changes in the LED, ignoring the temperature-dependent effects observed in constant voltage drive.

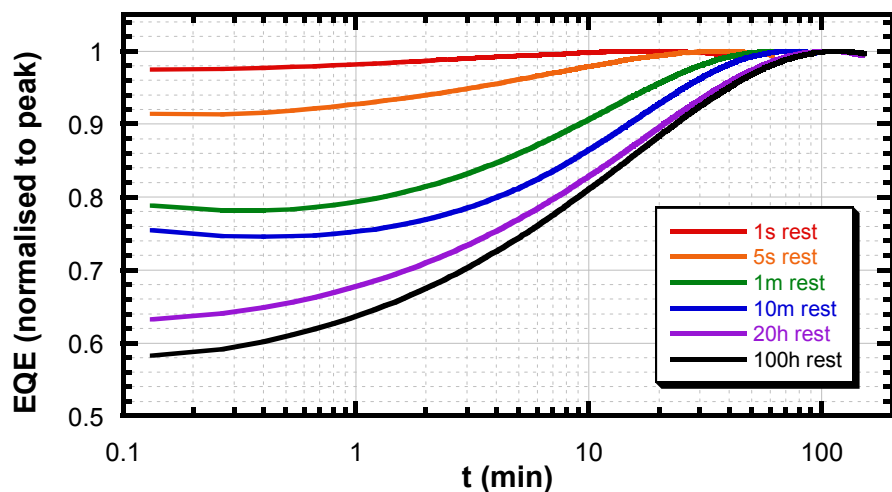


Figure 6.13: A series of successive constant-current (50 mA/cm^2) drive cycles, separated by varying rest periods. The logarithmic time axis helps to show the turn-over point where a peak is reached.

The experiment shows that the quantum efficiency recovers towards its undriven state upon resting of the LED, continuing to do so for a significant period of time. In this case, approximately half the recovery takes place in the first minute, but even after 20 hours recovery is still taking place. During recovery, the quantum efficiency of the device gradually drops, and the amount of subsequent driving required to return it to the peak gradually increases. Note that the data were collected in the order specified above, and not sequentially from “1 second rest” up to “100 hours rest”. This ensures that the progression of time-to-peak is not simply due to the advancement of device degradation, which as seen in Figure 6.12 could have the same effect.

Figure 6.14 shows the same data again, but with a time offset added, such that the peaks of all 6 data sets coincide. In this way, the final stages of the drive-induced enhancement process can be compared as a function of the rest period used. The data show that the recovery process is not equivalent to a time-reversed back-tracking of the enhancement. If it were so, these curves would all lie over one another and the final stages of approach to peak quantum efficiency would always be the same. This implies that the enhancement does not involve a collection of identical states, which would de-populate or reset with equal

probability. Instead, for very short rest periods the subsequent increase in efficiency is rather steep, whilst for very long rest periods, the device approaches its peak much more slowly. This can be thought of as a “first-in first-out” behaviour, indicating a distribution of activation energies for the enhancement and recovery processes. For short rest periods, only the sites with low activation energy are able to recover, and these are correspondingly fast to become enhanced once again on re-application of the drive current. Higher activation energy sites take longer both to enhance and to recover.

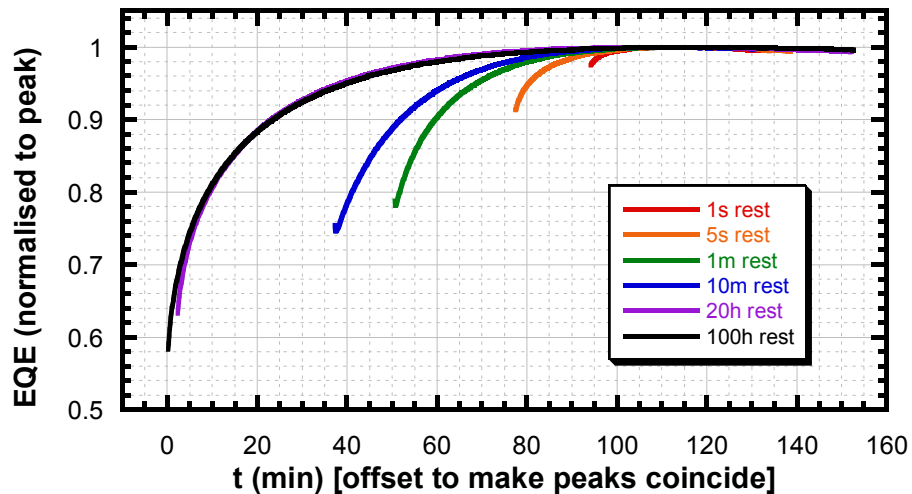


Figure 6.14: The same data as in Figure 6.13, with a time offset added to allow direct comparison of the peaks.
Linear time axis gives equal weight to all data sets.

A third representation of the same data, in Figure 6.15, shows the data sets consecutively in the order of measurement, with the tail end of the original degradation cycle approximately extrapolated by a single exponential fit.

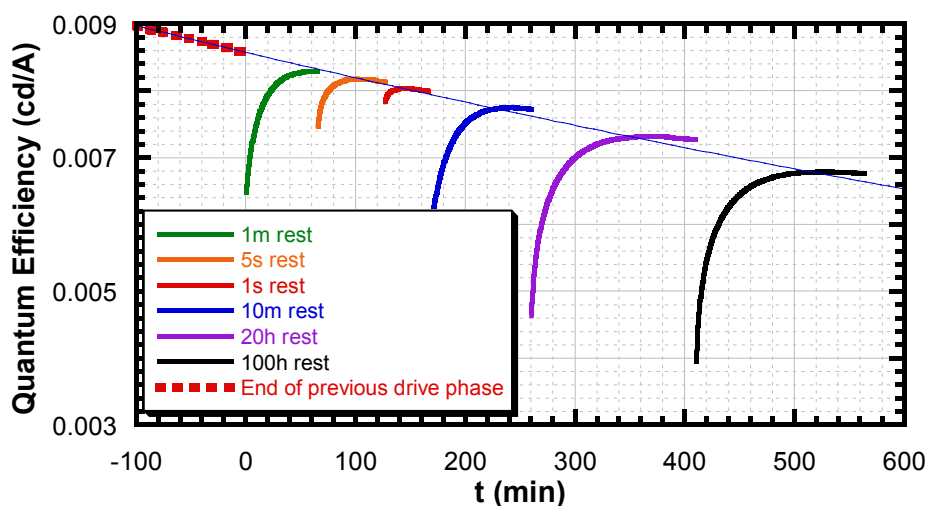


Figure 6.15: The same drive cycles as above, plotted sequentially without normalisation.
The tail end of the pre-drive cycle is also shown, extrapolated with a single exponential fit.

The data show an excellent fit to the ongoing degradation curve, which as previously seen has an exponential lifetime of approximately 2000 minutes. The marginal outperformance at later times can be explained with reference to the original degradation curve of F8BT (Figure 6.10) which shows the decay lifetime continually increasing. The data shown here are thus entirely in agreement with the trend for the device.

One might assert that the apparent progress of recovery beyond 20 hours is an artefact of the continuing degradation in the LED. Thus the reduction in terminal efficiency would make the enhancement seem proportionately larger when the data are normalised. Figure 6.16 therefore shows plots of the absolute change in luminance as measured by the Test Box photodiode. The data show that despite the ongoing degradation after the 20 hour test, the total amount of luminescence attributable to enhanced emission in the 100 hour test is still greater. This proves conclusively that recovery is not complete after 20 hours.

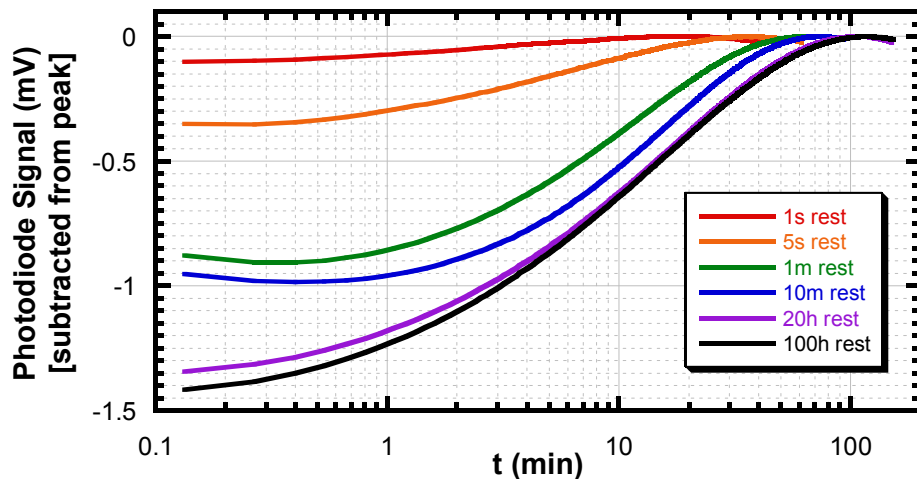


Figure 6.16: Absolute changes in luminance during the same experiments.

6.3.5 Summary of findings

Following these experiments, a number of further characteristics have been revealed.

- Under constant current drive, the long-term degradation of the device begins with a rapid decay in quantum efficiency. The lifetime for the degradation process lengthens significantly as the device ages, so the relative resilience of the device to degradation can be increased by electrical driving.
- The portion of the total electroluminescence introduced by the effect is very resilient to the early degradation processes. As seen in Figure 6.11, even when the underlying electroluminescence quantum efficiency has degraded by 75 %, the absolute additional quantum efficiency realised through enhancement is virtually unchanged. The effect is eventually subject to degradation.

- The observed end of enhancement is usually determined by the onset of degradation, which competes for influence on the total quantum efficiency. Testing of heavily degraded devices, with longer decay lifetimes, can reduce this effect.
- Whilst degradation is irreversible, enhancement recovers spontaneously when the drive current is removed. Recovery is 50 % complete in about 1 minute, but continues to proceed beyond 20 hours.
- Short periods of recovery are followed by a very steep return to saturation when the current is re-applied. Longer periods of recovery lead to a much shallower run-up towards saturation. The data suggest a distribution of activation energies, with some states readily set and reset, and others requiring a much longer time period for a successful change of state.

6.4 Photoluminescence efficiency and light-assisted recovery

The electroluminescence quantum efficiency of an LED depends on a number of factors, but in the most general way can be expressed as in Equation 6.1.

$$\eta_{EL} = \gamma \cdot r_{st} \cdot \eta_{PL} \cdot k \quad (6.1)$$

γ is the exciton formation efficiency (per charge passed through the device)

r_{st} is the singlet-triplet ratio

η_{PL} is the radiative efficiency, including photonic and quenching effects

k is the outcoupling efficiency

Thus, the radiative efficiency is a direct contributor to the electroluminescence efficiency. This section describes the investigation of this property.

6.4.1 Radiative efficiency

The radiative efficiency is the probability that a singlet exciton will undergo radiative recombination to emit a photon. Generating the singlet excitons by photoexcitation, relative measurements can be straightforwardly made by using the PL microscope (Section 3.3.4) and recording the photoluminescence intensity before and after changes have been made to the device.

A 115 nm F8BT device was placed on the microscope stage and connected to the constant current source. An initial photoluminescence measurement was taken, using low intensity blue illumination, followed by an

electroluminescence measurement at 10 mA/cm^2 . The device was then driven for 60 seconds at 100 mA/cm^2 , to force enhanced emission to take place. Another pair of PL and EL measurements were then recorded. Figure 6.17 shows the results. The data show a significant increase in the electroluminescence intensity at constant current, of approximately 40 %. The true increase was in fact larger, since once again the electroluminescence intensity was seen to increase in the seconds before the first measurement was recorded. Meanwhile, the photoluminescence intensity is almost unchanged. The observed increase of 0.9 % is well within the temporal fluctuations of the mercury lamp excitation source.

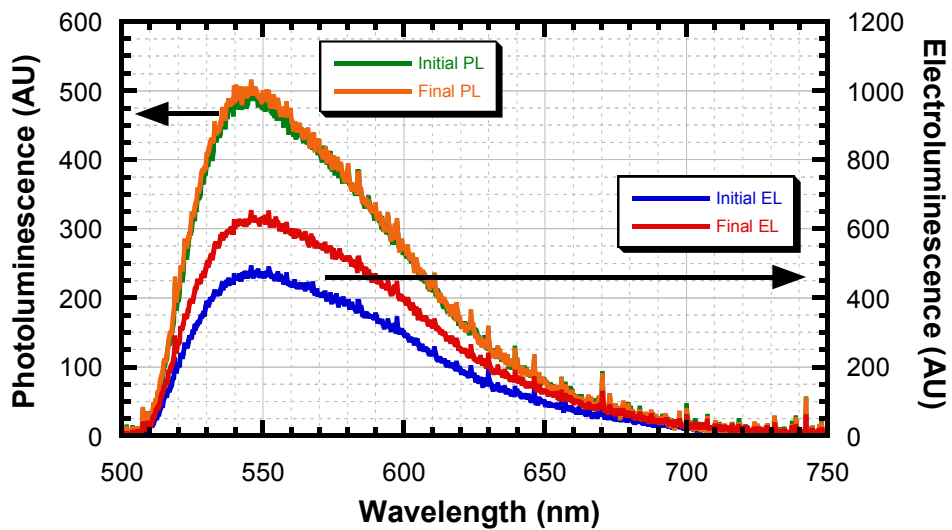


Figure 6.17: PL and EL before and after driving at 100 mA/cm^2 for 60 seconds.
PL measured under weakest intensity blue illumination. EL measured at 10 mA/cm^2 .

Therefore despite the sizeable increases in EL quantum efficiency, the PL efficiency is unaffected. One possible cause is the difference between the regions of polymer probed by the EL and PL efficiency measurements. The PEDOT:PSS/F8BT/Ca system's recombination zone is pinned strongly to the anode side of the device. This is because there is no barrier for electron injection from calcium into F8BT, and a relatively high electron mobility, coupled with a hole injection barrier of at least 0.8 eV at the anode and a relatively low hole mobility. Thus an F8BT device would be expected to be space-charge limited for electrons and injection limited for holes¹⁹. All injected holes should recombine within a very short distance of the anode, leading to emission within one exciton diffusion length, approximately 10 nm^{20} , of the anode.

The extent to which PL probes the polymer bulk can be calculated. The absorption coefficient determines the rate of attenuation of the probe beam intensity with depth. When significant intensity reaches the metal mirror formed by the cathode, optical interference becomes important. In order to calculate the probe intensity profile for the 115 nm device studied here, the absorption coefficient must first be found. Figure 6.18 shows the absorption spectrum of a 62 nm F8BT film spun on Spectrosil-WF, in the region of interest. The measurement was made on a HP8435 UV-Vis absorption spectrometer as described in Section 3.3.2.

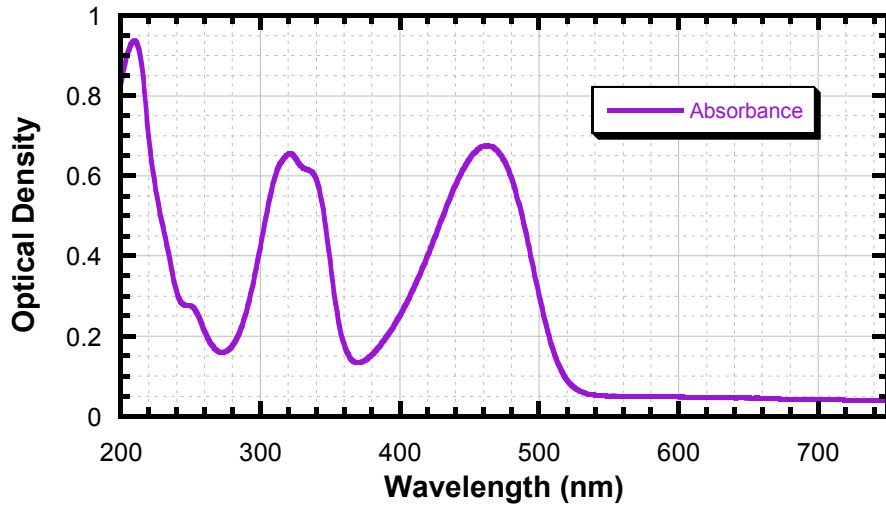


Figure 6.18: Absorption spectrum of a 62 nm F8BT film, using the UV-Vis spectrometer.

The blue illumination from the microscope is around 465 nm, where the optical density of the film is approximately 0.67. Equation 6.2 gives the relationship between optical density and absorption coefficient.

$$\alpha = \left(\frac{OD}{d} \right) \cdot \ln(10) \quad (6.2)$$

Taking the optical density, OD , as 0.67 and film thickness, d , as 62 nm, the absorption coefficient α for F8BT in this spectral region is given as $2.5 \times 10^7 \text{ m}^{-1}$. This is a thickness-independent property of the material. Equation 6.3 yields the fraction of the incident power penetrating the film.

$$T = e^{-\alpha d} \quad (6.3)$$

Taking the calculated absorption coefficient, and the film thickness this time as 115 nm representing the LED, the transmitted light, T , reaching the back surface of the film is approximately 5 % of the incident power at $\lambda = 465 \text{ nm}$. Therefore the contribution due to reflection off the back cathode can to a first approximation be disregarded, along with the associated interference effects. The depth profile of the probe intensity is then simply an exponential decay, with the intensity falling by approximately 25 % in the top 10 nm of the polymer, calculated from Equation 6.3.

Thus whilst EL probes predominantly the top 10 nm of the polymer layer, around 25 % of the PL occurs in the same region. If the EL efficiency increase is caused by an increase in the radiative efficiency, even if it is localised near the anode, this should be measurable by a PL experiment. No such change is observed in the PL behaviour, so the change in EL efficiency is not attributable to a change in the radiative efficiency of singlet excitons in the polymer.

6.4.2 Light-assisted recovery

During the PL measurements, another feature of the drive-induced enhancement effect was noted. After prolonged excitation from the mercury lamp, the subsequent electroluminescence efficiency was significantly diminished. This was most clearly seen when the illumination iris was partially closed, so that only a portion of the pixel was illuminated. More intense illumination yielded a more rapid diminution of the electroluminescence. It is important to note that all genuine PL measurements presented in this Chapter were recorded using very brief illumination at low intensity, such that no noticeable reduction in efficiency was caused by the measurement itself. Figure 6.19 shows the emission from a 100 nm F8BT device in normal EL mode, in EL with a localised spot of photoexcited luminescence, and in EL+PL after 30 seconds of illumination. The reduced luminescence is clearly visible. The current density was 100 mA/cm^2 , at which the device had been previously measured to produce 2500 cd/m^2 .

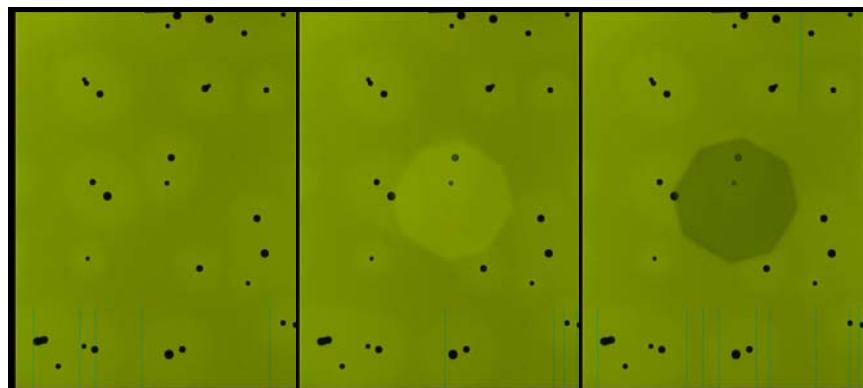


Figure 6.19: (a) Initially the device, driven at 100 mA/cm^2 shows a scattering of non-emissive black spots. These are present from the time of fabrication, and are believed to be caused by microscopic holes in the cathode²¹.
(b) At the onset of UV excitation, the sum of EL and PL components is slightly greater than the EL alone.
(c) Within 30 seconds, the total emission from EL and PL combined is less than the surrounding EL.

Photo-oxidation is an important degradation path for polymer LEDs, and commercial applications particularly in the automotive industry will certainly require UV filters to protect the polymer layers. Indeed Chapter 4 elucidated a photoactivated degradation mechanism at the electroluminescent polymer interface with PEDOT:PSS. Photodegradation is a permanent effect, resulting in chemical changes in the polymer. The observed reduction in electroluminescence efficiency seen in this experiment was however reversible on continued driving of the device, and after a period of time which varied with the drive current applied, the negative image of the illumination spot completely disappeared. Figure 6.20 shows the same area of the LED as Figure 6.19, but shifted slightly upwards. The photoexcitation remains in the centre of the pixel, and the upper spot brightens under electrical driving. The effect observed by illumination of the LED is not photo-oxidation, but rather a reversal of the drive-induced enhancement effect. Illumination of the polymer layer after enhancement forces the device to recover to its low quantum efficiency state.

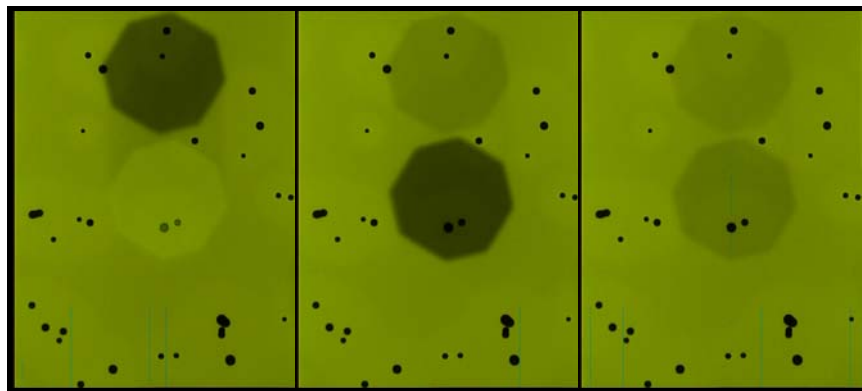


Figure 6.20: (a) After precisely 2 minutes of illumination seen in Figure 6.19, the device is shifted ‘upwards’, illuminating a new spot (central), revealing the first spot in EL-only and leaving a partially exposed trail between the two. (b) After another 2 minutes, the illumination is switched off. The two spots have each been photoexcited for 2 minutes, but the upper spot has been subsequently driven for 2 minutes. (c) After 2 more minutes, both dark spots have substantially progressed towards matching the surrounding EL.

A quantitative experiment was performed on a 100 nm F8BT LED. The LED was driven from its pristine state at 10 mA/cm^2 , exposed to intense UV at 360 nm (2.3 mW/mm^2) and measured at several stages. Although the polymer absorption coefficient is only one-third as large at this wavelength (compared to the blue previously used), the illumination intensity from the mercury lamp is more than 20 times greater. Figure 6.21 shows the results. The data for the first 5 minutes show a very clear progression in the electroluminescence, with the quantum efficiency seen to more than treble in this time. Exposure to strong UV for one minute resets the quantum efficiency almost to its initial state, and this increases once again with further driving. The microscope is not equipped with a facility for red illumination, but a 633 nm, 10 mW HeNe laser with spot size approximately 1 mm^2 was shone onto the LED, which failed to induce recovery of the LED. This power intensity is four times greater again than the UV illumination.

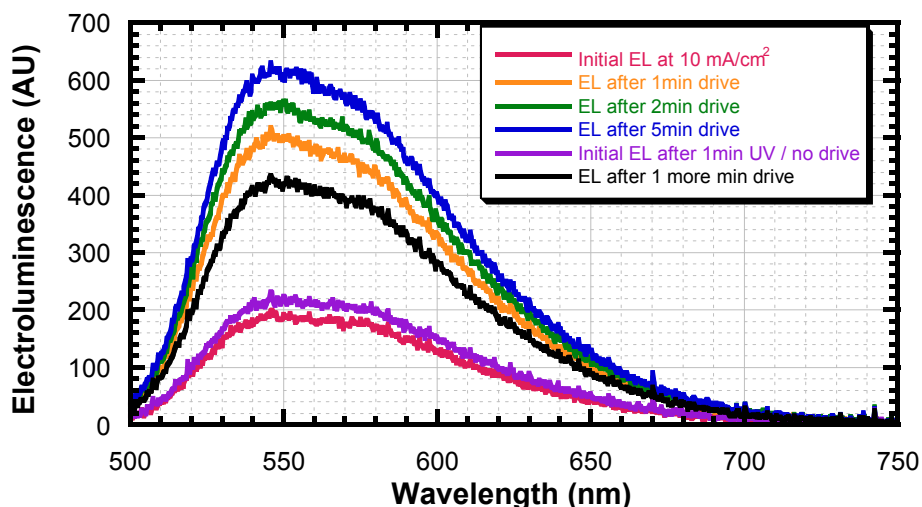


Figure 6.21: A series of electroluminescence measurements, before (red) and during (yellow, green and blue) the effect. Also, the EL after one minute of UV exposure (violet) and after another minute of drive (black).

There are two possible mechanisms to rationalise this finding, which cannot at this stage be distinguished. The question rests on the exact cause of recovery: indirect thermal activation or direct excitation by individual photons above a threshold energy. At first sight, it seems that light above the bandgap is required to induce recovery. However, analysis of the thermal power dumped into the LED shows that thermal heating due to the band-gap absorption may be indirectly responsible. Light above the band-gap is strongly absorbed, and even accounting for F8BT's high PL efficiency of 80 %, 20 % of the absorbed light is dumped as heat into the polymer layer. A further 20 to 25 % of the remaining energy is also lost as thermal relaxations in the polymer before and after emission. This equates to 40 % of the absorbed light, or approximately 90 mW/cm², since the optical density of the film even at this wavelength ensures that the majority of the incident light is absorbed. The Joule heating due to driving is rather less, at approximately 30 mW/cm² under the conditions used here to drive the device. Conversely, with red illumination which falls below the band-gap, only a tiny proportion of the incident light is absorbed and converted to heat. Photothermal deflection spectroscopy measurements²² have shown that the thermal yield due to F8BT absorbing in the red is at least 3 orders of magnitude below that in the π - π^* absorption. Thus despite the greater intensity of red illumination, the power dumped into the polymer layer from this source is much less than 1 % of that in the case of UV. It is therefore impossible to state on the grounds of this data whether the reset phenomenon is activated by single photons above the bandgap, or simply by their heating effect on the polymer.

6.4.3 Summary of findings

- Radiative efficiency is unaffected by the drive-induced enhancement effect
- The enhancement is reset by certain schemes of illumination
- Data cannot yet differentiate the cause of light-assisted recovery between:
 - thermal activation due to heating and
 - directly induced recovery by interaction with photons above a threshold energy

6.5 Spectral changes

Since the radiative efficiency of photogenerated singlet excitons is unaffected by the enhancement effect, it is important to determine whether some other radiative channel is activated by the effect. This may be typified by a different spectral signature, and spectral analysis will allow any such change to be identified.

6.5.1 Electroluminescence changes due to drive-induced enhancement

The data in Figure 6.21 were re-analysed to identify changes in the EL spectrum before and after driving, and after resetting by UV illumination. Figure 6.22 shows the normalised EL profile before and after driving. F8BT has at least two independent emissive species, at 2.11 and 2.27 eV, and it appears from the data that the bluer species has increased relative to the redder one. This may indicate a real rebalancing of the emissive species, or be due to an optical effect caused by a shift of the recombination zone within the device. However the noise present in this data set make a full spectrally-resolved comparison difficult.

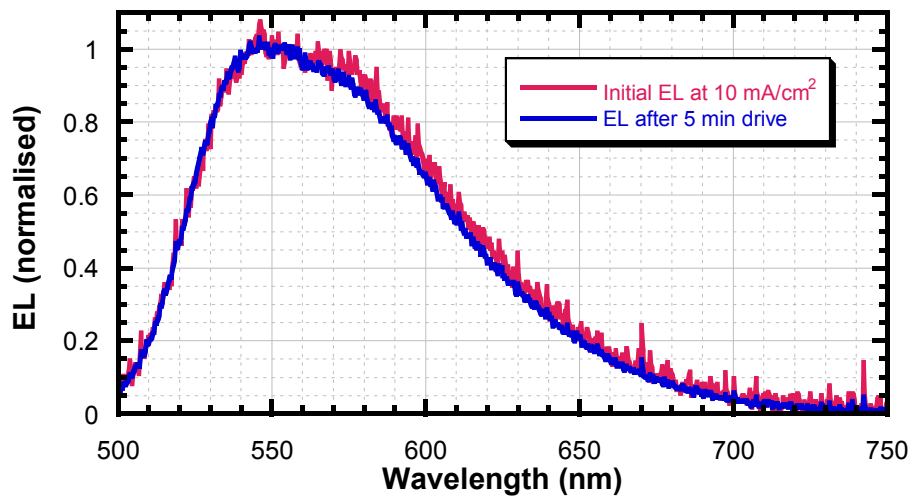


Figure 6.22: Electroluminescence before and after enhancement, normalised between 550 and 555 nm.

Figure 6.23 shows the measurements taken after UV exposure. The same trend is seen but to a lesser degree. It is possible that the changes seen in the first case were due to heating in the LED, and that during this second cycle the already-heated LED does not experience such a large thermal change.

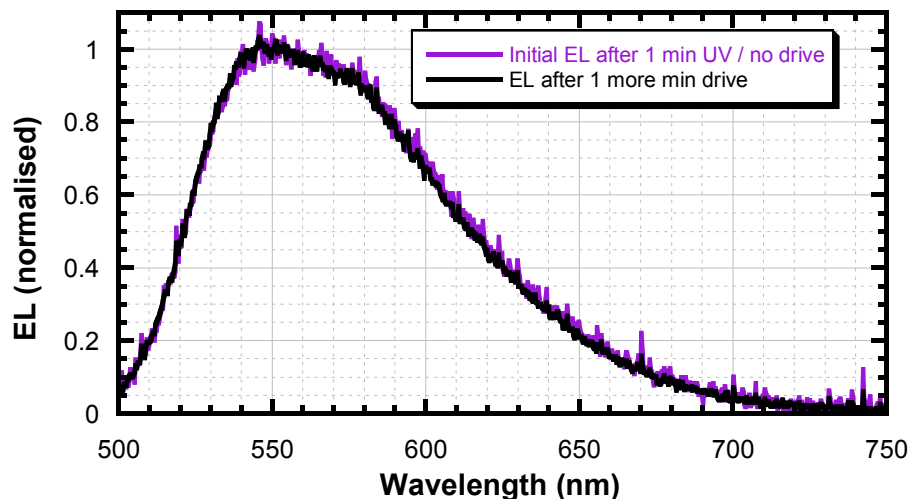


Figure 6.23: Normalised electroluminescence at 10 mA/cm² following UV excitation to reset the effect.

In order to determine whether the changes in spectral weighting are correlated with the changes in absolute intensity (quantum efficiency), a number of values are tabulated in Table 6.4. Two measures are used to quantify the state of the LED. The EL intensity at 615 nm relative to that at 550 nm gives a measure of the spectral shape of the emission. (The relative intensity at 615 nm was found by fitting a straight line between 600 and 630 nm.) The absolute intensity at 550 nm gives a measure of the progress of the effect.

		First Cycle	Second Cycle	Relative size of change in 2 nd vs 1 st
Relative intensity at 615 nm vs 550 nm	Before driving	0.519	0.520	48 %
	After driving	0.482	0.501	
	Change	-7.60 %	-3.67 %	
Absolute intensity at 550 nm (AU)	Before driving	187	217	41 %
	After driving	612	421	
	Change	+228 %	+94 %	

Table 6.4: Comparison of changes in peak intensity with changes in relative spectral weightings.

The data show that the shift in spectral shape was only 48 % as large after the second cycle, compared to the first, while the change in absolute EL intensity was 41 % as large in the second case. The two figures compare favourably, indicating that the LED changes in the second cycle are consistent with both a spectral re-weighting and an efficiency increase of around 45 % that seen in the first cycle. The spectral shift which appeared negligible in Figure 6.23 is well correlated with the degree of enhancement observed, and no other phenomenon, such as heating, is required to make the data agree. Additionally, the top row of data in the table indicates that after the UV recovery process, the spectral shape is almost identical to that in the pristine LED when first driven. This contradicts any suggestion that physical heating (Joule heating or absorbed light) is responsible for the spectral changes during electroluminescence, since the UV illumination during the reset cycle has been shown to provide heating at even higher levels than the electrical driving of the device.

As noted previously, noise levels were too high in the data presented to reliably calculate the relative spectral change as a strict function of wavelength. Therefore, another device was analysed, using deliberately extended integration times to minimise the presence of random noise. Figure 6.24, obtained by dividing the EL spectrum after 15 minutes of driving at 10 mA/cm² by that from before, shows a relatively featureless slant, with a possible very broad peak extending from 600 to 700 nm. The lack of well-defined features at the two main emissions of F8BT suggests a lack of any real rebalancing between the two modes.

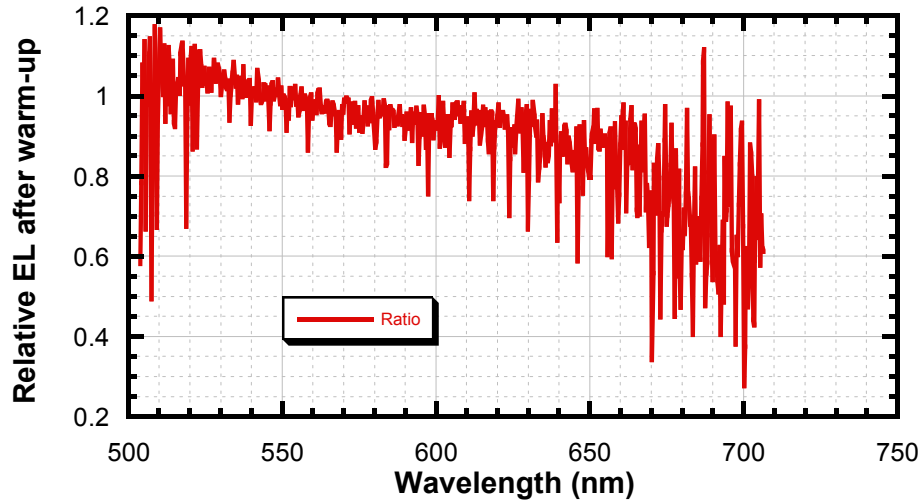


Figure 6.24: Relative changes in spectral intensity of EL after 15 minutes at 10 mA/cm^2 .

Furthermore, modelling work conducted by Dr P.K.H. Ho of the Cavendish Laboratory²³, which takes into account not only optical but also quenching mechanisms at metallic surfaces, suggests that the increase in spectral weighting in the blue part of the spectrum is consistent with a small shift in the recombination zone away from the anode. This is logically consistent, since the only possible direction that the recombination zone could move is away from the anode, at which it is otherwise well localised.

6.5.2 Electroluminescence changes due to thermochroism

Conjugated polymers are subject to thermochroism, whereby temperature changes cause changes in the luminescence spectrum²⁴. To compare thermochroism to the spectral changes observed, the same LED was cooled *in situ* and re-measured. Due to the physical constraints of cooling the LED on the microscope stage, a crude but effective method was employed. After measuring the initial EL spectrum (following 15 minutes' enhancement at 10 mA/cm^2 , at an ambient temperature of approximately 25°C), a can of compressed air was used to cool the exposed glass surface of the device. Inverting the can causes liquid propellant to be expelled, which deposits on the glass and quickly evaporates, cooling the whole device. Within seconds, the device was sufficiently cool to cause liquid water to condense on the surface. This was wiped away, and the compressed air can used upright to provide a stream of dry air, preventing further condensation and any associated light scattering from the surface. The electroluminescence spectrum was now re-measured, at an estimated temperature of 5°C . Figure 6.25 shows the relative change in EL spectrum on cooling the device. The observed changes in the spectrum are qualitatively different from those in Figure 6.24. (If thermochroism was responsible in both cases – heating previously and cooling in this case – the two graphs would be mutually reciprocal.) In the case of cooling the LED, a significant feature is observed where the high-energy emission is curtailed. This shows that the spectral changes due to thermochroism are not consistent with and cannot account for the changes observed during enhancement.

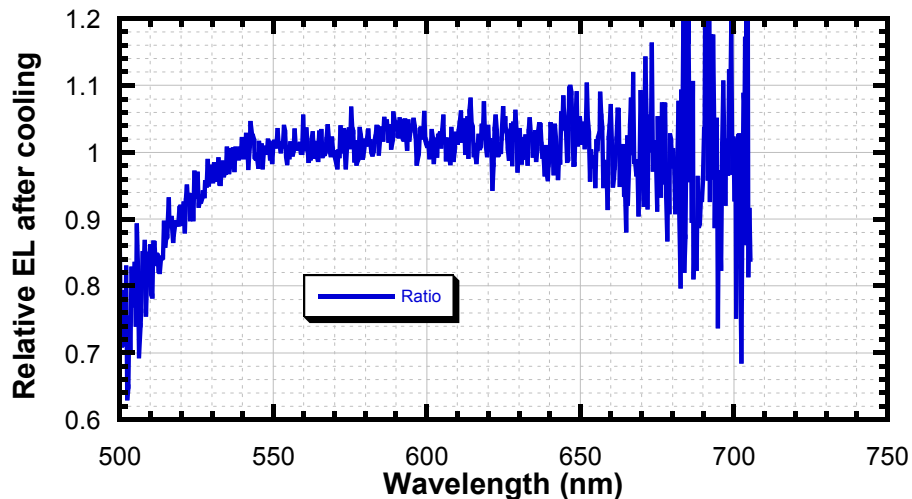


Figure 6.25: Electroluminescence at ~ 5 °C divided by electroluminescence at ~ 25 °C.

6.5.3 Photoluminescence changes due to drive-induced enhancement

It has already been demonstrated that the total photoluminescence efficiency is unchanged by the enhancement effect. If the changes in the EL spectrum are really due to a shift in the recombination zone there should be no change in the PL spectrum, which is produced by photogenerated excitons. The same two PL spectra shown in Figure 6.17, before and after driving, are used to produce a plot of the relative change in PL intensity as a function of wavelength, shown in Figure 6.25. In comparison with the changes in electroluminescence, any spectral shift or skew in the photoluminescence appears to be negligible. A slight negative skew is visible, but a linear fit to the relatively low-noise region between 520 and 650 nm shows that the gradient of the skew is at least 60 times smaller in the case of PL. (The R^2 correlation coefficient for the linear fit in EL was 0.8, but in PL just 0.3, suggesting only a weak correlation here.)

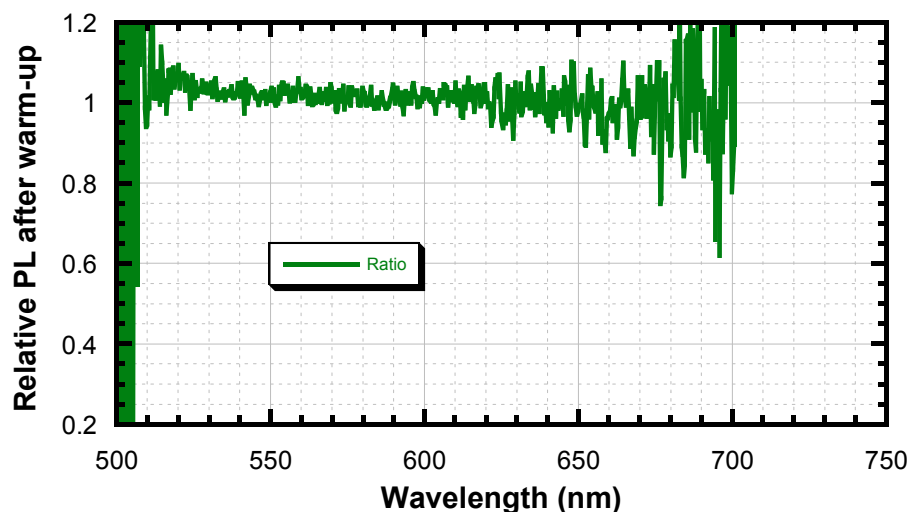


Figure 6.26: Relative change in PL under blue illumination after enhancement. Axes identical to Figure 6.24.

It is important to determine whether this faint “echo” of the skew seen in EL is indeed real. Such a feature could arise due to partial overlap of the emission sites probed in EL with those probed in PL. This might be particularly true if the EL were known to be strongly confined to a layer within the polymer, whilst the PL probed the entire bulk. Once again, however, it is important to note that an overlap of around 25 % between PL and EL is expected. Therefore, the lack of a significant effect on the PL spectrum cannot be attributed to spatial separation of the EL and PL regions of the polymer. Consequently, it can be concluded that the PL spectrum, like the PL efficiency, is essentially unaffected by the drive-induced enhancement effect.

6.5.4 Summary of findings

- The electroluminescence spectrum experiences an almost featureless skew in favour of short wavelengths, as the drive-induced enhancement effect progresses
- Thermochroism cannot explain the observed spectral changes
- The skew is consistent with a small shift of recombination zone away from the anode
- The photoluminescence spectrum appears to be unaffected, even though PL and EL overlap significantly in terms of the sites they access
- No new emissive states are generated by drive-induced enhancement, nor are the emissive properties of the existing sites significantly modified

6.6 Charge backflow and thermal activation

It has been seen that the spectral changes in electroluminescence do not indicate the introduction of any new emissive states, nor the modification of any existing emissive sites. This suggests that changes at the interfaces, altering the charge injection balance, are likely to be responsible for the observed phenomena. Having seen that the effect occurs independently of cathode and anode choice, it is most likely that any interfacial changes take place just inside the polymer layer itself, rather than in any physical or chemical interaction with the respective electrode. An obvious candidate for reversible changes in a disordered semiconductor such as a conjugated polymer is charge trapping (see Section 2.4.7). An experiment was therefore performed in the Test Box to analyse post-driven LEDs for the release of trap charge.

6.6.1 Charge backflow

The Test Box (Section 3.4.5) was connected to the constant current source, to drive a 70 nm F8BT LED at 1 mA/cm^2 . After 48 hours of driving, when the quantum efficiency had increased to 200 % of its initial

value and fallen back to +130 % due to degradation, the current source was disconnected and a digital electrometer attached in its place. The measured charge as a function of time is shown in Figure 6.27

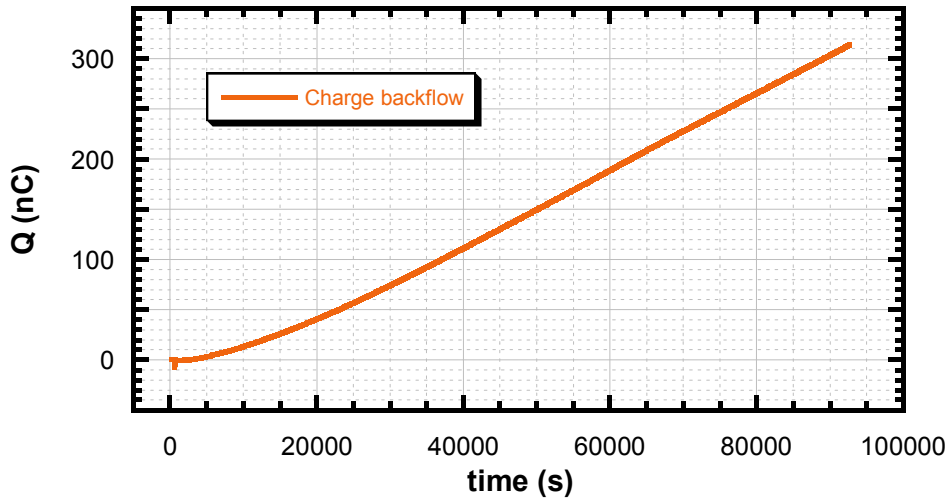


Figure 6.27: Accumulated charge flow registered by electrometer after driving the device.

The data appear to show two effects superimposed: a positive linear drift possibly due to the electrometer's own characteristics, and a decaying contribution following some other functional form, which may be representative of the charge actually released from the LED. The behaviour of the electrometer was separately tested using a passive resistor in place of the LED. This confirmed the electrometer-drift hypothesis, by revealing a drift that was extremely close to linearity. The electrometer output can therefore be summarised as a measure of the total charge flowing out of the test LED, superimposed over an underlying systematic drift. The constant drift can be subtracted by fitting the long-term behaviour to a straight line.

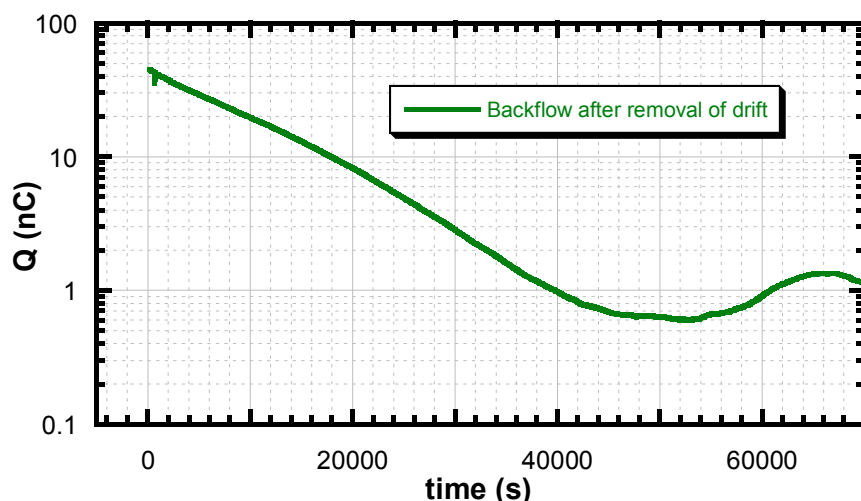


Figure 6.28: Charge backflow from LED (same as Figure 6.27), after subtraction of the linear drift.

Shows the total charge remaining inside the device as a function of time.

Fitting the data from Figure 6.27 to an exponential decay plus a linear drift produces an excellent fit at early times, but becomes dominated by low-level fluctuations as the signal diminishes in magnitude. The early portion of the data, with the drift removed, is shown in Figure 6.28. The *y*-axis shows a signal which decays towards zero as charge flows out of the device. Thus at any given time, the value of the function represents the *total charge remaining inside the device*, and at time zero the charge stored initially can be read off.

The deviation from exponential decay is apparently due to a temperature increase caused by entering the room where the experiment was running. Small thermal effects in both the test LED and the electrometer led to a deviation of just 1 nC from the trend over the course of the last 8 hours plotted. The current at this time is small enough that such a deviation (equivalent to a current of approximately 30 fA) becomes significant. However, the first 12 hours (~43,000 s) are adequate to achieve a reasonable exponential fit to the data. Analysis of the sense of charge flow confirms that the observed current is in the reverse direction to that used in driving the device. This is expected from the extraction effect of the built-in voltage on any charge liberated inside the LED, just as observed in the case of polymer photovoltaics when exposed to light above the bandgap. In this case, however, the device remains enclosed in the light-tight box.

As a final check on the attribution of the linear drift to the electrometer itself, the experiment was repeated with the electrometer connected up in reverse. The linear drift (Figure 6.29 inset) was once again present and displayed the same drift direction, whilst the underlying decay was reversed. This further confirmed that the drift was due to the equipment whilst the decay was a real effect. Once again, after subtraction of the drift (Figure 6.29) small environmental fluctuations become significant at late times in the measurement. Additionally, just before 44,000 s, the auto-ranging of the electrometer causes a small glitch in the processed data. A more rapid switch-over from drive to detection in this second experiment reveals an initial fast decay, which was not visible in the previous data set.

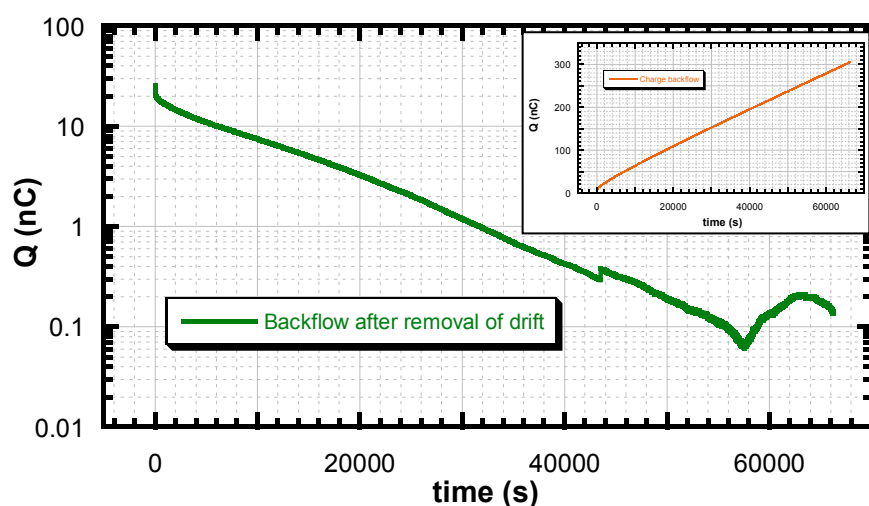


Figure 6.29: Charge backflow with electrometer in opposite polarity. Inset: raw data before removal of drift.

Together these experiments show that charge is liberated from the LED over a period of minutes and hours following the drive cycle. The fast decay during the first hundred seconds, followed by a persistent long tail, is consistent with the timescales described earlier for the persistence of the drive-induced enhancement effect and its recovery.

6.6.2 Magnitude of liberated charge

It has already been described that F8BT LEDs are predominantly space-charge limited in terms of electrons, and contain negligible numbers of bulk holes in comparison. This is a consequence of the favourable injection and transport properties of electrons in F8BT, and of the contrasting situation for holes, and leads to the aforementioned pinning of the recombination zone at the anode. As a result, the bulk of an F8BT LED may be considered to be a unipolar space charge limited device.

In the special case of a unipolar space charge limited device, the maximum charge injected into the polymer layer is given by Equation 6.4^{25,26}

$$Q = \frac{3}{2} CV \quad (6.4)$$

where C is the geometric capacitance of the device and V is the applied bias minus the built-in voltage (V_{bi}) due to the electrode work-function difference. For large biases (negligible V_{bi}) this value is equal to 3/2 times the charge on the equivalent capacitor. The capacitance is given by Equation 6.5

$$C = \frac{\epsilon \epsilon_0 A}{d} \quad (6.5)$$

where ϵ is the relative permittivity of F8BT, ϵ_0 is the permittivity of free space, A is the area of the capacitor and d is the thickness. The injected charge is therefore given in full by Equation 6.6.

$$Q = \frac{3\epsilon \epsilon_0 A V}{2d} \quad (6.6)$$

Pulsed electroluminescence measurements²⁷ and impedance spectroscopy measurements²⁸ have confirmed that d should be taken as the thickness of F8BT layer only, namely 70 nm, and the same impedance spectroscopy measurements²⁸ produce a value for ϵ_{F8BT} of approximately 3.3. The pixel area in the measurements shown was 10 mm². The voltage data gathered immediately before disconnecting the constant current drive indicate an applied voltage of 2.47 V in the first experiment and 2.44 V in the second case. The built-in voltage between calcium ($\phi = 2.9$ eV) and PEDOT:PSS ($\phi = 5.1$ eV) is 2.1 V, leaving net

forward biases of approximately 0.25 V in the two experiments. According to this data, Equation 6.6 states that the total charge present in the polymer layer, in both experiments, should be approximately 1.5 nC.

The discharge graphs in Figures 6.23 and 6.24 provide the total quantity of stored charge, by reading off the y -axis at $t=0$. They indicate releases of 45 and 25 nC, both of which significantly exceed the maximum allowable space-charge inside the device in the unipolar case. It is important to note that all data points in the series are based off the first value collected. This first value therefore provides the “zero-level”, and any charge released before this point – i.e. after the electrometer is switched in and before the first measurement is recorded – is simply disregarded. As a result these experimental figures *exclude* all “instantaneous” charge released from the device, such as fully mobile charge carriers which are known to be predominantly extracted from the device in the first microsecond to millisecond²⁹, and more importantly any capacitive discharge through the low-resistance electrometer which will certainly be complete within a fraction of a second. The figures are therefore not increased by the unwanted contribution from capacitor charge (which in this case would come to only 10 nC anyway) and indeed may underestimate the total charge backflow through the loss of the first seconds of data.

Equation 6.4 is based on the boundary condition that space-charge limited injection ceases when the bulk space charge completely cancels the field. Therefore any trapped charge *is* included in the predicted upper limit for space-charge, since it is electrostatically indistinguishable from mobile charge. Even if 100 % of the charge inside the polymer layer were trapped, this would not be enough to account for the delayed release of charge recorded by experiment.

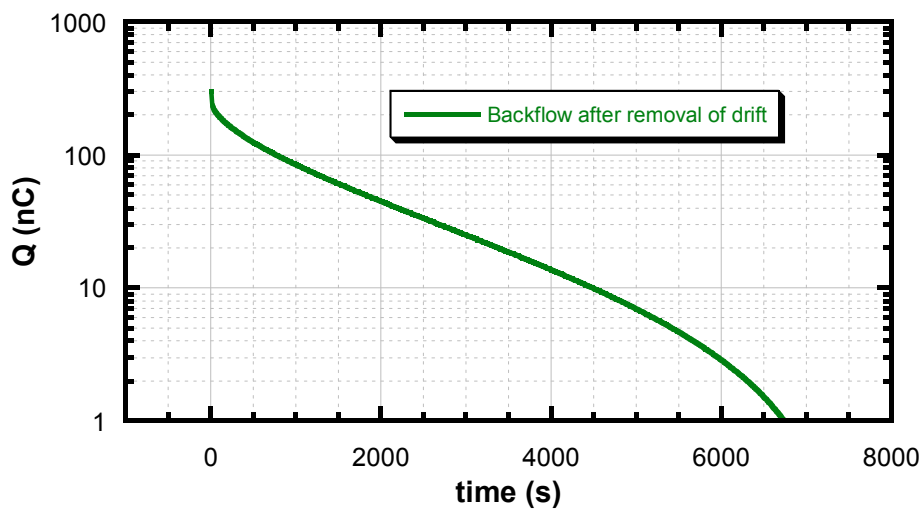


Figure 6.30: Charge backflow measured after fast switching from drive to measurement.

Further experiments confirm the excess of delayed charge released from the LED. In order to better capture data, the set-up was altered so that the LED was driven with the Test Box’s own internal voltage source.

This had the advantage of specifying an exact voltage with which to drive the device. Additionally, the electrometer could be left connected to the external drive contacts of the box, and with the flick of a switch on the front of the box, the device would be disconnected from the constant voltage drive and connected across the electrometer. By manually commencing measurement within a split-second of this event, the absolute minimum of delayed charge would be lost.

Figure 6.30 shows an extreme case. A 50 mm^2 , 70 nm device was driven at 2.7 V for 20 minutes, after which time the quantum efficiency began to plateau. The switch was made from internal drive to external measurement, and data collected.

To obtain an accurate value for the capacitance of this device, rather than calculate it, the device was measured on a HP4192A impedance analyser at 0 V_{DC} , 0.05 V_{\sim} and 100 Hz, and found to have a capacitance of 12 nF. From Equation 6.4, the total charge stored in the polymer, with $V - V_{bi} = 0.5 \text{ V}$ should therefore be approximately 9 nC. However Figure 6.30 indicates a figure nearer to 300 nC – a massive difference which is clearly inconsistent with unipolar behaviour.

Since unipolar charge injection must cease when the space-charge limited condition is reached, the quantity of charge is simply too large to attribute to trapping of majority electrons inside the LED. In order to see an excess of charge stored in the device, the polymer must contain either separately trapped electrons and holes, or some sort of neutral or bound state which decays by releasing these charges.

Holes, when successfully injected into the polymer, find themselves immediately surrounded by a large excess of electron density. If any of these charges are to avoid permanent recombination, they must either become individually trapped in the midst of these electrons, or else combine into a long-lived bound state which cannot access the fast relaxation process of radiative decay. The triplet exciton is one obvious example of such a state, however its lifetime at room temperature is estimated at significantly less than $1 \mu\text{s}^{30,31}$, which does not compare with the timescales observed for recovery of enhancement.

6.6.3 Thermal activation

It was postulated in Section 6.4.2 (Light-assisted recovery) that the observed recovery of the effect may be due either to absorptive heating of the polymer layer or to direct photon-mediated effects. In Section 6.5 it was demonstrated that virtually all the incident light under blue illumination is absorbed by the polymer. Accounting for the PL efficiency and the thermalisation of excitons before they re-emit, this results in up to 40 % of the incident power being deposited as heat in the film. This Section, with its long-term measurements of discharge, has shown the sensitivity of recovery to variations in ambient temperature.

Direct measurements of thermal activation of recovery are complicated because of the difficulty in accurately controlling the temperature of the polymer film, or the time it remains at elevated temperature, while it is concealed behind a relatively thick layer of glass. Nevertheless, a number of very simple exploratory measurements were made to determine whether heating of the LED could lead to recovery of the effect. A device driven through drive-induced enhancement was placed in a drying cabinet at 120 °C for 5 minutes. On cooling to room temperature and re-testing it was found to have recovered to a degree equivalent to more than 6 hours' rest at room temperature. Noting that 120 °C is comparable with the T_g of F8BT of around 115 °C³² annealing to which is known to change the electrical and optical properties of conjugated polymers^{33,34}, the experiment was repeated on another device, heating to only 60 °C. Recovery was seen, to a greater degree than expected from resting alone, but not to the extent recorded at 120 °C.

In order to characterise the thermal response more systematically, a series of experiments were carried out on a single pixel at a range of temperatures. Due to the geometry of the Test Box, and its compact design, the most straightforward way to access a range of temperatures was to place the entire box on a hotplate, and measure the actual temperature attained by use of a thermocouple inserted deep into one of the screw holes in the die-cast box. Whilst this resulted in a severely limited range of accessible temperatures, room temperature was already identified as producing slow recovery on the boundaries of satisfactory measurement, whilst 120 °C would cause responses too fast to usefully measure. Therefore the accessible range, though small, substantially covers the range of interest.

Measurements were attempted at room temperature (21 °C), 35 °C, 50 °C and 60 °C. At elevated temperatures, a large metal block was used as a buffer and heat reservoir between the hotplate and the Test Box, to reduce disastrous temperature surges caused by the hotplate switching. The entire system was raised to its measurement temperature before the drive phase was started, because the time required to stabilise the temperature was so long. The room temperature data has already been presented in Figure 6.29. The actual recorded temperature in that case was 21 °C. Measurements at ~50 °C and ~60 °C yielded good data sets at actual temperatures of 48 °C and 59 °C. However, the 35 °C data proved to be unusable. The relatively long timescale of the experiment, coupled with the switching of the hotplate, led to a temperature which fluctuated by several degrees, producing a jagged data-set which could not be adequately fitted to a curve.

Table 6.5 shows the exponential lifetimes, defined as the time taken for the best fit exponential to reach e^{-1} of its initial value, for the three satisfactory temperatures. As previously discussed, the charge backflow does not consist of a single exponential, even though at long times one exponential comes to dominate. As a result, the apparent exponential lifetime changes as a function of the time-scale under examination. Two lifetimes are therefore listed in each case. The first, τ_1 , includes all good data (before thermal fluctuations become significant at long times), whereas the second, τ_2 , excludes the start of the data where the short-lived exponential contributions are found, by fitting only to data collected at times greater than τ_1 .

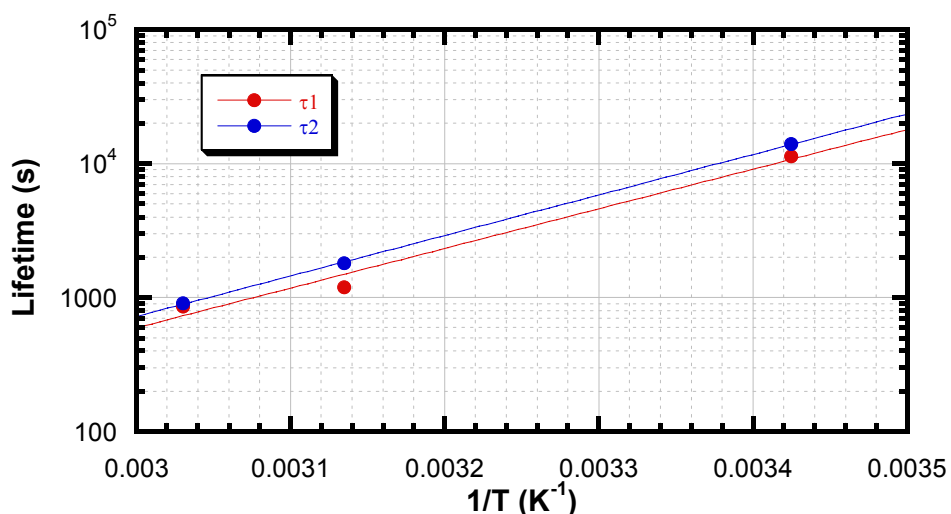
T /°C	τ_1 /s	τ_2 /s
21	11,400	14,000
48	1,200	1,800
59	860	910

Table 6.5: Exponential lifetimes as a function of temperature

If the rate-limiting process in the recovery of F8BT LEDs is thermally activated, then an Arrhenius equation, Equation 6.7, should apply.

$$A \propto e^{-\left(\frac{E_a}{k_B T}\right)} \quad (6.7)$$

A represents the rate, inversely proportional to the lifetime τ , E_a represents the activation energy for the thermally activated process, k_B is Boltzmann's constant and T is the thermodynamic temperature. Therefore, on an Arrhenius plot (showing $\ln(\tau)$ against $1/T$), the activation energy E_a will be given by the gradient multiplied by k_B . Figure 6.31 shows such a plot for the data in Table 6.5.

**Figure 6.31: Arrhenius plot of recovery lifetimes at elevated temperatures.**

The gradients in the two cases are very similar. Using the calculated uncertainty in the gradients as a best estimate for the uncertainty in the final results, E_a is calculated to be 0.59 ± 0.08 eV and 0.61 ± 0.01 eV respectively. Taking into account the uncertainties in the exact temperature achieved and the lifetimes extracted, a more realistic precision of 0.6 ± 0.1 eV is suggested.

There is in fact a barrier of approximately 0.6 eV inherent in the device structure. The work-function of the calcium cathode is 2.9 eV, and the LUMO of F8BT is 3.55 eV. This is ideal for electron injection, but

means that in the absence of any local doping^{35,36}, electron extraction through the same electrode would be blocked by a 0.65 eV barrier. This is of course one of many possible candidates for the thermally activated process. However, evidence suggests that this is merely a coincidence. The recovery from enhancement takes place not only in short circuit as seen here, but also in open circuit as originally observed, where there is no sink for charge extracted from the device. Additionally, and more significantly, it is not restricted to calcium-cathode devices. A batch of devices made with magnesium cathodes (work function 3.7 eV) instead of calcium, and 75 nm F8BT, still showed the characteristic slow extraction of charge, even though there is no barrier for extraction of electrons from F8BT into magnesium.

6.6.4 Summary of findings

- The recovery process is accompanied by a release of charge which flows out of the device in the reverse direction to the original drive current
- The charge flow is initially very fast, and lengthens out with time. It can be represented by an exponential function at long times
- The quantity of delayed charge released (even without the “instantaneous” discharge in the first ~1 second) is greatly exceeds the theoretical limit for a unipolar space charge limited device
- F8BT LEDs are believed on the grounds of injection and transport imbalances to be predominantly space-charge limited for electrons and effectively free of holes in the bulk. However the quantity of charge detected demands that neither free nor trapped electrons can be solely responsible, since this would significantly violate the space-charge limit
- Recovery of the drive-induced enhancement process can be accelerated by heating of the device
- The recovery process appears to be thermally activated, with an activation energy of approximately 0.6 eV for the predominant components at long times
- Although the standard calcium-cathode devices studied contain a possible barrier for electron extraction at the F8BT/Ca interface, other devices with no such barrier show similar behaviour

These findings point to two possible causes. Ionic motion similar to the behaviour of an LEC (Section 2.4.7) cannot yet be ruled out. Alternatively, a trap-filling process may be responsible, in which the trapped charge is prevented from recombining, lifting the unipolar space charge limit.

6.7 Reverse bias and mobile ions

Mobile ions provide a possible simple explanation for the large quantities of charge observed in reverse-bias recovery. Much work has been published on the subject of light-emitting electrochemical cells^{12,37}. In

the analysis of de Mello *et al*¹² mobile ions move through a solid polymer electrolyte such as poly(ethylene oxide) (PEO) which is blended with the emitting polymer, in such a way as to maximise the field at each of the injecting contacts and minimise the barriers for charge injection. In this way, injection of both charge carriers becomes essentially ohmic, and the resulting improvement in injection balance leads to increased efficiencies. A notable feature of polymer LECs is that they display strongly time-dependent behaviour over a typical period of 15 seconds after switching on¹². It is important to establish whether such ionic effects are a possible cause for the drive-induced enhancement effect.

6.7.1 Possibility of ionic effects

As already indicated, the time-dependent processes seen in the drive-induced enhancement effect are strongly reminiscent of mobile-ion effects. The observation of an increase in device conductivity is consistent with injection enhancement by ionic drift. Besides the charge balance effects identified with LEC behaviour, there is another route by which ions may be responsible.

There has been some debate as to whether free ions found inside the polymer can act as non-radiative recombination sites for excitons. Measurements by de Mello *et al*¹² on PPV showed no measurable quenching of luminescence by lithium ions up to concentrations as high as $10^{21} / \text{cm}^3$. Photogenerated charges, in contrast, have been seen to display quenching at levels nearer to $10^{18} / \text{cm}^3$ in PPV³⁸. A study on the F8BT/Ca system itself³⁹ concludes that quenching due to the presence of the Ca^{2+} ion is highly significant, and most likely produced by diffusion of the neutral calcium atom into the film, where it dopes the polymer by contributing its valence electrons to form a polaronic state.

On commencement of driving, the applied field will tend to cause any ions to drift. This would leave the polymer bulk depleted of ions. If ions cause quenching, this would cause an increase in the bulk photoluminescence efficiency. PL efficiency measurements can therefore be used to distinguish between the scenarios, and the data in Section 6.4.1 show no evidence for changes in the bulk PL during driving. Therefore, of the two possible *ionic* causes, the charge-injection balance mechanism remains the only realistic model by which mobile ions could be responsible for the quantum efficiency increase.

Since the ions are confined to the film, they cannot flow in the external circuit, but rather relax by redistributing within the film. However an external current is observed during this process, which can be understood as a dissipation of the image charges created by the ions in the electrodes. A rigorous analysis of the external current may be made by considering the depolarisation current as the film relaxes to its neutral state. This is achieved by considering the effective dipoles created by the separation of ions within the film. Equation 6.8 defines the polarisation of the material as the dipole moment density.

$$P = \frac{Np}{V} \quad (6.8)$$

P is the polarisation, N is the number of dipoles, p the dipole moment and V the volume. If each positively charged ion attracted to the cathode is assumed (a) to have a charge of $+e$ and (b) to have an equal and opposite partner at the anode, then each pair of ions forms an effective dipole, with separation equal to the film thickness. (If there is an immobile counter-ion somewhere in the bulk, then the mean dipole moment will be reduced by one-half.) This yields equation 6.9

$$P = \frac{Nex}{V} \quad (6.9)$$

where e is the charge on an electron, and x is charge separation distance. The volume of the film is equal to its area multiplied by its thickness, which produces Equation 6.10

$$P = \frac{Ne}{A} \frac{x}{d} \quad (6.10)$$

where A is the area of the film, d is the film thickness, and x/d is then equal to 1 for a pair of mobile ions or where a mobile ion is balanced by a charge on the counter-electrode, and $\frac{1}{2}$ where the counter-ion is immobile. When a dielectric depolarises, the depolarisation current density is simply the rate of change of polarisation (Equation 6.11).

$$j = \frac{dP}{dt} \quad (6.11)$$

where j is the current density, I/A . Integrating with respect to time, and multiplying both sides by A , produces Equation 6.12

$$Q = Ne \frac{x}{d} \quad (6.12)$$

where Q is the total charge flowing. Therefore, in the special case where $x/d = 1$, the number of charges at each interface is equal to the total charge seen to flow in the external circuit.

Taking the example already seen in Figure 6.30, an external charge flow of 300 nC was seen from a device with area 50 mm^2 and thickness 70 nm . This is equivalent to an ion density of approximately $5 \times 10^{17} / \text{cm}^3$, assuming singly-charged ions. This figure is comparable to the lowest concentration of ions measured by

de Mello *et al* in PPV-based devices, but is at least an order of magnitude below where they first reported measurable ionic effects upon the injection properties.

6.7.2 Reverse bias – absence of recovery

If mobile ions are present inside the device, they should be subject to drift in any applied field – not just the applied forward bias during normal driving. The band diagrams in Figure 6.32 show that, due to the relative work-functions of the electrodes, short-circuiting the device externally leads to a strong reverse field internally. The work function difference is 2.2 V, so that ignoring any interface dipoles + 2.2 V external bias leads to flat band conditions internally. It is expected, therefore, that any ionic drift in forward bias should be reversed even in short circuit. It has already been seen that recovery takes place in open circuit, where diffusion and mutual Coulomb effects would be the sole driving forces for re-distribution of ions inside the device. Reverse bias should therefore lead to accelerated recovery.

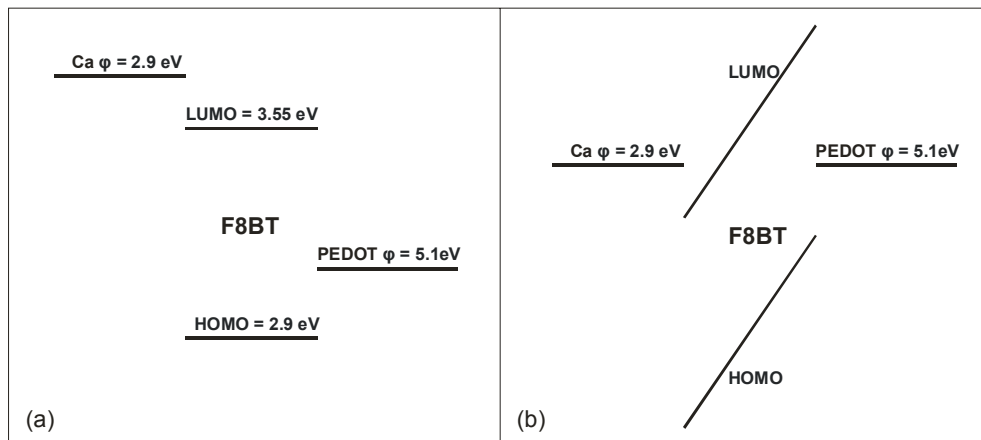


Figure 6.32: Energy levels (a) in open circuit and (b) in short circuit.

A series of experiments were conducted on a single device which had been recently driven through the initial stages of degradation, so that this would not interfere with the measurements. Several identical pixels on the same device were used, all identically pre-driven. Figure 6.33 shows these experiments in the order in which they were conducted. The first four traces shown were conducted on four separate pixels, and the 5 % spread in absolute quantum efficiencies is quite typical for different pixels on the same device. The fifth trace was conducted on the same pixel as the first trace, and thus shows slightly more advanced degradation, but otherwise similar characteristics. All show traces which are broadly similar in shape. The rested device without further treatment (first trace) does appear to show less drive-induced enhancement than the rest. Nevertheless it can be concluded that once the device has been rested, no significant further changes take place on application of a reverse bias.

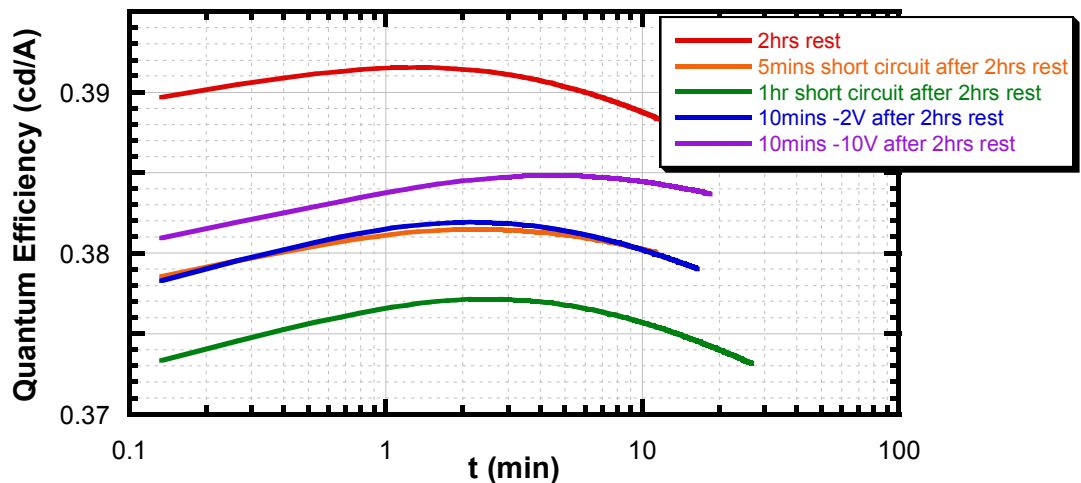


Figure 6.33: Drive-induced enhancement at 50 mA/cm² in pixels rested for 2 hours and then treated as shown.

Having examined the effect on a rested device, a recently-driven device was now subjected to reverse bias. Immediately after measuring the final trace in Figure 6.33, the pixel was subjected to -10 V reverse bias for 10 minutes, and then re-measured. The surprising results are shown in Figure 6.34, including the data previously shown. The traces shown are both recorded on the same pixel, and *in both cases* after 10 minutes at -10 V reverse bias. The only difference is that the first trace had previously been rested for 2 hours, whilst the second one was driven in forward bias immediately prior to the reverse bias treatment. Remarkably, the reverse bias cycle does not reverse the effect, as the LEC theory would predict. Rather, it seems to increase the effect, but only when it is already in place.

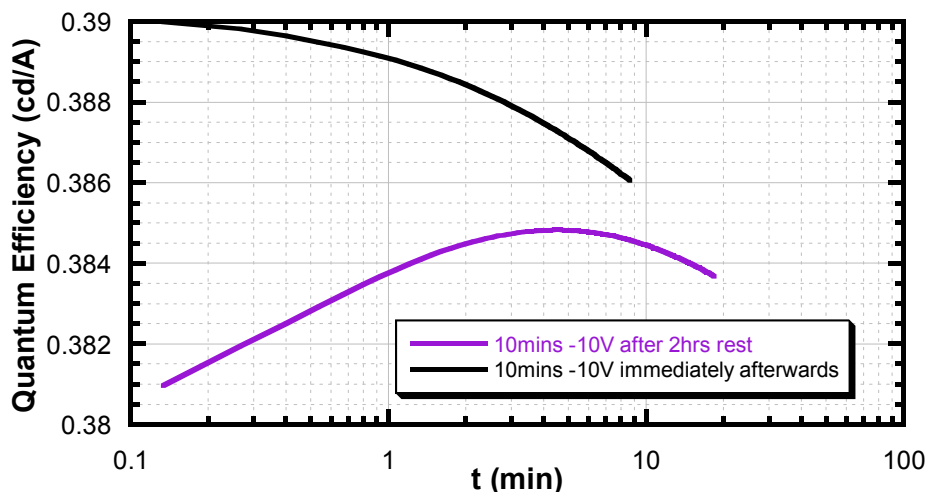


Figure 6.34: The final trace from Figure 6.33, and the same pixel immediately placed in -10 V reverse bias for 10 minutes and then re-measured.

Successive measurements on the same pixel show that the degree of enhancement is related to the reverse bias applied. Figure 6.35 shows a number of such cycles. Short circuit appears not to behave significantly

differently to open circuit, but strong reverse biases do cause an enhancement of the initial quantum efficiency. The effect of 20 minutes at -10 V reverse bias is much more significant than 20 minutes at -5 V. The -10 V pre bias notably produces an identical result in 20 minutes here as it does in just 10 minutes in the previous graph. So by applying a reverse bias, the recovery appears to be frozen out, and the effect is actually stabilised and somehow enhanced.

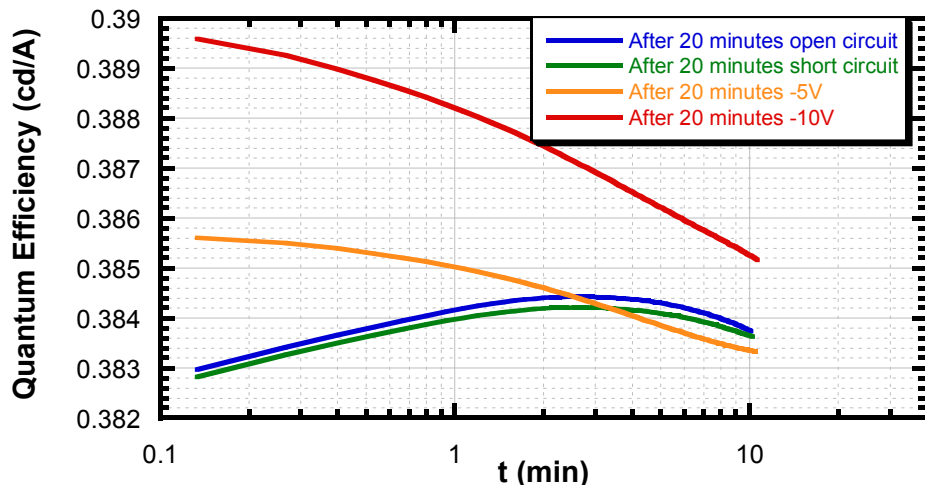


Figure 6.35: Quantum efficiency at 50 mA/cm² after specified treatments immediately following driving.

This augmentation of the drive-induced enhancement effect by reverse bias is plainly incompatible with the theory of mobile ion drift enhancing injection. Rather it appears that some state is formed during forward bias driving of the device, which can be stabilised and enhanced by reverse bias (where no current is injected). Conversely, this state cannot be produced by reverse bias alone, implying that the forward passage of current through the device is vital for the effect to be seen.

6.7.3 Pulsed drive with reverse bias

As a further, more controlled test of this finding, the experiment was extended to a pulsed-mode drive scheme. Under direct-drive pulses from the 8116A pulse generator (Section 3.4.4.2), a drive voltage for both “on” and “off” portions of the cycle can be specified. In this way, the forward bias can be alternated with a reverse bias to study the effect.

A 100 nm F8BT device was initially measured in the Test Box, under direct drive from the 8116A pulse generator. The drive cycle used was 4.3 V “on” for 100 µs, repeated at 100 Hz, and 0 V “off”. This produced a duty cycle of 1 %. As previously noted, the 0 V external bias in the “off” phase is equivalent to an internal bias of -2.2 V. Even though this duty cycle implies an internal bias of +2.1 V for 1 % of the time and -2.2 V for 99 % of the time, drive-induced enhancement was still observed, as seen in Figure 6.36. It

should be noted that this data was collected without any correlated current information, so it does not directly represent quantum efficiency. Any net ionic drift during such a drive cycle should be dominated by the 99 % of the duty cycle which is reverse-biased.

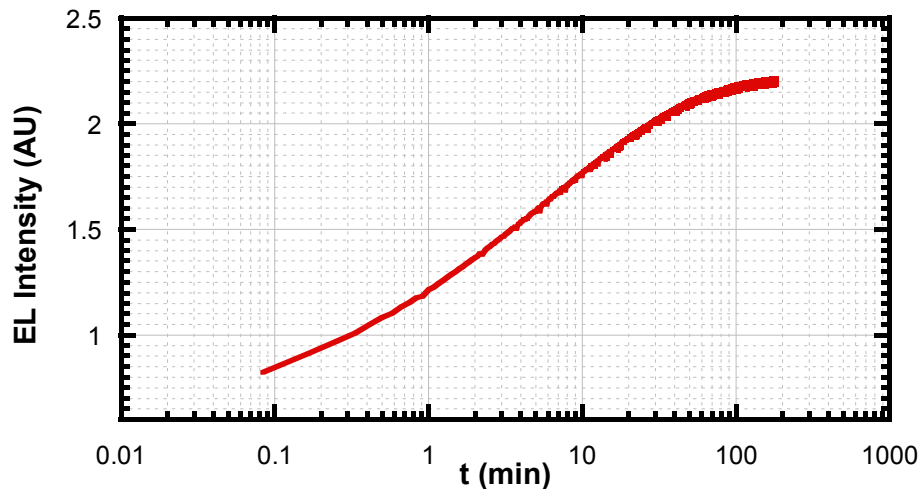


Figure 6.36: Electroluminescence under pulsed voltage conditions.

Current is unknown, so quantum efficiency cannot be determined from this data.

Having observed the enhancement effect under these conditions, and determined its approximate time-scale, the LED was transferred to the Pulse Rig (Section 3.4.4). Although the Rig contains a dedicated pulse generator, in this instance the LED was once again direct-driven by the 8116A pulse generator, whilst measurements were taken with the Pulse Rig's current probe and photomultiplier tube. This allowed transient measurement of both current and light output, rather than just time-averaged data. A new pixel was selected, and automated data collection was commenced immediately at 1-minute intervals. The initial data set, similar in shape to those collected at all stages of driving, is shown in Figure 6.37.

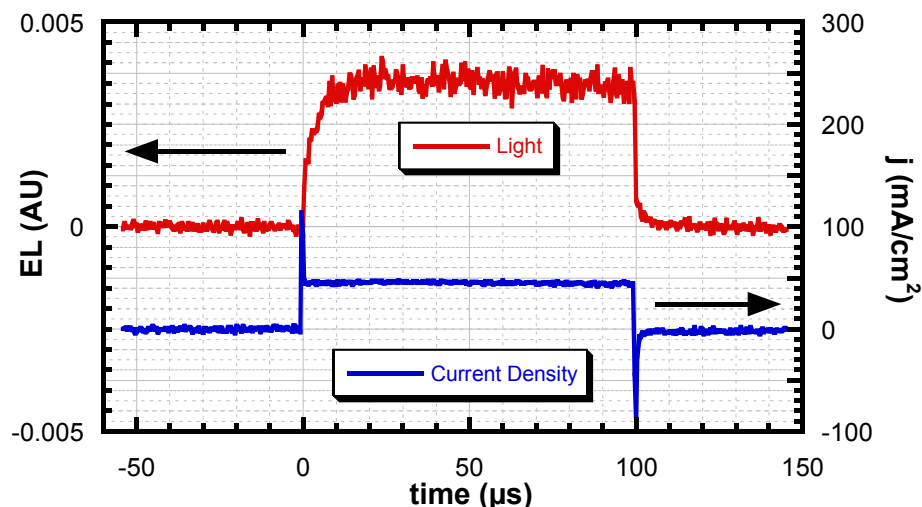


Figure 6.37: Transient light output and current density at start of measurement.

The data show the electroluminescence rising through the first $\sim 20\ \mu\text{s}$ and then plateauing at what may be considered to be the DC value. The current density shows charging and discharging spikes, characteristic of the parallel plate capacitor arrangement, with a remarkably flat current characteristic in between. To extract the data from this and subsequent measurements, both light and current were determined by averaging between 20 and 99 μs . Figure 6.38 shows the first 100 minutes of processed light intensity data, collected with the photomultiplier tube, compared with the previously seen data from the photodiode. The light intensity data collected by the PMT show excellent correlation with the photodiode data. Although not immediately apparent to the eye, a series of data points from 12 to 49 minutes are missing from the PMT data due to an unintended pause in the data collection. This section is bridged by a straight line on the graph.

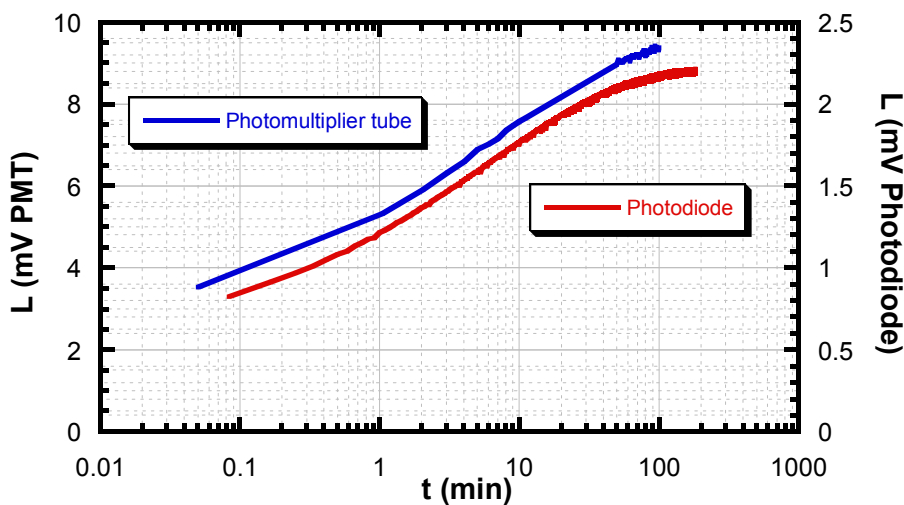


Figure 6.38: Light intensity under pulsed drive as measured by the photodiode and PMT.

The experiment was repeated on further fresh pixels, substituting the 0V “off” phase with +1V, -4V and -8V. Having collected and processed both light intensity and current density data, quantum efficiency (in arbitrary but mutually consistent units) was calculated by dividing one by the other. Figure 6.39 shows the complete set of results. Again, reverse bias between drive cycles leads to an enhancement of quantum efficiency. This phenomenon extends not only to enhancement by values below 0 V, but continues in the opposite direction to show a reduction in quantum efficiency when the device is pre-biased at +1 V, which as previously stated is still a reverse bias from the point of view of the polymer bulk. Note that the strong reverse bias does not cause *faster* saturation of the enhancement process. Instead, in all four cases the quantum efficiency still depends on the forward bias cycles to determine the progress of the effect. The identical forward bias evolution is then amplified to varying degrees by the pre-bias. Thus the reverse-bias enhancement is still dependent on the accumulated degree of forward bias drive.

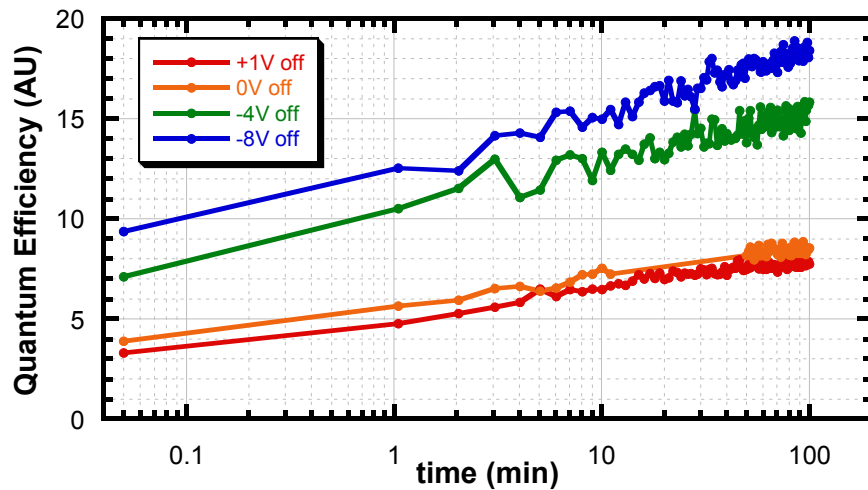


Figure 6.39: Quantum efficiency during driving pixels at 4.3V “on” (1 %) and specified voltage “off” (99 %).

The phenomenon of luminescence enhancement by pre-biasing the LED has been previously noted in pulsed experiments by Pinner²⁹ and in DC⁴⁰ but although explanations including ions and traps were postulated, no direct evidence was presented. It is extremely interesting from a device perspective if the device efficiency can apparently be more than doubled by applying a negative pre-bias, and without stressing the device by passing any additional current. Moreover, this effect is more universally observed across polymers, such as in the PPVs studied by Pinner, and it may be that the F8BT case is unique only in taking so long to set in and subsequently displaying such a long lifetime.

6.7.3 Summary of findings

- PL shows that any ionic effects must be due to injection enhancement, rather than quenching
- The implied ionic density would be less than $10^{18}/\text{cm}^3$
 - This ion density is an order of magnitude lower than a reported threshold for LECs
- Reverse bias should reverse any ionic drift, but no such reversal is seen
 - Reverse bias after resting the device has no effect
 - Reverse bias after driving enhances the effect
 - Ionic drift is therefore not compatible with experiment
- Reverse pre-bias in pulsed mode produces an enhancement in efficiency which:
 - has been reported before, but not satisfactorily explained
 - is present even in materials which do not appear to show enhancement under DC drive
 - may be a result of the same sort of enhancement, even when seen in other polymers

6.8 Impedance spectroscopy

Impedance spectroscopy is a valuable tool for investigating the properties of a dielectric layer inside a capacitive structure such as a polymer LED⁴¹⁻⁴⁷. In order to further probe the nature of the changes inside the polymer layer responsible for the change in quantum efficiency, this technique was used to analyse the capacitance of a device before and after drive-induced enhancement. An HP4192A impedance analyser was used for the measurements presented here.

6.8.1 Capacitance measurements after drive-induced enhancement

Impedance scans can be performed as a voltage sweep at constant frequency, or a frequency sweep at constant voltage. A series of preliminary voltage sweeps showed that when driven above approximately +2 V, where the device turns on, persistent changes were caused in the underlying capacitance at low voltage. This phenomenon was therefore analysed by driving a 75 nm F8BT LED under forward bias at +3 V for varying periods of time, and subsequently measuring the capacitance below the turn-on voltage. Figure 6.40 shows the initial results.

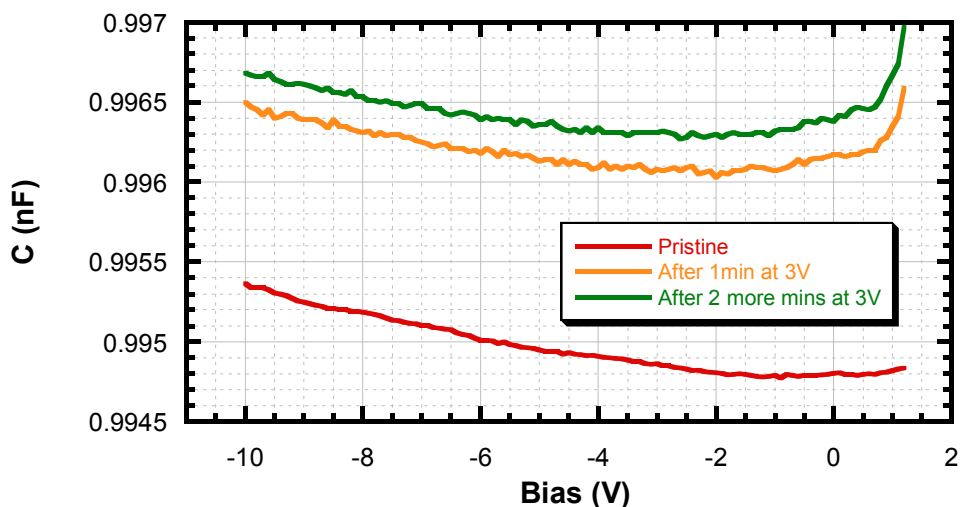


Figure 6.40: Device capacitance as a function of voltage, below turn-on. Scan direction towards -V.

The “pristine” curve shows the capacitance of a new un-driven device, starting at +1.2 V and continuing to -10 V in steps of 0.1 V. The amplitude of voltage oscillations was 50 mV, the oscillation frequency was 10 kHz, and the number of averages taken at each point was 100. The whole curve took a little over 3 hours to compile. After collection of this first curve, to ensure that no permanent changes had occurred as a result of the prolonged subjection to -10 V of reverse bias, the voltage was returned to 0 V while still measuring.

The measured capacitance was seen to return immediately to 0.9948 nC, exactly as it had read when passing through zero before the reverse bias was applied.

Two further curves were collected, after driving the device in forward bias for 1 minute and 2 minutes respectively. The number of averages at each point was reduced to 10, which reduced the total time for data acquisition to approximately 20 minutes. Each of the two curves shows an enhanced capacitance after driving, which is particularly evident near 1.2 V, where data collection began. Both show a capacitance which reduces with applied bias (and passing time), until a minimum is reached at approximately -2 V (6 minutes after the start of measurement). Beyond this point, the underlying rise as seen in the pristine sample takes over, with the capacitance remaining elevated, indicating a persistent effect.

To gauge the persistence of the effect, two further measurements were taken, after 24 hours and 5 days of rest respectively. These are shown in Figure 6.41.

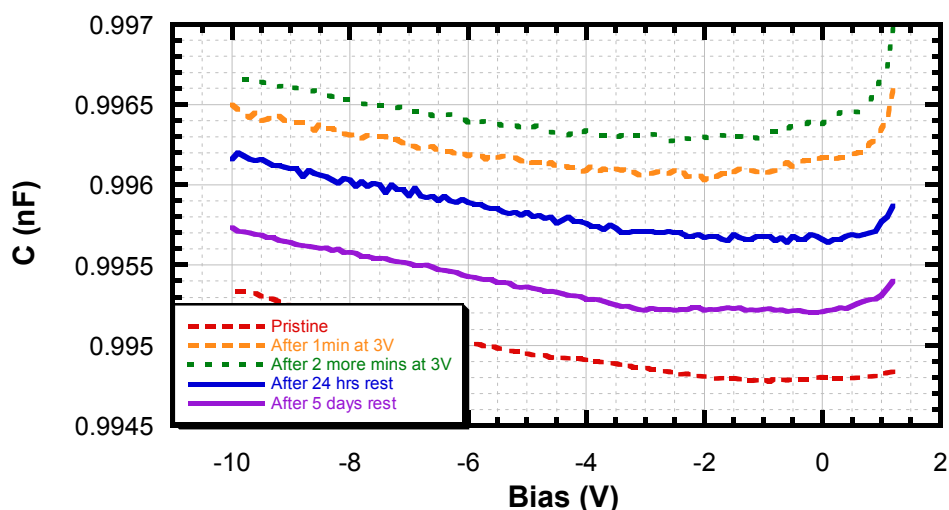


Figure 6.41: Data from Figure 6.40 (dotted) with two further traces collected after resting the device.

The graph clearly shows relaxation of the effect, on a timescale of hours to days. Beyond 24 hours, there is still significant relaxation. The enhanced capacitance at the high end of the voltage range is still seen, so cannot be entirely attributed to the fast-decaying portions of the enhancement effect seen shortly after driving. The fact that an entire day's rest still shows significant changes on a scale comparable to the immediate measurement can be explained by noting that the “immediate” measurements began at least 10 seconds after driving and took some time to acquire. Thus the strongest components of the effect would already have decayed. Ongoing decay in the effect can be seen in the two uppermost dotted traces, which decay sufficiently during measurement that the minima are located further towards reverse bias (later time) than in the solid lines below.

In tandem with the drive-induced enhancement effect, an increase in capacitance is thus observed. Note that, for two reasons, a redistribution of charged ions inside the polymer cannot be found responsible. Firstly, any movement of ions in forward bias would increase the apparent capacitance in forward bias but *decrease* it in reverse bias. Secondly, the strong reverse bias inherent in the technique would rapidly reverse the effects of forward bias; thus the persistence observed cannot be explained by ionic motions.

6.8.2 Summary of findings

- The capacitance of the LED is seen to increase and decay along with drive-induced enhancement
- The magnitude of the change is small, at 1.4 parts in 1000, but easily measurable
- Relaxation is still detectable more than 24 hours after driving
- Possible causes are:
 - an increase in the dielectric polarisability of F8BT during enhancement
 - a small contraction of the polymer layer
 - a favourable trap charge distribution inside the polymer

6.9 Charge Modulated PDS

Charge Modulated PDS is a recent enhancement to the Photothermal Deflection Spectroscopy apparatus in the Optoelectronics Group, and was implemented for the express purpose of examining the enhancement effect (see Section 3.4.6). It allows for measurements of the change in absorption caused by driving a device *in situ*. By using a double lock-in technique, intrinsic absorptions due to the materials in the device (ITO, PEDOT:PSS, metal, glass, even the polymer itself) are eliminated, as are Joule heating effects due to driving the device. All that remains is the change in absorption on driving.

6.9.1 Measurements on a drive-enhanced device

F8BT devices were fabricated in the normal way, on small substrates using wide-stripe ITO and round-ended cathode pixel masks, without encapsulation. The F8BT layer thickness was 65 nm. Devices were tested by CM-PDS as described in Section 3.4.6.3, across the range of photon energies accessible by the PDS Rig. A representative trace is shown in Figure 6.42. The device was driven at 2.9 V, corresponding to an approximate current density of 5 mA/cm^2 . The PDS Rig usually normalises the measured deflection amplitude according to the instantaneously measured intensity of the heating beam. However, since in this experimental configuration the lock-in frequency is different from the beam modulation frequency, no

useful spectral data for the lamp is collected. The Figure therefore presents the raw unmodified deflection data, along with a previously measured spectral response for the xenon lamp.

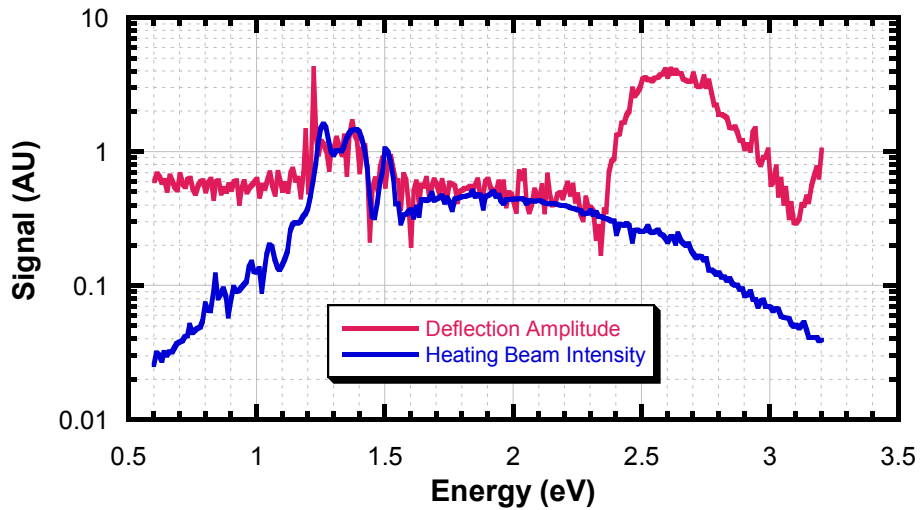


Figure 6.42: Recorded deflection (raw data) for an F8BT LED driven in the charge modulated PDS experiment, and the spectral shape of the illumination source.

Figure 6.43 shows the data after dividing through by the heating beam intensity, and correcting for the photodiode calibration, as is necessary in all PDS measurements.

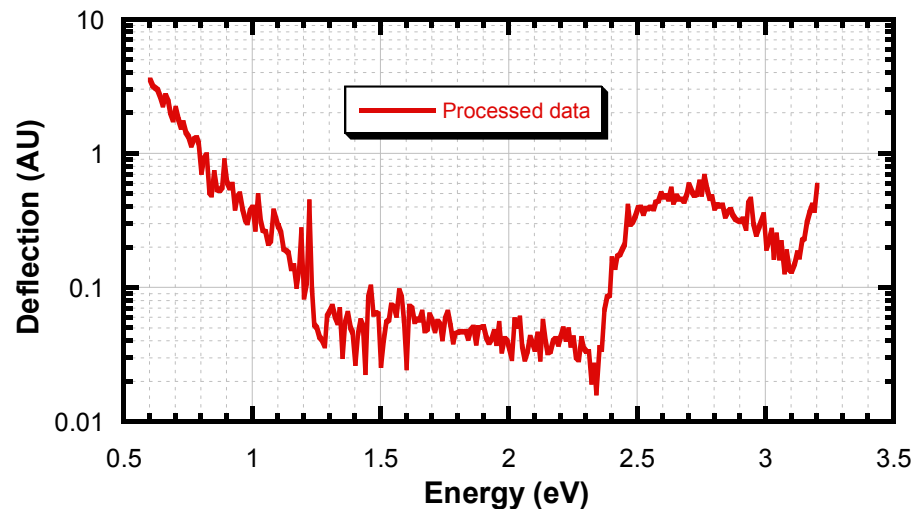


Figure 6.43: Deflection data from Figure 6.42 after correcting for beam intensity and system response.

The final data required to interpret the experiment is the phase signal, collected separately. In the standard PDS Rig configuration, an absorption signal registers a phase equal to or very near $+90^\circ$. Since such scans show some absorption at all wavelengths, the phase very rarely deviates far from this value. When it does, the phase signal generally becomes noisy and indicates a noise floor in the measured data itself. In the

charge modulated system configuration, the sample is illuminated from the back surface, and thus the probe beam deflects in the opposite direction when absorptions are present. Thus an absorption will show a phase of -90° . Substantial portions may be expected where no discernible absorption signal can be detected.

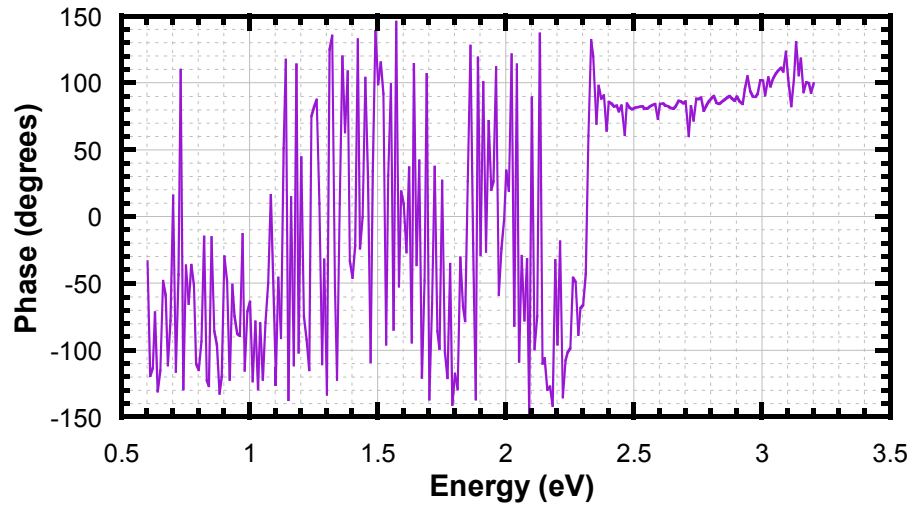


Figure 6.44: Phase data from experiment in Figures 6.42 and 6.43.

At least 3 regimes are visible: 0.6-1.2 eV, 1.2-2.1 eV and 2.3-3.2 eV.

The collected phase data seen in Figure 6.44 reveal at least three sections: Below ~ 1.2 eV the phase is noisy but centred around approximately -90° , indicating an absorption feature. Between 1.2 eV and 2.0 eV it is apparently random and extremely noisy, except for a possible tendency towards -90° in the region of the known artefact at 1.85 eV where the probe laser lies. This section can therefore be considered noise-limited. Finally, above 2.3 eV the phase recorded is $+90^\circ$, indicating a negative change in absorption on driving, i.e. a bleaching of the absorption in this region. The small section between 2.1 and 2.3 eV may indicate an induced absorption feature like that at low energies, but for now is treated as part of the central noise-limited section.

The complete picture is revealed in Figure 6.45. Two experimental points are worthy of note. First, the absolute deflection values as measured by the PDS Rig were several orders of magnitude below the usual peak values observed in a normal absorption PDS experiment. This is one reason why the noise floor appears to be so high. Secondly, PDS signals are known to saturate at high signal strength, such as usually seen above the band-gap, or perhaps in this configuration due to the presence of glass, ITO, PEDOT:PSS and metal components. Nevertheless, if there is any saturation, the change in signal strength is enough to be detected, even if it should be noted that the system response may be non-linear as a result.

The main bleaching signal coincides perfectly with the $\pi-\pi^*$ absorption of F8BT. Bleaching of this signal is expected in an operational device⁴⁸. The spur above 3.1 eV is not present in other measurements made on

these devices, and appears to be an experimental anomaly in this data set alone. The absorption signal is interesting, and its origin is unclear. It is reminiscent of the polaron absorption reported in F8BT, but is lacking the accompanying signal expected at higher energy³⁰. The exponentially increasing absorption towards low energies is also reminiscent of the exponential trap distributions well-known in disordered organic semiconductors⁴⁹.

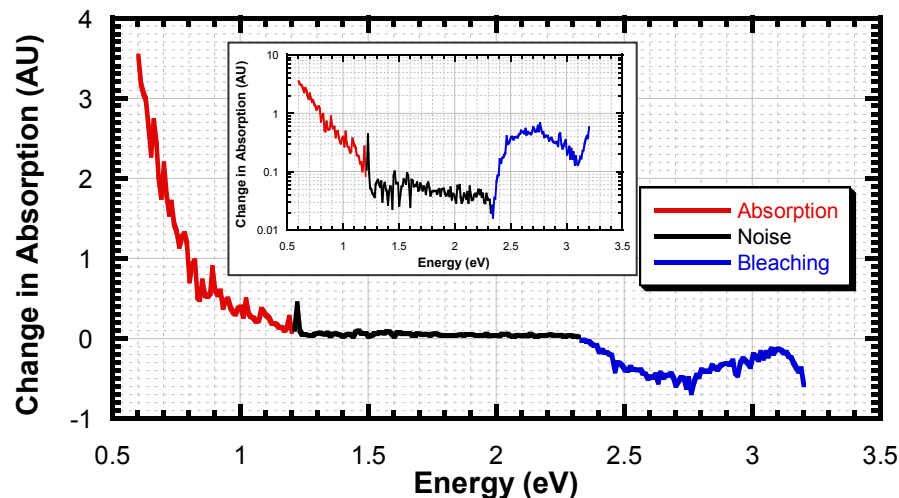


Figure 6.45: Charge-modulated PDS on an F8BT device driven at 2.9V. Inset: Same data on a log scale.

The absorption distribution is interestingly consistent with the thermal activation measurements presented in Section 6.6.3. Although a “best-estimate” 0.6 eV activation energy was measured at that time, a distribution of states was suggested by the lengthening lifetime observed in experiment. The lowest energy states were expected to depopulate extremely rapidly, whilst the highest energy states have a very low initial population. Thus an intermediate value of 0.6 eV was seen when studying the device as a whole.

In Section 6.4.2 (Light-assisted recovery), light above the band-gap was seen to be effective in resetting the effect, but the mechanism for this phenomenon (absorptive heating, or direct single-photon action on the active species) could not be distinguished. If the data presented here can be interpreted as revealing a range of trap depths, that would suggest that the action of light above the band gap is only effective as an indirect result of the polymer’s high absorption coefficient in that range, causing a heating of the polymer layer.

6.9.2 Summary of findings

Charge-modulated PDS has revealed a feature in the absorption of an F8BT LED during driving.

- Bleaching of the $\pi-\pi^*$ absorption is observed, as expected
- An absorption is seen below approximately 1.2 eV

- The absorption resembles part of the characteristic polaron absorption, but may in fact be due to direct absorption by a distribution of trapped charges
- The characteristic energies are consistent with the earlier thermal activation measurements

6.10 Transient measurements

Transient measurements have previously been used to investigate the charge transport behaviour of polymer LEDs, as discussed in Section 3.4.4 and Chapter 5. Here, the Pulse Rig provides evidence for the changing injection properties of the anode interface.

6.10.1 Sharpness of turn-on

Experiments were conducted on a 100 nm F8BT device, under pulsed electrical drive, 4 V in amplitude, 100 μ s in length, and repeated at 17 Hz. Figure 6.46 shows the normalised EL before and after a 30-minute period of enhancement under these conditions. The actual increase in EL intensity after driving was 390 %. However, the current rose by 30 %, leaving a net increase in quantum efficiency of nearly 300 %.

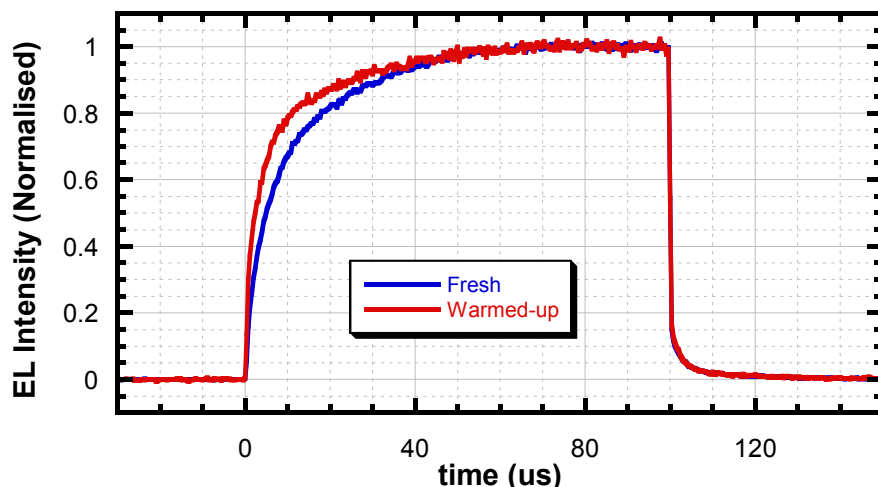


Figure 6.46: Normalised EL transients at 4 V before and after drive-induced enhancement.

As seen in the Figure, the electroluminescence rise-time becomes significantly faster after drive-induced enhancement. Figure 6.47 shows a magnified view of the first microsecond of this data. The signal around 200 ns is caused by electrical noise at the onset of the drive pulse. It indicates an inherent effective delay in the system caused by early triggering of the oscilloscope and is not indicative of any resolution limitation. Due to the high peak EL intensity during the “enhanced” measurement, an OD 1.0 filter was used to

attenuate that measurement, and consequently the (unattenuated) electrical noise level is amplified relative to the “fresh” measurement when the data sets are normalised.

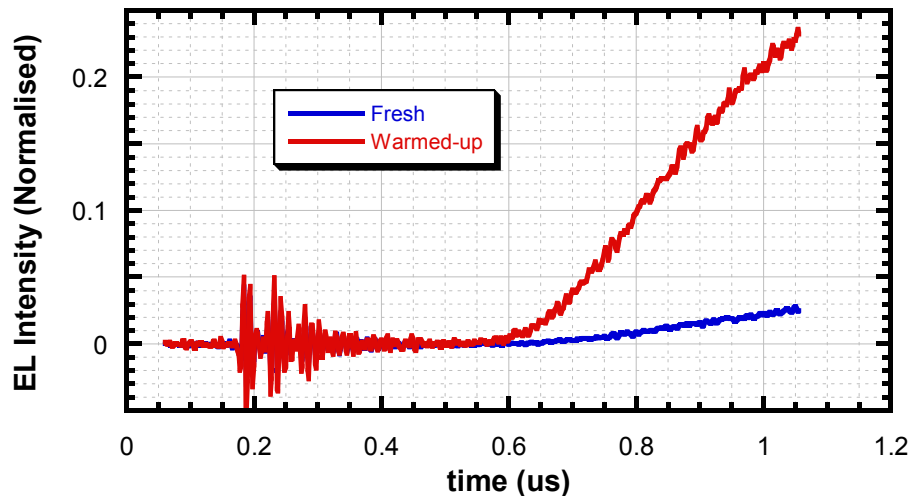


Figure 6.47: First microsecond of normalised data seen from same experiment as Figure 6.46.

Three points are made clear by the data. First, the delay time to onset of electroluminescence is independent of the presence of enhancement. This appears around 600 ns on the plot, which is actually an overestimate due to the non-zero oscilloscope sync offset and the characteristic delay on the PMT. The real delay time, around 400 ns, is characteristic of the time taken for fast carriers, namely electrons, to drift through the polymer layer under the applied field and this is apparently unaffected by enhancement. Secondly, once the electrons have arrived at the anode, light emission climbs very much more quickly after enhancement, reaching 21 % of its long-term value in the first microsecond compared to just 2.5 % in the fresh measurement. This hints at a reduction in the barrier for hole injection, which is predicted to be 0.8 eV by comparing the work function of PEDOT:PSS and the HOMO of F8BT. The arrival of electrons at the interface itself produces an increased field to assist injection of holes. However this enhanced field becomes effective more quickly after enhancement than it does before. Thirdly, since the traces have been normalised (by a factor of approximately 4.9), the absolute gradient of the onset of electroluminescence is many times faster after enhancement than the approximate 8-fold increase depicted in the normalised graph.

Since electrons take the same time to transit the film in both cases, as evidenced by the constant delay time, the device changes cannot be attributed to any variation in electron transport. The space-charge limited injection current, which already benefits from ohmic injection, therefore is unchanged by the onset of drive-induced enhancement. The increased current density (Section 6.2.2) and quantum efficiency must therefore be attributed to an enhancement of hole injection at the anode.

6.10.2 Summary

- Electron transport is unaffected after drive-induced enhancement
- Hole injection commences more readily after drive-induced enhancement than before
- Hole injection is therefore improved by the enhancement process

6.11 Experimental summary

This section brings together the experimental results presented in this Chapter.

6.11.1 Findings and implications

- Present in F8BT and its blends only (at DC), with any choice of injecting anode
- Higher work-function cathodes show faster drive-induced enhancement, perhaps due to higher field required to achieve comparable current
- Produces a dramatic rise (up to $60\times$ observed) in electroluminescence external quantum efficiency
- No corresponding change in photoluminescence quantum efficiency
- Device conductivity increases
 - Perhaps initially due to heating
 - But continues for the duration of the enhancement process, up to hundreds of hours

The lack of a change in PL quantum efficiency suggests that the underlying cause is a variation in the charge injection balance. Electrons are the majority carrier in F8BT, so a small increase in hole injection properties will marginally increase the current and dramatically increase the quantum efficiency. A reduction in the electron extraction properties would increase the quantum efficiency but decrease the current. Changes in hole injection would likely be caused by processes at or adjacent to the anode contact, which makes the observation of drive-induced enhancement with both PEDOT:PSS and ITO remarkable, since the two anodes are vastly different in composition, morphology and behaviour. The only features in common are the broadly similar work functions around 5 eV and the F8BT polymer itself. Changes at the cathode are less likely to be responsible, because holes are not expected to reach this area, and electron injection from calcium is ohmic, making it very insensitive to changes in cathode properties. Together, these findings suggest a change in the polymer, adjacent to the anode contact.

The observed acceleration in drive-induced enhancement through use of higher work-function cathodes is an interesting corollary. In such cases, electron current becomes injection limited, and thus the charge

balance is automatically improved. This also leads to a corresponding increase in hole injection at constant current, and suggests a link to the total quantity of holes injected.

- The electroluminescence spectrum is very slightly skewed after drive-induced enhancement
- The photoluminescence spectrum is unaffected

Optical modelling of devices shows that the slight skew in EL spectrum can be caused by a very small drift in the recombination zone away from the anode. This is consistent with enhanced hole injection, since the increased hole density would likely penetrate further into the device.

- The effect is spontaneously reversible with the following properties:
 - Thermally activated
 - Accompanied by a backflow of charge
 - Initially fast to recover, but lifetime lengthens as time passes
 - Best estimate of activation energy ~ 0.6 eV
- The quantity of charge is many times greater than the unipolar space charge limit

The lengthening lifetime indicates a distribution of states, most highly populated at low energies (which are released fastest). Relaxation of these states yields free charges which exit the device. The quantity of charge observed demands that these states cannot be uncountered electron traps, since such large quantities of charge cannot be stored unbalanced inside the LED. Co-operative trapping is postulated, whereby one species is trapped and at least partially electrostatically compensated by the local presence of the counterspecies. Thus a large quantity of charge can be stored without violation of space-charge limits. The charges may be prevented from recombining by the depth of the traps.

- Light above the bandgap resets the effect, probably by indirect heating
- An absorption signature is detected by charge-modulated PDS

These results are consistent with the thermally activated process already described.

- Reverse bias does not reverse the drive-induced enhancement process
- Reverse bias actually augments the effect:
 - Only if the effect is already in place (i.e. device has been driven)
 - Does not work as an alternative to driving
 - Harder reverse biases are more effective

This is a remarkable observation, because it implies that mobile ions in the device cannot be responsible. Mobile ions, as in an LEC configuration, redistribute during driving so as to enhance the injection field at the contacts. However, reverse bias should have the opposite effect, by transporting the ions away from the interface. Moreover, mobile ions cannot explain the requirement for pre-driving in order for reverse bias to have an effect. It appears that driving is required to create the active states, and that reverse bias somehow stabilises and enhances them, perhaps by physical separation of the electrons and holes, rather than allowing their normal relaxation process.

- The dielectric capacitance of the device varies with the enhancement effect
 - Polarisability of the polymer layer increases during drive, or
 - The layer thickness decreases during drive, or
 - There is a favourable distribution of trap charge in the polymer
- This relaxes in the same way as the drive-induced enhancement effect itself
- The greatest increase observed (a few minutes after driving) was 0.14 %

These observations are consistent with the idea of charge trapping inside the polymer layer. The relative smallness of the measured change can be partially attributed to the timescale required for measurement.

- Transient EL shows a faster turn-on after driving, consistent with enhanced hole injection

6.12 Candidate theory

Having thoroughly characterised the effect, a candidate theory is now proposed to explain the observations.

6.12.1 Outline of hypothesis

The quantum efficiency increase is caused by an improvement in the charge injection balance inside the LED, through enhancement of hole injection at the anode. The enhanced hole injection is a result of the trapping of large quantities of one or other charged species adjacent to the interface. Much of this space charge is cancelled by local charges of opposite sign. Locally, at the anode, the dipolar effect of the non-concentric space-charge fields leads to a very steep potential drop, reducing the thickness of the triangular barrier to hole injection, and thus increasing the hole injection rate.

Figure 6.48 shows an idealised representation of a luminance-voltage (LV) characteristic for a polymer LED, with turn-on at 2.3 V. A second similar trace with the turn-on voltage shifted down to 2.2 V is also

shown. This signifies the state of the LED after the drive-induced enhancement effect, when hole injection is assisted and the onset of light emission is consequently at a lower voltage. Comparing the two curves at low voltage, a very significant increase in luminance is expected during the enhancement effect at constant voltage, whilst at high voltage a much less significant shift is seen.

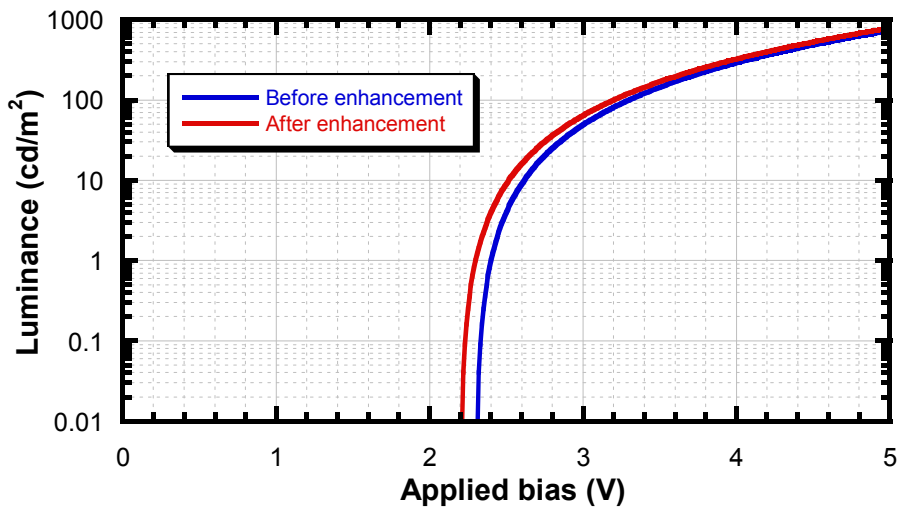


Figure 6.48: Representation of the likely change in the luminance-voltage (LV) characteristic.

6.13 Detailed consequences of hypothesis

By following through the logical consequences of the hypothesised theory, comparisons can be made with the observations from real devices.

6.13.1 Initial charge balance

Driving the LED leads to bipolar injection which is initially very poorly balanced. Injection of holes at the anode is subject to a large barrier of about 0.8 eV, restricting the supply of holes, as depicted schematically in Figure 6.49.

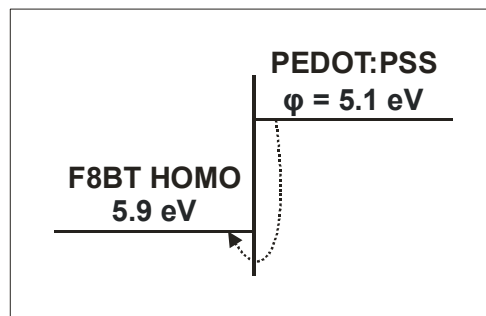


Figure 6.49: Barrier for hole injection into F8BT.

6.13.2 Effect of electron accumulation at anode

According to Murata¹⁶, the PEDOT:PSS interface with F8BT provides a barrier for electron extraction from the polymer. The consequent accumulation of electrons at the interface enhances the field, causing a significant portion of the potential to be dropped adjacent to the interface.

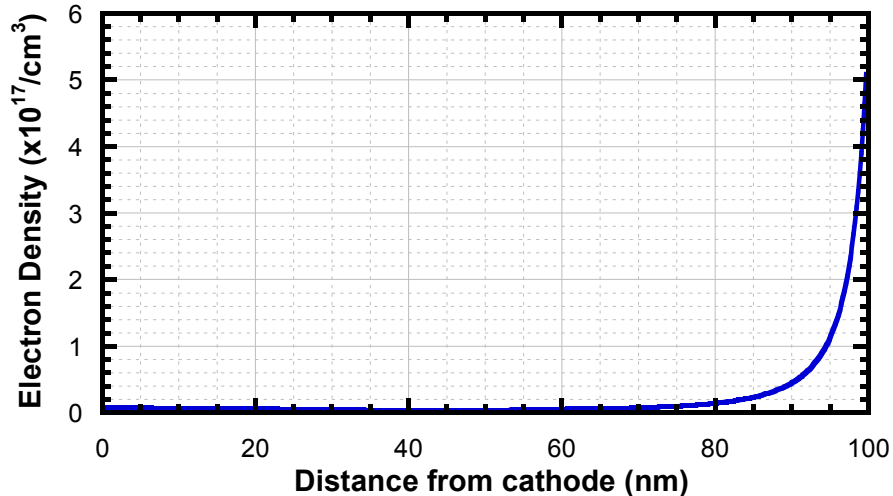


Figure 6.50: Modelled electron density with applied bias of 0.2 V above flat band conditions, i.e. ~2.4 V.

Figure 6.50 models a 100 nm thick F8BT device (using the model described in Section 3.5 and employed in Chapter 5) with ohmic injection of electrons and no extraction at the anode, under an applied bias of approximately 2.4 V – similar to that used in the experiments presented in this Chapter. The accumulation of electrons at the anode interface can be clearly distinguished. Repeated modelling shows, as expected, that at higher applied biases the electron density is greater and more closely pinned to the anode. The enhancement of hole injection by electron space charge is depicted schematically in Figure 6.51. No such barrier to electron extraction is predicted in the ITO-only case. This may explain the relatively slow progress of drive-induced enhancement in ITO-only devices.

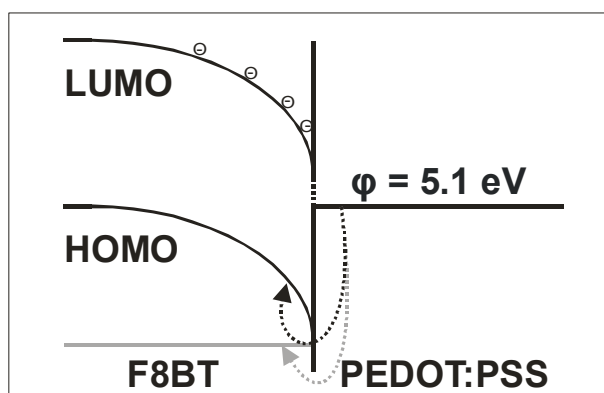


Figure 6.51: Schematic – accumulation of electrons enhances hole injection.

6.13.3 Necessity of trapping

Under normal circumstances equilibrium is soon reached. The mutual Coulomb repulsion of the electrons limits their ultimate concentration adjacent to the anode, and holes injected into this electron field are likely to undergo rapid recombination, since recombination rate is proportional to the local concentration (as seen in Section 2.4.5). However if one of the charge carriers becomes trapped, the recombination process may become frustrated. Electrons and holes continue to experience each other's mutual Coulomb attraction, but cannot achieve the activation energy required to de-trap the and proceed to radiative recombination. If all the charge backflow measured in Section 6.6.2 were concentrated within 10 nm of the anode in that most extreme example, the average equivalent charge density would be $5 \times 10^{19} / \text{cm}^3$. This is high, but not physically unrealistic. The precise means for the prevention of recombination is not addressed here.

Since holes and electrons can now co-exist without rapid recombination, they are essentially both trapped – one species in a real trap and the other Coulombically attracted to it. The holes appear to cancel some of the electron charge as seen from the cathode, allowing further electron injection to take place. This leads to a gradual increase in the electron density adjacent to the anode, which can be dynamically balanced by concomitant hole injection. There need not be any special interface trap sites in order for the trapping to be predominantly located near the anode contact. Rather, the increased electron and hole densities in this region mean that trap-filling transitions are correspondingly more likely to occur.

The charge carrier trapped in F8BT is very likely to be holes, since F8BT is known to be a good electron transporter with heavily trapped hole transport^{1,50}. However, the mechanism here does not require any assignment of the sign on the trapped charge, since the counterspecies is taken to be also present locally.

6.13.4 Barrier narrowing

As injection proceeds from both contacts, a new configuration emerges, depicted in Figure 6.52.

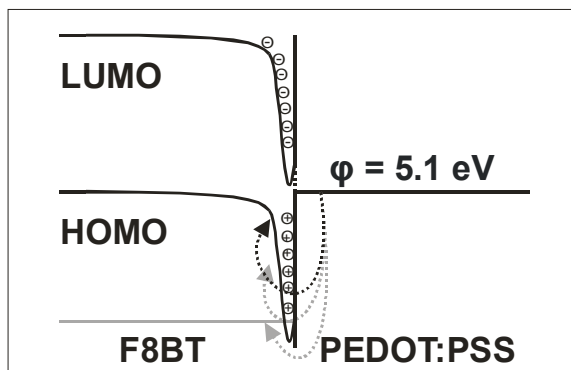


Figure 6.52: Schematic – high density of local charges, with field dropped across a shorter distance.

The addition of localised trapped hole charge density lifts the unipolar charge density limit for electrons. The enhanced local electron density produces a much sharper band bending near the anode, while the holes, localised in the immediate vicinity of the anode, cause local band bending in the opposite sense to that created by the electrons. The net result, effectively due to a dipole sheet created by the non-coincident electron and hole space charge fields, is a very sharp modulation of the band curvature near the anode, seen as a severe narrowing of the barrier for injection.

The expected behaviour for a net dipole would to re-orient so as to oppose the applied field. However, the device is in a dynamic equilibrium, with recombinant electrons and holes constantly replaced by fresh injection from the electrodes. This favourable situation produces the narrowing of the triangular barrier for hole injection into the polymer, and reduces the energy difference between initial and final states for hole injection. Hole injection is therefore significantly enhanced, leading to the increase in quantum efficiency.

6.13.5 Recovery and back-current

Under the proposed framework, the observed recovery of the undriven state can be understood as a thermally-activated de-trapping, followed by either recombination or extraction at the contacts. It is possible that any such recombination process could be experimentally observed as a very delayed emission process, if a single-photon detection apparatus were employed to count such events. The back-flow of charge, by extraction at the electrodes, has been experimentally confirmed in this Chapter.

6.13.6 Excess back-current

The presence of significant quantities of hole space charge inside the polymer means that the device as a whole cannot be considered exclusively electron space-charge limited. The co-operative trapping process allows injection of excess charge. According to the hypothesised theory, successful extraction of charge from the device during the recovery process competes with the internal recombination route. Thus the externally measured recovery current, though large, is likely to be an underestimate of the true quantity of trapped charge.

6.13.7 Reverse bias enhancement

One of the most unexpected features of the enhancement effect was the experimentally observed enhancement produced by applying a reverse bias after driving. As noted above, the dipole sheet has a tendency to orient counter to the applied field. In forward bias this is only prevented by the dynamic

equilibrium which constantly replenishes the recombined electrons and holes. In reverse bias, however, there is no injection, and any reorganisation of the dipole sheet will lead to a configuration which is favourable in the subsequent forward bias. On re-application of the forward bias, the net charge separation responsible for the dipole sheet is significantly more extreme than before, and the field drop adjacent to the anode correspondingly stronger. This would explain the initial increase in enhancement, by further improvement of the hole injection properties, following a period of reverse bias.

It should be noted that F8BT itself contains a permanent dipole, in the benzothiadiazole unit. Any realignment of this unit near the interface could be in part responsible for the observations. However, the permanent dipole is present regardless of whether the device has been recently driven, whilst augmentation of the drive-induced enhancement effect requires that the effect be present already.

6.14 Implications for device physics

For devices based on F8BT, the drive-induced enhancement effect appears to be a significant consideration at low applied bias, current density and luminance. As seen in Section 6.4.2, it can even become an issue at useful operational intensities.

6.14.1 Presence in other polymers

The importance of drive-induced enhancement in other light-emitting polymers has been largely ignored in this Chapter, primarily because the initial tests showed that, if present, it did not occur on a timescale accessible by DC experiments. However the reverse bias efficiency enhancements, seen here under pulsed electrical drive of F8BT with a reverse bias in the off-phase, *have* been reported in other polymers.

Pinner²⁹ reported such a phenomenon in a PPV copolymer, entirely unrelated to F8BT. Studies during the experimental work for this thesis showed the same effect in the blue copolymer discussed above in Section 6.2.3, which did not show evidence for long-term drive-induced enhancement. Published work on luminescence enhancement in small-molecule devices at constant voltage, after reverse pre-biasing, shows increased luminescence but cannot unambiguously explain the observations⁴⁰.

LEDs based on F8 have shown signs of drive-induced enhancement when subjected to low duty-cycle pulsed electrical drive.

Pulsed mode transient electroluminescence experiments on many polymers yield an intriguing hint at the presence of drive-induced enhancement, namely the logarithmic rise in luminance with time at constant voltage, as seen in DC measurements in Section 6.3.2 and whenever the course of long-term transients are plotted⁵¹. In the case of pulsed-mode electrical driving, although a series of universal features have been identified and explained^{11,29}, there is no established explanation in the literature for a “third rise” in the electroluminescence, which is nevertheless often observed at “long” times, after the initial transients have settled⁴⁶. Experimental work conducted during the investigations presented in this thesis, largely through varying the active area⁵², showed that the “third rise” was not attributable to heating effects. In the absence of any other explanation, it may be that this final rise, matching the logarithmic shape of the long-term electroluminescence increase in F8BT, is simply a shorter time-scale manifestation of the same effect, and that to some extent drive-induced enhancement is present generally across a range of polymers. Such a finding would produce a natural mechanism for the enhancement of efficiency by reverse pre-biasing of polymer LEDs, by analogy with the F8BT case described in this Chapter. Though reported before now, this aspect of device operation has never been assigned a satisfactory explanation.

6.15 Conclusions

The previously unreported reversible enhancement in EL quantum efficiency in F8BT LEDs on driving has been studied and attributed to an enhancement in hole injection properties at the anode. Ionic effects have been ruled out, and the phenomenon has been attributed to trap-assisted enhancement of the local field at the anode.

The effect has been shown to be enhanced, rather than reset, by the subsequent application of reverse bias. Application of this phenomenon under pulsed drive has been shown to provide efficiency improvements without any apparent detriment to the device. Moreover, this improvement has been seen in polymers which did not show any evidence for drive-induced enhancement on the timescales accessible by DC experiment, but which nevertheless showed the logarithmic rise characteristic of drive-induced enhancement when examined under transient pulsed electroluminescence. The reverse-bias enhancement of electroluminescence efficiency, which appears to be part of the drive-induced enhancement effect, is therefore an important consideration for all organic electroluminescence applications.

This is commercially important because many practical products are likely to be driven under pulsed conditions. This work explains for the first time why quantum efficiency is maximised by application of a reverse bias in the off phase. Indeed, it implies that in many cases reverse pre-biasing is required to

optimise the device performance. Such an enhancement in device performance, with no apparent penalty, is of great significance as light-emitting polymer technology continues to find commercial applications.

6.16 References

- ¹ A. J. Campbell, D. D. C. Bradley, and H. Antoniadis, *Appl. Phys. Lett.* **79**, 2133-2135 (2001).
- ² A. S. Dhoot and N. C. Greenham, *Materials Research Society Symposium Proceedings* **725**, 8.2.1-8.2.6 (2002).
- ³ D. G. Ma, J. M. Lupton, R. Beavington, P. L. Burn, and I. D. W. Samuel, *J. Phys. D-Appl. Phys.* **35**, 520-523 (2002).
- ⁴ T. W. Lee and O. O. Park, *Appl. Phys. Lett.* **77**, 3334-3336 (2000).
- ⁵ P. W. M. Blom, M. J. M. DeJong, and S. Breedijk, *Appl. Phys. Lett.* **71**, 930-932 (1997).
- ⁶ P. W. M. Blom, M. J. M. DeJong, and M. G. Vanmunster, *Phys. Rev. B-Condens Matter* **55**, R656-R659 (1997).
- ⁷ A. J. Campbell, M. S. Weaver, D. G. Lidzey, and D. D. C. Bradley, *J. Appl. Phys.* **84**, 6737-6746 (1998).
- ⁸ N. Tessler, N. T. Harrison, D. S. Thomas, and R. H. Friend, *Appl. Phys. Lett.* **73**, 732-734 (1998).
- ⁹ N. Tessler, *Adv. Mater.* **11**, 363-370 (1999).
- ¹⁰ J. C. Sturm, W. Wilson, and M. Iodice, *IEEE J. Sel. Top. Quantum Electron.* **4**, 75-82 (1998).
- ¹¹ D. J. Pinner, R. H. Friend, and N. Tessler, *J. Appl. Phys.* **86**, 5116-5130 (1999).
- ¹² J. C. deMello, N. Tessler, S. C. Graham, and R. H. Friend, *Phys. Rev. B-Condens Matter* **57**, 12951-12963 (1998).
- ¹³ J. C. deMello, N. Tessler, S. C. Graham, X. Li, A. B. Holmes, and R. H. Friend, *Synth. Met.* **85**, 1277-1278 (1997).
- ¹⁴ G. G. Malliaras and J. C. Scott, *J. Appl. Phys.* **85**, 7426-7432 (1999).
- ¹⁵ A. R. Schlatmann, D. W. Floet, A. Hilberer, F. Garten, P. J. M. Smulders, T. M. Klapwijk, and G. Hadzioannou, *Appl. Phys. Lett.* **69**, 1764-1766 (1996).
- ¹⁶ K. Murata, S. Cina, and N. C. Greenham, *Appl. Phys. Lett.* **79**, 1193-1195 (2001).
- ¹⁷ G. Greczynski, T. Kugler, and W. R. Salaneck, *Thin Solid Films* **354**, 129-135 (1999).
- ¹⁸ G. C. M. Silvestre, M. T. Johnson, A. Giraldo, and J. M. Shannon, *Appl. Phys. Lett.* **78**, 1619-1621 (2001).
- ¹⁹ P. K. H. Ho, J. S. Kim, J. H. Burroughes, H. Becker, S. F. Y. Li, T. M. Brown, F. Cacialli, and R. H. Friend, *Nature* **404**, 481-484 (2000).
- ²⁰ C. Silva,; (2003).
- ²¹ J. S. Kim, P. K. H. Ho, C. E. Murphy, N. Baynes, and R. H. Friend, *Adv. Mater.* **14**, 206-+ (2002).
- ²² A. J. A. B. Seeley, *Unpublished*, (2000).
- ²³ P. K. H. Ho, *Personal Communication* (2002).
- ²⁴ J. W. Yu, M. Hayashi, S. H. Lin, K. K. Liang, J. H. Hsu, W. S. Fann, C. I. Chao, K. R. Chuang, and S. A. Chen, *Synth. Met.* **82**, 159-166 (1996).
- ²⁵ U. Wolf, S. Barth, and H. Bassler, *Appl. Phys. Lett.* **75**, 2035-2037 (1999).

- 26 M. W. Klein, D. H. Dunlap, and G. G. Malliaras, *Phys. Rev. B* **64**, 195332 (2001).
- 27 J. Wang, R. G. Sun, G. Yu, and A. J. Heeger, *Journal of Applied Physics* **91**, 2417-2422 (2002).
- 28 A. J. A. B. Seeley, *Unpublished*, (2002).
- 29 D. J. Pinner, *Ph.D. Thesis, University of Cambridge*, 2000.
- 30 A. S. Dhoot and N. C. Greenham, *Adv. Mater.* **14**, 1834-1837 (2002).
- 31 A. S. Dhoot, *Personal Communication* (2002).
- 32 J. Morgado, E. Moons, R. H. Friend, and F. Cacialli, *Adv. Mater.* **13**, 810-+ (2001).
- 33 L. M. Herz and R. T. Phillips, *Phys. Rev. B* **61**, 13691-13697 (2000).
- 34 M. Ariu, D. G. Lidzey, M. Sims, A. J. Cadby, P. A. Lane, and D. D. C. Bradley, *J. Phys.-Condes. Matter* **14**, 9975-9986 (2002).
- 35 M. Gross, D. C. Muller, H. G. Nothofer, U. Scherf, D. Neher, C. Brauchle, and K. Meerholz, *Nature* **405**, 661-665 (2000).
- 36 F. Huang, A. G. Macdiarmid, and B. R. Hsieh, *Appl. Phys. Lett.* **71**, 2415-2417 (1997).
- 37 Q. B. Pei, G. Yu, C. Zhang, Y. Yang, and A. J. Heeger, *Science* **269**, 1086-1088 (1995).
- 38 D. D. C. Bradley and R. H. Friend, *J. Phys.-Condes. Matter* **1**, 3671-3678 (1989).
- 39 M. Stoessel, G. Wittmann, J. Staudigel, F. Steuber, J. Blassing, W. Roth, H. Klausmann, W. Rogler, J. Simmerer, A. Winnacker, M. Inbasekaran, and E. P. Woo, *J. Appl. Phys.* **87**, 4467-4475 (2000).
- 40 D. C. Zou, M. Yahiro, and T. Tsutsui, *Jpn. J. Appl. Phys. Part 2 - Lett.* **37**, L1406-L1408 (1998).
- 41 J. H. Krieger, S. V. Trubin, S. B. Vaschenko, and N. F. Yudanov, *Synth. Met.* **122**, 199-202 (2001).
- 42 I. H. Campbell, D. L. Smith, and J. P. Ferraris, *Appl. Phys. Lett.* **66**, 3030-3032 (1995).
- 43 Y. F. Li, J. Gao, G. Yu, Y. Cao, and A. J. Heeger, *Chem. Phys. Lett.* **287**, 83-88 (1998).
- 44 M. Meier, S. Karg, and W. Riess, *J. Appl. Phys.* **82**, 1961-1966 (1997).
- 45 G. Paasch and S. Scheinert, *Synth. Met.* **122**, 145-147 (2001).
- 46 W. Riess, H. Riel, T. Beierlein, W. Brutting, P. Muller, and P. F. Seidler, *IBM J. Res. Dev.* **45**, 77-88 (2001).
- 47 G. Yu, Y. Cao, C. Zhang, Y. F. Li, J. Gao, and A. J. Heeger, *Appl. Phys. Lett.* **73**, 111-113 (1998).
- 48 I. H. Campbell, D. L. Smith, C. J. Neef, and J. P. Ferraris, *Appl. Phys. Lett.* **78**, 270-272 (2001).
- 49 H. L. Gomes, P. Stallinga, H. Rost, A. B. Holmes, M. G. Harrison, and R. H. Friend, *Appl. Phys. Lett.* **74**, 1144-1146 (1999).
- 50 A. J. Campbell, D. D. C. Bradley, and H. Antoniadis, *J. Appl. Phys.* **89**, 3343-3351 (2001).
- 51 S. Das, G. B. Talapatra, A. Chowdhury, and A. J. Pal, *J. Appl. Phys.* **88**, 6457-6461 (2000).
- 52 C. I. Wilkinson, D. G. Lidzey, L. C. Palilis, R. B. Fletcher, S. J. Martin, X. H. Wang, and D. D. C. Bradley, *Appl. Phys. Lett.* **79**, 171-173 (2001).

7. Conclusions and Further Work

In this Chapter, the major findings of the preceding Chapters are reviewed. Suggestions are put forward for further work which would build on those findings.

7.1 Interactions of PFB and PEDOT:PSS

It was demonstrated that whilst the PEDOT:PSS complex is used as an anode in conjugated polymer LEDs, the PSSH majority component undergoes an electrochemical reaction with PFB when the two materials are in direct contact. The reaction was studied using PDS, and by varying the sample properties it was seen to be:

- Confined to the interface between PFB and PSSH
- Unaffected by baking of the PSSH layer
- No further advanced by annealing the layers in contact
- Activated by light above the band-gap

The reaction was compared to previous work on the degradation of PFB-based devices during electrical driving. Micro-Raman work on degraded devices had revealed a characteristic rebalancing of two particular spectral peaks which indicate the progress of degradation. Electrochemically oxidised PFB shows the same Raman rebalancing as the degraded LED, and similar absorption spectral changes to those seen in PFB in contact with PSSH. Thus electrical degradation, electrochemical oxidation and light-activated PFB-PSSH interaction are all traced to the formation of the same species in the PFB. Those species are suggested to be radical cationic and dicationic states of PFB, induced by the protonic doping of PFB by PSSH.

The PFB:PSSH interface is therefore found to be unstable against changes induced by electrical driving or above band-gap illumination. This is likely to extend to all triarylamine-based polymers in contact with

PSSH, and probably to the small-molecule triarylamines when used in contact with polyaniline doped by the closely-related camphor sulphonic acid.

7.2 Morphology and electroluminescence transients

A series of devices containing TFB and F8BT were examined under pulsed electroluminescence, revealing a morphology-dependent spike transient at turn-on. The spike was most pronounced in bi-layer devices, and progressively less so through the blend, block copolymer and random copolymer variants.

Simple estimates were made for the electron and hole mobilities in the two polymers by application of the Mott-Gurney equation for space-charge limited currents in unipolar devices. The values found compare favourably with device-based data found in the literature, where available.

$$\begin{array}{ll} \mu_h(\text{F8BT}) = 1.2 \times 10^{-8} \text{ cm}^2/\text{Vs} & \mu_h(\text{TFB}) = 2.0 \times 10^{-6} \text{ cm}^2/\text{Vs} \\ \mu_e(\text{F8BT}) = 4.9 \times 10^{-5} \text{ cm}^2/\text{Vs} & \mu_e(\text{TFB}) = 6.5 \times 10^{-8} \text{ cm}^2/\text{Vs} \end{array}$$

These values were entered into a numerical model which was used to simulate the behaviour of F8BT-only, TFB-only and bi-layer devices. The F8BT-only model showed a good fit to experiment without significant modification. The TFB-only model showed a poor fit to experiment, and this was attributed to the poor extraction of charges from TFB between electrical pulses and a possible underestimate of the hole mobility. The bi-layer model showed clear evidence for the turn-on spike transient, which was not present in the single layer simulations. It correctly predicted both the maximum magnitude of the transient, and the applied bias at which it would occur.

By running the numerical model multiple times to different end-points, the evolution of space charge inside the device could be visualised. The turn-on spike was thus traced to a feedback mechanism between the transport of one charge carrier and the subsequent injection rate of the other. No new physics or hidden device parameters were required to justify the presence of the spike.

7.3 Drive-induced enhancement effect in F8BT LEDs

The behaviour of F8BT-based LEDs at low applied bias was studied. The quantum efficiency of such devices was seen to increase by a factor of up to 60 during the early stages of driving.

The effect was found to be recoverable with resting, heating or illumination of the device, but not by reverse bias application. It was accompanied by very large quantities of charge measured exiting the device during recovery in the dark. There was no measurable change in the photoluminescence efficiency or spectrum, whilst the electroluminescence spectrum suggested a small shift in the recombination zone away from the cathode.

Ionic motions were ruled out by the irreversibility of the effect on application of a reverse bias. A charge trapping model was proposed, probably caused by hole trapping near the anode, in which the large coexistent and non-recombinant electron and hole space charge densities generate a very sharp electric field drop in the region of the anode, due to their imperfect coincidence. The enhanced electric field yields improved hole injection into the polymer, alleviating the limiting step for injection balance and efficient light emission in F8BT devices.

The effect was linked to the previously reported enhancement of electroluminescence in conjugated polymer LEDs through negative pre-biasing of the pixels. It was noted that whilst drive-induced enhancement on the timescale of minutes and hours is confined to F8BT, the negative pre-bias benefits are common to many polymers, and may be attributable in those polymers to an analogous effect with smaller trapping energies and much faster time constants.

7.4 Further investigations

The work presented in this thesis suggests a selection of possible follow-up work.

The investigations of the drive-induced enhancement effect may be followed up by a fuller characterisation of F8BT as a charge-transporting material. Deep-level transient spectroscopy¹ and thermally stimulated currents²⁻⁴ may yield quantitative data on the trap distributions and a definitive assignment of the enhancement effect to electrons or holes.

The intriguing link between negative pre-biasing of polymer LEDs to enhance efficiency, and the enhancement effect, could be examined in greater detail. A clearer establishment of the link between the two effects in F8BT may lead to an understanding of the processes which enhance efficiency in other polymer LEDs after negative pre-bias.

It may be instructive to measure an F8BT LED in recovery (after driving through the enhancement process), by monitoring the device in the dark with a sensitive photomultiplier tube or other photon detection

apparatus. If there really are significant quantities of electrons and holes confined Coulombically, then detrapping might be expected to yield a proportion of delayed recombination events and subsequent light emission. This would be a very direct probe of the recovery process.

Pulsed measurements similar to those made in Section 6.10 have been made on F8BT devices before and after degradation (not presented in this thesis). They appear to show that electrical degradation is characterised by an increase in the barrier to hole injection. Further characterisation of this effect may prove instructive, particularly in the light of the protonation experiments in Chapter 4, and the interface dipoles explained in Section 4.6.2 which lead to reduced hole injection in PFB.

In the light of the proposed mechanism for the interaction between PFB and PSSH, it would be interesting to compare the behaviour of other nitrogen-containing polymers such as TFB and the carbazoles.

The pulsed measurements on complex heterostructures would greatly benefit from a model allowing 2- or 3-D distributions of polymer, rather than the simple 1-D model currently employed. Additionally, the freedom to set up any specified start conditions, for example to simulate residual charge distributions from a previous pulse, would be very instructive.

7.5 New experiments

A collection of new techniques have been developed during work on this thesis, which show promise for future application in the investigation of polymer LEDs.

The charge modulated PDS experiment has been demonstrated to produce results (e.g. bleaching of the $\pi-\pi^*$ absorption) as expected from theory. The experiment should be fully characterised, and the implications of extrinsic phenomena on the data produced should be thoroughly examined.

Although no data was presented in this thesis (except example in Section B.4.1.2), a monochromated transient experiment was designed, built and tested, to allow transient electroluminescence data to be gathered as a function of both time and wavelength. This should prove useful in the investigation of bi-layer LEDs in particular where device evolution may lead to a redistribution of the recombination zone around the heterojunction.

There is an ever-increasing interest in understanding the degradation processes in polymer LEDs. The Test Box provides a useful platform for measurements of drive and resting behaviour over extended periods of

time, with complex drive schemes including pulsed drive, switched drive, constant voltage and constant current all readily accessible.

7.6 Conclusions

In conclusion, a number of phenomena associated with the use of polyfluorene-based polymers in LEDs have been investigated. Trapping and degradation have proved to be significant factors in the short-term and long-term evolution of device performance, and a greater understanding of these processes will undoubtedly be gained as the field advances.

Three new experiments have been designed and are available for further investigations.

7.7 References

- ¹ *H. L. Gomes, P. Stallinga, H. Rost, A. B. Holmes, M. G. Harrison, and R. H. Friend, Appl. Phys. Lett. **74**, 1144-1146 (1999).*
- ² *N. Von malm, J. Steiger, H. Heil, R. Schmechel, and H. Von seggern, J. Appl. Phys. **92**, 7564-7570 (2002).*
- ³ *P. Stallinga, H. L. Gomes, H. Rost, A. B. Holmes, M. G. Harrison, R. H. Friend, F. Biscarini, C. Taliani, G. W. Jones, and D. M. Taylor, Physica B **274**, 923-926 (1999).*
- ⁴ *M. Meier, S. Karg, K. Zuleeg, W. Brutting, and M. Schwoerer, J. Appl. Phys. **84**, 87-92 (1998).*

A. The PDS Rig - Notes

In this Appendix, information is presented to assist future users in the maintenance and running of the PDS Rig. The user is referred to Section 3.3.3 for a summary of the principles of operation of the Rig, and the important changes made during the execution of this work.

A.1 Part-by-part Tour

This section lists the main components of the Rig. It is recommended that this be read while looking at the Rig itself.

A.1.1 Computer and software

The Rig runs on a Power Macintosh desktop computer, equipped with GPIB interface for communication with the apparatus. The LabView environment is installed on the computer, and the PDS Rig controller application is a suite of applications which runs within LabView, to control the experiment. The PDS Rig controller application was written by Dr D.S. Thomas, updated and modified by the author.

A.1.2 Heating Beam delivery

The heating beam is generated by a 100 W xenon arc lamp. The lamp housing is custom-built for this application by Light Support Ltd. A dedicated power supply provides two power channels, for the lamp itself and for the cooling fan, controlled by switches on the supply front panel. The chopper wheel is a two-slit (50:50 on/off) foil, mounted on a motor/sensor unit. It has a dedicated controller unit which measures the sensor signal to ensure frequency and phase matching of the wheel with the selected signal. The 13 Hz reference signal is provided externally by the Stanford lock-in amplifier. This frequency is selected to avoid interference from mains hum, and to maximise the signal strength without introducing undue 1/f noise.

The first filter wheel (open to view) is for rejection of higher order diffracted beams, so that for instance an 800 nm beam does not contain a 400 nm component. This is located *before* the beam enters the monochromator, while the beam is still in air. Ten low-pass filters are present, and as a scan proceeds from short wavelength to long, the filters are introduced in a trailing manner, at <400 nm, 400 nm, 450 nm, 475 nm, 500 nm, 550 nm, 640 nm, 800 nm, 1100 nm and 1950 nm. The filters do not have perfectly sharp cut-offs, and the monochromator passes a range of wavelengths, so introducing a filter at exactly its nominal cut-off point would change the spectral composition of the beam and create an artefact. The stepper motor which turns the filter wheel is driven by the monochromator's external port. The computer therefore addresses the stepper motor by sending commands to the monochromator. The second filter wheel (inside the bolt-on box at the monochromator's input slit) contains five neutral density filters and one blank, to allow the beam to be attenuated if it becomes too strong. This wheel is part of the monochromator and is addressed by communication with the monochromator's interface.

The monochromator contains a 3-sided turret bearing three diffraction gratings. Each grating has a different blaze angle, giving each one an optimal spectral region for operation. Grating 1 is used for the shortest wavelengths. The monochromator also contains an entrance slit and an exit slit, which can be varied in width but *not* independently. The range available is 50 μm to 2 mm. The widest slits should always be used, to allow the maximum light intensity to pass. This also allows a greater bandpass, which reduces the resolution of the experiment, but not unacceptably so. The monochromator exit slit is equipped with a *f*/number-matching optic to direct the processed beam into a multimode fibre leading to the optical table.

A.1.3 Probe beam delivery

The probe beam is provided by a fibre-coupled Peltier-cooled laser diode. The beam is delivered to the optical table by fibre to minimise local noise. At the time of writing, the useful life of the original laser had expired, and a replacement is on order from Point Source Ltd.

A.1.4 Optical table

The heating beam arrives (red fibre) and is collimated then split by a glass optical flat. A proportion of the beam goes to the dual photodiode, which is used to normalise the experiment for lamp intensity. This photodiode presents its outputs to the analogue lock-in amplifier. The main beam is focused onto the sample surface. The probe beam arrives (steel-clad fibre) and is directed transversely across the sample surface, at exactly the point where the heating beam hits. It first passes through a cylindrical lens to produce a

squeezed narrow-waist beam where it passes over the sample surface. It proceeds to the paired quadrant photodiode, which detects the beam deflection.

The quadrant photodiode measures the instantaneous left/right position of the probe laser beam. The DC component of this deflection drifts during the course of an experiment, leading to possible signal saturation if the photodiode output drifts too far. (This occurs when the output signal equals the supply voltage). To counteract the DC drift, the photodiode is mounted on an electronic translation stage. A die-cast metal box on the beam generation table selects between “manual” and “automatic” operation. In manual mode, the stage can be moved by use of the hand-held remote controller, also on the beam generation table. In automatic mode, the stage is moved under computer control, by using an output from the Stanford lock-in. Automatic mode *must* be enabled during an experimental run.

A.1.5 Rack trolley

On the rack trolley are mounted two lock-in amplifiers and a shelf containing several other components. The analogue lock-in takes a sync signal from the Stanford lock-in, and uses it to measure the intensity detected by the dual photodiode, for normalisation purposes. The Stanford lock-in is the main piece of measurement apparatus. It measures the deflection value, and passes this back to the computer. It also measures the output of the analogue lock-in, provides the sync frequency for the whole experiment, and acts as an interface for the electronic translation stage.

The laser diode is kept on the rack shelf. Also present is a power supply which feeds the dual photodiode. A die-cast box contains batteries which provide a very stable power source for the deflection photodiode.

A.2 Replacement parts

Several items can be considered consumables for the PDS Rig.

A.2.1 Batteries

The deflection photodiode requires two PP9 batteries to provide a stable power source. These are housed in the die-cast box on the rack trolley. They require replacement approximately once per month, regardless of the use of the Rig. This is a simple matter of unscrewing the box and replacing the batteries.

A.2.2 Xenon lamp bulb

The bulb in the xenon lamp has a limited lifetime, and once it becomes unstable, noise is introduced into the experiment. Spares should be kept to hand at all times. Depending on usage, bulbs should last between 2 and 6 months.

The bulb required is an “XBO 100 OFR”, manufactured by Osram and available from Light Support Ltd. “100” denotes a 100 W bulb, and “OFR” denotes “ozone free”. The bulb filters out hard UV which otherwise would generate problematic levels of ozone in the lab.

Bulb replacement is not difficult but must be done with care, since the glass envelope contains pressurised xenon and can explode if broken. A leather apron and Kevlar gloves (both available in the support office) and a face shield (kept near the PDS Rig) must be used whenever the lamp housing is taken off.

The lamp must be switched off, completely cooled and disconnected before work begins. Screws on the rear of the housing release the enclosure. (The adjustment allen key on the top of the box must be removed if present to allow the enclosure to lift off.)



Figure A.1: Inside the lamp housing. The bulb is shown, including fixed clamp (bottom) and wired clamp (top).

The bulb is secured top and bottom by metal rings adjusted with an allen key. The bottom connection of the bulb is fixed, whilst the top connection is free to move (see Figure A.1). Bulbs come in a protective plastic housing, and it may be helpful to re-attach the housing (stored nearby) before removing the old bulb, and keep the new bulb in its housing until after it is installed. To avoid any risk of shattering the bulb, the bottom must be released first and re-secured last, since torque applied at the top of the bulb could break it.

Noting the orientation of the bulb (see the pointed tip inside the bulb), the bottom should be released and lifted free. Only then should the top be released. The new bulb can now be inserted to the top ring, secured, inserted into the bottom ring, and finally secured again. The plastic safety housing can now be removed. The old bulb should be disposed of following current laboratory procedures. The lamp case can finally be re-assembled and screwed shut.

A.2.3 Cuvette

Occasionally the Spectrosil-B cuvette may become damaged or cracked. In such a case, it should be replaced with an exact copy as detailed in the laboratory Equipment Record. Such a replacement cuvette is currently on standby in the lab, and since they are made to order, one should always be kept on hand to avoid delaying experiments.

A.2.4 Fluorinert FC-104™ (3M Corp)

A stock of the deflection fluid, Fluorinert, is available in The Cave and is reserved for PDS use. There should be enough for several years' use. Fluorinert is no longer in production, and when this runs out, an alternative will have to be found.

A.3 Maintenance

Besides replacement of consumables, the most important maintenance task is to align the beam production optics. This maximises the power throughput, to optimise the strength of the PDS signal and therefore the speed and quality of data acquisition. It should be done whenever the bulb is replaced. Additionally, lifetime-limited components (namely laser and lamp) can be managed to prolong their useful life.

A.3.1 Alignment of optics

The lamp must first be focused to produce maximum flux through the 2mm slit. This is done by focusing onto a blackened screen. Eye protection should be worn, and a welding mask is available for this purpose. The screen should be placed 20 to 25 cm from the front of the lens housing, to ensure the correct beam divergence after passing through the slits. (The lamp must be moved to achieve this.) The rear mirror, used to return light emitted in the backwards direction, must be released and withdrawn as far as possible. The controls for this are on the rear of the housing. The lamp should then be focused by use of the two lenses in

the lens assembly at the front. They are adjusted with plastic knobs on the lower side of the lens assembly tube which should be loosened only enough to allow the lenses to slide. They are not very free-running and may be difficult to adjust. The lamp bulb itself can be moved within the housing, by means of the controls indicated externally. When an image has been satisfactorily formed on the blackened screen, and the lenses fastened into place, the rear mirror can be moved forward until it produces an identical but inverted image, by focusing the reflected light back through the bulb itself. The mirror can be adjusted in the other two dimensions by use of the screws on the rear, to ensure than both images are concentric and providing maximum possible light flux at the centre.

The lamp must now be realigned with the monochromator. The *f*/number coupling optic at the exit slit must be removed, so that the outgoing light shines directly onto the curtain beyond. The monochromator should be set to pass light in the green region of the spectrum, for maximum sensitivity by the naked eye. The lamp should now be manoeuvred into place until the maximum amount of light is seen on the curtain beyond. Finally, the *f*/number coupling optic must be replaced. It should be adjusted to provide the maximum light throughput to the sample area, which can be achieved by eye, using a piece of white paper to scatter the light at a location behind the sample position where the illumination spot size is suitably large.

A.3.2 Lifetime of laser and lamp

The laser and the xenon lamp bulbs have limited lifetimes. The deterioration of the laser is characterised by noise on the lock-in display even without a sample in place. This is due to growing instability in the laser, and the onset appears to be quite sudden. At first it occurs sporadically for short periods, and measurements can be made as long as the instability does not cut in. Eventually, measurement becomes impossible and the laser must be replaced. The laser lifetime can be prolonged by only powering it up as required.

Lamp replacement is inevitable and relatively frequent. Nevertheless, it helps to turn off the lamp power (leaving the fan on at least for a while) when not in use. Lamp degradation can be characterised by a visible instability in the projection of the main beam. This produces power fluctuations at the sample surface which can reduce data quality.

A.4 Experimental procedure

The general operation is described in Section 3.3.3.

A.4.1 Software

The LabView environment should be started and the “PDS RIG” Virtual Instrument loaded. This can be found on the local hard drive, inside “New LabView Progs 5\PDS Progs”. Ensuring that all the other apparatus is switched on, the “Play” icon in LabView should be pressed. This will *not* start a scan, but rather will initialise the program and set up communications with the apparatus. The “Mono Remote” window will appear. This is the control panel for the monochromator, allowing specification of wavelength, grating, order-sorting filter, slit width and attenuation filter. After specifying a quantity, the corresponding “Go” button must be clicked to enact the change. No other change can be made until this is complete. For grating changes, this takes approximately 1 minute. All other changes take a matter of seconds. All these settings can be specified directly on the Mono Remote panel. However, “Filter” is the only one which does not provide feedback to the computer. Thus the computer is unaware of the initial state of this filter, and assumes it is in position 1. It is therefore vital, after checking that the computer believes it is set to filter 1, to manually rotate the filter wheel until this filter is in position. The correct filter, marked on the wheel, is completely transparent in the visible, and located adjacent to filter 10 which appears black. Filter 1 produces a faint blue/purple fluorescence when illuminated by the xenon lamp.

A.4.2 Sample positioning

The aluminium vice containing the sample cuvette is removed by sliding it out of the spring-clamp. This is taken intact to the glovebox (taking care not to pump the port below 0.8 atm, marked as -0.2 on the circular pressure gauge), or wherever the sample is to be exchanged. The cuvette and sample holder are released by loosening the finger-tight screw on top. The sample should be inserted into the sample holder and immersed in Fluorinert in the cuvette. Care should be taken not to crack the cuvette by over-tightening or by inadvertently pumping the pass box down below 0.8 atm when taking it into the glovebox. The entire aluminium vice should be placed back in the spring-loaded clamp, with the front surface of the sample illuminated by the heating beam. The sample stage should be manoeuvred such that the probe laser passes approximately over the surface of the sample.

To prepare for lining up a sample, the “Mono Remote” window should be used to set the slit width to 2000 µm, the grating to 1 (high-energy), the attenuation to 1 (no neutral density filter), the order-sorting filter to 1 (highest energy), and the wavelength near the peak absorption of the polymer, and often in the region of about 440 nm. Note that under manual control, the software does not automatically select a suitable grating for the specified wavelength, even though it does so during experimental operation. Even so, grating 1 should always be used for this step. On the Stanford lock-in the buttons near the top left should be used to set 100 ms time constant and 100 mV sensitivity (see Figure A.2). The translation stage control

should be set to Manual, and the hand-held control used to manoeuvre the translation stage left or right until the DC reading (centre display on lock-in) reads between -1 and +1 V.



Figure A.2: Front panel of the Stanford lock-in. All settings are as required for alignment.

Now an iterative process begins to optimise the sample position, by maximising the measured deflection on the lock-in. Two controls only are required (see Figure A.3). The *z*-axis control – a micrometer screw – moves the sample backwards and forwards *along* the *z*-axis (along which the heating beam shines) and the *y*-axis control – a small silver knob – moves the sample *about* the *y*-axis (vertical). Between these two, the sample can be aligned as close as necessary to the passing probe laser beam.

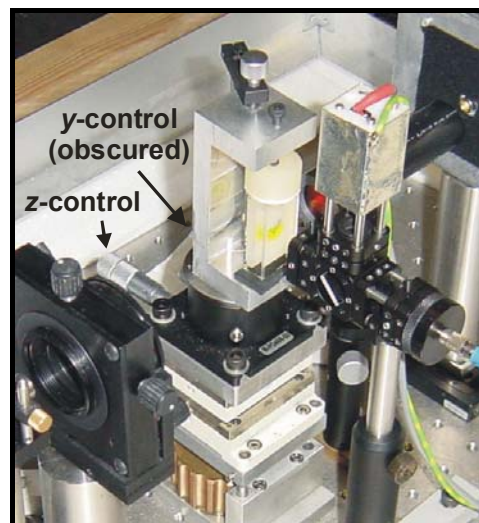


Figure A.3: Adjustment controls for aligning sample.

While monitoring the deflection amplitude (left-hand display on the lock-in), the *z*-axis control should be progressively varied until the deflection is maximised. The *y*-control should then be optimised, before repeating the cycle. Whenever the DC value (centre display on lock-in) exceeds ± 1 V, the electronic translation stage should be moved electronically to bring it back into alignment. By repeating this cycle, a strong signal of perhaps 10 mV (and certainly more than about 2 mV) should be achieved. When the signal can no longer be increased, alignment is complete. The crane should be used to lower the soundproofing box over the table, before the scan is commenced.

A.4.3 Running a scan

After sample alignment, the scan can be started. The “PDS Rig” window should be brought to the front, and the electronic translation stage controller *must* be set back to Automatic. A typical set of parameters (see Figure A.4) would be: “eV” (to select measurement following discrete steps in energy), start at 3.2 eV, finish at 0.6 eV, step size 0.01 eV, “TC Adjust” On (to automatically vary the time constant as the experiment increases in sensitivity), “Ave Adjust” On (to automatically increase the number of averages at high sensitivity), and Factor 1. By always scanning the same range of energies in the same step size, one single calibration file can always be used. The “factor” adjustment forces the rig to take that many multiple measurements at each step. Raising it to 2 or even 5 can increase the sensitivity of a noisy scan, but lengthens the acquisition time correspondingly. The boxes at the bottom of the window are prompts for notes on the current sample, which are copied directly into the output file.

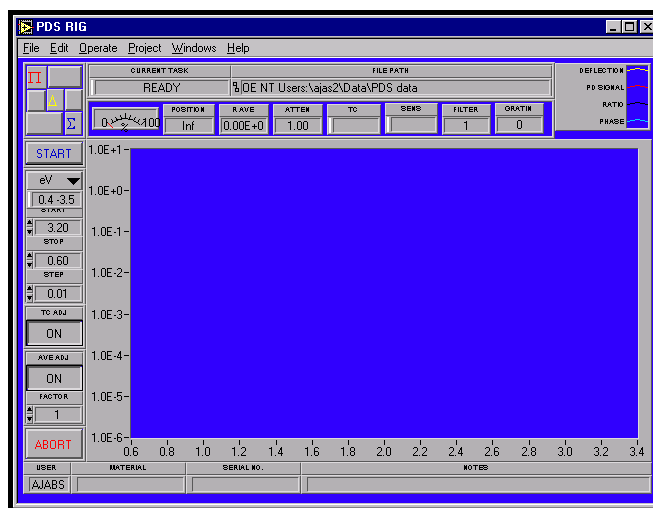


Figure A.4: PDS Rig main screen. Plots appear in the blue panel.

When all settings have been made, the “Start” button can be pressed. The program will prompt for a save location and then proceed to measure, plotting a graph as it goes. The black line represents the “ratio” (see below), which is the best estimate of absorption. It is recommended to save directly to the server. Since data acquisition can take many hours, it is useful to examine the data file remotely by FTP or direct connection to the server, which does *not* disrupt the scan.

A.5 Calibration and data processing

Although the PDS rig has an internal normalisation process, to account for the spectral features of the xenon lamp, it cannot automatically correct for the sensitivity gradient of the dual photodiode itself (which

performs the normalisation) nor any wavelength-dependence of the cuvette and Fluorinert. Therefore a calibration run is occasionally necessary. This calibration data can then be combined with any experimental scan to give a true representation of the absorption.

A.5.1 Calibrating the rig

A “black” sample should be prepared, for example lamp black, or black spray paint, on a glass substrate. The purpose is to provide above saturation-level absorption throughout the wavelength range of the rig. A standard scan should be run on this sample, using the same range and spacing of measurements (e.g. 3.2 to 0.6 eV in steps of 0.01 eV) as is used in experimental measurements. The “Ratio” column of this data file provides the calibration data, and should be saved for later use.

Usually the calibration file follows a straight line, and it may be better to replace the measured calibration data with a smoothed data set, to avoid the introduction of unwanted noise. If this is done, then as in this thesis it should be clearly stated. Noise is particularly problematic in such calibration runs because the high signal strength causes a short time-constant to be selected, and may not allow sufficient time for the analogue lock-in to settle after a filter-change. Thus spike-artefacts can be a big problem.

Figure A.5 shows a typical calibration data set, on linear axes, highlighting the danger of introducing unwanted noise if the raw calibration file were used to correct real experimental data. The best-fit straight line (after discarding obvious outliers) is also shown, and this is used for calibrating the real data shown in this thesis, to minimise the introduction of noise.

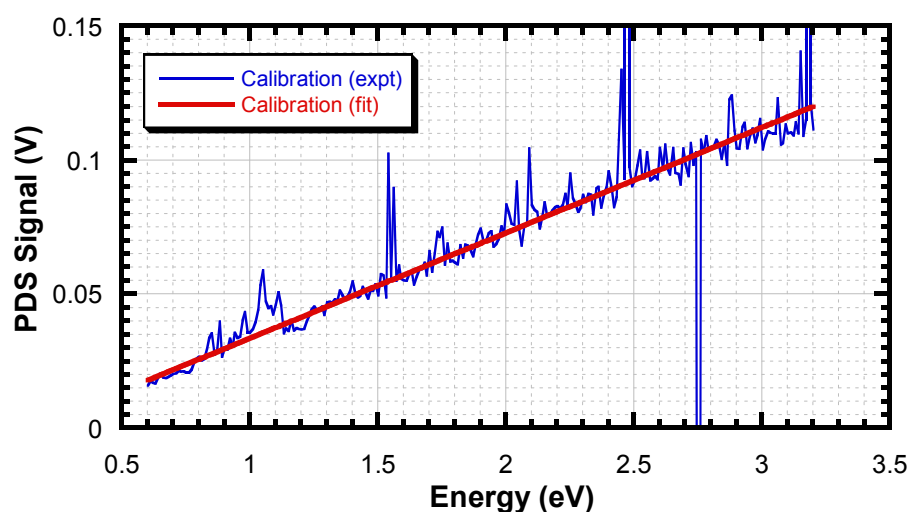


Figure A.5: Typical experimentally-obtained calibration data set, and best-fit straight line as used for correcting data in this thesis to avoid introduction of unwanted noise.
The largest noise spikes correspond to filter-changes in the illumination beam.

A.5.2 Data processing

The data file produced by the rig contains multiple columns. The first two columns contain the **wavelength** and **photon energy** at which the measurement was taken. The next column gives the measured **deflection magnitude**, in Volts. Column 4 contains the photodiode signal, which records the **illumination beam intensity**. Column 5 shows the *ratio* of the deflection to the beam intensity – that is, the **corrected deflection** after compensating for the spectral shape of the xenon lamp. Column 6 shows the **phase** data for the measured deflection, which normally measures around 80 to 100° for a strong absorption signal, and does not generally need to be examined in standard PDS. Columns 7 and 8 are reserved for the **calibration** and **absorption** data.

The calibration data should be cut-and-pasted in from a calibration data file using the same range and spacing of measurements. The final column of absorption data is then generated by dividing the “ratio” column by the “calibration” column.

A.5.3 Plotting

If a calibration file is used, the calibrated data should be plotted. Otherwise it may be sufficient to plot the raw “ratio” data. The chosen data must be plotted on a logarithmic *y*-axis to display the full dynamic range. It is usual to use Energy rather than Wavelength for the *x*-axis, which should be linear.

A.6 Errors during operation

Few problems should occur during operation. However, certain common problems may be easily rectified with reference to this section.

A.6.1 “Realign”

The PDS Rig status bar (in the main LabView window) displays the current status of the rig. Before the experiment starts, it should display “Ready”. During operation it will most often display “Taking Averages” and “Settle Filters” which are the two most time-consuming processes. “Change Grating” will appear twice during any full-spectrum measurement, for a minute or so each time. When the DC component of deflection goes outside ± 1 V, the computer triggers the lock-in to provide a voltage to the translation stage and realign it with the laser beam. If the translation stage is still set to Manual, this will have no effect, and the rig will

get stuck on the “Realign” state. The scan will proceed no further until the translation stage is set back to Automatic. Usually this will happen early in a scan, and the chosen spot on the measured sample may have been exposed to several hours of high-energy excitation by the time the problem is noticed. Therefore it may be preferable to begin re-measurement on a fresh area of the sample.

A.6.2 No deflection

If no deflection can be detected (left hand display on the lock-in), check the photodiode batteries by moving the electronic translation stage left and right. The DC signal (central display on the lock-in) should move between several volts positive and negative. If no such change is observed, and if the laser is reaching the photodiode and the battery unit knob is switched on (fully clockwise) then the batteries are dead and need replacing. When new they will give maximum deflections of more than ± 8 V, but will decay in time. If they go below about ± 3 V they should be changed immediately.

A.6.3 Crashdown

Crashdown refers to a phenomenon seen during PDS measurement where the first few data points show a collapse in the measured signal by an order of magnitude every two steps. The experiment then grinds almost to a halt as it attempts to ramp the sensitivity up to extremely high levels.

The cause of crashdown is actually an overload in the signal. If the signal becomes too large, an error is reported to the controller application, which does not understand error messages. Instead it believes it has seen a signal with zero intensity, and therefore ramps up the sensitivity by ranging down the lock-in. This of course exacerbates the problem. There is no simple solution, however re-booting the lock-in often helps in this situation. Reducing the alignment of the sample can be a last resort, as can beginning the scan at a slightly lower energy.

A.6.4 Probe laser artefact

A known artefact is sometimes present at 1.85 eV. This is the energy of the probe laser beam, and it can occur if the laser impinges too strongly on the sample surface. The width of the artefact is a useful indicator of the spectral resolution of the rig, since the spectral line-width of the laser is approximately 0.5 nm.

A.6.5 Failure to abort

If the user reaches the “Specify Filename...” stage and then chooses to Cancel in order to modify the scan parameters, the PDS Rig program will nevertheless go ahead and begin to measure, without successfully dumping the results to file. The user must therefore abort the scan when the main display returns.

A.7 Charge Modulated PDS experiment

The Charge Modulated PDS experiment uses a similar experimental set-up to the standard absorption PDS.

A.7.1 Rig conversion

The modification procedure for the Charge Modulated PDS experiment takes only a few minutes.

1. Exchange chopper wheel from 2-slot to 7/5 concentric wheel. (The wheel mounting must be removed from the aluminium bracket, taking care not to bend the wheel itself.) The illumination beam should pass through the inner section of the wheel only.
2. If required, insert cardboard shield to prevent stray light passing through the outer wheel.
3. On Chopper Unit front panel, change from 2-slot to 7/5-slot operation.
4. On Chopper Unit front panel, change from Sync Ext+ to Sync Int, so that the frequency is now specified by the Chopper Unit and not the lock-in amplifier.
5. On Chopper Unit front panel, change mode from H/S to +/-.
6. On Chopper Unit front panel, ensure that frequency is specified as 17 Hz.
7. Connect Drive Box (which powers the test LED) to F_{outer} on Chopper Unit front panel.
8. Remove lead which connects Sine Out (on lock-in front panel) to Sync In (on Chopper Unit).
9. Connect Out 1 (on Chopper Unit rear) to Ref In (on lock-in front panel). (Out 1 selects Difference Frequency, Out 2 would select Sum Frequency).
10. On lock-in front panel, change Trig from Sine to Pos Edge.
11. On lock-in front panel, turn OFF Source Internal.

The Rig can be straightforwardly returned to its original state by reversing these steps.

A.7.2 Scan preparation

The sample must be inserted into the powered sample holder (Figure A.6), and due to the non-encapsulated nature of the devices this will usually be done under nitrogen in the glovebox. Note that the holder is currently not well sealed (probably where the wires pass through). Whilst the standard holder remains sealed during pumping to 0.8 atm, the powered holder usually loses most of its Fluorinert. This should be properly sealed if the experiment is to be regularly used.



Figure A.6: Powered sample holder.

The LED is mounted in the sample holder, and silver dag is used to attach the contacts. The angled position of the LED ensures that the contacts do not obstruct the line-of-sight of the probe laser when it passes transversely across the front. The sample holder is then fixed into the aluminium clamp in reverse orientation, so that the incident heating beam can shine through the hole in the sample holder, and through the back of the device. Due to the protruding wires, the cuvette must be clamped slightly off-centre.

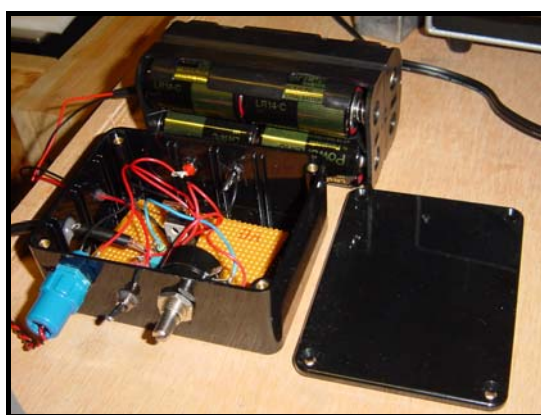


Figure A.7: The Drive Box, with its lid off.

The Drive Box converts the TTL output of the Chopper Unit into a modulated voltage supply with which to drive the test LED. A circuit diagram is provided in Figure 3.12. The two controls are an on/off switch and a rheostat controlling the voltage regulator. There is a pair of contacts (rear side of the box in Figure A.7) which are not modulated. These are useful for checking the currently-specified voltage, by connecting to a hand-held digital multimeter. The Drive Box is currently powered by a set of batteries, but could easily be modified to run off one of the existing PSUs in the rig.

The aluminium clamp and sample holder is re-inserted into the rig, such that the illumination beam arrives through the back of the sample and the probe laser passes across the front. The sample must be aligned in the rig by eye. This is perhaps the most difficult part, since in normal absorption PDS (as described earlier) the lock-in amplifier can be used. However in this case, no strong signal is expected. Nevertheless, after practice with the normal set-up, a reasonable alignment can be achieved.

A.7.3 Scan execution and data analysis

The scan is performed in precisely the same way as a normal absorption PDS scan (see Section A.4.3). However the photodiode signal data, usually used to normalise for the illumination beam intensity, will be useless. This is because the lock-in frequency is different to the beam chop frequency. Therefore a clean data set should be extracted from a standard absorption PDS measurement, carried out across the same range and spacing of data points, and this employed to manually generate the Ratio column. Calibration for the photodiode response must also take place, and these two could be combined into a single step if many measurements were to be taken.

In analysing the data, the phase information must be considered to ascertain whether the deflection is due to an absorption or an induced transparency. Due to the opposite orientation of the sample, the phase of an absorption is opposite to that in a standard absorption PDS measurement.

A.8 Brief description

The following text appears in a paper in which results from the PDS rig were presented¹. It provides a brief summary of the rig configuration which may be useful with minimal modification in future.

"Photothermal deflection spectroscopy (PDS) spectra were measured using a setup similar to that described by Jackson et al². The sample was illuminated using a combination of a Light Support MkII 100 W xenon arc source and a CVI DigiKröm DK240 monochromator. The probe beam was supplied by a

Point Source 670 nm fibre-coupled diode laser with temperature stabiliser for reduced beam pointing noise. Beam deflections were measured using a differentially amplified quadrant photodiode and a Stanford Research SR830 lock-in amplifier. Throughout the measurement, the samples were held in a hermetically sealed fused silica cuvette filled with Fluorinert FC-104 (3M Corporation, St. Paul, MN) as a deflection medium.”

A.9 Program and data files

The LabView files required to drive the rig are located as described on the local hard disc of the control machine. Copies are also stored on the OE NT Server, in the shared folder Groups\Optoelectronics\LabView Programs\PDS Rig. This folder also contains a representative calibration file for the system response, and a trace of the lamp intensity as measured by the photodiode. These files should be updated and replaced whenever changes are made to the rig.

A.10 Late information

At the time of writing, the probe laser is being replaced and a temporary replacement is in use. The old laser lasted 6 years, although the total lasing time is not known. The new laser has cost £2000 and has already taken more than 6 months to source. The new laser design requires a surface to act as a heat sink, and the temporary laser is working well, housed *inside* the vibration-proof box, on the air-supported table. The intensity of the present laser saturates both left and right channels on the quadrant photodiode very easily, leaving a net difference signal of either zero, full left or full right, with no intermediate gradation. This is clearly unsatisfactory, so an OD 1.0 neutral density filter has been attached at the laser aperture to reduce the intensity and prevent photodiode saturation.

A.11 References

-
- ¹ A. C. Arias, M. Granstrom, D. S. Thomas, K. Petritsch, and R. H. Friend, *Phys. Rev. B-Condens Matter* **60**, 1854-1860 (1999).
- ² W. B. Jackson, N. M. Amer, A. C. Boccara, and D. Fournier, *Appl. Optics* **20**, 1333-1344 (1981).

B. The Pulse Rig - Notes

This Appendix describes the Pulse Rig and provides instructions on usage and maintenance for future users.

B.1 Part-by-part tour

This section lists the main components of the Rig.

B.1.1 Computer and software

The rig runs on an IBM-compatible PC, running Windows, and the control software runs under the LabView environment. This computer is shared between the Pulse Rig and the Test Box. The control applications include parts written by Dr N. C. Greenham, Dr D. J. Pinner, and by the author. The computer controls both drive and detection sides of the apparatus.

B.1.2 Drive side

The drive side of the apparatus includes all those parts required to deliver a voltage pulse to the test LED.

B.1.2.1 Pulse Rig

The Pulse Rig itself is a custom-built board as described in Section 3.4.4. It takes inputs at 0 V and +12 V (logic), 0 V and +HV (output pulse amplitude) and 0 V and +10 V (modulated input, to trigger pulse output). The board shown in Figure B.1, when built into its vacuum chamber, has two further components. A drain resistor (explained in Section 3.4.4.2) is placed across the output contacts in the bottom right hand corner of the image. This is required to discharge the device and drain any remaining charge during the off

phase. Additionally, a damping resistor (Section 3.4.4.3) is placed between one of the outputs and the test LED (but before the drain resistor), to critically damp the system and prevent the resonant LCR oscillations which otherwise occur.

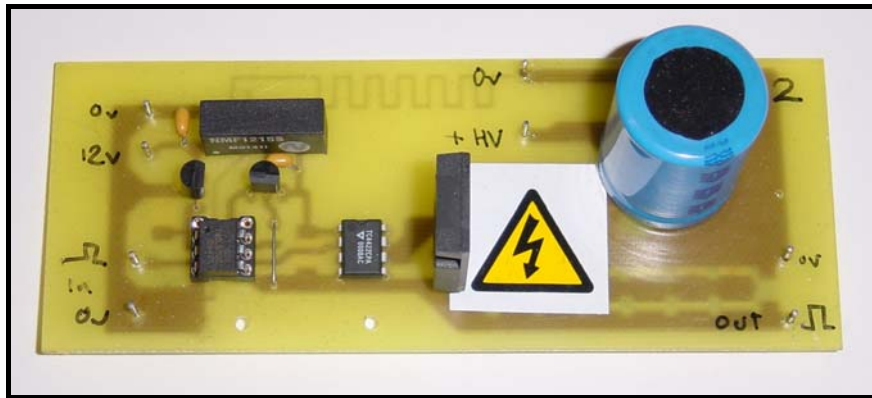


Figure B.1: The Pulse Rig board, with MOSFET located centrally.

B.1.2.2 Vacuum chamber

The Pulse Rig is housed in a vacuum chamber, shown in Figure B.2, which can be sealed and evacuated for the measurement of non-encapsulated devices. A cold finger is also present, attached to a liquid nitrogen reservoir, to facilitate low temperature measurements. For this purpose a thermocouple is available.



Figure B.2: The Pulse Rig vacuum chamber, showing Pulse Rig Board (centre), internal sample holder (left, device faces through window), current probe threaded by anode wire (left), liquid nitrogen reservoir (top left), external connections (top), voltage probe (uncoupled, top, with yellow sleeve) and vacuum connector (right).

A copper-block device holder is provided which provides contacts to all 8 pixels (and the ITO stripe) via centre-located pins. Pixel selections are made by attaching the supply contacts to the desired pair of pins. The copper block mounts on the cold finger, and provides a docking hole for the thermocouple. The disadvantage of using the vacuum chamber is that it must be returned to air pressure (and room

temperature) and opened in order to change the selected pixel. With 8 pixels on a single device this is time-consuming, and so the vacuum chamber is now used as a last resort only when low-temperature measurements are required. At all other times it serves solely as a convenient housing for the rig components.

B.1.2.3 ZIF sockets

A pair of modified ZIF (Zero Insertion Force) sockets have been prepared for the rig. These allow encapsulated devices to be easily attached to the Rig, and the pins on the rear allow pixel selection.

B.1.2.4 Red Function Generator

The main function generator provides the trigger signal for the Pulse Rig. It can be set manually using the front panel, or remotely from the computer. A Disable button on the front panel allows for quick switching of the pulse train. The adjacent “Complement” button reverses the on and off phases, which can be catastrophic when a 0.1 % duty cycle is exchanged for a 99.9 % duty cycle. This button is therefore covered to prevent accidental selection. The function generator produces two outputs. A trigger output synchronises the oscilloscope, and the main output goes to the Pulse Rig. This main output can be used to trigger the Rig (at 5–10 V on, vs 0 V off), or to drive the LED of interest directly, which allows a specified voltage (not just 0 V) to be chosen in the “off” phase. This is required for pre-bias experiments.

B.1.2.5 Green Function Generator

This function generator is used to trigger the red function generator when a train of pulses is required. No such measurements have been presented in this thesis. However the technique is available and therefore documented here. This function generator can also be operated under computer control.

B.1.2.6 Logic power supply

The logic power supply provides a 0 V and +12 V supply for the logic circuits on the pulse rig board. It also incorporates a high-voltage supply capable of providing 1 V to 300 V in 1 V increments, for use as the device drive source in the on-phase. However such high voltages are not currently required, whilst 1 V is too coarse for present experiments. This section of the power supply is therefore not currently used.

B.1.2.7 Drive power supply

This variable power supply provides the drive for the device in the on phase, with a readout accurate to 0.1 V and a range from 0 V to 150 V. The current can also be limited at will. The front-panel terminals of the PSU are festooned with electrolytic capacitors to prevent any electrical droop while the device draws power. The power supply is not computer controllable, and is therefore always specified manually

B.1.3 Detection side

The detection side comprises all those components which measure the state of the test LED.

B.1.3.1 Photomultiplier Tube

The PMT is used on its lowest sensitivity, and provides a fast response to changes in the light output from the LED. The PMT power supply is set to produce a 900 V potential for the PMT. The PMT is believed to behave linearly with output potentials of up to 50-80 mV. Any higher outputs should be suppressed by reducing the incident light intensity at the PMT aperture.

B.1.3.2 Voltage probe

A voltage probe is attached to the outputs, and produces a real-time output of the voltage presented at the LED contacts. The output must be multiplied by 10 to yield the actual voltage registered.

B.1.3.3 Current probe

An inductive current probe is provided, through which one of the two LED contacts must pass. A real-time output is obtained which must be multiplied by 5 A/V to yield the actual current registered. The probe saturates at approximately 50 μ As. In normal use, such conditions are not experienced in the Pulse Rig.

B.1.3.4 Digital Oscilloscope

The digital oscilloscope is the heart of the measurement apparatus. It has two channels, usually employed for Light and Current, but one of these can be exchanged to measure Voltage. Both PMT and voltage probe require the input impedance for that channel to be set to $1\text{ M}\Omega$, whilst the current probe requires $50\text{ }\Omega$. The

scope is usually set to average a number of measurements, typically 256, 512 or 1024. Data is acquired remotely from the PC, which causes the scope to clear its registers, collect a new set of data (with however many averages are specified by the computer) and send this data to the PC. Timebase and channel sensitivity are set locally, and are preserved during data acquisition.

Data exceeding the limits set by the top and bottom of the screen are designated out-of-range, and are automatically snapped to the screen limits. For individual measurements, or for very large excesses, this is visible as an obvious clipping at top and bottom. However for noisy data sets, the noise can be clipped, leading to a final average which contains clipped data, and is thus artificially low. This can be checked by pressing the “Clear Display” button, which clears all registers. The first few averages can then be seen on screen, and any clipping easily spotted.

B.1.3.5 Thermocouple sensor

The thermocouple sensor provides a direct readout in °C, for monitoring the device temperature during low-temperature measurements. There is no computer interface, so the value must be read off the digital display.

B.1.3.6 High-speed amplifier

A custom-built amplifier is available for pre-amplification of any one channel (usually current) before it enters the oscilloscope. The amplification magnitude is graduated in dB.

B.1.3.7 Monochromator

A CVI Digikröm DK240 monochromator has successfully been used to wavelength-select LED emission before measurement by the PMT.

B.2 Replacement parts

Barring the failure of individual components (see Section B.6.1 below), there are no consumables required during the normal use of the Pulse Rig.

B.3 Maintenance

Certain problems can arise during use of the Pulse Rig which need attention.

B.3.1 Oscillatory ringing

It is inevitable that there is an LCR component to the rig outputs, which is susceptible to oscillatory ringing effects. A damping resistor is included in series with the output, to critically damp the system. This should be varied according to the nature of the device under test.

B.3.2 Wire failure

The low-R silver coax cables used in parts of the rig are robust only when protected from folding by their plastic sleeves. When the cable ends are deliberately separated (e.g. to lead to a device) the softness of the silver becomes an issue and these wires are prone to fatigue, especially where they meet solid connectors. To avoid repeated replacement, the wires can be coated with a rubber cement, especially at junctions, to prevent excessive flexing.

B.4 Experimental procedures

The general operation is described in Section 3.4.4.

B.4.1 Software

The programs required to drive the Rig are located on the C drive of the adjacent PC. The LabView environment should first be started, and then the desired program or programs for drive and detection loaded. A series of such programs are available.

B.4.1.1 Basic data acquisition

The latest version of this program is called Pulse5c.vi. This VI was written by the author, but makes use of the oscilloscope data acquisition VI written by Dr N.C. Greenham. The front-end is shown in Figure B.3.

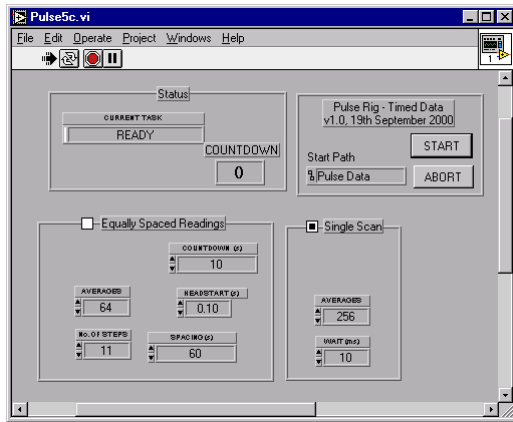


Figure B.3: Basic data acquisition VI.

After loading, the LabView Play button must be pressed to activate the VI. Two options are then available, selected by radio button. The right-hand option, “Single Scan” is the most basic method of data collection. The number of averages to be collected is specified, as is a “Wait” time in milliseconds (largely redundant) for specifying any required delay between starting the process and beginning the collection of real data.

Pressing Start, the user is then prompted to specify a filename. On accepting the filename, the process begins, starting with the specified Wait and then collecting the requisite number of averages by querying the oscilloscope. The scope clears its registers and collects a fresh set of data. All other scope parameters are unchanged by this interrogation.

“Equally Spaced Readings” allows a specified number of separate data sets to be collected, at specified time intervals. Since each measurement takes some time to acquire, the intervals specified are between successive starts-of-measurement, rather than defining the gap between measurements. This allows for accurate indication of the total time elapsed. Once again the required number of averages must be specified. Additionally a number of measurements, and a spacing between measurements (in seconds) are chosen. A “Headstart” parameter allows each measurement to be triggered a specified number of seconds early, so that averaged measurements (which can take tens of seconds to acquire) can be made not to lag the recorded time of measurement. A countdown timer, defaulting to 10 s, allows the operator to begin device drive manually at the exact moment of the start of the first measurement.

On pressing the Start button, the user is prompted to specify a folder name into which the data files will be placed. Each data file will be named according to a “00h00m30s” style format. When the folder name has been accepted, the countdown begins with a visual and audio prompt, so that the user can accurately determine the moment at which device drive should begin.

B.4.1.2 Data acquisition through monochromator

A program entitled Pulse.vi exists to allow data to be collected through a monochromator. This set-up allows both spectral and temporal transients to be elucidated, as demonstrated in Figure B.4. This VI was written by the author, but makes use of the oscilloscope data acquisition VI written by Dr N.C. Greenham and the monochromator access VIs written by Dr D.S. Thomas.

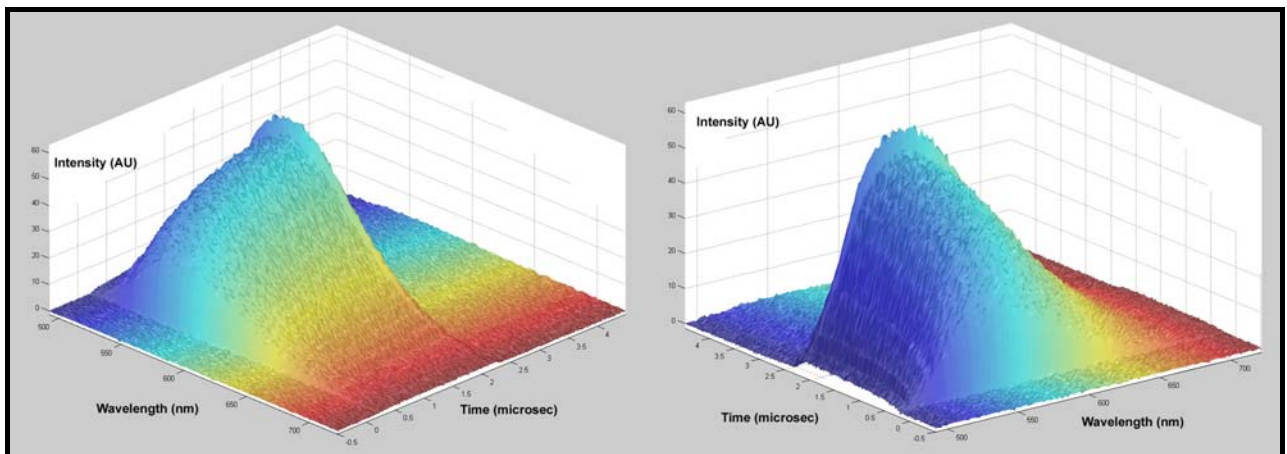


Figure B.4: Sample output from the monochromated transient experiment.

Plotted in MatLab and greyscale/colour images merged in Adobe Photoshop.

A CVI Digikröm DK240, identical to that used in the PDS Rig, was used to set up this experiment. This monochromator has a hand-held console used to specify aspects of the monochromator set-up, such as slit width. The wavelength and (if desired) the grating is chosen under computer control. The program, seen in Figure B.5, is designed to automatically select the most suitable grating for the chosen wavelength. (Grating 1 below 830nm, grating 2 below 1600nm, grating 3 otherwise.) In practice, therefore, only grating 1 is used. Nevertheless, a “Freeze Grating” toggle is available to prevent the computer from changing gratings.

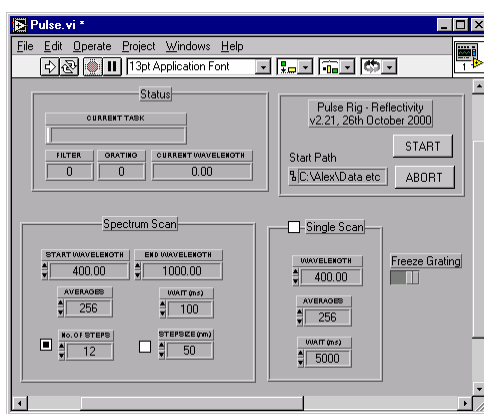


Figure B.5: Front-end for monochromated data collection.

Again, the LabView Play button must be pressed to initialise the VI. Three radio-button options are available. “Single Scan” works identically to the single scan option in the basic acquisition program, except that it first directs the monochromator to the specified wavelength. A single file (name chosen by the user) is generated by this option. “Spectrum Scan” is similar to the equally-spaced readings option in the basic acquisition program, except that instead of time-steps, wavelength steps are specified. A start and end wavelength is chosen, along with either a number of steps, or a step size. A series of files, named for example “520nm” are generated in the folder designated by the user.

B.4.1.3 Multiple pulse operation

The latest version of this program, seen in Figure B.6, is titled BOTH HPsAc.vi. It is used in the special situation where a train of a specified number of pulses is required, repeated at a specified interval. This VI was written by Dr D.J. Pinner and extensively modified by the author.

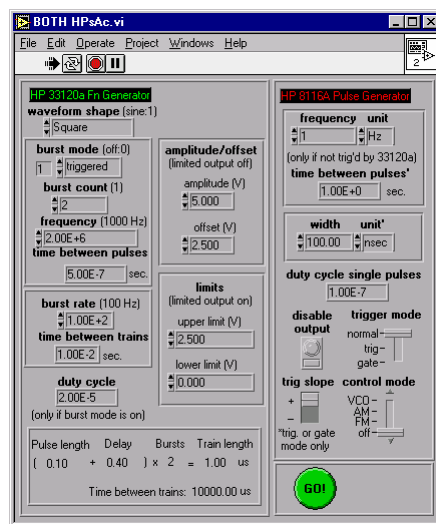


Figure B.6: Multiple pulse control VI.

Again, the VI must be initialised by pressing the LabView Play button. When Burst Mode: Triggered is specified, the lower-left panel turns on, providing a helpful summary of the currently-specified pulse train. This is the configuration required to achieve multi-pulse trains. The width of each individual pulse is specified through the red function generator, by using the second panel on the right hand side of the VI window. The number of pulses in each train is specified under “Burst Count” on the left hand side of the window. The time between *pulses in a train* (start-to-start) is specified as a frequency in the “Frequency” box on the left hand side. The box immediately below changes to reflect the implied time period. The *time between trains* (start-to-start) is also specified as a frequency, in the “Burst Rate” box. Again, the implied time is automatically calculated below. The duty cycle in the currently selected scheme is specified near the

bottom left of the window. The summary panel below shows a numerical schematic of the selection, which is underlined in red if a clash occurs between adjacent pulses or adjacent trains.

When the scheme is ready, it can be uploaded to the two function generators by pressing the green “Go” button. For a second or more during this process, the red function generator output goes high, putting the test LED into DC at the currently selected drive voltage. This could potentially destroy the LED, so it is recommended to turn off the PSU while the function generators are programmed. After automatic programming of the function generators, they are left in Remote mode. The front panel buttons are therefore disabled until the “Local” button on the front panel is pressed.

B.4.2 Encapsulated devices

Encapsulated devices are straightforward to measure. The device legs are inserted into the ZIF sockets, and the Pulse Rig output connections slid onto the chosen pins on the rear of the sockets, to specify the correct pixel. If a current measurement is required, one of the connections should be threaded through the hole in the current probe. The LED is then held in place, usually with Blu-Tac in a vertical orientation on an *xyz* translation-stage, and the PMT manoeuvred into position. When required, neutral density filters (to reduce the incident light intensity) are affixed with Blu-Tac directly to the front of the PMT. The apparatus is covered with a heavy black cloth to reduce stray light, and only then should the PMT be powered up.

B.4.3 Non-encapsulated devices

Non-encapsulated devices must be transported through air into the Pulse Rig vacuum chamber. Silver dag contacts should have been made centrally, and the device should be placed contacts-down onto the copper-block device holder, and the screws tightened. The pins on the holder are sprung to ensure good contact. The copper block is attached to the cold-finger of the cryostat, to hold it in place, and if the cryostat is to be used, the thermocouple is inserted into the hole in the side of the block. Pixel selections are made by attaching the Pulse Rig outputs to the chosen pins. The chamber is sealed by affixing the cover, and then pumped down with the trolley-mounted turbo pump. If required, liquid nitrogen can be introduced to the cryostat. The PMT can now be positioned against the viewing window, covered, and powered up.

B.4.4 Drive and data collection

The drive cycle is specified on the front panel of the red function generator. In order to correctly trigger the Pulse Rig, 10 V (or at least 5 V) pulses are used, with 0 V in the off phase. This is specified by selecting

“AMP” = 5.0 V and “OFS” = 2.5 V. Pulse length and repeat rate can be independently varied from the front panel. The function generator output can be halted and re-started by use of the “Disable” button. Pulse height is specified on the variable PSU.

The oscilloscope must be adjusted to display the region of interest. Several adjustment modes are available (eg timebase, channel), and within each mode the column of buttons at the left takes on the function detailed on the adjacent section of the screen. The touch-wheel allows the currently-selected parameter to be varied up or down. When the desired data can be seen on the scope screen, data acquisition can proceed by use of one of the VIs for that purpose.

B.4.5 Direct drive

In some circumstances it is desirable to drive the test device directly off the red function generator, bypassing the Pulse Rig board. This is particularly useful when a pre-bias is required, since the red function generator can be used to specify a bias for both “on” and “off” states. A separate BNC connector is provided on the top of the Pulse Rig chamber, directly wired to a pair of slip-on contacts identical to those emerging from the Pulse Rig itself. The red function generator signal cable can be moved to this position to effect direct drive.

B.5 Data processing

The generated data files are very simple, containing time (seconds) in column one, and signal level (Volts) in columns two and three. Voltage and current data must be converted using the factors described in Section B.1.3 above. Light intensity data is currently not calibrated, although with the aid of a known source, this could be done.

B.6 Problems during operation

A number of known problems occur from time to time and can be easily isolated.

B.6.1 PSU fuse

The variable PSU is internally fused, and this fuse sometimes fails. A spare should be kept near the Rig.

B.6.2 Electrical interference

Direct electrical interference through the metal table can cause the PMT output to become slewed. Isolating the PMT by inserting a sheet of paper between the table and the metal clamp seems to help. The PMT housing should also be prevented from contacting the aluminium Pulse Rig chamber.

B.6.3 Failure of multiple pulse trains

The trigger level on the red function generator is easily disturbed, and may have to be re-adjusted to ensure accurate triggering.

B.7 Program files

A full set of the latest VIs for driving the rig are kept on the OE NT Server under Groups\Optoelectronics\LabView Programs. These should be kept up-to-date.

C. The Test Box - Notes

This Appendix describes the maintenance and detailed operation of the Test Box. An overview of the Test Box is presented in Section 3.4.5, including full circuit diagrams. That Section also includes a review of the possible experimental arrangements. This Appendix provides further detail.

C.1 Part-by-part tour

The Test Box comprises the box, the drive apparatus, the measurement apparatus and the control computer.

C.1.1 Computer and software

A PC-compatible machine running the LabView environment is currently responsible for controlling the Test Box. This computer is shared with the Pulse Rig. The computer does not interface with the Test Box, but talks to various GPIB-enabled source/measure units which themselves supply or probe the Test Box.

C.1.2 The Test Box

The Test Box is housed in a die-cast box with multiple external connections and controls, as well as internal access to the LED mounting point, as seen in Figure 3.10. The box provides a socket for one large encapsulated device to be tested, an internal variable-voltage power source to drive the device under constant-voltage DC conditions, and a large-area Si photodiode with a smoothed output, to measure the light intensity. Further controls allow pixel selection (knob), complete device disconnection (switch), burst reconnection (sprung button), internal voltage supply control (knob) and external source selection (switch). External connectors are provided for power input (0 V, ± 12 V), external drive (labelled “Pulse”), DC Voltage (for sampling the currently selected voltage from the internal source) and Output Voltage (for measurement of the output from the photodiode circuitry).

C.1.3 Digital multimeters

Two HP 34401A digital multimeters are used in the rig. One connects to the photodiode output of the Test Box, and is used to measure the light intensity. The other is optional, and can be used in the case of constant current measurements to simultaneously monitor the applied voltage.

C.1.4 Electrometer

A Keithley 6517A electrometer can be used as a switchable constant voltage source. This is useful when a computer-controlled drive modulation is required. The electrometer is also used in charge measurement mode to monitor the charge backflow from a device after driving.

C.1.5 Constant current source

A Keithley 220 programmable current source is used when constant-current drive is required. It does not have a GPIB interface, but can be tripped on and off by using the electrometer voltage-source to provide a switching signal. Alternatively it can be manually initialised at the start of a measurement.

C.1.6 PSU

The PSU provides the power required for the internal voltage regulator on the Test Box board, as well as the op-amp in the smoothing circuitry.

C.1.7 The Pulse Rig

The Pulse Rig, or alternatively just the red function generator from the Pulse Rig, can be used as an external source to monitor the long-term EL evolution under pulsed drive.

C.1.8 Adaptors

There are a number of adaptors designed to modify the operation of the Test Box.

C.1.8.1 Small substrate adaptor

This adaptor mimics the form factor of the large substrates, but contains sockets for the insertion of small encapsulated devices, as shown in Figure C.1.

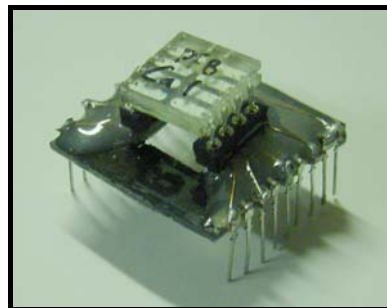


Figure C.1: Small substrate adaptor, with a small device mounted in place.

Large devices have a common cathode, and pixel-specific anode, whereas small devices have the reverse configuration. Therefore the internal voltage source is not suitable for use with this adaptor. It may be advantageous to build a new switch into the box to allow polarity reversal.

C.1.8.2 Pulse input adaptor

This adaptor, seen in Figure C.2 (front), modifies the PYE-type external source input, so that it will accept the slip-on contacts provided by the Pulse Rig.

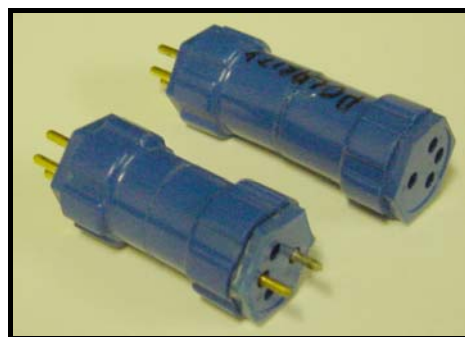


Figure C.2: Pulse input adaptor (front) and polarity adaptor (back).

C.1.8.3 Polarity reversing adaptor

This adaptor, seen in Figure C.2 (rear), reverses the polarity of the external input. When switching between large and small substrates, this avoids having to re-configure the outputs on the source unit.

C.2 Replacement parts and maintenance

There are no routine consumables for the rig, but certain parts require periodic attention.

C.2.1 Large-area Si photodiode

The photodiode performance may degrade, particularly if surface contamination becomes a problem. Replacements are kept near the Test Box.

C.2.2 Electrolytic feedback capacitor

In certain circumstances it has been useful to temporarily remove the electrolytic capacitor used for averaging purposes in the op-amp circuit. The presence of this capacitor should be checked before measurements are taken.

C.2.3 Feedback resistor

Experiments have shown that the feedback resistor on the Test Box is currently, at $10\text{ k}\Omega$, not large enough to provide adequate amplification through the op-amp. This resistor should be changed at the earliest opportunity for a $100\text{ k}\Omega$ or $1\text{ M}\Omega$ component.

C.2.4 Op-amp circuitry

The op-amp circuitry should be reviewed to ensure optimal operation. It appears that when the op-amp is not powered, the magnitude of signal from the photodiode alone exceeds that seen when the op-amp is in use. There is clear scope for improvement in the function of this part of the rig, and although it functions adequately, the performance should be much improved if this is addressed.

C.3 Experimental procedure

The operation of the Test Box is largely described in Section 3.4.5. Further details are given here.

C.3.1 Software

The latest version of the LabView controller application is entitled testbox8.vi. This VI, pictured in Figure C.3, was written by the author to control the experiment. Since the Test Box is designed to measure time-evolution of device parameters, there is no option for a “single scan”. All measurements are part of an “Equally Spaced Readings” series. The software is designed to measure a series of data points in the on-state, and optionally to rest the device for a period and then repeat the measurements. The “Cycles” setting specifies the number of on/off cycles to be tested, and for a single DC measurement this should be set to 1.

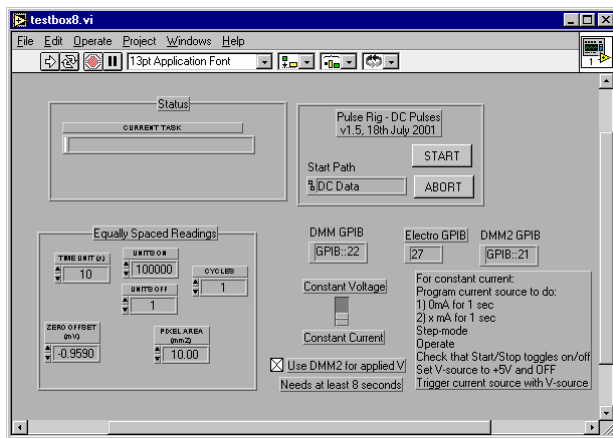


Figure C.3: LabView interface for Test Box.

Timings are based around a standard “Time Unit” specified in the designated box. Measurement then proceeds at time intervals based on this unit, with measurements taken at the end of each unit until the specified number of “Units On” has elapsed. This is followed by a number of “Units Off” during which no measurements are taken. The time unit should be set no lower than 5 s to allow time for data acquisition.

The “Zero Offset” box allows the zero-error on the Test Box to be compensated. With the Test Box closed and the device inactive, the dark signal should be read off the DMM and entered into this box. The GPIB addresses of the three addressable units are specified in the relevant boxes. Note that the format for the Electrometer GPIB address is different from the format for the two DMMs. “DMM” is designated as the DMM which measures the photodiode output. “DMM2”, when present and when the relevant check-box is crossed, is the one which measures the actual applied voltage during constant-current measurements. The “Pixel Area” box is redundant.

C.3.2 Experiment configuration

Of the three measurement schemes outlined in Section 3.4.5.2, the required configurations are.

A) Constant Voltage

DMM required, and “Constant Voltage” selected on VI. Voltage is provided internally from Test Box source, or externally if desired, but not under computer control.

B) Modulated Constant Voltage

DMM and electrometer required, with “Constant Voltage” selected on VI. Voltage is provided externally by the electrometer’s voltage source. This must be set to the desired voltage and then de-activated (on the front panel) before measurement commences. The driver application will automatically turn the test LED on and off according to the drive scheme specified.

C) Modulated Constant Current

DMM required (DMM2 optional). Electrometer voltage source set to provide +5 V to the current source trigger input, and then de-activated. Current source must be put in “Step” mode, with the first step specified as 0 mA for 1 s, and second step specified as x mA for 1 s, where x is the required current, calculated to provide the desired current density for the size of the currently selected pixel. Voltage limits should be set as required. The “Operate” light should be activated, and a check made that the “Start/Stop” button trips the current source on and off. The source should be left in the off state. The driver application will then use the electrometer voltage source to trip the current source on and off according to the drive scheme specified.

When DMM2 is to be used to acquire applied voltage data, the box should be checked and the basic time unit set no lower than 8 s, to allow time for data acquisition from both sources. For constant current measurements without modulation, it is sufficient to omit the electrometer, and trigger the current source manually. The VI will not fail even if it receives no response from the electrometer.

C.3.3 Running a scan

The test LED should be placed in the rig, using the adaptor if necessary, and the source/measure units configured to provide the required drive source. The chosen pixel should be selected on the front of the Test Box. Only after the lid is closed should the box be powered up. The experiment can then be begun under computer control.

C.4 Data analysis

Data files contain two or three columns. The first column is the time data, the second column is the luminance data, and the third column, when present, is the applied voltage. If absolute values of luminance are to be extracted from the data, then the Test Box must be recalibrated after any changes to the apparatus.

C.5 Charge backflow experiment

The charge backflow experiment is performed using the Test Box and the electrometer, first driving the device and then draining it through the electrometer. The most effective method is to connect the electrometer to the external drive contacts, and then drive the device using the internal voltage source. The switch can then be flipped to change almost instantaneously from drive to drain.

The LabView program required is called electro2.vi, shown in Figure C.4, and is based on the Pulse Rig data acquisition VI. (The “Averages” boxes are still present, and are redundant. The “Single Scan” option is also essentially redundant, since this experiment is only useful when a series of measurements are collected.)

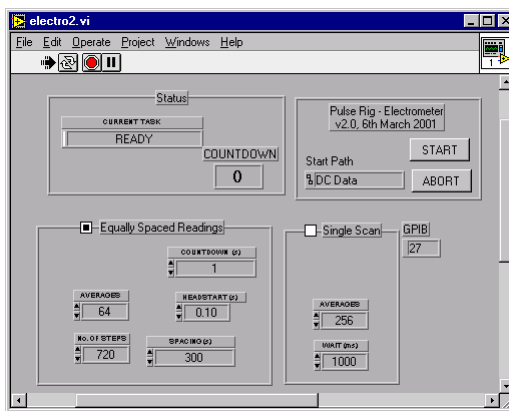


Figure C.4: Charge backflow controller application.

The electrometer must be manually configured into Q-mode, since the VI acquires data by reading and interpreting the front-panel display contents, rather than requesting a particular data type. The resulting data file contains a pair of columns, detailing the time of measurement and the accumulated charge measured.

An underlying approximately linear drift is present in such measurements, and should be eliminated during the data processing stage.

C.6 Program files

Up-to-date copies of all LabView programs should be kept on the OE NT Server in the Groups\Optoelectronics\LabView Programs folder.

